A Spitzer Survey of Asymptotic Giant Branch Stars: Dust Production and Mass Loss at Low Metallicity

A THESIS

SUBMITTED TO THE FACULTY OF THE GRADUATE SCHOOL

OF THE UNIVERSITY OF MINNESOTA

BY

Martha L. Boyer

IN PARTIAL FULFILLMENT OF THE REQUIREMENTS

FOR THE DEGREE OF

DOCTOR OF PHILOSOPHY

December 2008

Acknowledgements

It takes a village to raise a child, or a graduate student in this case. I would never be where I am today without the help and support of many people. Thanks to all of the members of the Department of Astronomy (faculty, staff, and students) for all of the support over the years. I've also had the luck to work with not one, not two, but THREE advisors: Chick, Bob, and Evan. Chick & Bob, thanks for sticking throughout my entire graduate (and even some of my undergraduate) career. I owe a great debt of gratitude to Bob for allowing me to launch my research with his *Spitzer* data - without it, I would still be trying to figure out what my thesis should be about. Thanks Chick for keeping me on track and connecting me to the right collaborators. Thanks to Evan who, as a recent addition to the "Brain Trust", helped me bring it all together. I should also point out that I have Evan to thank for getting into this whole mess in the first place. It was after taking his Astro 1011 class that I decided to apply for some Astro REUs, launching my entire career. Without that nudge, I'm sure I would have majored in a different, probably more sensible subject.

Next, an enormous amount of thanks is due to the folks over at Keele University in the UK. Specifically to Nye Evans, Jacco van Loon, and Iain McDonald. I worked very closely with Jacco and Iain especially and would have gotten absolutely nowhere without their innumerable edits, comments, and late-night email conversations. Thanks Jacco for being the unofficial forth member of the "Brain Trust". Thanks also to my other collaborators: Karl Gordon, Andrea Dupree, and Pauline Barmby.

In my opinion, my fellow grad students (and the occasional post-doc) have done as much as any advisor to help me along both professionally and personally. Thanks again Iain - it was, as we Americans would say, awesome to have another grad student to talk to who was working on the same projects. A big thanks to the U of M astro grads, especially the IR lab crew: Andrew, Dale, Gerry, Mike, Tea, and Geoff (the unofficial grad student) who kept me coming into work every day with the promise of shenanigans. Special shout-out to Andrew: sorry about the sandals, dude.

Last, but not least, thanks to Mom and the rest of the Boyer/Rowan clan for your encouragement, and thanks to Mike for your love and support.

A Spitzer Survey of Asymptotic Giant Branch Stars: Dust Production and Mass Loss at Low Metallicity

by Martha L. Boyer

Under the supervision of Robert D. Gehrz, Evan D. Skillman, & Charles E. Woodward

ABSTRACT

We conducted infrared (IR) surveys of ten Galactic globular clusters (GCs) and eight Local Group dwarf irregular galaxies using the *Spitzer Space Telescope*. The main objective of these surveys is to further the understanding of dust production in low metallicity environments akin to the early Universe. In GCs, we investigate the stars with IR excesses, attributed to dust, and the intracluster medium (ICM). The GC M15 is the most metal-poor Galactic GC, and is ideal for studying dust production at metallicity less than 1% solar. The most massive Galactic GC, ω Centauri, harbors three distinct populations of differing metallicities, providing the opportunity to study dust production at three metallicities within the same environment. The large population of dusty Asymptotic Giant Branch (AGB) stars present in the eight observed Local Group dwarf galaxies allows a statistically significant study of dusty stellar mass loss at a broad range of metallicities (2% – 19% solar). In all observed systems, we find large populations of dust enshrouded stars and, in some cases, dusty interstellar medium. The surplus of both interstellar dust and the dust producing stars in M15 is surprising, given its extremely low metal-content. No significant amount of ICM dust is detected in any other GC observed, suggesting that ICM dust does not survive long compared to its production rate and is thus a part of a stochastic process. In ω Cen, we see no

difference in dust production between the three populations, and overall, we see that dust is not formed in larger quantities than seen in M15. In dwarf galaxies, we see that circumstellar dust is prolific enough to create at least a small population of completely optically obscured AGB stars in each galaxy, regardless of the galaxy's metallicity, but higher metallicity galaxies tend to harbor more stars with slight IR excesses. These results suggest that dust production is not prohibited at very low metallicity, although it may be produced in smaller quantities.

Table of Contents

List of Tables

List of Figures

Chapter 1

Introduction

1.1 We are all Star Dust: Mass-losing Stars as the Drivers of Galactic Evolution and Enrichment

About 13 billion years ago, just after the Big Bang, the Universe was composed mostly of hydrogen and helium atoms, with traces of lithium and beryllium. The building blocks of life and planets, namely carbon, oxygen, nitrogen, iron, and other heavy elements (hereafter referred to as metals) did not exist. We know that metals are formed within the cores of stars and in supernovae and novae explosions, but how did these newly formed elements get out of stellar cores and into planets and interstellar gaseous nebulae? Supernovae and novae deserve partial credit for dispersing heavy elements around the Universe through energetic explosions, but it is the low mass stars that will never explode that are the real culprits. These stars, called Asymptotic Giant Branch (AGB) stars, quietly inject enriched material into their host galaxies, driving the evolution of the Universe by making it a more metal-rich (and planet-rich) place.

Most stars less massive than about 8 $M_{\odot}$, i.e., the vast majority of stars, will become AGB stars towards the end of their lives. During this phase of its evolution, a star develops a dense stellar wind that slowly expels up to 60% of the star's mass. The

expelled material is enriched in metals that were formed in the star's core, and this material eventually mixes with the Interstellar Medium (ISM) where it becomes available for the formation of new stars and planets. These newly formed, metal-enriched stars eventually evolve into AGB stars themselves, become even further enriched, and expelling new metals into the ISM. It is through this cycle that galaxies evolve, becoming more metal-rich with each passing generation of stars. AGB stars are the main source of enriched material and are therefore a major driver of galaxy evolution.

In addition to strong mass loss, AGB stars have another major distinction: they are strong producers of dust, made from grains of heavy metals. Dust grains are essential for planet formation, but dust cannot form on its own in the ISM due to the low density of dust-forming material. Dust can form in energetic explosions like supernovae, but these events often end up destroying the bulk of the dust they produce. It is only in the cool, dense outer layers of AGB stars that dust can form and survive in large quantities, and through mass loss, this dust ends up in the ISM (Gehrz 1989).

Dust production in the primordial Universe, before metals existed in large quantities, is not well understood. Traditionally, astronomers believed that environments containing very few metals cannot harbor much dust, but recent observations, including the observations discussed in this dissertation, reveal copious amounts of dust in these environments, demonstrating that there is still much to learn. One of the major objectives of this dissertation is to provide an understanding of how metal content affects dust formation. Through the study of AGB stars in the environments described here, which cover a broad range of sub-solar metallicities ([Fe/H] < 0), we hope to gain insight into how dust formed in the early Universe.

1.1.1 Asymptotic Giant Branch Stars

All low- to intermediate-mass stars ($0.8\ M_{\odot} < M < 8\ M_{\odot}$) go through three basic evolutionary phases before ending their lives as compact remnants. The first of these

phases occurs shortly after a star has exhausted hydrogen in its core on the Main Sequence, and begins to fuse hydrogen in a shell surrounding an inert He core. While in this phase, stars are known as Red Giants (RGs). The He core contracts during this phase, eventually reaching a temperature hot enough ($T \approx 10^8$ K) to ignite the He. Stars are then known as core He-burners, referred to as Horizontal Branch or Red Clump stars. In this phase, stars also burn hydrogen in a shell around the He-burning core. Once the He core is exhausted, the star will evolve towards the AGB, where it will burn hydrogen and helium in concentric shells around a tiny, degenerate C/O core. See Figure 1.1 for an illustration of the evolution of a 1 $M_\odot$ star.

Stars spend roughly 10^6 yr on the AGB and divide their time into two phases: the Early AGB (E-AGB) and the thermally pulsing AGB (TP-AGB; Habing & Olofsson 2003). During the E-AGB, the star is burning He in a shell around the core, but the extra energy output causes the star to expand, subsequently extinguishing the concentric H-burning shell. The convective envelope is then able to reach into the now inert H-shell, causing "second dredge-up" of H-burning products to the surface in AGB stars more massive than 4 $M_\odot$ (first dredge-up happens on the Red Giant Branch). Following second dredge-up, the H-shell reignites. Less massive AGB stars skip this second dredge-up, instead establishing an actively burning H-shell soon after exhaustion of core Helium.

The TP-AGB phase is marked by instability of the He-burning shell, caused by both the high temperature sensitivity of He-burning and the physical thinness of the shell (Lattanzio 2002). Changes in the energy input from the He-shell result in thermal pulses, which are characterized as the turning on and off of intershell convection and of the H-burning shell. While the H-shell is inert, the convective envelope can penetrate the H-shell, initiating the "third dredge-up" of material not only from the H-shell, but also from the He-shell, arising from intershell convection. AGB stars of all masses experience this third dredge-up. Thermal pulses occur periodically as the star ascends

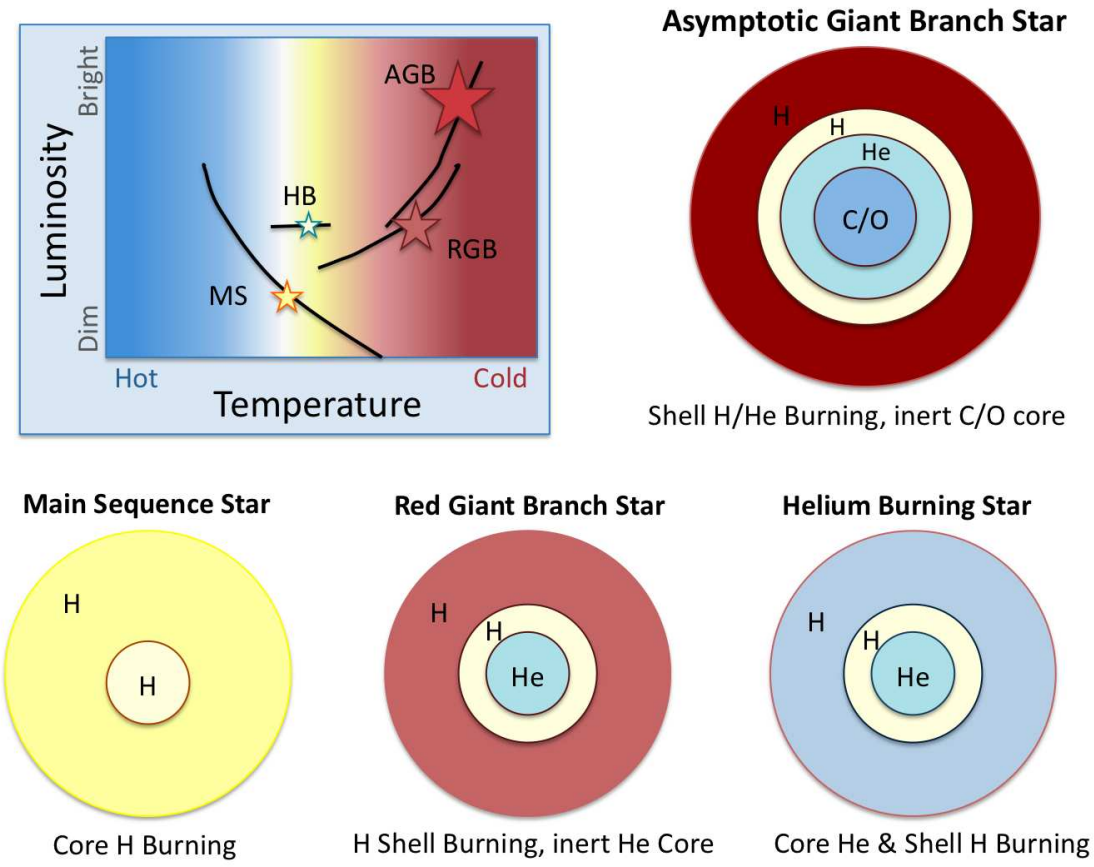

Figure 1.1: The Hertzprung-Russell diagram and the interior structure of AGB stars. Stars on the Main Sequence (MS) burn hydrogen in their cores before evolving to the Red Giant Branch (RGB) where they burn hydrogen in a shell around an inert helium core. Stars then evolve into helium-burning (HB) stars either on the Horizontal Branch or in the Red Clump, where they burn hydrogen in a shell around a helium-burning core. The final stage of stellar evolution is on the Asymptotic Giant Branch (AGB), where stars burn hydrogen and helium in shells around an inert C/O core.

the AGB.

The third dredge-up enriches the outer envelope of the star with Li, C, N, F, and s-process (or slow-neutron-capture-process) elements. The composition of the envelopes are generally divided into two groups: carbon-rich and oxygen-rich. Carbon stars are slightly cooler, with median temperatures of 2800 K, 400 K less than their O-rich counterparts. The cool temperature and high concentration of metals in AGB star envelopes provides the ideal environment for dust condensation.

1.1.2 Mass Loss

While the AGB phase of a star's evolution is one of the shortest ($\sim 10^6$ yr), it is also the most dramatic. AGB stars typically undergo radial pulses caused by an imbalance between gravitation and radiation pressures. These pulses cause variability of several magnitudes in optical wavelengths, each pulse lasting one to a few years. Pulsation allows dust condensation by creating high density regions in the cool outer regions of the circumstellar envelope. Radiation pressure on the dust grains and momentum coupling between the grains and the gas results in the formation of an additional slow, dense wind (Gehrz & Woolf 1971). This wind causes the star to lose 20% to 60% of its mass, making mass loss more important than nuclear burning in determining the star's characteristics and further evolution (van Loon 2006).

Astronomers have generally assumed that radiation pressure on dust grains is the dominate driver of AGB winds. If this is indeed the case, then low-metallicity stars that produce less dust should not be losing mass as efficiently as their higher metallicity counterparts. Substantial effort has gone into determining a metallicity dependence on mass loss (for a review, see van Loon 2006), but a consensus has not yet been reached. Some recent works (Schröder & Cuntz 2005; McDonald & van Loon 2007) have suggested that dust-driven winds may only be one part of a broader picture. Acoustic waves in warm chromospheres may also play a large role in driving winds

that may cause low-metallicity stars to lose mass *more* efficiently due to their warmer temperatures (Schröder & Cuntz 2005).

Due to limited observing capabilities, observations of mass-losing AGB stars have, until recently, been restricted to the Galaxy and the Magellanic Clouds. These observations have driven the development of stellar models, and since these environments are relatively enriched in metals, models are biased towards high-metallicity stars. Low-metallicity AGB star mass loss is therefore not well fit by current stellar evolutionary models, and new observations in this dissertation are among a growing data set designed to improve these models.

1.2 Stellar Populations: Star Clusters to Dwarf Galaxies

Two of the best environments in which to study low-metallicity AGB stars are Galactic globular clusters (GCs) and Local Group dwarf irregular galaxies (see Figures 1.2 and 1.3 for an map of the Local Group and the Galactic neighborhood). GCs were formed during the assemblage of the Galaxy and are thus highly evolved stellar systems. The vast majority of a GC's stellar population ($10^4 - 10^6$ stars) is formed during a single star-forming event, ensuring a uniform composition and distance. Since GCs are highly evolved and coeval, the stars remaining today have roughly the same mass. Galactic GCs orbit the Milky Way within ≈100 kpc, making them some of our Galaxy's nearest neighbors and allowing observations that can detect and spatially resolve stars to well below the tip of the Red Giant Branch. GCs span two orders of magnitude in metallicity, down to $\lesssim 1\%$ solar, which makes it possible to determine how metal content affects mass loss and other stellar characteristics. The stars in GCs are old, low-mass stars, which have less dramatic dust production and mass loss than their high-mass counterparts. However, the majority of stars in the Universe are low mass stars, making GCs an ideal place to measure mass return from one of the most abundant stellar types.

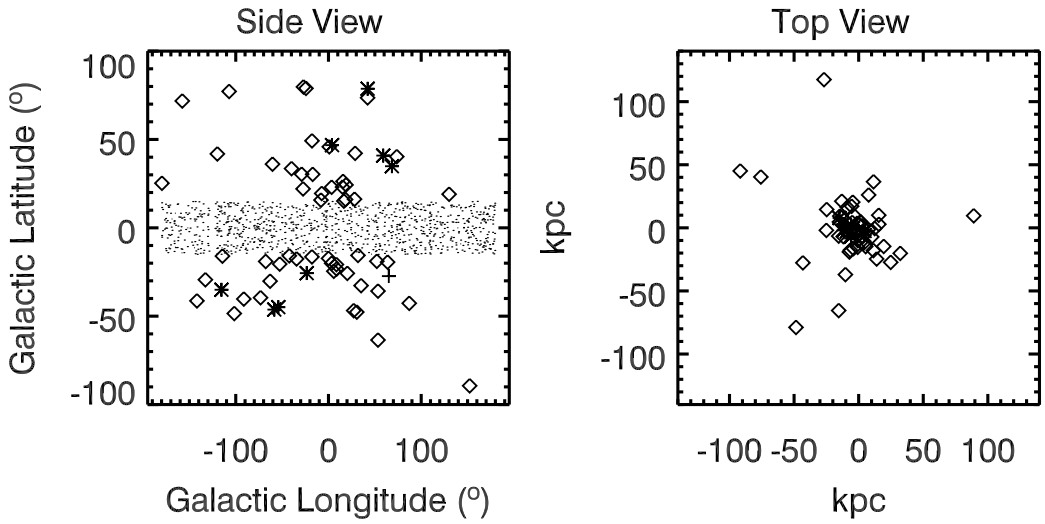

Figure 1.2: Distribution of the majority of Galactic GCs around the Milky Way. The shaded region shows the location of the Milky Way disk. Asterisks are GCs that have been observed with *Spitzer*, and the plus symbol is M15.

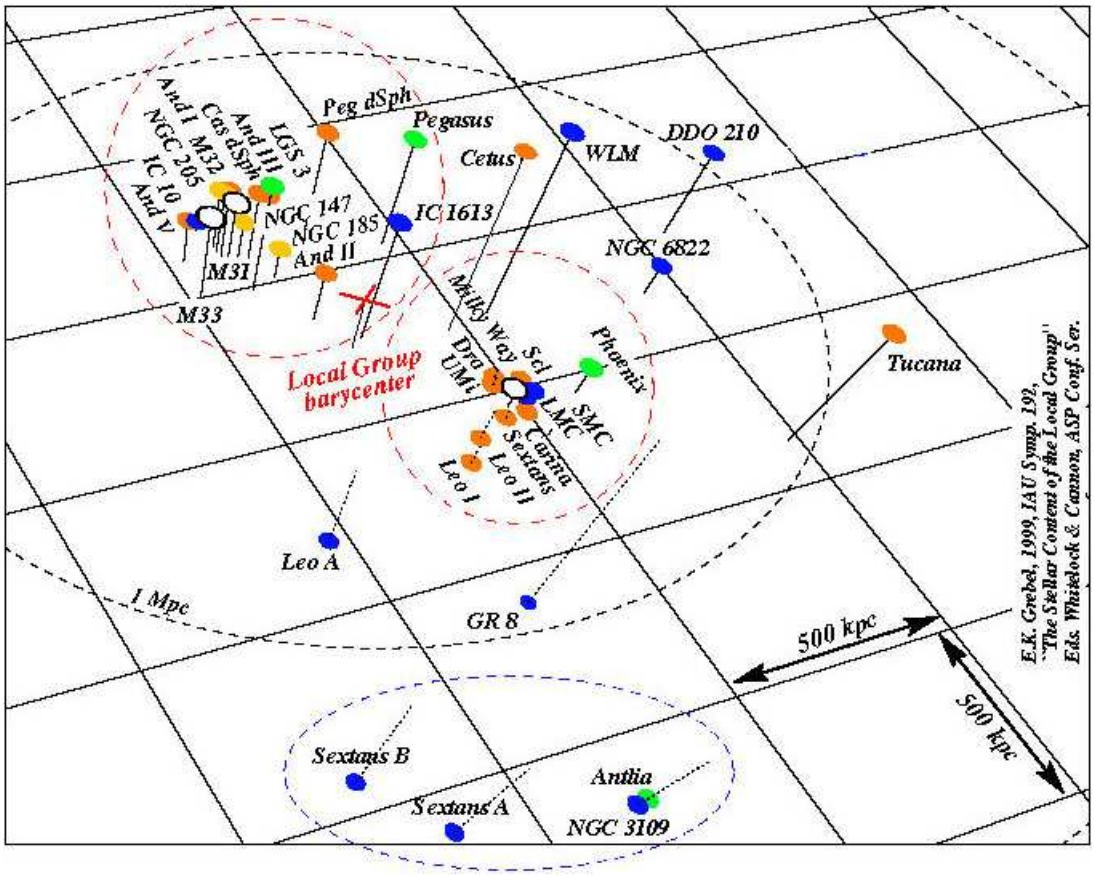

Figure 1.3: Map of the Local Group. Dwarf irregular galaxies discussed in this thesis are marked as blue and green dots. (From E.K. Grebel, 1999, IAU Symp. 192)

Unlike GCs, dwarf irregular galaxies are still forming new stars, making them ideal for studies of AGB stars over a broad mass range. Dwarf irregular metallicities span a similar range as GCs, allowing for studies of higher mass stars at very low metallicity. While the dwarf irregulars studied in this thesis are relatively nearby (they are within what is known as the Local Group), their larger distances makes them more difficult to observe than GCs. Luckily, the high luminosity of mass-losing AGB stars ensures that at least the most extreme stars remain detectable. Dwarf irregular galaxies are also important because they allow comparisons of mass-loss rates of AGB stars to star forming rates and interstellar gas and dust content. GCs, on the other hand, have no current star formation, and virtually no ISM (Hopwood et al. 1999; van Loon et al. 2006b; Barmby et al. 2008; Matsunaga et al. 2008).

1.3 The Infrared and The *Spitzer Space Telescope*

Wein's law states that the wavelength of the peak emission from a source ($\lambda_{\rm max}$) depends on its temperature (T): $\lambda_{\rm max} = (2900\ \mu{\rm m\ K})/T$, with hotter objects peaking at bluer wavelengths and cooler objects peaking at redder wavelengths. The underlying photospheres of AGB stars are cool ($T\ \approx\ 2000-4000$ K), corresponding to peak emission wavelengths of 0.7 μm $\lesssim\ \lambda_{\rm max}\ \lesssim 1.5\ \mu$m and placing AGB star peak emission in the near-infrared (IR) portion of the electromagnetic spectrum.

AGB stars with dusty atmospheres are more complicated. The dust itself may be heated to temperatures that push secondary peak continuum emission deeper into the IR portion of the electromagnetic spectrum. In addition to continuum dust emission, there are several dust emission features that are within the mid-IR spectrum, most notably the amorphous silicate features at 9.7 μm and 18 μm due to bending and stretching of the SiO molecules.

The presence of circumstellar dust can obscure AGB stars, making them very faint

or invisible in the optical and extremely bright at IR wavelengths. Based on these considerations, the IR is the best wavelength range for studies of mass-losing AGB stars. However, the IR is also a difficult part of the electromagnetic spectrum to observe. Large portions of the IR spectrum are absorbed by water and other molecules in the Earth's atmosphere, leaving few transmission windows to optimally conduct ground-based observations. In addition, ground-based telescopes operate at room temperature and therefore strongly emit in the IR longward of $\approx$5 μm, making stars appear faint compared to the background glow from the telescope. Making matters even worse, low-metallicity AGB stars tend to be very distant and are therefore already very faint.

Infrared observing capabilities vastly improved with the launch of the NASA *Spitzer Space Telescope* (Werner et al. 2004; Gehrz et al. 2007), which has significantly improved our ability to observe AGB stars. Detectors onboard *Spitzer*, two imagers and one spectrometer, cover the entire mid-IR to far-IR spectrum, a range that is ideal for AGB star observations. *Spitzer* is in an Earth-trailing orbit and is cryogenically cooled to $\approx$5 K, eliminating the problems of atmospheric absorption and warm ground-based telescopes and making *Spitzer* the most sensitive IR observatory in history. *Spitzer's* spatial resolution allows us to easily image individual AGB stars in the central regions of crowded globular clusters, and its unprecedented sensitivity allows us to detect and resolve AGB stars in the more distant, and therefore fainter, dwarf irregular galaxies.

1.4 The Organization and Motivation of this Dissertation

The main objective of this thesis is to determine the affect that metallicity has on stellar mass loss and dust production. This is accomplished with *Spitzer* observations of the most metal-poor GC (M15), the most massive GC (ω Centauri), eight other GCs, a super-metal-rich open cluster (NGC 6791), and eight metal-poor dwarf irregular galaxies. We present images and photometry of each of these systems at 3.6, 4.5, 5.8, 8.0, and 24 μm, along with a 5 – 15 μm spectrum of a planetary nebula in M15. We

also utilize ancillary data to help characterize point sources and ISM features in the *Spitzer* images.

Chapter 2 presents the first resolved detection of a dusty intracluster medium in a globular cluster: M15 (Boyer et al. 2006). It is surprising that M15, the most metal-poor GC, appears to be the *only* GC with intracluster dust. M15 also harbors a large population of dust-enshrouded stars, many of which appear to be AGB stars, and a dusty planetary nebula, one of only four planetary nebulae in GCs. In this chapter, we examine how much intracluster dust is expected based on mass loss estimates from the mass-losing stars present and compare this to the measured amount. We also examine possible intracluster stripping mechanisms and try to determine why M15 seems to be the odd-ball of the Galactic GC family.

In chapter 3, we examine the most massive GC, ω Cen (Boyer et al. 2008a). ω Cen is host to at least three separate stellar populations, each with a slightly different metallicity. These populations allow us to examine how metallicity affects AGB mass loss and dust production within a single environment. The very large population of stars in ω Cen provides us with a large enough sample to determine the point during a star's evolution when it begins to lose significant mass. We also examine the intracluster medium in ω Cen and compare what we find to the predicted stellar mass return from AGB star mass loss.

Chapter 4 presents a complete census of AGB stars in eight dwarf irregular galaxies and provides estimates of the number of AGB stars that are obscured at optical wavelengths (Boyer et al. 2008b). Mass loss rates of AGB stars are compared to the ISM content and star formation rates of each galaxy to determine if dusty AGB mass loss is the sole contributer to the ISM, or if galaxies are accreting new material or losing stellar mass in a non-dusty way.

A summary of chapters 2 through 4, plus a summary of related work that I have participated in as part of my dissertation research, is presented in chapter 5. Here, we

describe a follow-up study of AGB stars in ω Cen, a search for intracluster dust in eight Galactic GCs, and a study of AGB mass loss in the super-solar-metallicity open cluster NGC 6791. Chapter 6 briefly describes studies that are either ongoing or are planned to further our understanding of AGB star mass loss.

Chapter 2

Dust Production at Extremely Low Metallicity: AGB Stars and the Intracluster Medium in M15

A slightly modified version of this chapter appears in the Astronomical Journal, with the following bibliographic reference: Boyer, M. L., Woodward, C. E., van Loon, J. Th., Gordon, K. D., Evans, A., Gehrz, R. D., Helton, L. A., Polomski, E. 2006, AJ, 132, 1415. Reproduced with the permission of the American Astronomical Society.

Abstract

We present *Spitzer Space Telescope* IRAC and MIPS observations of the galactic globular cluster M15 (NGC 7078), one of the most metal-poor clusters with a [Fe/H] = -2.4. Our *Spitzer* images reveal a population of dusty red giants near the cluster center, a previously detected planetary nebula (PN) designated K648, and a possible detection of the intra-cluster medium (ICM) arising from mass loss episodes from the evolved stellar population. Our analysis suggests $(9 \pm 2) \times 10^{-4}$ $M_{\odot}$ of dust is present in the core of M15, and this material has accumulated over a period of $\approx 10^6$ yrs, a timescale

ten times shorter than the last galactic plane crossing event. We also present *Spitzer* IRS follow up observations of K648, including the detection of the [Ne II] λ12.81 μm line, and discuss abundances derived from infrared fine structure lines.

2.1 Introduction

Mass-loss in evolved stellar populations affects the chemical evolution of the interstellar medium (ISM), and mass loss from individual stars governs post-main-sequence evolution. The amount and duration of mass-loss that occurs in giant stars remains one of the most uncertain parameters in stellar evolution theory and the effect of these processes on the inferences derived from stellar population models can be significant. Given the wide use of these models (e.g., in inferring stellar masses of high-redshift galaxies), understanding the mass-losing process is vital for a range of problems in astrophysics. Although dust constitutes a small fraction of the total mass lost, it is frequently used as a marker as it is optically thin and its thermal emission is readily detectable in a variety of environments.

Globular clusters (GCs), believed to have formed during the assemblage of the Galaxy, are coeval samples of stars at common, well-determined distances with nearly uniform initial compositions. GCs enable study of the chemical enrichment of the ISM arising from mass ejection during the post-main-sequence evolution of stars. Red giant stars, especially those ascending the asymptotic giant branch (AGB), are expected to develop winds that inject processed material into the intra-cluster medium (ICM) during post-main-sequence evolution. These winds contain gas and solid-phase materials, the latter in the form of dust grains that condense from the metals. However, detection of thermal emission arising from ICM dust has been elusive, suggesting that the ICM in GCs is 100-1000 times less massive than expected from current stellar evolution theory and observations of mass-losing stars in clusters and in the solar neighborhood.

The circumstellar environments of stars in the late stages of evolution, when most mass loss occurs, are most effectively detected and studied in the infrared. IR surveys conducted by *IRAS*, the Two Micron All Sky Survey (2MASS), and the *Infrared Space Observatory* (*ISO*) revealed populations of dust-enshrouded AGB and red supergiant (RSG) stars in the Galactic bulge (van Loon et al. 2003), the Large Magellanic Cloud (LMC; Zijlstra et al. 1996; van Loon et al. 1997; Trams et al. 1999), and Galactic Globular Clusters (Ramdani & Jorissen 2001; Origlia et al. 2002)). GCs are expected to contain dust from episodes of mass-loss in red giant branch (RGB) and AGB stars. The IR excess of their circumstellar dust emission is expected to peak between 20 and 30 μm, and thus, photometry at wavelengths larger than 20 μm is necessary to estimate accurate dust masses lost by such stars. The amount of dust present in the ICM will vary depending on the cluster escape velocity, the time since the last crossing of the Galactic disk in which the ICM could have been stripped away by the ISM, and the number of mass-losing stars. In general the dust in the ICM of GCs is expected to be $\simeq 10^{-2}$ to 10^{-3} $M_{\odot}$ for most Galactic clusters. GCs have reasonably homogeneous (in age and metallicity) well-understood stellar populations, so observations of ICM dust are reasonably straightforward to interpret to yield mass-loss rates and duty cycles.

Previous attempts to detect the ICM in GCs suggest that the ICM density is well below that expected from predictions of the mass-loss input from RGB and AGB stars, even considering the low metallicity of GCs. The lowest 3 σ upper limits to the ICM mass for 70 K dust are $\sim 6 \times 10^{-5}$ $M_{\odot}$ (Hopwood et al. 1999). Detecting thermal emission from the elusive ICM in GCs is observationally challenging. Origlia et al. (2002) reported *ISO* observations of the IR thermal emission from the winds of individual RGB stars in six massive GCs (47 Tuc, NGC 362, ω Cen, NGC 6388, M15, and M54) showing that, in those systems, stellar winds from these stars are enriching the ICM. Although thermal emission from the ICM material might be expected to be detectable, many attempts to do so with IR and millimeter observatories have produced only a single secure

detection of ICM dust, a tentative (3.5 σ) detection of thermal emission in the core of the metal-poor GC M15 (Evans et al. 2003). Overall this result suggests that the ICM dust in GCs is significantly less massive than expected from current stellar evolution theory and observations of mass-losing stars in GCs and the solar neighborhood.

The causes of the paucity of ICM emission have been proposed to be ram-pressure stripping of ICM gas during Galactic plane passage, blowout by nova explosions, fast winds from the stars themselves, radiative ejection by the sheer luminosity of cluster stars, and continuous ram pressure from hot gas in the Galactic halo. However, the dominant state of the ICM is unclear. Sensitive searches for neutral H in the ICM at radio wavelengths have yielded upper limits of 0.1 $M_{\odot}$ (Birkinshaw et al. 1983), with a possible detection of $\approx$200 $M_{\odot}$ in NGC 2808 (Faulkner et al. 1991) and a 5 σ detection of 0.3 $M_{\odot}$ in M15 (van Loon et al. 2006b). Perhaps much of the ICM is ionized, as suggested by the high electron densities measured from pulsar timing in 47 Tuc (Freire et al. 2001). However, Hα searches have as yet been unsuccessful.

ICM dust grains in radiative thermal equilibrium should attain temperatures of 50-80 K because of the high energy density of starlight within a GC (Forte et al. 2002) and thus be detectable as an IR excess (above the photospheric emission) in GCs at mid- to far-IR wavelengths. Here we present observations of the Galactic GC M15 with the *Spitzer Space Telescope* (Werner et al. 2004; Gehrz et al. 2007), whose instrumental sensitivity enables detection of dust masses as low as 4×10^{-9} $M_{\odot}$ (assuming a population of grains radiating in thermal equilibrium, with integration times down to the background confusion limit) and therefore permits an unequalled opportunity to search for and set stringent limits on the "missing" ICM.

2.1.1 M15

M15 (NGC 7078), with [Fe/H] = –2.4 (Sneden et al. 1997), is one of the most metal-poor GCs. It is a well-studied cluster, as it is home to the first planetary nebula (PN)

Table 2.1. M15 properties

Parameter	Value[a]
[Fe/H]	-2.4
Core Radius (arcsec)	4.1
Z-height (kpc)	4.79
τ_c (yr)	4×10^7
$M_{cluster}$ ($M_\odot$)	2×10^6
v_{esc} (km s^{-1})	40.9
L ($L_\odot$)	5.8×10^5
$E(B\text{-}V)$	0.11
D (kpc)	9.98 ± 0.47

[a] Values reproduced from Evans et al. (2003), except E(B-V) from Schlegel et al. (1998) and distance from McNamara et al. (2004).

discovered in a GC (K648, also designated as Ps-1; Pease 1928; Howard et al. 1997; Alves et al. 2000) and to the first GC low-mass X-ray binary source (X2127+119; Auriére et al. 1984; Charles et al. 1986). At least eight millisecond pulsars are also associated with the cluster (Kulkarni & Anderson 1996). M15 is generally believed to be a core-collapse GC, with a small, dense core containing approximately 4000 $M_\odot$ (Phinney 1996).

Properties of M15, reproduced from Hopwood et al. (1999), are listed in Table 2.1. Updated values as listed by Evans et al. (2003) include the escape velocity v_{esc} from Webbink (1985) and the time τ_c since the last Galactic plane crossing from Odenkirchen et al. (1997). The reddening and the distance are updated from Schlegel et al. (1998) and McNamara et al. (2004), respectively. Galactic coordinates for M15 are $l = 65.01°$ and $b = -27.31°$, placing the cluster ~ 4.5 kpc south of the galactic plane.

The total dust mass expected in a GC can be estimated using the following equation:

$$M_{\rm dust} = \frac{\tau_{\rm c}}{\tau_{\rm HB}}\ N_{\rm HB}\ \delta M\ \frac{10^{\rm [Fe/H]}}{100}, \tag{2.1}$$

where $\tau_{\rm HB}$ is the horizontal branch (HB) lifetime, $N_{\rm HB}$ is the number of HB stars, [Fe/H] is the cluster metallicity, and δM is the dust mass lost from each star at the tip of the RGB. The factor of 100 is the solar gas-to-dust ratio, which is scaled for the metallicity of M15 by adding the [Fe/H] factor. Using values typical of Population II stars and this relationship, the expected dust mass in M15 has been estimated to be 3.7×10^{-3} $M_{\odot}$ by Evans et al. (2003) and 2.0×10^{-3} $\rm M_{\odot}$ by Hopwood et al. (1999).

M15 is also home to the PN K648. K648 was the first GC PN discovered, and subsequently it has been extensively studied at UV, optical, and IR wavelengths to determine the chemical composition of the ejecta nebula and parameters of the central star (Barker 1983; Adams et al. 1984; Howard et al. 1997; Bianchi et al. 2001; Dinerstein et al. 2003; Garnett & Lacy 1993). The study of post-AGB stellar evolution in old, metal-poor, low-mass stars in GCs or the Galactic halo can be greatly enhanced if the by-products of stellar nucleosynthesis can be measured. Enriched material produced in the RGB and AGB stages of stellar evolution are dispersed into outer layers of the stellar system and subsequent mass-loss processes lead to the formation of a PN. Few PNe in the Galactic halo population have been identified, and only four of these PNe, including K648, BB-1, DdDM 1, and H4-1, are associated with GCs (Jacoby et al. 1997). Below, we present findings derived from a 5–15 μm IR spectrum of K648.

2.2 Observations

Image observations of the GC M15 were obtained on 2004 October 29 UT with the Multiband Imaging Photometer for *Spitzer* (MIPS; Rieke et al. 2004) camera through the 24 and 70 μm filters and with the Infrared Array Camera (IRAC; Fazio et al. 2004) at 3.6, 4.5, 5.8, and 8 μm, conducted as part of the Gehrz Guaranteed Time Observing Program (GGTOP; PID 124). Raw data were processed with the *Spitzer* Science Center (SSC) pipeline version S11.4.0. To avoid saturation in IRAC, high dynamic range (HDR) mode was implemented, using 0.4, 10.4, and 98.6 s exposures.

Table 2.2. Observational Summary

Instrument	AORkey	Exposure Time[a] (s)	Coverage	pixel size ($''$/pixel)
IRAC	12030208	10.4	$9.5' \times 9.5'$	1.22
MIPS 24 μm	12030464	9.96	$11' \times 12'$	1.245
MIPS 70 μm	12030464	10.49	$8.5' \times 14.5'$	4.925
IRS	15733760	60 (SL)		

[a] Exposure time of individual BCD images. For IRAC, only medium exposure HDR frames are listed.

For each IRAC channel, 55 frames at seven dither positions were obtained with each HDR exposure time. With the MIPS camera, 596 dithered frames were taken at 24 μm along with 256 dithered frames at 70 μm.

Spitzer IRS spectra of the PN and other red sources detected in the IRAC images have been obtained as part of a follow-up program using GGTOP time, and these data are discussed below. Table 2.2 summarizes the observations discussed in this thesis.

2.2.1 IRAC

The IRAC Basic Calibrated Data (BCD) images were post-processed to correct for various instrumental artifacts and were mosaicked using the 2005 May 9 version of the SSC Legacy MOPEX software (Makovoz & Marleau 2005). The MOPEX cosmetic correction was used to eliminate mux-bleed and column pull-down as described by the IRAC Data Handbook, version 3.0.[1] The background matching correction was used to minimize pixel differences in overlapping areas of the mosaics. The MOPEX mosaicker also eliminated cosmic rays and other outliers in the data. The final IRAC mosaics are

[1]See http://ssc.spitzer.caltech.edu/irac/dh/iracdatahandbook3.0.pdf

not subsampled; thus, the pixel size of each final tiled image is $1\farcs22$ pixel^{-1} covering an area ~ 50 arcmin^2 around the core (RA = $21^{\rm h}29^{\rm m}58\fs38$, decl = $+12^\circ10'00\farcs6$ [J2000.0]) of M15 plus an off-field region of the same size $7'$ to the north or south. A three-color image combining 3.6, 4.5, and 8 μm is presented in Figure 2.1*a*. The diffuse ICM is not detected in the IRAC mosaics, even at 8 μm. However, the planetary nebula (K648) and several other dusty stellar objects become quite prominent at 8 μm.

Point-source photometry was conducted using several stellar extraction routines including GlimpsePhot[2], DAOphot (Stetson 1987), and the astronomical point-source extraction (APEX) tool contained in the SSC MOPEX package. Severe stellar crowding towards the cluster core in the IRAC bands made reliable point-response function (PRF) photometry challenging. The best photometric results (95% agreement to 2MASS K–band fluxes) were obtained by performing PRF fitting on the BCD images with APEX. Array-location dependent-photometric correction weights were applied before PRF fitting to minimize systematic error in the point-source extraction flux. The images were then corrected with the background-matching routine, and outliers were eliminated by the mosaicker.

PRFs were created for 3.6 and 4.5 μm data using the PRF estimate routine provided in APEX. At least 20 stars were chosen to make each PRF in areas with the smallest amount of crowding. The PRFs provided by the *Spitzer* Science Center (SSC)[3] that were made in flight in 2005 January for 5.8 and 8 μm are sufficiently over-sampled, so there was no need to create new PRFs for these channels. Probable point sources with fluxes at least 4 σ above the background were then identified and selected for extraction on co-added images that had been corrected for array distortion. Final flux extractions were performed at these world coordinate positions on the corrected BCD images using PRF subtraction.

---

[2]See http://www.astro.wisc.edu/sirtf/

[3]See http://ssc.spitzer.caltech.edu/irac/psf.html

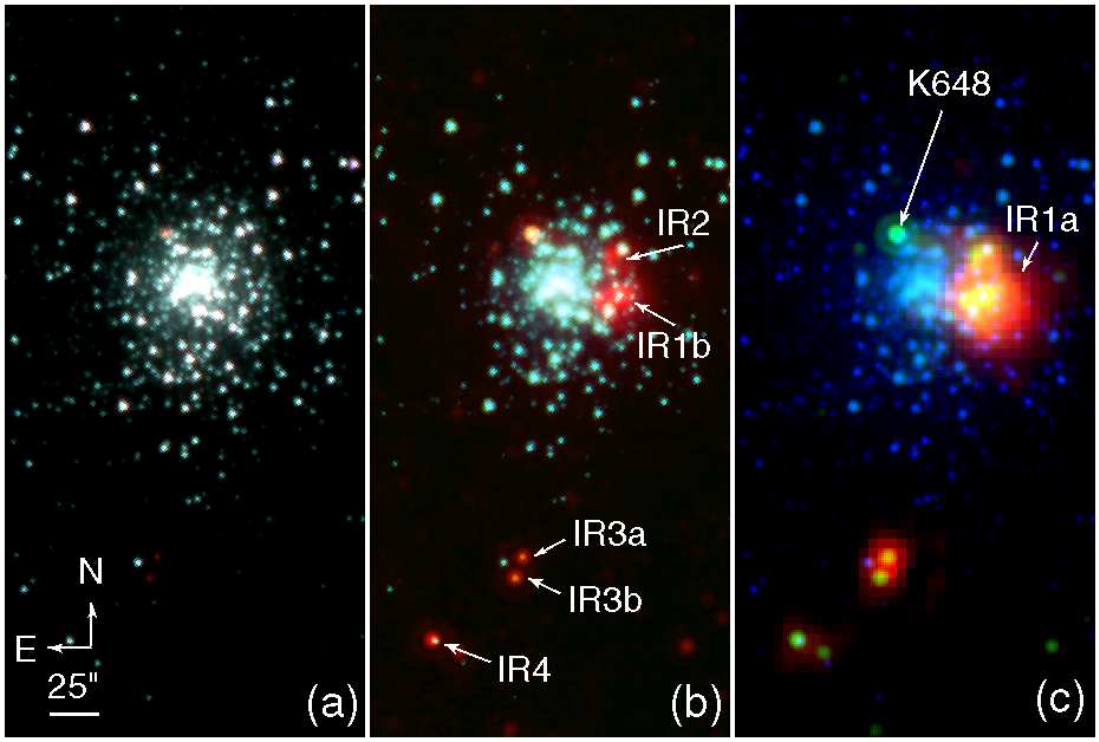

Figure 2.1: Three-color images of the core of M15 (NGC 7078) spanning 3.6 to 70 μm. The field shown is $3' \times 6'.3$. (*a*) Blue is 3.6 μm, green is 4.5 μm, and red is 8 μm. The PN (K648) becomes visible near the upper left of the cluster core. (*b*) Blue is 5.8 μm, green is 8 μm, and red is 24 μm. The ICM becomes visible as two resolved high surface brightness patches (IR2 and IR1b) off-center from the cluster core. Three dusty sources, IR3a, IR3b, and IR4, also become prominent at 24 μm. (*c*) Blue is 8 μm, green is 24 μm, and red is 70 μm. The two ICM clouds are no longer resolved at 70 μm (IR1a).

After applying the appropriate photometric color correction (as discussed in the IRAC Data Manual, ver. 3.0) and comparing APEX 3.6 μm fluxes with 2MASS K–band fluxes (Skrutskie et al. 2006), the average K – [3.6] color is that of a K0 giant star. If we then assume that the majority of the stars we detected with *Spitzer* are K0 giant stars, then our fluxes are consistent with 2MASS K-band fluxes to within approximately 5%. To further check our photometric results, we compared the fluxes from 30 of the stars we detect to K-band fluxes from Cohen et al. (2005). The median K – [3.6] color for these sources is 0.09, which is also consistent with K0 giant stars (see Fig. 2.2).

Color-magnitude diagrams (CMDs) derived from the IRAC point-source photometry are presented in Figure 2.3. An RGB is clearly evident, with the tip occurring near $F_{3.6}$ = 14 mJy. Stars with 3.6 μm flux > 11.2 mJy are possibly saturated in the long-exposure frames, so only medium-exposure (10.4 s) BCDs were used for the PRF subtractions and flux extraction. Flux densities for stars with colors redward of the RGB are listed in Table 2.3 (see §2.3.1).

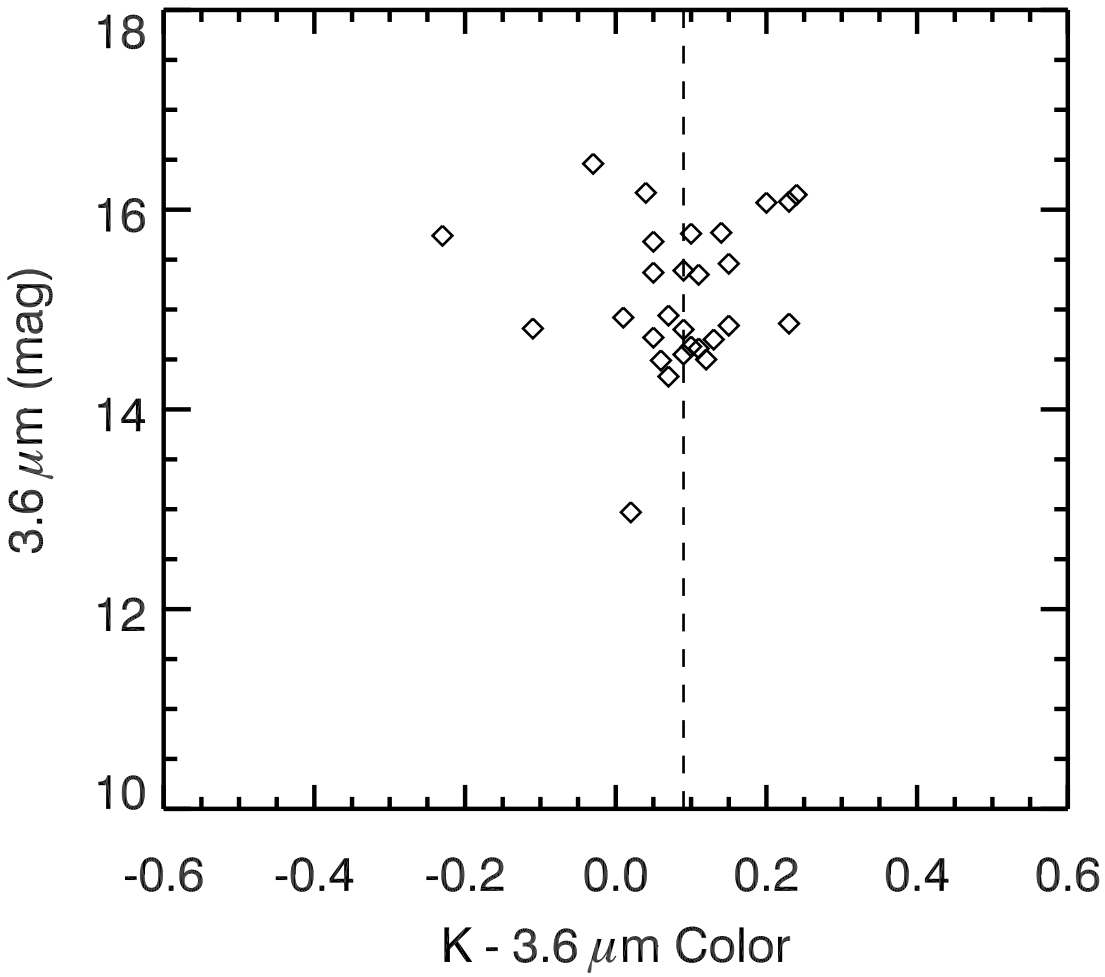

Figure 2.2: Color magnitude diagram showing K – [3.6] colors. K magnitudes are from Cohen et al. (2005). The dashed line corresponds to the median color, which is consistent with K giant stars.

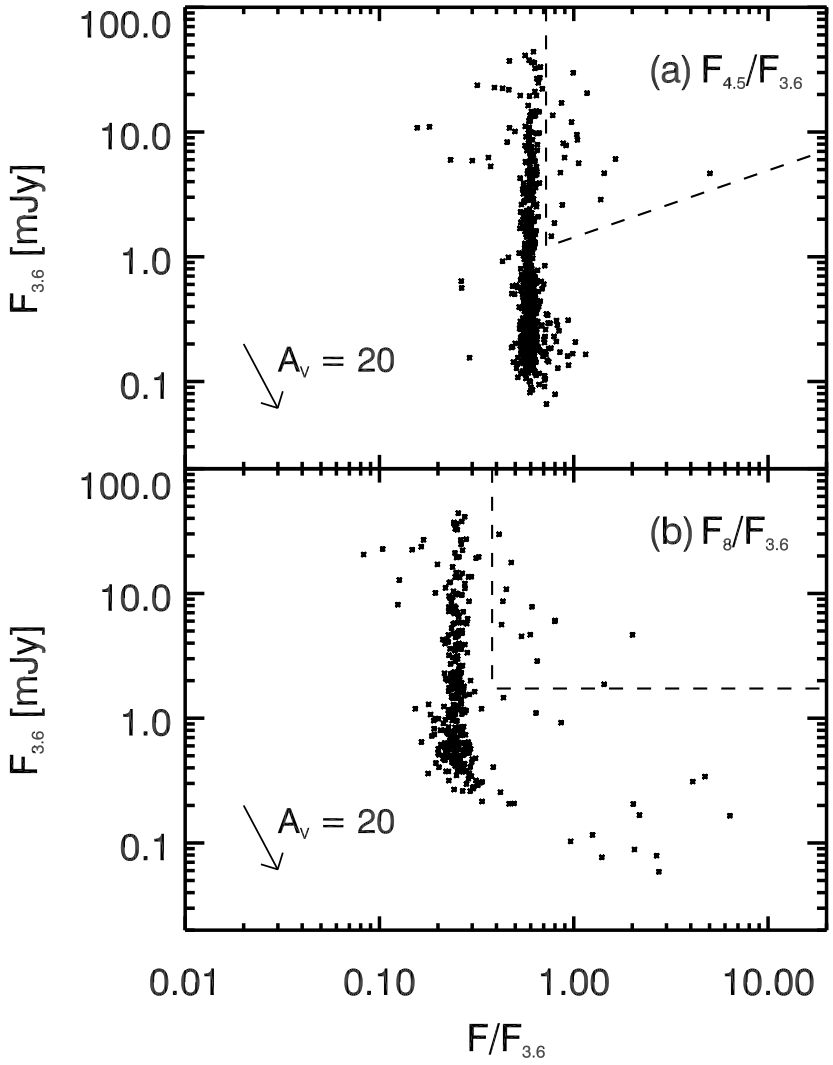

Figure 2.3: IRAC CMDs for M15. Fluxes are not color-corrected or dereddened. (*a*) CMD for 4.5 μm–3.6 μm color vs. 3.6 μm flux. (*b*) CMD for 8 μm–3.6 μm color vs 3.6 μm flux. The uncertainties in the photometry are given in Fig. 2.5. The regions enclosed by the dashed lines (*right of vertical, above horizontal*) are the mass-loss regions. The locations of these stars are plotted in Fig. 2.8, and their fluxes are listed in Table 2.3.

Table 2.3: Flux Densities of Dusty IR Sources

ID[a]	r (arcsec)	3.6μm (mJy)	4.5μm (mJy)	5.8μm (mJy)	8μm (mJy)	24μm (mJy)
2MASS J21295231+1210515	0.212	13.99 ± 0.70	10.87 ± 0.54	7.02 ± 0.35	4.22 ± 0.21	0.44 ± 0.02
2MASS J21295264+1210440	0.201	6.24 ± 0.31	10.21 ± 0.51	8.64 ± 0.43	5.09 ± 0.25	0.66 ± 0.02
SSTU J212953.55+120910.7	0.982	8.91 ± 0.45	9.28 ± 0.46	6.80 ± 0.34	3.91 ± 0.20	0.45 ± 0.02
2MASS J21295383+1209338	0.200	6.15 ± 0.31	1.43 ± 0.07	5.22 ± 0.26	5.00 ± 0.25	0.61 ± 0.02
2MASS J21295473+1208592	0.032	4.80 ± 0.24	6.87 ± 0.34	5.23 ± 0.26	2.92 ± 0.15	0.30 ± 0.02
2MASS J21295618+1210179	0.030	21.08 ± 1.05	24.61 ± 1.23	22.05 ± 1.10	>1.78 ± 0.09	2.93 ± 0.02
2MASS J21295678+1210269	0.271	30.65 ± 1.53	30.35 ± 1.52	>6.19 ± 0.31	12.86 ± 0.64	1.25 ± 0.02
2MASS J21295703+1209376	0.242	4.79 ± 0.24	23.99 ± 1.20	17.84 ± 0.89	9.78 ± 0.49	...
2MASS J21295712+1210043	0.190	11.11 ± 0.56	1.73 ± 0.09	4.79 ± 0.24	5.08 ± 0.25	...
2MASS J21295716+1209175	0.250	17.59 ± 0.88	15.18 ± 0.76	12.41 ± 0.62	3.56 ± 0.18	0.67 ± 0.02
2MASS J21295758+1209552	0.301	12.34 ± 0.62	12.00 ± 0.60	>0.27 ± 0.01	3.45 ± 0.17	...
2MASS J21295756+1210276	0.022	6.06 ± 0.30	...	>0.62 ± 0.03	2.55 ± 0.13	0.44 ± 0.02
2MASS J21295815+1209466	0.493	18.20 ± 0.91	28.30 ± 1.41	21.12 ± 1.06	8.83 ± 0.44	1.66 ± 0.02
2MASS J21295828+1209280	0.202	4.85 ± 0.24	4.13 ± 0.21	0.91 ± 0.05	0.33 ± 0.02	...
2MASS J21295832+1209128	0.181	8.03 ± 0.40	7.32 ± 0.37	5.40 ± 0.27	4.98 ± 0.25	0.50 ± 0.02
2MASS J21295881+1209285	0.301	9.78 ± 0.49	10.12 ± 0.51	5.39 ± 0.27	2.27 ± 0.11	0.47 ± 0.02
2MASS J21295937+1210029	0.420	8.35 ± 0.42	7.35 ± 0.37	8.61 ± 0.43	1.06 ± 0.05	...
SSTU J212959.69+120739.0[b]	4.722	0.31 ± 0.04	0.29 ± 0.02	0.26 ± 0.02	1.47 ± 0.07	2.37 ± 0.02
2MASS J21295981+1211107	0.231	6.41 ± 0.32	5.73 ± 0.29	4.14 ± 0.21	...	0.28 ± 0.02
2MASS J21295996+1207282[c]	0.100	0.34 ± 0.03	0.25 ± 0.02	0.24 ± 0.02	2.05 ± 0.10	2.52 ± 0.03
2MASS J21300062+1209284	0.140	2.95 ± 0.15	4.05 ± 0.20	>0.12 ± 0.01	1.94 ± 0.10	0.22 ± 0.02
2MASS J21300097+1210375	0.054	5.78 ± 0.29	6.11 ± 0.31	4.41 ± 0.22	2.50 ± 0.12	0.31 ± 0.02
2MASS J21300277+1206557[d]	0.010	9.34 ± 0.47	6.18 ± 0.31	4.04 ± 0.20	3.29 ± 0.16	3.66 ± 0.02

Note.—Flux densities are color corrected and dereddened using $E(B\text{-}V) = 0.11$ and A_λ values from Indebetouw et al. (2005).

[a] Standard 2MASS designations are listed for all stars that have a 2MASS counterpart located within r = 0.″5 of the *Spitzer* coordinates. Otherwise, stars are listed with standard *Spitzer* designations, where U stands for "unidentified."

[b] Designated as IR3a in text: 3.6, 4.5, and 5.8 μm fluxes were determined with aperture photometry in IDL, as this source was not detected by APEX at these wavelengths.

[c] Designated as IR3b in text: 3.6, 4.5, and 5.8 μm fluxes were determined with aperture photometry in IDL, as this source was not detected by APEX at these wavelengths.

[d] Designated as IR4 in text.

2.2.2 MIPS

The MIPS Data Analysis Tool (DAT; Gordon et al. 2005), version 2.96, was used to do the basic processing and final mosaicking of the individual MIPS images. In addition, extra processing steps on each image were carried out before mosaicking using programs written specifically to improve the removal of MIPS detector instrumental signatures. At 24 μm the extra steps included readout offset correction, scan-mirror-dependent flat fields, a scan-mirror-independent flat field, array averaged background subtraction, and exclusion of the bias-boost images. At 70 μm, the extra steps were column average subtraction and pixel time filtering both with the exclusion of the regions around the bright sources. The pixel sizes of the final mosaics are $1\farcs245$ and $4\farcs925$ for 24 and 70 μm, respectively. The 24 μm mosaic covers a 90 arcmin^2 area and the 70 μm mosaic covers a $5\farcm0 \times 10\farcm0$ area, each centered on the core of M15.

The MIPS mosaics (Fig. 2.1*b*, *c*) show a possible ICM detection at 24 and 70 μm. The 24 μm image shows two high surface brightness patches of material, both offset from the core by $\simeq 17''$ towards the west (IR1b and IR2). The 70 μm image shows only one high surface brightness patch which is likely an unresolved image of both 24 μm regions. The integrated fluxes of the ICM detections at both wavelengths were determined using basic aperture photometry in IDL, version 6.0. A $130\farcs5$ square aperture centered at R.A. = $21^{\rm h}29^{\rm m}56\fs50$; decl. = $+12\arcdeg09'53\farcs32$ (J2000.0) yields fluxes of 159.4 $\pm$ 0.1 mJy at 24 μm and 691.2 $\pm$ 61.0 mJy at 70 μm. The 70 μm flux agrees well with that found by Evans et al. (2003) with *ISO* observations using the same aperture size and position (Table 2.4). Also visible in the MIPS mosaics are the PN at 24 μm and several dust-enshrouded stars, some of which are also visible in the 8 μm image and may or may not be associated with the cluster.

Point-source-photometry was performed on the 24 μm mosaic using StarFinder (Diolaiti et al. 2000), which is well suited for the stable and well-sampled MIPS 24 μm PSF.

Table 2.4. ICM Dust (IR1a) Flux Densities

λ μm	F_λ[a] mJy	Instrument/ Mission
0.56	4667 ± 233	*HST* WFPC2[b]
1.25	10857 ± 186	2MASS
1.65	10450 ± 204	2MASS
2.16	7342 ± 134	2MASS
3.6	3669 ± 1	IRAC
4.5	2336 ± 1	IRAC
5.8	1442 ± 1	IRAC
8.0	757.7 ± 0.5	IRAC
24	159.4 ± 0.1	MIPS
60	515 ± 155	*ISO*[c]
70	691.2 ± 61.1	MIPS
70	578 ± 173	*ISO*[c]
90	303 ± 91	*ISO*[c]

[a] Aperture size is 130.5 × 130.5 arcseconds, corresponding to the ISO aperture from Evans et al. (2003). All fluxes are dereddened with E(B-V)=0.11. A_λ values come from Rieke & Lebofsky (1985) and Indebetouw et al. (2005).

[b] From image U5B80101R from the public HST archives.

[c] From Evans et al. (2003).

A STinyTim (Krist 2002)[4] model PSF with a temperature of 100 K and smoothed to account for pixel sampling was used for the stellar extractions. It has been shown that the smoothed STinyTim PSFs are excellent matches to observed MIPS 24 μm PSFs (Engelbracht et al. 2007). CMDs comparing 24 μm to 3.6 and 8 μm are presented in Figure 2.4, and the uncertainties in the IRAC and MIPS photometry are summarized in Figure 2.5.

2.2.3 IRS

Associated with our imaging programs, observations of the PN K648 (Pease 1928; Howard et al. 1997; Alves et al. 2000) in M15 were obtained with the *Spitzer* Infrared Spectrograph (IRS) on 2005 November 17.77 UT using the short-wavelength (5–15 μm), low resolution module (SL) in staring mode. All observations used the IRS blue peak-up array at the target position of the PN, R.A. = $21^{\rm h}29^{\rm m}59\overset{\rm s}{.}41$; decl. = $+12\overset{\circ}{.}10'25\overset{''}{.}70$ (J2000.0), and the entire Hα nebulosity of K648 (cf. Fig. 2 of Alves et al. 2000) was contained within the spectrograph slit. The slit dimensions are $57'' \times 3\overset{''}{.}6$, and the slit was oriented $18\overset{\circ}{.}92$ west of north. The SL spectroscopic astronomical observing templates consisted of five cycles of 60 s ramps. IRS BCDs were processed with version 13.0.1 of the IRS pipeline. A description of the IRS instrument and its operation is available in Houck et al. (2004). Details of the calibration and raw data processing are specified in the IRS Pipeline Description Document, version 1.0.[5]

Post-pipeline processing was conducted to remove instrumental artifacts, perform background subtractions, and combine extracted spectral segments. Fatally bad pixels were interpolated over in individual BCDs using bad-pixel masks provided by the SSC. Multiple data collection events were obtained at two different positions on the slit using *Spitzer's* nod functionality. The two-dimensional BCDs were differenced to remove the

[4]Available at http://ssc.spitzer.caltech.edu/archanaly/contributed/stinytim.tar.gz

[5]See http://ssc.spitzer.caltech.edu/irs/dh/PDD.pdf

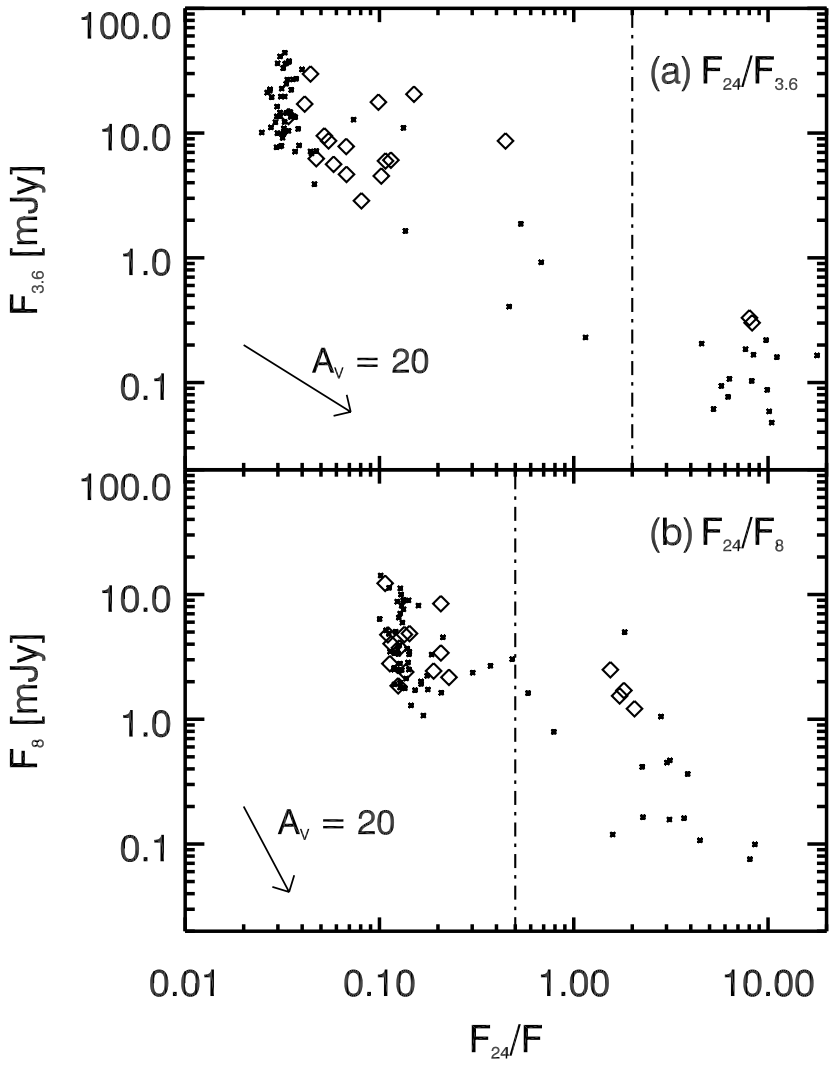

Figure 2.4: MIPS CMDs for M15. Fluxes are not color corrected or dereddened. (*a*) CMD for 24 μm–3.6 μm color vs. 3.6 μm flux. (*b*) CMD for 24 μm–8 μm color vs. 8 μm flux (see Fig. 2.5 for uncertainties in the photometry). The diamonds mark the mass-losing stars identified in Fig. 2.3. The dash-dotted lines mark the approximate division between AGB and post-AGB stars (Groenewegen 2006). IR3a, IR3b, and IR4 each fall well within the post-AGB region in (*b*), while only IR3a and IR3b fall within the post-AGB region in (*a*). The IRAC colors of the other mass-losing sources suggest that they are AGB stars.

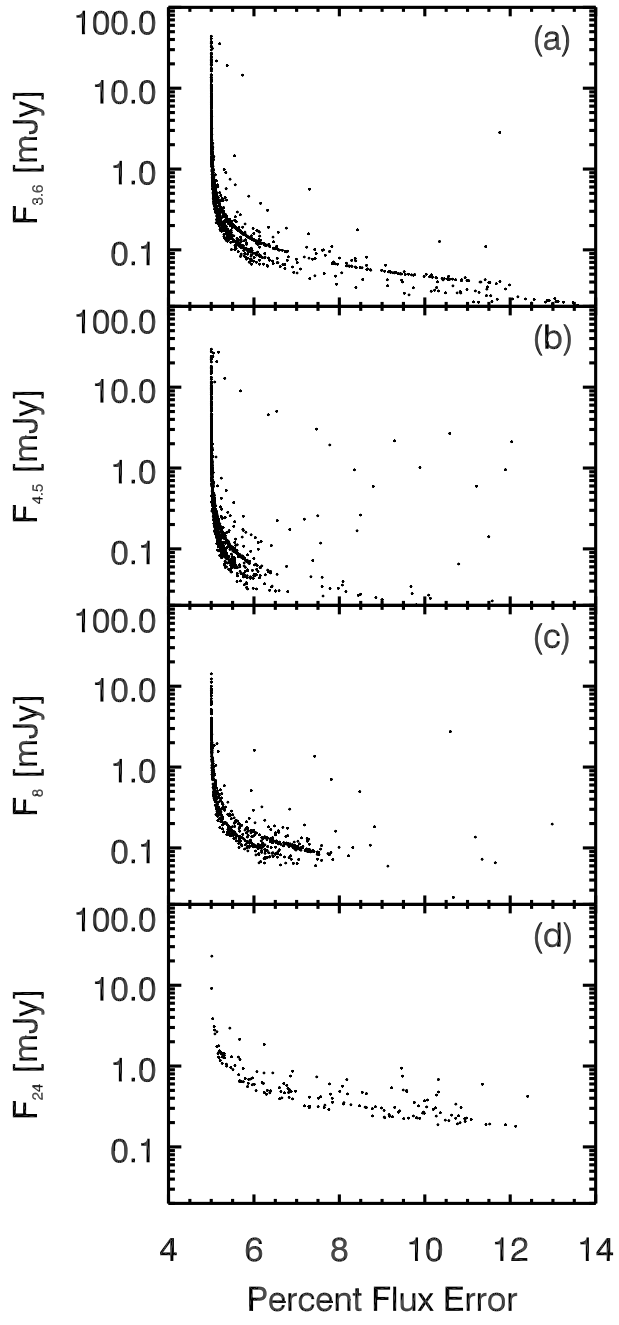

Figure 2.5: Photometry errors for the IRAC 3.6, 4.5, and 8 μm and MIPS 24 μm bands.

background flux contribution and then the data were extracted with the *Spitzer* IRS Custom Extractor (SPICE, ver. 1.1-beta15)[6] using the default point source extraction widths. The extracted, background corrected data were combined using a weighted linear mean into a single output data file and clipped at the 3 σ level. At the time of reduction, the errors generated by the SSC pipeline were not reliable enough for sound interpretation and so the errors were estimated from the standard deviation of the flux at each wavelength bin. When there were fewer than three points in a wavelength bin, we took the error to be the quadrature sum of the errors in the files. The resulting spectrum is presented in Figure 2.6 and derived line fluxes are summarized in Table 2.5. The spectral lines were fitted using a least-squares Gaussian routine that fits the line center, line amplitude, continuum amplitude and slope of the continuum. The full-width at half-maximum was fixed at the resolution limit of the low-resolution module. Integrating the flux over the 8 μm IRAC bandpass yields a flux that agrees with the IRAC flux within the uncertainty limits. The strongest line in the mid-IR spectrum is the [Ne II] 12.81 μm line, followed by hydrogen recombination lines H I 6-5 (Pfα) = 7.46 μm and H I 7-6 (Huα) = 12.37 μm. Emission from S^{3+} is evident in the spectrum, although the fit to the line flux of [S IV] 10.52 μm is of marginal signal-to-noise ratio (S/N $\approx$ 2.3), while no [Ar III] 8.99 μm is seen. Our detections of the mid-IR neon and sulfur lines are the first reported in the literature for K648. Abundance estimates derived from these forbidden lines are discussed in §2.3.2.

2.3 Discussion

Our *Spitzer* images of M15 for the first time clearly show both the stellar dust producers and the ICM dust (Fig. 2.1), allowing a direct comparison to be made between the dust injection and dust survival rates. The brightest source of 70 μm emission, IR1a, is

[6]See http://ssc.spitzer.caltech.edu/postbcd/doc/spice.gui_manual.html

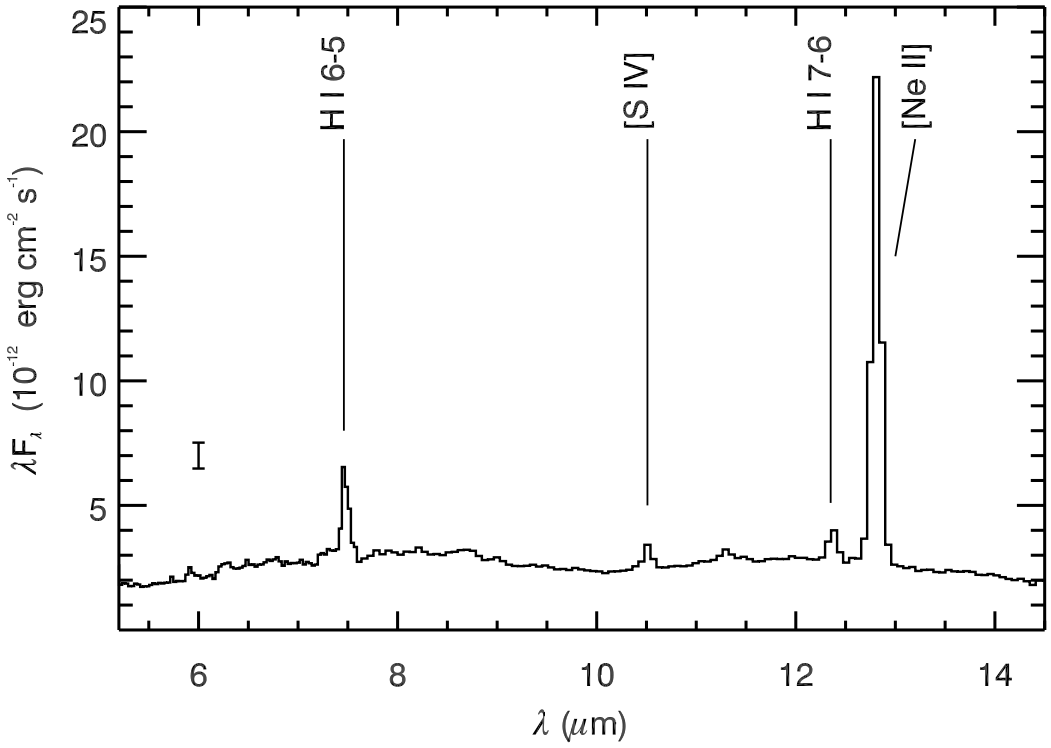

Figure 2.6: *Spitzer* IRS spectrum of the PN K648 obtained with the SL module. The most prominent emission line in the spectrum is [Ne II] 12.81 μm, in addition to weak H recombination lines and the [S IV] line. The representative error bar (*lower left*) shows the average photometric uncertainty in the spectrum. No strong dust continuum is evident in the IRS spectrum.

Table 2.5. Spitzer Infrared Line Fluxes of K648

λ μm	Ion/Line	Flux[a] ergs cm^{-2} s^{-1}
12.81	[Ne II]	$(1.74 \pm 0.08) \times 10^{-13}$
12.35	H I 7 − 6	$(9.75 \pm 3.08) \times 10^{-15}$
10.51	[S IV]	$(8.24 \pm 3.56) \times 10^{-15}$
7.46	H I 6 − 5	$(4.38 \pm 0.68) \times 10^{-14}$

[a] Integrated line fluxes assuming a fixed IRS instrumental resolution of 0.0404 μm, and a Gaussian line profile.

blended at 70 μm but visible as separate objects in the MIPS 24 μm map, IR1b and IR2. These sources are completely invisible on the IRAC maps, even at 8 μm. A three-color image of 8, 24, and 70 μm, in which the 8 and 24 μm images are degraded to match the 70 μm resolution, is presented in Figure 2.7. This figure illustrates that IR1a is not unresolved stellar emission but a starless dust cloud(s) that is likely to be of an intracluster nature. The next brightest objects at 70 μm are a pair of sources, IR3a and IR3b, that are situated at the fringes of the cluster and may not be physically associated with the cluster. IR3b was previously detected by 2MASS, but there are no known previous detections of IR3a. The probability of detecting nonmember red sources in the field is sufficiently small to suggest that these sources are associated with the cluster. The only other 70 μm source, IR4, is also located on the fringes of the cluster. Radial velocity measurements from Pilachowski et al. (2000) confirm its membership. Table 2.3 lists fluxes for IR3a, IR3b, IR4, and other possibly dusty sources, described in §2.3.1. All three of these sources have mid-IR colors that are consistent with post-AGB stars (Fig. 2.4; Groenewegen 2006). In addition to these sources, the PN K648 (Ps 1) is also detected in all IRAC bands and at 24 μm. The strong 24 μm dectection is likely due not only to dust, but also to line emission from [O IV] at 25.88 μm and/or [Fe II]

at 25.98 μm.

2.3.1 Mass-losing Stars

Figure 2.8 shows the locations of the mass-losing AGB stars in M15. The coordinates and IRAC fluxes of these sources are listed in Table 2.3. These stars were identified by their locations on the IRAC CMDs (Fig. 2.3), redward of the RGB. We find 24 mass-losing/dust-enshrouded stars and consider this a lower limit (due to potential source confusion) of the total number in the cluster. These stars also fall just redward of the RGB in the MIPS CMDs as well, which suggests that they could be post-AGB stars. Their IRAC colors, however, indicate that it is more likely that they are AGB stars that are approaching the end of the AGB phase of their evolution (Groenewegen 2006). The stars blueward of the RGB can be explained by the absorption in the fundamental bands of CO in the 4.5 μm band and SiO in the 8 μm band. The red, mass-losing stars in M15 populate an uneven spatial distribution about the core of the cluster as projected on the sky (Fig. 2.8). These stars are offset from the core in the same sense as IR1a, IR1b, and IR2, and the distribution is less cusped than the visual light. Since M15 is 13.2 Gyr old (McNamara et al. 2004), most stars currently on the AGB have a zero-age main sequence mass of $\simeq 0.8\ M_{\odot}$. These stars will soon end their lives as white dwarfs of $\simeq 0.5\ M_{\odot}$, having lost approximately $0.3\ M_{\odot}$ during their post-main sequence evolution. The loose spatial distribution of this population could therefore be due to mass segregation, in which lower-mass stars are displaced to the outer regions of the cluster due to their high velocities, leaving a preferential concentration of high-mass stars near the center of the potential well of the cluster (Spitzer 1987).

The MIPS CMDs (Fig. 2.4) identify a population of approximately 23 post-AGB stars (Groenewegen 2006). The colors of IR3a, IR3b, and IR4 are similar to the colors of this population. These stars are bright at 24 μm, but they are not detected above the background at 70 μm (Table 2.3). They are distributed around the cluster center

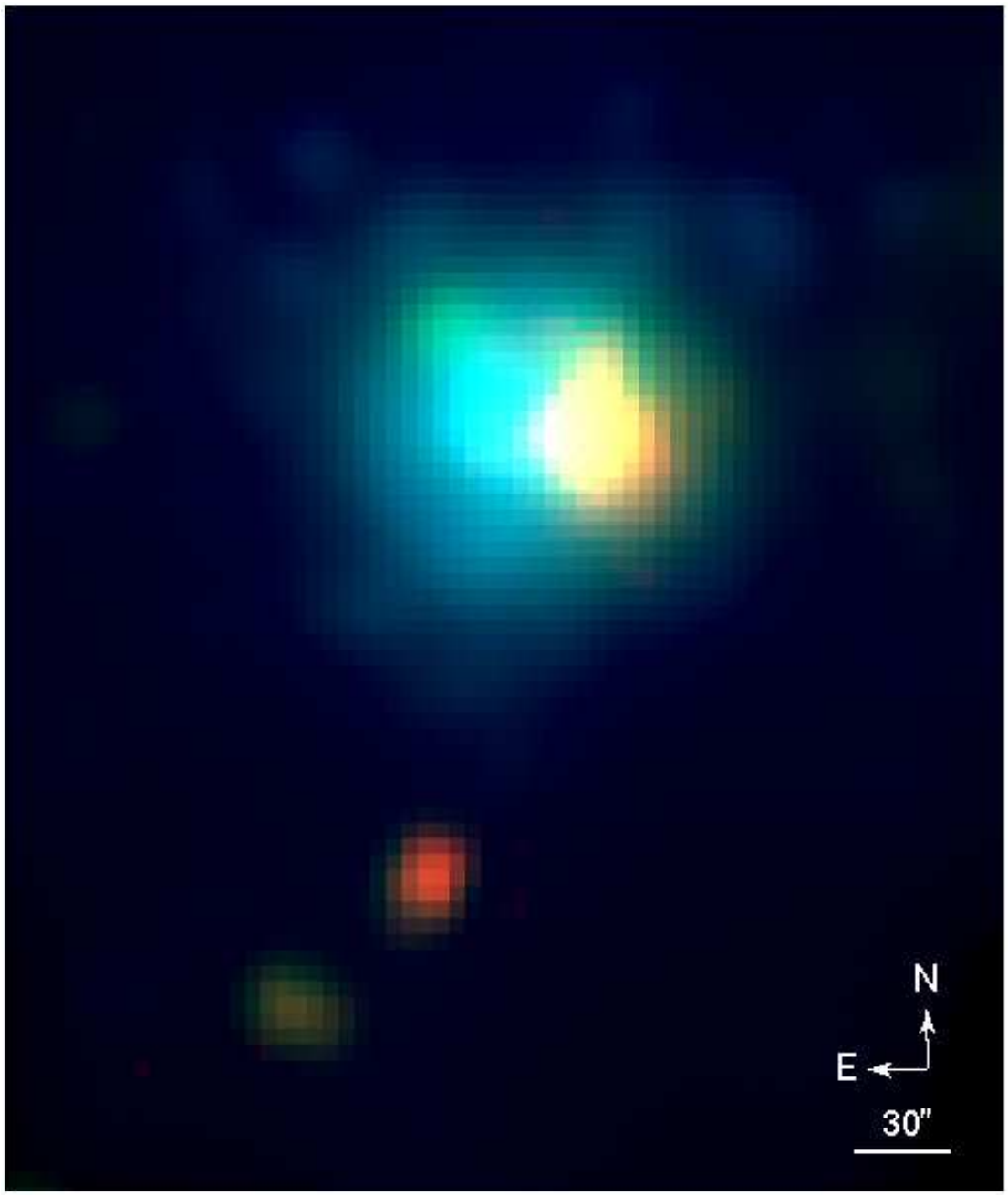

Figure 2.7: Three-color image of 8 (*blue*), 24 (*green*), and 70 μm (*red*) images. The 24 and 8 μm images were rebinned to the 70 μm image pixel size of $4\farcs925$ then convolved with the 70 μm *Spitzer* PRF. This image shows that the 70 μm emission is not unresolved stellar emission.

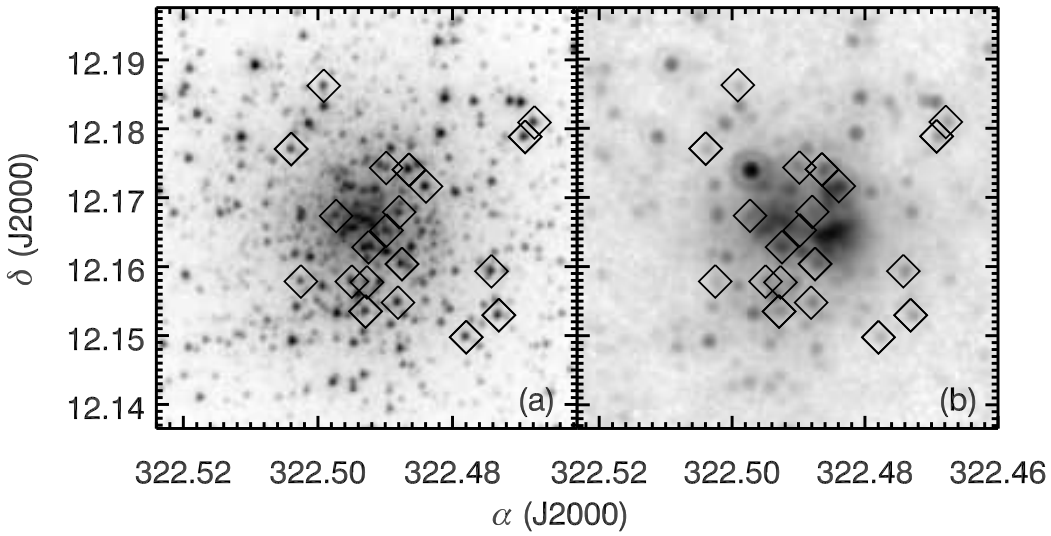

Figure 2.8: Locations of mass-losing stars in M15. (*a*) the 3.6 μm mosaic; (*b*) the 24 μm mosaic. All of the stars marked are located redward of the RGB.

at an average radius of approximately $3\farcm3$, and their positions are biased towards the southern side of the cluster, near IR3a, IR3b, and IR4. Mass segregation is most likely responsible for their locations at the fringes of the cluster.

Although M15 is one of the most massive Galactic GCs, it is surprising to find many dusty objects, as the cluster metallicity of [Fe/H] = −2.4 places it among the most metal-poor Galactic GCs. Dust forms from metal condensates, and it is difficult to understand how dust grains can form at such low metal abundances. It is likely that the metals condensing to form dust are produced in the stars themselves and brought to the surface near the end of their evolution. The fact that dust production does not seem to be inhibited at metallicities $\lesssim$ 1% solar implies that stellar mass-loss must already have contributed dust very early on in the evolution of the Universe. Dust observed at high redshift is usually believed to originate in supernovae explosions that result from core collapse in massive stars, but our observations suggest that at least some of the dust formed within the first few 100 million yr may have been produced by stars of only a few solar masses (e.g., main sequence lifetime from models by Vassiliadis & Wood 1993).

Various investigators (Daulton et al. 2002; Amari et al. 2001) suggest that dust grains can form more easily at low metallicity in carbon stars, as these stars produce carbon themselves. With less initial oxygen abundance to start with, it is easier for these stars to achieve C/O > 1 in their carbon shells. With excess carbon available (after locking up equal amounts of C and O in CO), the formation of carbon-chain molecules, from which dust grains condense, can proceed. However, although there is evidence for high molecular abundances in stellar atmospheres at low metallicity, dust production in these stars may be less efficient due to a lack of SiC seeds (Sloan et al. 2006). Furthermore, van Loon (2006) suggests that the low optical depth in carbon stars in the Magellanic Clouds points against large dust-to-gas ratios at low metallicity.

For low-mass oxygen-rich stars, one would not expect this evolution to lead to effective dust production, as dredge-up only increases the C/O ratio and does not facilitate the formation of oxygen-rich dust grains. In any case, for oxygen-rich stars it is well established that nucleation sites must be available on which to condense dust grains (Jeong et al. 1999). These seeds are likely to be TiO or something similar, including secondary elements that are not produced by the star itself. Other *s*-process seeds, such as Zr, may be dredged-up in the atmospheres of these stars, but the limiting factor for dust production with such seeds is the oxygen abundance, as more oxygen will be locked into CO after dredge-up. Unfortunately, our observations do not allow us to draw any conclusions as to the abundances of secondary elements in the mass-losing stars in M15.

The suspicion is that stars do adjust their structure until they finally can shed their mantles as demonstrated by K648 in M15. From the analysis of spectra of GC giant stars, a picture is emerging in which metal-poor stars do become very cool while nonetheless exhibiting early-type spectra because the low metal abundances give rise to weak absorption. They may not form much dust, but they may still be able to form enough of it to drive a wind. The mid-IR spectrum of 47 Tucanae V1 suggests typical silicate dust grains and a typical mass-loss rate of 10^{-6} $M_{\odot}$ yr^{-1} (van Loon et al. 2006b).

2.3.2 IR Spectrum of K648

Although UV and optical line ratios derived for K648 from previous investigations provide constraints on relative abundance ratios, several important α-capture elements, such as S, Ar, and Ne, have ground configurations that produce only IR fine structure. If lines from these ions are not observed and introduced into abundance models, the total abundance of these elements becomes uncertain (Dinerstein et al. 2003). Often, measuring emission-line flux from [Ne II] 12.81 μm, [S IV] 10.51 μm, and [Ar III] 8.99 μm is observationally challenging from the ground. However, the sensitivity of the *Spitzer*

IRS affords an opportunity to set stringent limits on the emission-line flux of these ions, resulting in better constrained estimates on derived abundances. In addition, new radiative transition rates and collision strengths are now available as a result of the IRON project (Hummer et al. 1993) to improve the accuracy of derived abundance ratios. Below, we discuss the analysis of our *Spitzer* measurements (Table 2.5) of the [S IV] and [Ne II] lines in K648 and present a reanalysis of the S/O and Ne/O ratios with contemporary atomic parameters using a simple model. Undertaking a full photoionization analysis of K648 (e.g., Howard et al. 1997) using the *Spitzer* IR line fluxes is beyond the scope of this paper.

Hβ:

Accurate extinction corrections of UV and optical lines with respect to Hβ are required for abundance determinations. Interstellar extinction estimates to K648 range over $0.2 \leq A_V \leq 0.6$ (Garnett & Lacy 1993). However, at mid-IR wavelengths, extinction is minimal ($\lesssim 0.02$ mag), and the Pfα and Huα line detections (Fig. 2.6) enable us to estimate the emitted Hβ flux directly. Assuming case B (Osterbrock 1999), and adopting a $T_e = 12,500$ K and density of $\approx 10^3$ cm^{-1} (Garnett & Lacy 1993), we derived $F(\mathrm{H}\beta) = (1.91 \pm 0.30) \times 10^{-12}$ ergs cm^2 s^{-1} and $F(\mathrm{H}\beta) = (1.13 \pm 0.36) \times 10^{-12}$ ergs cm^2 s^{-1} from the Pfα and Huα lines, respectively, using the intrinsic hydrogen emissivity ratios tabulated in Hummer & Storey (1987). These two estimates are in reasonable agreement (within the formal error) with each other, considering there is an absolute photometric uncertainty of $\approx 5\%$ (Houck et al. 2004) between the two spectral orders (5.2–8.7 and 7.4–14.0 μm). Our average $F(\mathrm{H}\beta)$ of $(1.52 \pm 0.23) \times 10^{-12}$ ergs cm^2 s^{-1} is in good agreement with previous observational estimates, especially those obtained with large apertures (Garnett & Lacy 1993), and we adopt this value in our abundance analysis.

Neon:

The ratio of [Ne II] 12.81 μm line flux to our derived average value of Hβ was used to estimate the Ne^+/H^+ abundance. We have adopted a collisional strength $\Upsilon(T) = 0.283$ (appropriate for $T_e = 10^4$ K, Saraph & Tully (1994)) and an A_{if} value of 8.59×10^{-3} s^{-1} from the NIST database and assumed an electron density of $N_e = 1.7 \times 10^3$ cm^{-3} (Garnett & Lacy 1993). Rate coefficients, q_{fi} (Hummer et al. 1993) and the population levels were computed assuming that Ne^+, a $2p^5$ ion, is a two-level atom. Following Rank et al. (1978), we define the relative abundance of Ne^+/H^+ as

$$\frac{Ne^+}{H^+} = \frac{(4\pi\ j_{\mathrm{H}\beta}/N_e N_p)N_e}{h\nu_{fi}A_{if}f_f} \times \frac{I([\mathrm{Ne\ II}])}{I(\mathrm{H}\beta)}, \tag{2.2}$$

where the Hβ volume emissivity, $4\pi j_{\mathrm{H}\beta}/N_e N_p$, is 1.0301×10^{-25} ergs cm^3 s^{-1} interpolated for the assumed N_e (Hummer & Storey 1987), $f_f = 9.86 \times 10^{-4}$ is the population ratio of the upper to lower state, and I([Ne II]), the observed neon line flux, is $(1.74 \pm 0.08) \times 10^{-13}$ ergs cm^{-2} s^{-1} (Table 2.5). This yields a ratio of $Ne^+/H^+ = (1.53 \pm 0.21) \times 10^{-5}$. The relative abundance of Ne^{2+}/H^+ was estimated from optical measurements of the [Ne III]λ3869 and [Ne III]λ3967 lines (Adams et al. 1984) and dereddened assuming $c = 0.12$ and a Seaton (1979) extinction law. Using the [Ne III]-to-Hβ ratios (see Table 2.6), the relative populations were computed using a multi-level atom program incorporating the best available A_{ij}(s^{-1}) and collision strengths from the NIST database and the literature (Moore et al. 2004), which is similar to code originally described by Shaw & Dufour (1995). Summing over all ions, we find a total Ne/H= $(2.39 \pm 0.27) \times 10^{-5}$ and a Ne/O $= 0.48 \pm 0.14$, adopting O/H $= (5.0 \pm 1.3) \times 10^{-5}$ (Peña et al. 1993).

Table 2.6. Sulfur and Neon Abundances for K648

Quantity	Value
T_e(K)	12,500
n_e(cm^{-3})	1,700
I([S II]6717,6731)/I(Hβ)[a]	$(1.69 \pm 1.12) \times 10^{-3}$
S^+/H^+	$(6.30 \pm 3.00) \times 10^{-9}$
I([S III]9532)/I(Hβ)[b] ...	$(7.59 \pm 3.37) \times 10^{-3}$
S^{2+}/H^+	$(2.55 \pm 1.13) \times 10^{-8}$
I([S IV]10.51 μm/I(Hβ)[c]	$(5.42 \pm 2.54) \times 10^{-3}$
S^{3+}/H^+	$(1.10 \pm 0.52) \times 10^{-8}$
Total S/H	$(4.28 \pm 1.28) \times 10^{-8}$
I([Ne III]3967)/I(Hβ)[d] ..	$(2.7 \pm 0.9) \times 10^{-3}$
Ne^{2+}/H^+	$(3.69 \pm 1.23) \times 10^{-6}$
I([Ne III]3969)/I(Hβ)[d] ..	$(1.19 \pm 0.30) \times 10^{-1}$
Ne^{2+}/H^+	$(4.89 \pm 1.23) \times 10^{-6}$
I([Ne II]12.81 μm/I(Hβ)[c]	$(1.15 \pm 0.18) \times 10^{-1}$
Ne^+/H^+	$(1.53 \pm 0.21) \times 10^{-5}$
Total Ne/H	$(2.39 \pm 0.27) \times 10^{-5}$
O/H[e]	$(5.0 \pm 1.3) \times 10^{-5}$
[S/O][f]	–2.64
[Ne/O] [f]	+0.54

[a] From Barker (1983).

[b] From Barker (1983). Note lines are blended.

[c] Hβ flux derived from *Spitzer* observations of H I recombination lines (see §2.3.2).

[d] From Adams et al. (1984). Measured values corrected for extinction (see §2.3.2).

[e] From Peña et al. (1993).

[f] $[X] = \log_{10}(X_{\rm Object}) - \log_{10}(X_\odot)$.

Sulfur:

The relative sulfur abundance was computed in a similar manner to the neon abundance described in §2.3.2, although all relative populations were determined using the Moore et al. (2004) code. The *Spitzer* observation of [S IV] was used to determine the S^{3+}/H^{+} population, while the optical fluxes reported by (Barker 1983) corresponding to Hβ [assuming $j(\mathrm{H}\alpha)/j(\mathrm{H}\beta) = 2.81$; Osterbrock 1999] were used to estimate the relative S^{2+}/H^{+} and S^{+}/H^{+} abundances (Table 2.6). We find an upper limit to the total S/H of $(4.28\pm1.28)\times10^{-8}$, which is ≈ 2.5 lower than that inferred by Garnett & Lacy (1993). Adopting $\mathrm{O/H} = (5.0 \pm 1.3) \times 10^{-5}$ (Peña et al. 1993) yields $\mathrm{S/O} = (8.56 \pm 3.39)^{-4}$.

Abundance Comments:

Our new estimates of the $[\mathrm{S/O}] \leq -2.64$ and $[\mathrm{Ne/O}] = +0.54$ confirm that K648 is under-enriched in S as compared to O (Garnett & Lacy 1993), while Ne/O is enhanced with respect to solar. The Ne enhancement is seen in other halo population PNe, such as BB-1 (Dinerstein et al. 2003). Garnett & Lacy (1993) argued that contamination of He-burning products by α-captures at high temperature could account for enhanced Ne. Bianchi et al. (2001), based on analysis of *Hubble Space Telescope* (*HST*) Faint Object Spectrograph (FOS) spectra of the central star, suggest that the nebular shell was ejected by a low-mass He-burning progenitor that has subsequently undergone a late thermal pulse, perhaps similar to the evolution of objects akin to FG Sge (Gehrz et al. 2005). Our derived neon abundance using the fine-structure line suggests that dredge-up from the stellar core may be an important mechanism to pollute the expelled nebular materials from slowly evolving, young PNe.

2.3.3 Dust in the ICM

Assuming that the diffuse emission detected in the *Spitzer* images arises from ICM material, we can compute a dust mass using the observed SEDs. The approximate

temperature of the ICM dust was derived by least-squares fitting a graybody model to the SED using fluxes measured in a $130\farcs5 \times 130\farcs5$ aperture centered at the same right ascension and declination coordinates in images at all wave bands. Our choice of aperture size is equivalent to that used by Evans et al. (2003) to facilitate direct comparison. The large wavelength range of the *Spitzer* SED enables us to distinguish between the contribution of a stellar blackbody (peaking near 0.64 μm and dominated by K0 stars), and that of thermal radiating dust, which generates an IR excess at wavelengths greater than 24 μm. Use of a two-component model, incorporating a stellar blackbody that peaks near 4699 ± 58 K and a dust blackbody that peaks near $T_{\rm d} = 70 \pm 2$ K, gives a rough fit to the data (Fig. 2.9; Table 2.4). The fit produces a large reduced χ^2 value of 5.26, suggesting that the integrated flux within our aperture sums the emission from stars of many disparate spectral types that is not well represented by a simple, single emissivity and temperature blackbody. Another source of uncertainty in the fit is the effect of crowding in 2MASS data. This could lead to oversubtraction of the background and overestimation of the flux densities (van Loon et al. 2005).

The mass of the ICM was determined using the methodology described in Evans et al. (2003). We assume that the dust is optically thin, which yields the following expression:

$$\frac{M_d}{M_\odot} = 4.79 \times 10^{-17}\ f_\nu({\rm mJy})\ \frac{D^2_{\rm kpc}}{\kappa_\nu B(\nu, T_d)}, \tag{2.3}$$

where $D_{\rm kpc}$ is the distance to M15 in kiloparsecs (Table 2.1), κ_ν is the dust absorption coefficient in cm^2 g^{-1}, $B(\nu, T_d)$ is the Planck function in cgs units, and T_d is the dust temperature. At 70 μm, f_ν is 691.2 $\pm$ 61.1 mJy (Table 2.4), and κ_ν is taken from Ossenkopf & Henning (1994) to be 56 $\pm$ 11 cm^2 g^{-1}, assuming a standard Mathis-Rumpl-Nordsieck dust distribution (Mathis et al. 1977) and an ISM-type composition consisting of graphite and silicate grains. We derive a total dust mass of $(9 \pm 2) \times 10^{-4}\ M_\odot$, which agrees within a factor of 2 with the value cited by Evans et al. (2003)

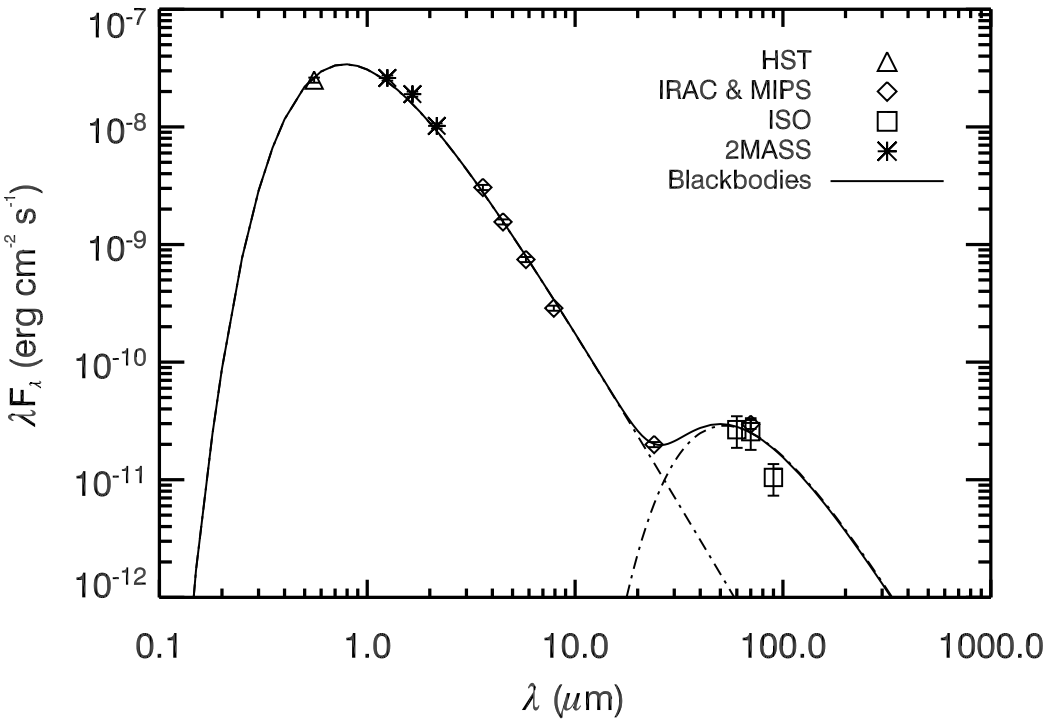

Figure 2.9: SED of the stellar and dust components near the core of M15. Fluxes (see Table 2.4) were obtained by using a square aperture centered on the dust emission at *ISO* wavelengths. The best two-blackbody fit ($\chi^2 = 5.26$) yields 4698 $\pm$ 58 and 70 $\pm$ 2 K for the stellar and dust components, respectively. The dash-dotted lines are the individual blackbodies, while the solid line is the sum of the two blackbodies.

of $(4.8 \pm 1.6) \times 10^{-4}$ $M_{\odot}$, and is approximately 2-4 times smaller than the dust mass predicted by equation (2.1). The discrepancy between the *Spitzer* and *ISO* calculated dust masses may be largely due to the different choice of κ_{ν}, as the ICM flux densities at 70 μm agree within the errors stated (Table 2.4). The most uncertain parameter in the dust mass estimate is κ_{ν}, as its value depends largely on composition and density assumptions. Therefore, we note that κ_{ν} could be up to an order of magnitude larger than the value we have invoked here.

The diffuse emission from ICM dust in M15 is located approximately 17″ to the west of the cluster core. The paucity of diffuse dust toward the cluster center, where the gravitational potential well is steepest, is puzzling. One possible explanation for this asymmetry is a collection of millisecond pulsars (PSRs) near the core of M15 (Sun et al. 2002). Seven PSRs are located within 17″ of the core (Fig. 2.10), and the radiative environs associated with these objects could lead to destruction of dust grains by sputtering or other ablation processes and may also inhibit dust production in stellar winds. The PSR nearest to the ICM dust distribution observed in the MIPS image, PSR2129+1210F, is located on the northeast outer edge of the 70 μm emission (Taylor et al. 1993). If, on the other hand, each mass-losing star has contributed 0.15 $M_{\odot}$ to the ICM on average (assuming that each star will lose 0.3 $M_{\odot}$ over its entire lifetime), then we see that an ICM dust mass of 1×10^{-3} $M_{\odot}$ corresponds to mass lost from $\sim 10^2$ stars. This suggests that the ICM is short-lived, as this many stars will have passed through the AGB superwind phase, defined as the phase in which the mass loss rate exceeds the nuclear burning mass consumption rate (van Loon et al. (1999) suggest $\dot{M} \sim 10^{-4}$ to 10^{-5} $M_{\odot}$ yr^{-1} for low-mass stars), in only $\approx 10^6$ yr, which is much shorter than the cluster's relaxation timescale. The ICM dust therefore cannot be expected to have relaxed and assumed the global shape of the gravitational potential well. If this is the case, the offset of the dust cloud from the center of the cluster would not come as a surprise.

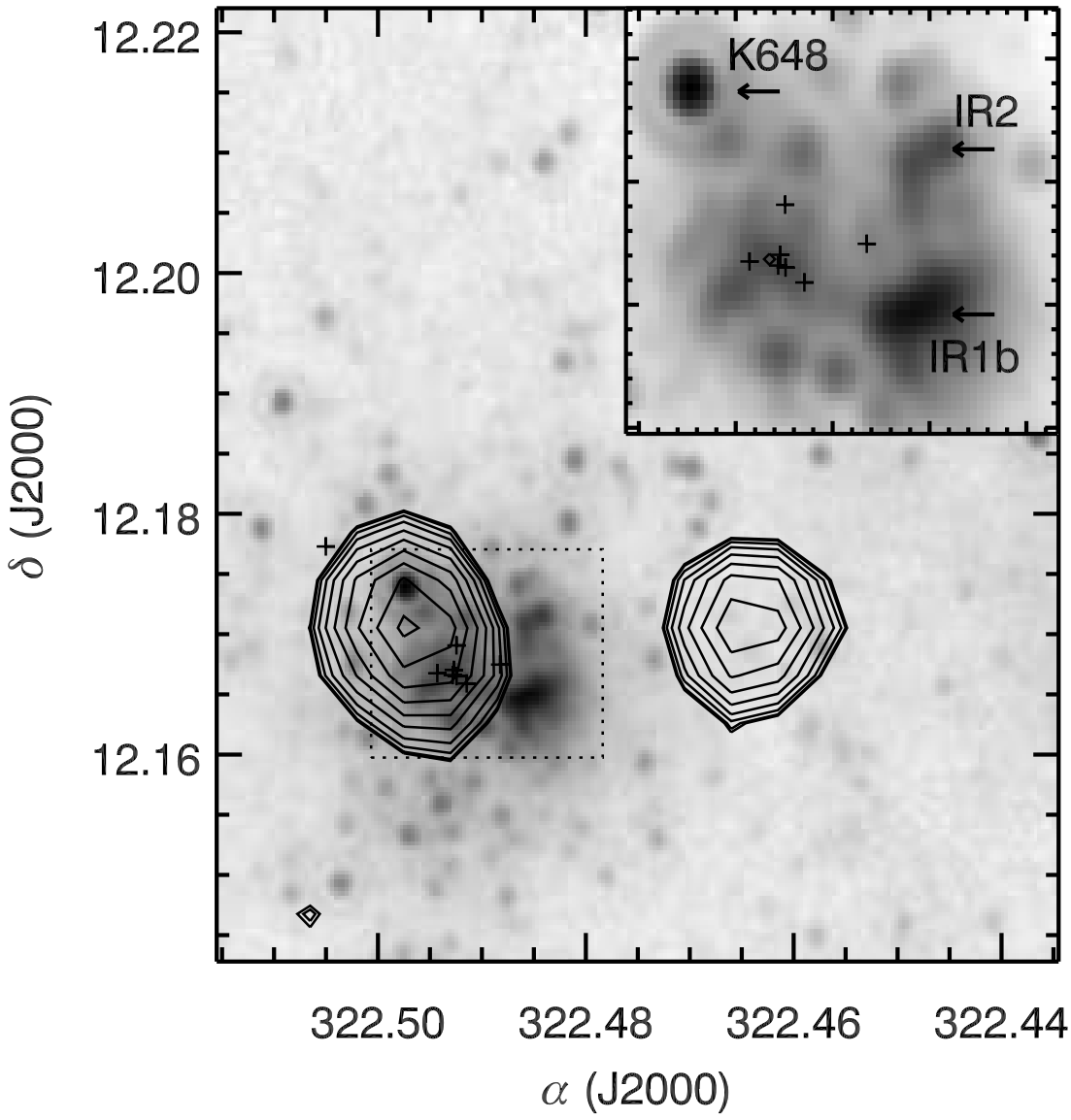

Figure 2.10: MIPS 24 μm mosaic overlaid with radio contours (1.4 GHz, Condon et al. 1998). There are 10 contour levels ranging from pixel values of 1.56 to 5.0 mJy beam^{-1} on a square root scale. Pulsar locations are marked with a plus symbol, and the center of the cluster is marked by a diamond. The inset (*dotted lines*) has dimensions of approximately $1\farcm3 \times 1\farcm0$.

Sources of the ICM dust include the post-main-sequence mass-losing stars identified in Figure 2.8. If we assume that the dust-to-gas ratio scales in proportion to metallicity during the superwind phase, as indicated by Marshall et al. (2004), then at the metallicity of M15, a dust mass loss of 10^{-10} $M_{\odot}$ yr^{-1} is expected (Becker 2000). With this mass-loss rate, we again find that the dust has been accumulating for approximately $1{\times}10^{6}$ yr, significantly shorter than the time between subsequent passages of the Galactic plane (Evans et al. 2003). This short timescale suggests that dust does not survive long in the ICM. Processes that could be responsible for removing dust from the ICM include ram pressure by the Galactic halo gas, radiation-driven outflow or photo-destruction.

2.4 Conclusions

Analysis of our *Spitzer* image data on the core of the GC M15 show strong evidence for the presence of intercluster medium (ICM) dust in the cluster core, with a mass of $(9 \pm 2) \times 10^{-4}$ $M_{\odot}$ and an equilibrium temperature of ≈ 70 K. This is the first secure, high signal-to-noise ratio detection of ICM dust in a GC. Also present surrounding the core are populations of dusty AGB and post-AGB stars, along with the planetary nebula K648. Using IRS spectral data, we have observed both the [S IV] and [Ne II] fine structure lines in K648 and have derived abundance estimates.

The unique capabilities of *Spitzer* have enabled us to identify both the interstellar dust and the dust producers in M15. This is surprising at such low metallicity ([Fe/H] = –2.4) and may have implications for dust production in the early universe. The mass of the ICM dust in M15 suggests that it has been accumulating for $\sim 10^{6}$ yr, which is a factor of 10 shorter than the time since the last Galactic plane crossing. The dust mass is also approximately 4 times smaller than the mass predicted by Evans et al. (2003). Both of these results imply that such dust does not survive long compared to its production rate, and is thus part of a stochastic process.

Chapter 3

A *Spitzer Space Telescope* Atlas of ω Centauri: The Stellar Population, Mass Loss, and the Intracluster Medium

A slightly modified version of this chapter appears in the Astronomical Journal, with the following bibliographic reference: Boyer, M. L., McDonald, I., van Loon, J. Th., Woodward, C. E., Gehrz, R. D., Evans, A., Dupree, A. K. 2008, AJ, 135, 1395.

Abstract

We present a *Spitzer Space Telescope* imaging survey of the most massive Galactic globular cluster, ω Centauri, and investigate stellar mass loss at low metallicity and the intracluster medium (ICM). The survey covers approximately 3.2× the cluster half-mass radius at 3.6, 4.5, 5.8, 8, and 24 μm, resulting in a catalog of over 40,000 point-sources in the cluster. Approximately 140 cluster members ranging 1.5 dex in metallicity show

a red excess at 24 μm, indicative of circumstellar dust. If all of the dusty sources are experiencing mass loss, the cumulative rate of loss is estimated at $2.9 - 4.2 \times 10^{-7}$ $M_{\odot}$ yr^{-1}, 63% – 66% of which is supplied by three asymptotic giant branch stars at the tip of the Red Giant Branch (RGB). There is little evidence for strong mass loss lower on the RGB. If this material had remained in the cluster center, its dust component ($\gtrsim$ 1×10^{-4} $M_{\odot}$) would be detectable in our 24 and 70 μm images. While no dust cloud located at the center of ω Cen is apparent, we do see four regions of very faint, diffuse emission beyond two half-mass radii at 24 μm. It is unclear whether these dust clouds are foreground emission or are associated with ω Cen. In the latter case, these clouds may be the ICM in the process of escaping from the cluster.

3.1 Introduction

Despite their old age and low metal content, Galactic globular clusters (GCs) are now known to be dust factories (Ramdani & Jorissen 2001; Origlia et al. 2002; Evans et al. 2003; Boyer et al. 2006; van Loon et al. 2006a; Lebzelter et al. 2006; Ita et al. 2007). This has important implications for our understanding of mass loss from low-mass and metal-poor stars and for the replenishment of the interstellar medium (ISM) within old, metal-poor stellar systems, such as GCs, dwarf spheroidal (dSph) galaxies, and galactic halos.

All stars more massive than $\simeq$ 0.8 $M_{\odot}$ lose a significant fraction of their mass before they deflagrate or leave a compact remnant (see reviews by Iben & Renzini 1983; Chiosi & Maeder 1986). In the final stages of evolution, most stars enter higher stages of nuclear burning, and the products of this nucleosynthesis are transported to the stellar surface through convection or rotation. The chemically enriched mass that is recycled (with some delay) into the ISM has a significant impact on any further star formation, and drives the chemical evolution within galaxies. In particular, the enrichment of the ISM by dust is of great importance, as grains play important roles in

many ISM processes, including the formation of molecular hydrogen (Gould & Salpeter 1963) and planet formation. The winds of low and intermediate-mass stars on the upper red giant and asymptotic giant branches (RGB and AGB) and massive red supergiants are prolific dust producers (Gehrz 1989). The dust is an integral part of the driving mechanism of the most massive winds (e.g., Gehrz & Woolf 1971; Jura & Morris 1985; Gail & Sedlmayr 1987), and our understanding of red giant mass loss relies heavily on the details of the dust condensation process (e.g., Salpeter 1974; Gauger et al. 1990; Höfner & Dorfi 1997) — which is poorly understood in particular at low metallicity (for a review, see van Loon 2006).

GCs are exquisite laboratories in which to study stellar winds because they represent the closest match to a single stellar population at metallicities that span over two orders of magnitude down to $\lesssim 1\%$ solar (cf. Gratton et al. 2004). Mass loss remains important throughout the history of a GC (van Loon & McDonald 2008); even in old GCs, stars lose $\sim$30% of their mass, most or all of which is removed from the cluster via a host of mechanisms including ram-pressure stripping during Galactic plane crossings. RGB mass loss may be responsible for the blue horizontal branches observed in metal-poor GCs (Rood 1973), and evidence for mass loss is seen in the line profiles of chromospherically active or pulsating red giants in GCs (Dupree et al. 1984; Cacciari et al. 2004; McDonald & van Loon 2007; Meszaros et al. 2008).

There is mounting evidence for mass loss from GC red giants in the form of dusty winds (Ramdani & Jorissen 2001; Origlia et al. 2002). The first spectroscopic identifications of silicate dust are in the tip-AGB star V1 in the massive GC 47 Tucanae (van Loon et al. 2006a) and subsequent identification of minerals in other AGB stars in 47 Tuc with *Spitzer* IRS observations (Lebzelter et al. 2006). With [Fe/H] $= -0.7$, 47 Tuc is a metal-rich GC, providing an environment similar to that found, for instance, in the Small Magellanic Cloud. To probe uncharted terrain, it is important to study

dust in GCs at lower metallicity. The surprising detection of both interstellar and circumstellar dust and gas in the metal-poor GC M 15 (Evans et al. 2003; Boyer et al. 2006; van Loon et al. 2006b) demonstrates that dust forms even in extremely metal-deficient environments.

3.1.1 ω Centauri

The most massive Galactic GC, ω Centauri, contains enough stars in the dusty wind phase for an empirical reconstruction of the evolution of mass loss. Its gravitational well ($v_{\rm esc}$ = 44 km s^{-1}; Gnedin et al. 2002) could retain interstellar matter if winds are slow. ω Cen is located approximately 15° out of the Galactic plane at a distance of ≈5 kpc (Lub 2002; van de Ven et al. 2006; Del Principe et al. 2006), so it is possible to probe the stellar population to the cluster core.

The bulk of the stars in ω Cen have [Fe/H] = −1.7 (Norris 1996; Smith et al. 2000), a metallicity much lower than the environments in which circumstellar dust has traditionally been studied. Complications arise because ω Cen also harbors a small fraction of stars up to an order of magnitude more metal-rich (Lee et al. 1999b; Pancino et al. 2000, 2002) and an intermediate population of stars with an abnormally high helium content (Norris 1996, 2004). Red giants in ω Cen display a range in surface abundances, from oxygen-rich, M-type stars with titanium oxides, stars enhanced in CH or in cyanide (CN), to genuine carbon stars with molecular carbon (C_2; van Loon et al. 2007). These disparate populations cause difficulties in stellar evolution studies of ω Cen, but since stars from the metal-rich and metal-poor populations can be distinguished by means of optical spectroscopy, ω Cen presents us with a unique opportunity to study the dust and mass loss within a single environment as a function of atmospheric chemistry.

Consensus has yet to be reached regarding the formation history of the different subpopulations (Sollima et al. 2005; Stanford et al. 2006; Villanova et al. 2007). The spread and peculiarities in elemental abundances in ω Cen have been interpreted as evidence

that this GC may be the remnant nucleus of a tidally disrupted dSph (Zinnecker et al. 1988; Freeman 1993). If so, ω Cen may offer us insight into the mass loss and chemical enrichment in the much more distant nucleated dSphs, and perhaps dSphs in general.

Here, we present NASA *Spitzer Space Telescope* (Werner et al. 2004; Gehrz et al. 2007) images of ω Cen and a catalog including the magnitudes of over 40,000 point-sources from 3.6 to 70 μm. The 24 μm mosaic, which enables reliable detection of individual circumstellar dust shells near the peak wavelength of their spectral energy distributions (SEDs), provides the most dramatic improvement over previous data. We make use of proper motion (van Leeuwen et al. 2000) and radial velocity (van Loon et al. 2007) measurements to separate cluster members from the substantial foreground stellar and background galaxy populations. Optical spectroscopic information permits us to compare the contributions from stars of different composition and evolutionary status to their infrared (IR) emission and dust production. Our observations are discussed in § 3.2, photometry and the ω Cen point-source catalog are described in § 3.3. The color-magnitude diagrams (CMDs), stellar populations, mass loss, and the intracluster medium (ICM) dust are discussed in § 3.4, and our conclusions are presented in § 3.5.

3.2 Observations

We used the NASA *Spitzer Space Telescope* to obtain image maps of the GC ω Cen (Program Identification [PID] 20648, PI: van Loon) with the Infrared Array Camera (IRAC; Fazio et al. 2004) and the Multiband Imaging Photometer for *Spitzer* (MIPS; Rieke et al. 2004). Observations are centered at R.A. = $13^{\rm h}26^{\rm m}45\overset{\rm s}{.}9$, decl. = $-47^\circ28'37\overset{''}{.}0$ [J2000.0] and map the cluster to at least 3.2 times the half-mass radius ($r_{\rm hm} = 4.8'$; Harris 1996) at each wavelength. Observation details are summarized in Table 3.1.

Images centered at 3.6, 4.5, 5.8, and 8 μm were obtained with IRAC on 2006 March 26 UT. We observed in high dynamic range mode, enabling us to correct saturated

Table 3.1. Observational Summary

Parameter	IRAC	MIPS
λ (μm)	3.6, 4.5, 5.8 and 8	24 and 70
Program ID	20648	20648
Date (UT)	2006 Mar 26	2006 Feb 22 and Mar 02
AORkey	14955264	(1495)5520, 5776, 6032, 6288, 6544, and 6800
Coverage	$35' \times 35'$	24 μm: $35' \times 55'$ 70 μm: $21' \times 55'$
Single Frame . . . . . Exposure Time (s)	10.4	24 μm: 9.96 70 μm: 10.49
Average Depth . . . (no. frames)	10	24 μm: 67 70 μm: 36
Pixel Size . . . . . (arcsec pixel^{-1})	1.22	24 μm: 1.25×1.30 70 μm: 4.93×5.03
PSF size	3.6 μm: $1.7'' \times 1.6''$ 4.5 μm: $1.6'' \times 1.6''$ 5.8 μm: $1.6'' \times 1.7''$ 8 μm: $1.8'' \times 1.8''$	24 μm: $5.3'' \times 5.9''$

Note. — Observations are centered at R.A. = $13^{\rm h}26^{\rm m}58\overset{\rm s}{.}4$, decl. = $-47°45'21\overset{''}{.}8$ [J2000.0]

sources in the long exposures (10.4 s) with their counterparts in the short exposures (0.4 s) while still achieving a high signal-to-noise ratio for the fainter sources. Images were taken at nine dither positions in a cycling pattern to build redundancy against outliers and artifacts. The resulting image map contains a total of 441 images and covers an area approximately $35' \times 35'$ around the cluster center.

MIPS images at 24 and 70 μm were obtained on 2006 February 22 UT and 2006 March 02 UT with seven scan legs of approximately 0.5° in length. The resulting mosaics combine 4,620 images for each wavelength and cover a total area of approximately $35' \times 55'$. We designed our MIPS observing campaign with the intention of obtaining only 24 μm data, and the MIPS 70 and 160 μm data were obtained automatically (see Rieke et al. 2004). Due to the non-functioning half of the 70 μm array, the 70 μm data do not have complete coverage. The warm state of the telescope during the observations saturated the 160 μm array, rendering the 160 μm data useless. MIPS observation details are summarized in Table 3.1.

Raw MIPS and IRAC data were processed with the *Spitzer* Science Center (SSC) pipeline, version S13.2.0[1]. The Basic Calibrated Data (BCD) were post-processed with portions of the 2006 March 01 version of the SSC Legacy MOPEX software (Makovoz & Marleau 2005). For IRAC, after applying an array distortion correction, we implemented the MOPEX background-matching routine to minimize pixel offsets in overlapping areas of the mosaics and the MOPEX mosaicker to eliminate cosmic rays and other outliers. No further cosmetic corrections were applied to the BCDs before performing point-spread-function (PSF) photometry. The final mosaics have a pixel size of $1\farcs22$ pix^{-1}. A three-color image of the first three IRAC bands is presented in Figure 3.1a, in which very few sources appear with a red or blue excess.

For the MIPS 24 μm data, we created and applied scan-mirror-dependent and scan-mirror-independent flat fields for all images excluding the bias boost images, any image

[1]http://ssc.spitzer.caltech.edu/archanaly/plhistory/

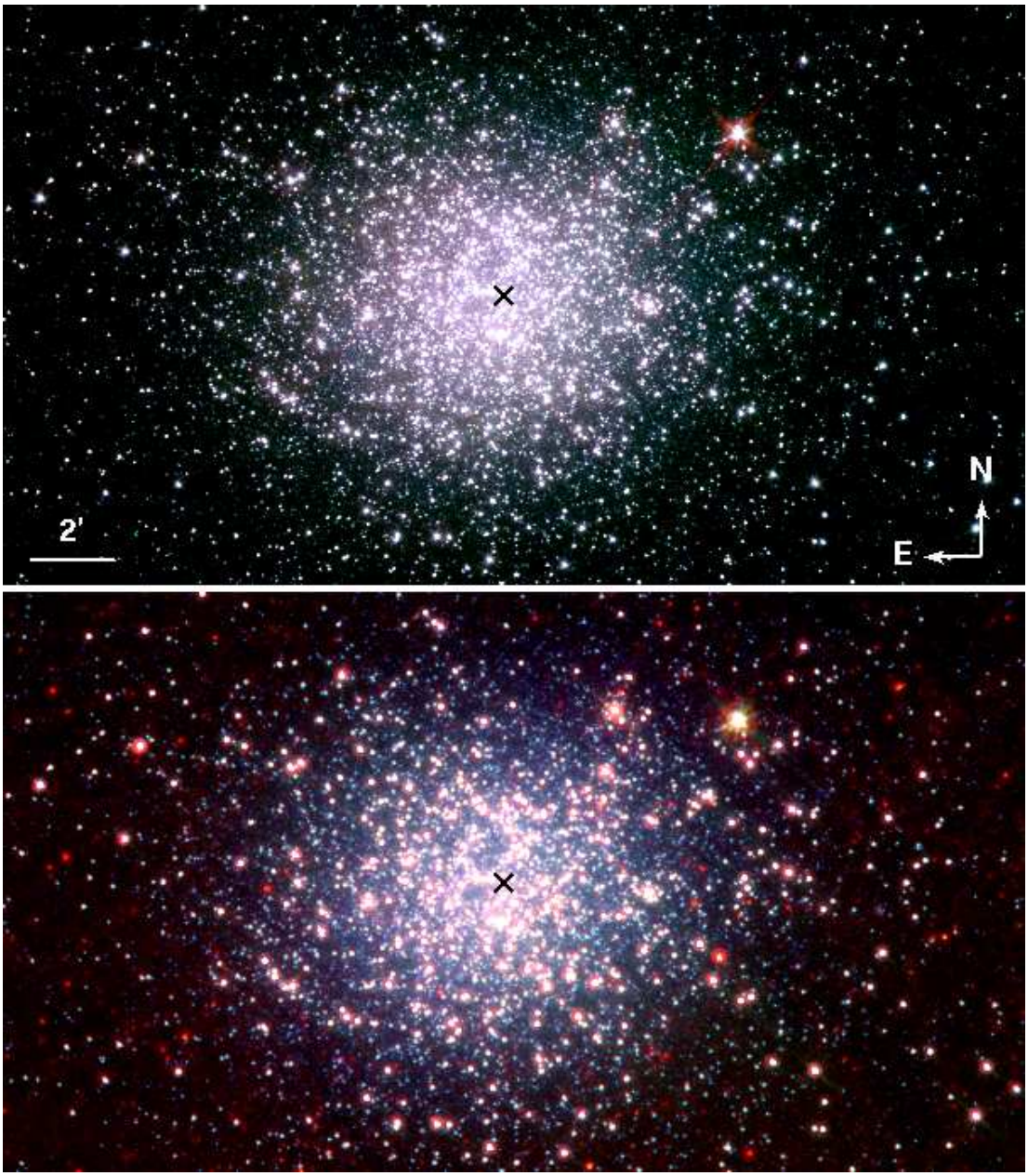

Figure 3.1: Three-color images of ω Cen. Upper panel: Blue is 3.6 μm, green is 4.5 μm and red is 5.8 μm. Lower Panel: Blue is 3.6 μm, green is 8 μm and red is 24 μm. The black "X" marks the cluster center. Dusty stars and/or background galaxies become visible at 8 and 24 μm and appear red in the lower panel. No obvious intracluster medium dust clouds are visible.

within $10'$ of the cluster center, and any image containing a very bright source. A 2-degree polynomial fit was applied over the entire image to subtract the zodiacal background. At 70 μm, we first performed pixel time-filtering and column filtering with SSC contributed software from D. Fadda and D. Frayer[2]. We then implemented the MOPEX background-matching and mosaic routines at both 24 and 70 μm before proceeding with point-source extraction. An IRAC and MIPS three-color image is presented in Figure 3.1b, in which several cool dusty objects appear green at 8 μm and red at 24 μm.

3.3 Photometry

3.3.1 Point-Source Extraction

Point-source extraction for 3.6 – 24 μm was done with the DAOphot II photometry package (Stetson 1987). PSFs were created using a minimum of 20 isolated stars. Sources brighter than 4 σ over the background were chosen for extraction from the mosaic image. Any remaining outliers and other extended objects were eliminated from the sample with a sharpness cut-off, which identifies sources broader or narrower than the PSF. Photometric completeness at each wavelength was determined through false star tests; 50% and 90% completeness limits are listed in Table 3.2.

[2]http://ssc.spitzer.caltech.edu/mips/filter/

Table 3.2. Completeness Limits for Different Cluster Radii

Wavelength (μm)	50% Complete (mag)	90% Complete (mag)
3.6	16.7 ± 0.1	15.9 ± 0.1
4.5	16.7 ± 0.1	15.9 ± 0.1
5.8	16.0 ± 0.1	14.5 ± 0.1
8	15.8 ± 0.1	14.3 ± 0.1
24	11.9 ± 0.1	11.6 ± 0.1

Note. — Completeness limits were determined from false star tests. These limits reflect the average over the entire cluster coverage; photometry is less complete in the core than on the outskirts of the cluster.

The final fluxes and flux uncertainties are color-corrected according to the IRAC and MIPS Data Handbooks versions 3.0 and 3.2.1, respectively (*Spitzer* Science Center 2006a,b), using a 5000 K blackbody, which is the approximate temperature of a typical RGB star. Fluxes in the point-source catalog described in § 3.3.2 have *not* been corrected for reddening. Where the reddening correction has been applied for analysis of the data, A_λ values are taken from Indebetouw et al. (2005) and $E(B-V) = 0.11$ (Lub 2002). The pixel-phase-dependent photometric correction described by Reach et al. (2005) was also applied to 3.6 μm fluxes and their uncertainties. This correction was applied only to 3.6 μm because it is not well defined for the other *Spitzer* wavelengths. The flux uncertainties that we report in the *Spitzer* catalog described in section § 3.3.2 include both the uncertainties quoted by DAOphot and the calibration uncertainties specified by Reach et al. (2005) for IRAC and Engelbracht et al. (2007) for 24 μm. All fluxes were converted to stellar magnitudes using the zero fluxes reported in the *Spitzer* Data Handbooks. The photometric uncertainty as a function of source magnitude is given in Figure 3.2.

3.3.2 The Point-Source Catalog

We have created a point-source catalog of $>$ 40,000 ω Cen objects detected at 3.6, 4.5, 5.8, 8, and 24 μm. An extraction from this catalog is given in Table 3.3, where column one is the source number, column two is the source ID, columns 3 – 7 are *Spitzer* magnitudes, column 8 is the membership probability (van Leeuwen et al. 2000), columns 9 and 10 list source type labels, and column 11 lists the Leiden identifiers (LEID) from van Leeuwen et al. (2000). The source ID follows the standard *Spitzer* naming convention, giving the truncated (J2000) coordinates. The complete *Spitzer* catalog is available electronically through the Centre Données de Strasbourg (CDS).

Cluster members and non-members were identified by cross-correlating the *Spitzer*

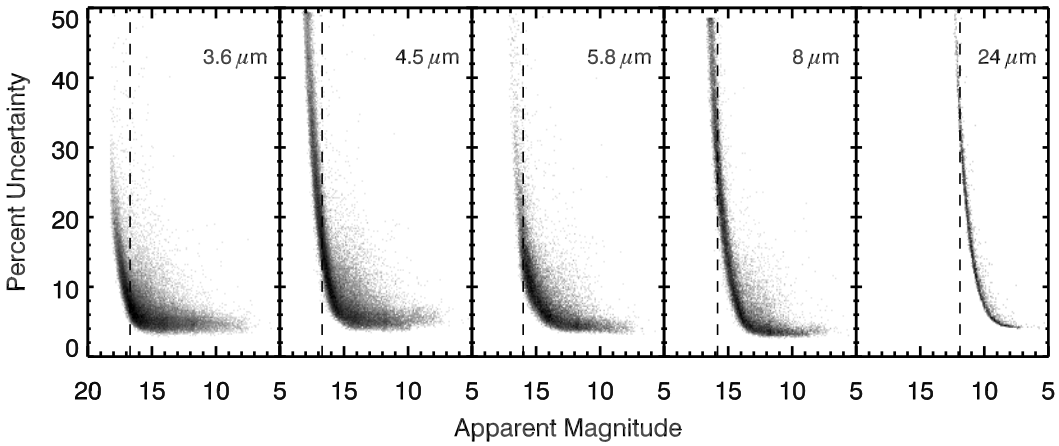

Figure 3.2: Photometric errors. The x-axis is binned by 0.1 magnitudes, and the y-axis is binned by 0.2 percentage points. The dashed lines mark the limit where photometry is 50% complete (see Table 3.2). The errors for the bulk of the stellar population are low, but climb steadily at the faintest magnitudes.

source coordinates with those in the van Leeuwen et al. (2000) proper motion catalog. The van Leeuwen et al. (2000) catalog is not as deep as our survey nor is the coverage as wide, so many *Spitzer* sources do not have proper motion measurements. van Leeuwen et al. (2000) derived positions and proper motions by cross-referencing with the International Celestial Reference Frame as defined by the Hipparcos catalog and extended to a denser grid of stars by the Tycho-2 catalog. The coordinates of the *Spitzer* sources are systematically offset from the van Leeuwen et al. (2000) sources, with mean offsets of $\Delta\alpha = +0.40''$ and $\Delta\delta = +0.25''$ and standard deviations of $0.15''$ and $0.10''$, respectively. Coordinates in the *Spitzer* catalog are not corrected for this offset.

If a source in any IRAC band was not associated with another IRAC, MIPS, or van Leeuwen et al. (2000) object, we considered it a false detection and dropped it from the *Spitzer* catalog. MIPS 24 μm sources that do not have IRAC or optical counterparts remain in the catalog since the very red SEDs of many MIPS sources peak in the mid-IR and are thus fainter than the sensitivity limits in the bluer *Spitzer* bandpasses.

Also included in the *Spitzer* catalog are notes in columns 9 and 10 indicating if the source is a galaxy, AGB, anomalous RGB (RGB-a), or Horizontal Branch (HB) star, based on its locations on the CMDs (see § 3.4.1). The catalog also indicates sources that are super-Ba- or CN-rich and/or are M-type (M), carbon (C), or post-AGB stars (P), as identified by van Loon et al. (2007).

The differing resolution between IRAC and MIPS has caused some sources that are isolated in IRAC to be blended in the 24 μm mosaic, which produces an artificially red [8] – [24] color. To determine which sources are potentially affected by blending, we convolved the 8 μm mosaic with the 24 μm PSF and identified sources with elevated fluxes in the convolved mosaic compared to the unaltered mosaic (Fig. 3.3). These sources are marked with "B24", for "blended at 24 μm", in column 10 of the *Spitzer* catalog.

Table 3.3: Sample Source Catalog

No.	Source ID[a]	Apparent Magnitude					Membership[b] (%)	Candi-date[3]	Note[d]	LEID[e]
		3.6 μm	4.5 μm	5.8 μm	8 μm	24 μm				
(1)	(2)	(3)	(4)	(5)	(6)	(7)	(8)	(9)	(10)	(11)
18562	J132626.28−472520.06	8.49(05)	8.52(06)	8.53(04)	8.47(04)	8.48(05)	100	···	CN	35090
18563	J132626.28−473229.59	14.04(09)	14.16(07)	14.24(07)	14.32(07)	···	···	···	···	···
18564	J132626.28−471144.58	16.58(08)	16.37(09)	15.86(13)	···	···	···	···	···	···
18565	J132626.28−474102.18	16.77(09)	16.68(16)	16.33(18)	···	···	···	···	···	···
18566	J132626.29−473737.68	17.51(12)	17.71(46)	···	···	···	···	···	···	···
18567	J132626.29−471200.23	17.20(11)	17.13(20)	···	···	···	···	···	···	···
18568	J132626.29−473049.11	13.59(05)	13.58(07)	13.68(06)	···	···	100	HB	···	47097
18569	J132626.29−472651.06	13.23(05)	13.20(06)	13.18(05)	13.16(10)	···	98	···	···	39111
18570	J132626.30−471915.97	17.04(09)	17.00(22)	···	···	···	···	···	···	···
18571	J132626.30−473515.89	17.30(14)	17.55(27)	···	···	···	···	···	···	···
18572	J132626.30−471416.24	16.00(06)	···	16.21(19)	···	···	···	···	···	···
18573	J132626.30−474159.18	13.22(06)	13.24(06)	13.28(04)	···	···	86	···	CN	72019
18574	J132626.31−471627.20	9.34(04)	9.28(06)	9.31(05)	9.29(04)	9.30(06)	18	···	P	16018
18575	J132626.31−473111.71	14.94(08)	15.06(11)	···	···	···	···	···	···	···
18576	J132626.31−472320.08	13.98(06)	13.99(05)	14.00(05)	14.02(06)	···	···	···	···	···
18577	J132626.31−474246.15	17.80(20)	17.95(52)	···	16.08(35)	···	···	Galaxy	···	···
18578	J132626.32−473543.47	13.12(04)	13.18(09)	13.11(08)	13.18(08)	···	···	···	···	···
18579	J132626.32−472534.32	10.13(05)	10.15(06)	10.15(05)	10.16(04)	10.18(09)	100	···	···	36061
18580	J132626.32−474718.12	···	15.72(08)	···	15.67(26)	···	···	···	···	···
18581	J132626.33−473132.57	12.23(08)	12.28(07)	12.24(06)	12.02(06)	···	100	RGB-a	···	49082

NOTE.—Magnitude uncertainties are quoted in parentheses. For example, a magnitude of 8.49 ± 0.05 is listed as 8.49(05).

[a] To save space, the Source ID is truncated to show only the source coordinates. The full electronic catalog, available through CDS, includes the *Spitzer* prefix (SSTOCEN).

[b] Membership likelihoods are quoted as a percentage from van Leeuwen et al. (2000).

[c] Candidate AGB, RGB-a, and HB stars and candidate galaxies are identified by their positions on optical and *Spitzer* CMDs.

[d] The Note column specifies whether a source is CN- or super-Ba-rich and/or is a M-type (M), carbon (C), or post-AGB (P) star, as indicated by optical spectra (van Loon et al. 2007). The note also indicates if a source is potentially affected by blending at 24 μm (B24, see § 3.3.2).

[e] The LEID identification numbers are assigned to *Spitzer* sources via cross-identification with van Leeuwen et al. (2000).

3.3.3 Luminosity Functions and Completeness

Luminosity functions for epoch two are displayed in Figure 3.4. The distance modulus used to determine absolute magnitudes is 13.58, given a distance of 5.2 kpc (Del Principe et al. 2006). In the top panels, known non-members are excluded and of the remaining sources, only those that are in at least two adjacent wavebands are included. The IRAC luminosity functions show a strong change in slope near an absolute magnitude of –2 that may be the RGB bump or the RGB clump, both of which are located at absolute magnitudes of ≈ -2 – 0 in the near-IR data of several GCs (Valenti et al. 2007), depending on the metallicity of the cluster. The HB is also visible at 3.6, 4.5, and 5.8 μm just beyond an absolute magnitude of zero as either a bump or change in slope.

The tip of the RGB (TRGB) is difficult to determine from the luminosity functions, as the source counts are low at absolute magnitudes brighter than -5. The sparse population of AGB stars above the TRGB is expected in GCs since this phase of stellar evolution is particularly short-lived and also because the very low mass of stars in GCs ($M_{\rm AGB} \simeq 0.6 - 0.8\ M_{\odot}$) prevents AGB luminosity from climbing much above the TRGB. Nevertheless, the source counts of known cluster members (lower panels of Fig. 3.4) do drop by a factor of 3 to 4 past the bins, which are 0.2 magnitudes wide, centered at absolute magnitudes of -5.9, -6.1, -6.1, -6.1, and -6.3 at 3.6, 4.5, 5.8, 8, and 24 μm, respectively. The K-band TRGB for ω Cen is located at $\approx -6.04 \pm 0.16$ magnitudes (Bellazzini et al. 2004). At 3.6 μm, the TRGB location is -6 magnitudes for many stellar populations, including the Large Magellanic Cloud (LMC; van Loon et al. 2005) and smaller stellar populations such as the Local Group dwarf irregular galaxy WLM (Jackson et al. 2007a).

Photometric completeness in each waveband was determined by performing false star tests, for which 2% of the total stellar population that mimicked the luminosity function was added to each mosaic at random positions and PSF photometry was

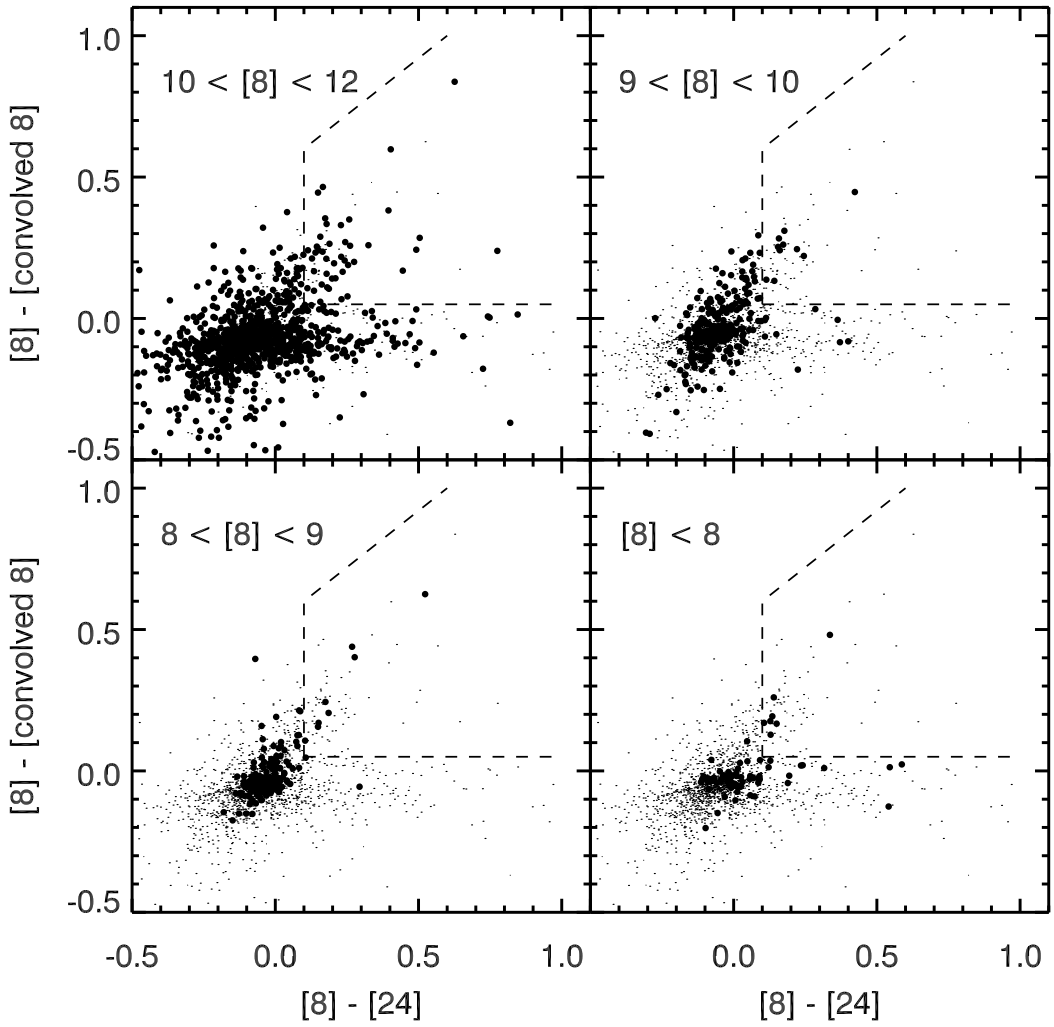

Figure 3.3: Color-color diagram showing which individual sources are affected by blending at 24 μm. We convolved the 8 μm image with the 24 μm PSF and extracted point sources from the resulting image. Each panel shows the entire population in small points, with the 8 μm magnitude range indicated in each panel plotted in large, filled circles. Sources that have red [8] – [convolved 8] colors are affected by blending, whereas sources with red [8] – [24] colors and [8] – [convolved 8] ≈ 0 are truly red and likely harbor dust. We find that up to 25% of the population with [8] – [24] > 0.1 is affected by blending.

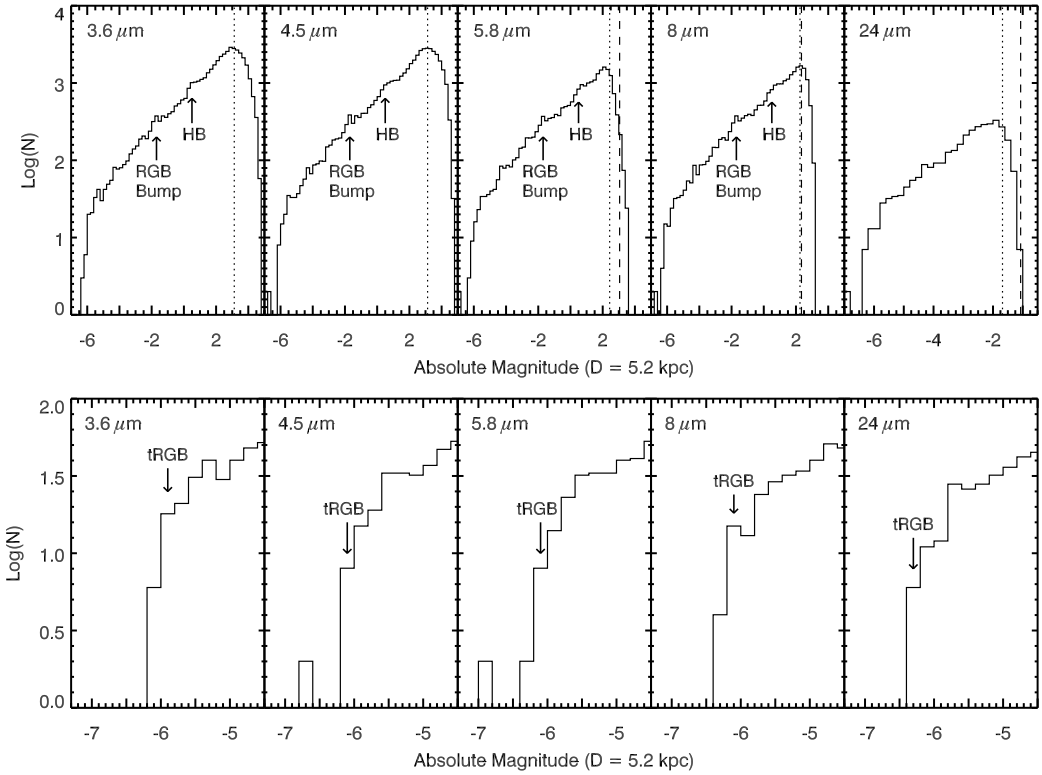

Figure 3.4: Luminosity functions for 3.6, 4.5, 5.8, 8, and 24 μm. The bin size is 0.2 magnitudes and fluxes are corrected for reddening ($E(B-V) = 0.11$; Lub 2002). In the upper panels, only sources detected in at least two bands are plotted and known non-members are excluded. In the lower panels, only known cluster members are plotted (van Leeuwen et al. 2000). The dashed lines show the 3 σ sensitivity limit for each band (at 3.6 and 4.5 μm, the sensitivity limit is fainter than the plot area shown), and the dotted lines mark the 50% completeness limits. The photometry is nearly complete down to the 3 σ sensitivity limit at 5.8 – 24 μm, but is less complete at the shortest wavelengths due to severe stellar crowding in the cluster core. In the upper panels, the arrows indicate changes of slope that show the position of the RGB Bump/Clump and the HB. In the lower panels, the tip of the RGB (TRGB) is marked as the point where the source counts drop by a factor of $\approx$4.

performed to attempt to recover these false stars. The test was carried out 100 times for each wavelength. Dotted lines mark the 50% completeness limits in the upper panels of Figure 3.4, which are listed in Table 3.2. The dashed line in Figure 3.4 marks the sensitivity limit at each bandpass, and shows that the photometry is the most incomplete at 3.6 and 4.5 μm, which is likely due to severe stellar crowding in the cluster core at these wavelengths. Photometry at 5.8 – 24 μm is 50% complete to within two magnitudes of the 3 σ sensitivity limits.

3.4 Discussion

3.4.1 The Color-Magnitude Diagrams

Figure 3.5 displays the optical (van Leeuwen et al. 2000), the near-IR (Sollima et al. 2004), and our mid-IR CMDs. The CMDs are corrected for reddening, as discussed in § 3.3, with A_B values from Rieke & Lebofsky (1985), but the effect of reddening on the mid-IR magnitudes is minimal. The IRAC and MIPS CMDs shows very little structure aside from the RGB, and at longer wavelengths, a very broad, faint red plume. Mid-IR isochrones that include all known RGB/AGB properties, molecular bands, and dust considerations have yet to be developed. For reference, the brightest IRAC sources are labeled with large filled circles in Figure 3.5, and the three brightest M-type stars are also labeled with their LEID numbers. Bright IRAC sources that are not labeled are not cluster members. Figure 3.6 shows the same CMDs with different source types labeled in color. Black points are confirmed cluster members (confirmed non-members are not plotted) and gray points, which are mostly located at the faint end of the RGB, do not have matches in the proper motion catalog.

Absorption in molecular bands may be responsible for some of the spread towards red colors on the RGB, but cannot cause colors as red as those of the dustiest stars. However, while many of the very red stars on the mid- to lower-RGB in Figure 3.5 may

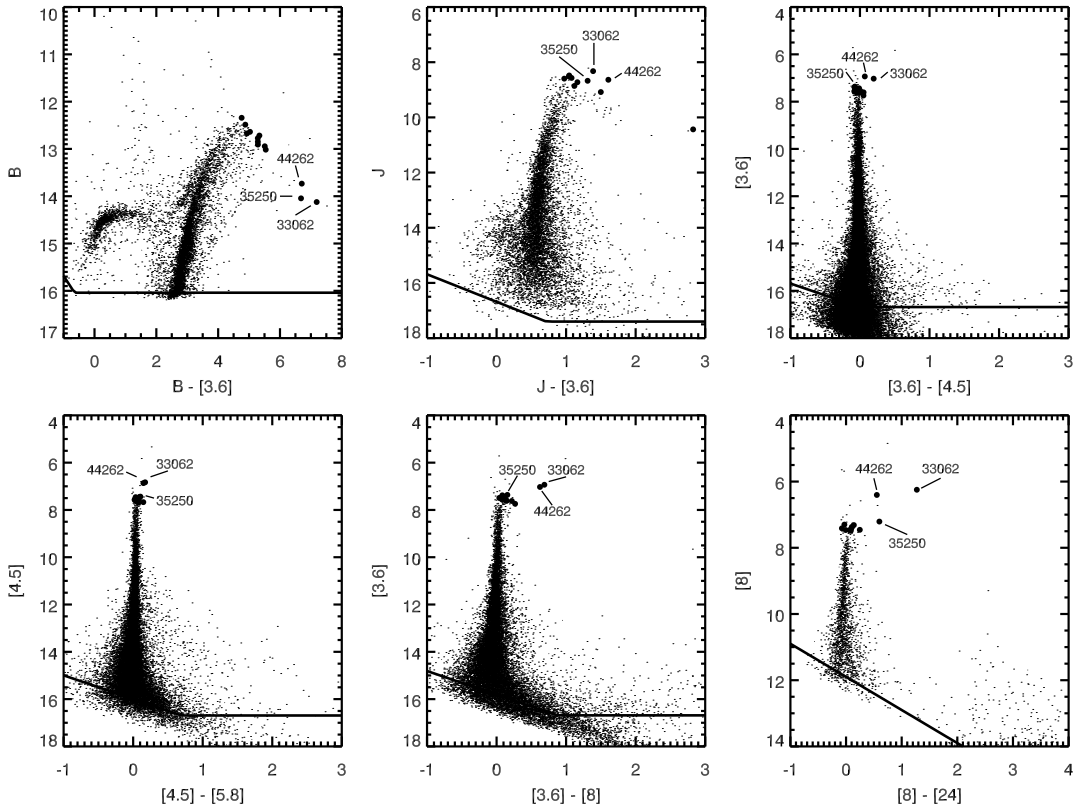

Figure 3.5: CMDs for ω Cen. Fluxes are corrected for reddening ($E(B-V) = 0.11$; Lub 2002). B magnitudes are from van Leeuwen et al. (2000) and J magnitudes are from Sollima et al. (2004). The solid lines mark where the photometry is 50% complete in the case of *Spitzer* or mark the detection limit from van Leeuwen et al. (2000) and Sollima et al. (2004). The brightest confirmed cluster members at IRAC wavelengths are marked with large filled circles in each panel to show their evolution over color-magnitude space (non-members remain small dots). The three most extreme M-type stars are labeled with their LEID numbers.

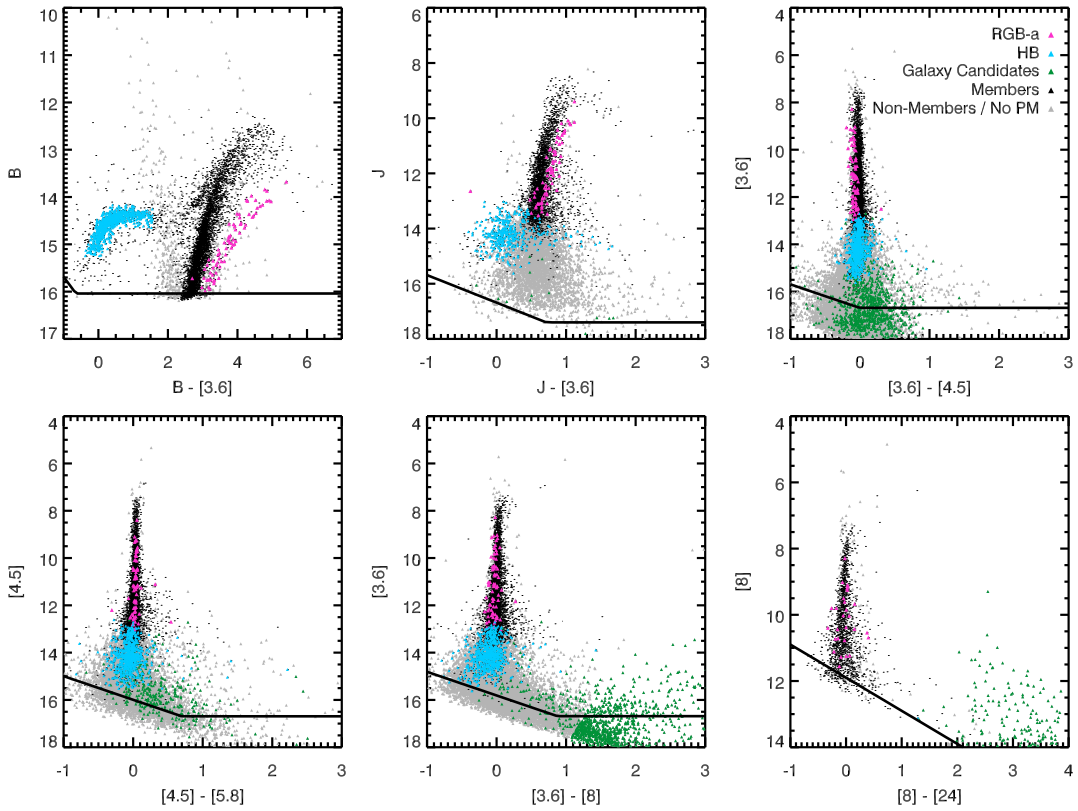

Figure 3.6: CMDs for ω Cen. Same as Figure 3.5, with different source types plotted in colors. Black points are confirmed cluster members (van Leeuwen et al. 2000), gray points are not included in the van Leeuwen et al. (2000) proper motion (PM) catalog, green points are possible background galaxies, blue points are HB stars, and magenta points are sources belonging to the RGB-a. HB and RGB-a stars were identified by their positions on the B – [3.6] CMD. IRAC samples the Rayleigh-Jeans tail of the Planck function, so at *Spitzer* wavelengths, the HB does not separate from the RGB as in optical CMDs, nor does the RGB-a except for a trend towards slightly blue [3.6] – [4.5] colors. Background galaxies are identified by their [3.6] – [8] and [8] – [24] colors and appear very red at 8 μm due to PAH emission and at 24 μm due to dust emission.

be dusty, it is very likely that some of the these sources are red due either to mismatches across bands, photometric errors, or contamination from cluster non-members.

The B – [3.6] CMD clearly displays the RGB, AGB, and HB. Also visible as a sparsely populated branch to the red of the RGB is the RGB-a (magenta points). The plume of stars that falls intermediate to the RGB and the HB is mostly due to foreground contamination (Bellazzini et al. 2004), however the brighest cluster members in this plume ($B \lesssim 13$, $1 \gtrsim B$ – [3.6] $\gtrsim 3$) include post-AGB stars such as LEID 16018, 30020, 32015, 32029, and 43105. Note that while van Leeuwen et al. (2000) found that 16018 and 32029 are cluster non-members, van Loon et al. (2007) determined through optical spectroscopy that they do in fact belong to ω Cen. As such, their membership probabilities have been set to 100% in the *Spitzer* catalog.

We identified HB stars (blue points) by their positions on the optical CMD (van Leeuwen et al. 2000). Since the IR samples the Rayleigh-Jeans tail of the Planck function, the HB becomes indistinct from the RGB in the IR. The stellar density profile shown in Figure 3.7 shows a paucity of HB stars in the center of the cluster. The non-central peak of the HB density profile is explained by the dominance of the cluster luminosity by bright AGB and RGB stars in the most crowded regions.

RGB-a stars are those located on the red branch of the RGB in optical and near-IR CMDs (see Fig. 5 of Sollima et al. 2004). The offset of the RGB-a from the main RGB in optical and near-IR CMDs has been attributed to a metallicity difference between the RGB-a and the regular RGB (Lee et al. 1999b; Pancino et al. 2000, 2002; Origlia et al. 2003). Except for a slight blue excess in the [3.6] – [4.5] colors, no metallicity separation is evident in the *Spitzer* CMDs.

3.4.2 The Asymptotic and Red Giant Branches

Inspection of the luminosity functions (Fig. 3.4) suggests that the stellar count begins to decrease at an accelerated rate near an absolute magnitude of -5 at each wavelength.

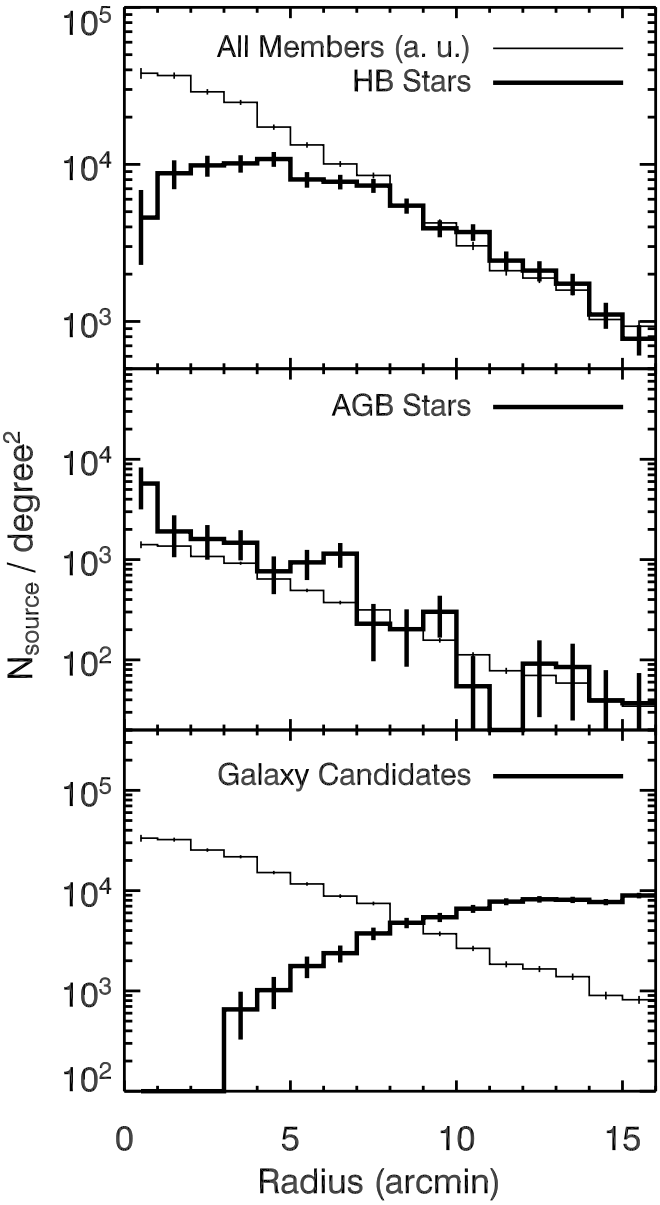

Figure 3.7: Source density profiles for ω Cen. The thick line shows possible HB stars in the top panel, AGB stars in the middle panel, and galaxy candidates in the lower panel. For comparison, the density profile for all cluster members is shifted down to match each profile at $r = 8.5'$ and plotted in arbitrary units (a.u.) as a thin line. The AGB stars appear to be slightly more centrally concentrated than the general ω Cen population, and there is a paucity of HB stars and galaxy candidates in the cluster center. The HB and AGB profiles might be explained by the lower and higher flux densities of HB and AGB stars, respectively, than the general stellar population rather than a real difference between the profiles.

We chose this magnitude as the divide at all *Spitzer* wavelengths between mass-losing AGB candidates and the rest of the stellar population. We identify 75 mass-losing AGB candidates, several of which have a red excess, although mass-loss can occur even without a dusty circumstellar envelope (McDonald & van Loon 2007). The AGB population is slightly more centrally concentrated than the total stellar population (Fig. 3.7), which is probably due to decreasing completeness of fainter sources towards the core.

The locations on the CMD of stars that are identified as CN- and super-Ba-rich by optical spectroscopy (van Loon et al. 2007) are marked in Figure 3.8a. The term super-Ba-rich distinguishes stars with enhanced Ba through pre-enrichment from those that are enriched beyond this, probably due to internal mixing processes. The super-Ba-rich stars dominate the stars brighter than [24] $\approx$ 8.5, supporting the suggestion by van Loon et al. (2007) that these stars are enriched in Barium due to third-dredge up, and therefore delineate the thermal pulsating AGB. The super-Ba-rich stars may also be enriched in carbon, but not so much as to warrant their classification as genuine carbon stars.

Figure 3.9 shows the [8] – [24] CMD for cluster members, non-members, and sources without proper motion measurements. Sources affected by blending at 24 μm are not plotted. The location on the CMD of the majority of sources without proper motion measurements suggests that most are likely galaxies. Stars brighter than [24] $\approx$ 10 with [8] – [24] $>$ 0.1 likely harbor dust, while sources fainter than [24] $\approx$ 10 are dusty if [8] – [24] $>$ 0.2. Also marked in Figure 3.9 and listed in Table 3.4 are 16 stars of interest, identified by van Loon et al. (2007) as six M-type stars (open squares), five carbon stars that show C_2 bands (open triangles), and five post-AGB stars (closed circles), including Fehrenbach's star (Fehrenbach & Duflot 1962) near [24] = 9.25.

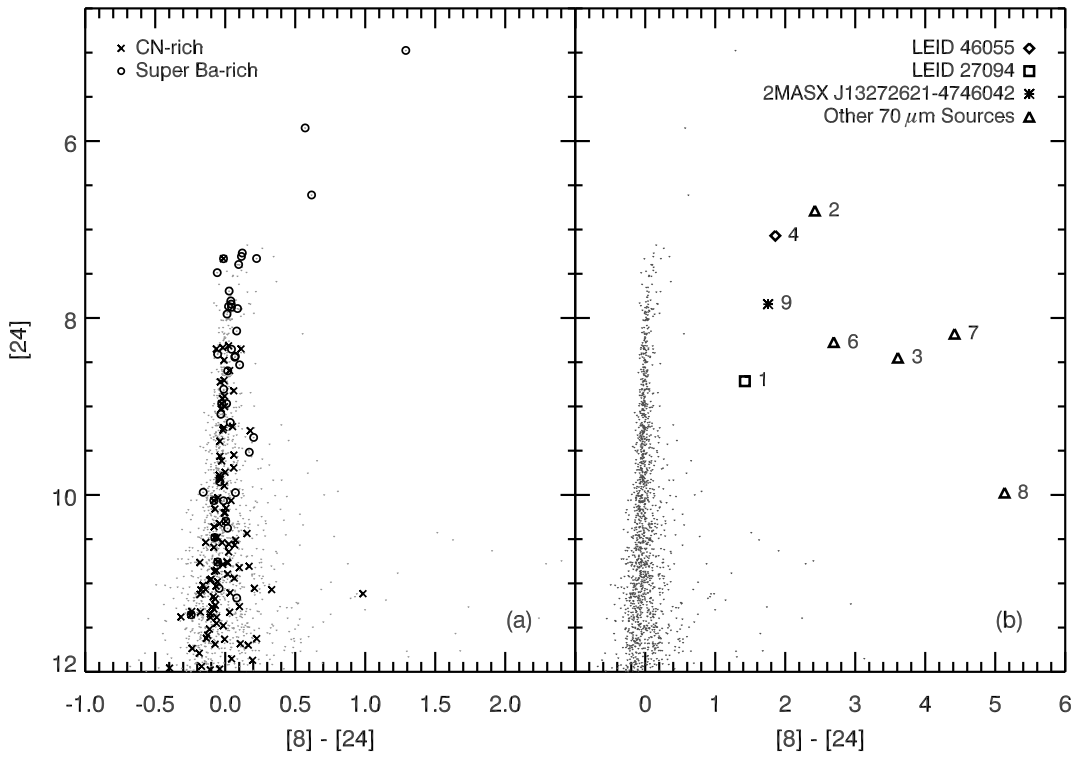

Figure 3.8: [8] – [24] CMDs showing the location of various stellar populations. Panel (a) shows super-Ba-rich and CN-rich stars as identified by their optical spectra (van Loon et al. 2007); super-Ba-rich stars delineate the upper part of the AGB possibly due to third dredge-up. Panel (b) shows the 70 μm sources. Two of these are spatially coincident with cluster members (LEID sources), and one is a resolved spiral galaxy (2MASX J13272621–4746042). The numbers to the right of each symbol correspond to the source numbers in Tables 3.7 and 3.8. All sources show excess 24 μm emission.

Table 3.4: *Spitzer* Magnitudes of M-Type, Carbon, and post-AGB Stars identified by van Loon et al. (2007)

LEID	Source ID[a]	$m_{3.6}$	$m_{4.5}$	$m_{5.8}$	m_{8}	m_{24}	Source Type
14043	J132750.37−471542.79	11.75(06)	···	11.77(04)	···	···	Carbon Star
16018[b]	J132626.31−471627.20	9.34(04)	9.28(06)	9.31(05)	9.29(04)	9.30(06)	Post-AGB
30020	J132549.95−472259.76	12.62(05)	12.62(06)	12.61(06)	12.66(04)	···	Post-AGB
32015	J132538.44−472401.79	10.26(05)	10.23(07)	10.22(07)	10.27(04)	10.27(09)	Post-AGB
32029	J132605.17−472342.43	9.11(05)	8.96(05)	8.82(04)	8.81(04)	8.48(05)	Post-AGB
32059	J132628.13−472340.56	8.45(05)	8.52(06)	8.52(04)	8.40(05)	8.40(05)	Carbon Star
33062	J132630.19−472427.89	6.96(05)	6.88(06)	6.74(05)	6.27(04)	4.98(05)	M-Type
35094	J132628.81−472523.60	8.43(05)	8.56(07)	8.48(05)	8.50(05)	8.43(05)	M-Type
35250	J132737.72−472517.37	7.39(05)	7.45(06)	7.35(05)	7.23(04)	6.61(05)	M-Type
35252	J132738.29−472505.60	14.21(04)	14.07(10)	14.49(08)	14.15(10)	···	M-Type
41071	J132614.42−472805.39	9.82(04)	9.93(06)	9.89(05)	9.81(04)	9.97(08)	Carbon Star
42044	J132605.35−472820.80	7.59(04)	7.74(06)	7.67(04)	7.55(05)	7.33(05)	M-Type
43105	J132627.22−472847.47	9.56(04)	9.54(06)	9.46(04)	9.44(04)	···	Post-AGB
44262	J132646.37−472930.35	7.05(05)	6.85(05)	6.68(04)	6.42(04)	5.85(05)	M-Type
44484	J132726.37−472916.93	8.44(06)	8.63(05)	8.53(05)	8.51(05)	8.44(05)	M-Type
52030	J132601.59−473306.08	7.40(05)	7.48(06)	7.44(05)	7.32(04)	7.33(05)	Carbon Star
53019	J132544.03−473324.79	13.03(05)	13.07(06)	13.03(04)	12.77(10)	···	Carbon Star

NOTE.—Magnitude uncertainties are quoted in parentheses. For example, a magnitude of 11.75 ± 0.06 is listed as 11.75(06).

[a] To save space, the Source ID is truncated to show only the source coordinates. The full electronic catalog (available through CDS) includes the *Spitzer* prefix (SSTOCEN).

[b] Fehrenbach's Star (Fehrenbach & Duflot 1962).

van Loon et al. (2007) obtained optical spectra for five of the extremely red faint cluster members ([24] > 10 and [8] – [24] > 0.8); these stars range from [Fe/H] = −1.5 to [Fe/H] = −2, and two of the stars are abnormally hot ($T \approx 7000$ K). The remaining three stars appear to be normal RGB stars. Visual inspection suggests that none of these five sources are affected by blending at 24 μm, however, it is possible that HB stars or RGB stars that have little or no emission at 24 μm are spatially coincident with background galaxies, causing them to appear to have red colors. This may also be the case for the other ≈10 faint, extremely red stars that are matched to cluster members.

Spitzer studies of GCs that do not have proper motion or radial velocity unambiguous confirmation of membership will suffer from contamination from red field stars mistaken for dusty cluster stars. Many of the bright 24 μm sources in our images are field stars, including a variable M-type star with a period of 509 days (LEID 34041). Proper motion measurements allowed us to identify almost all bright and red cluster members in Figure 3.9 against field stars, with only one bright star remaining for which no proper motion information is available. This bright source is most likely LEID 55017, which is a confirmed cluster non-member. The proper motion of LEID 55017 is large enough that the *Spitzer* coordinates are ≈4″ different from the van Leeuwen et al. (2000) coordinates.

It is expected that metal-rich stars form more dust in their winds than their low metallicity counterparts due to the higher abundance of condensable material. We have metallicity information from van Loon et al. (2007) for 32 of the ≈140 dusty stars in Figure 3.9. The brightest potentially dusty stars in the cluster range −2.25 < [Fe/H] < −1.25, i.e. nearly the entire breadth of metallicities encountered in ω Cen. In fact, of this small sample, the reddest stars have [Fe/H] ≤ −1.5 (Fig. 3.10) and two of the three brightest dusty stars (LEID 33062, 44262, 35250) have [Fe/H] ≤ -2.0, which suggests that dust production is not inhibited at these low metallicities.

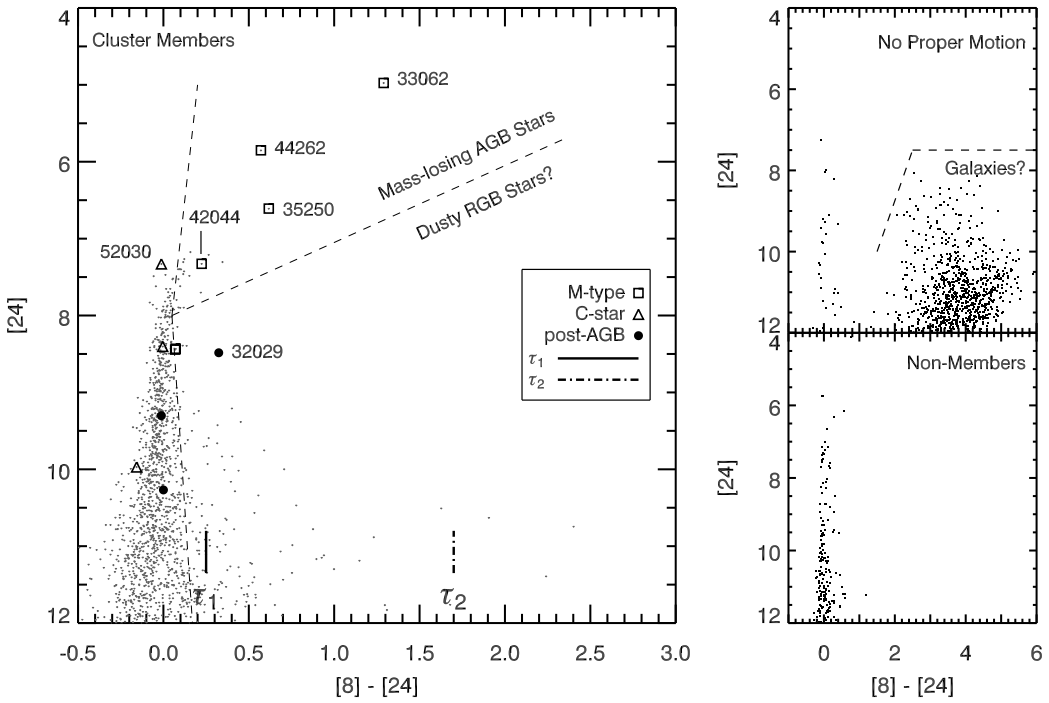

Figure 3.9: [8] – [24] CMDs for ω Cen. Cluster members are plotted in the left panel, non-members are plotted in the lower right panel, and sources lacking proper motion measurements are plotted in the upper right panel. Sources that are potentially blended at 24 μm (see § 3.3.2) are not plotted. Regions including AGB mass-losing stars and dusty RGB stars are separated by dashed lines in the left panel. The colors corresponding to two sample optical depths (τ_1 and τ_2) are also marked on the left. See Table 3.5 for the values of τ for different dust compositions. M-type stars, carbon stars, and post-AGB stars identified by their optical spectra (van Loon et al. 2007) are also labeled, and the most extreme examples are also labeled with their LEID numbers. Almost all bright and red cluster members in this CMD have been identified against field stars, with only one bright star remaining for which no proper motion information is available. This source may be LEID 55017, which has a large proper motion and is not a cluster member. The bright luminosities and red colors of the three brightest M-type stars suggest that these three stars dominate the cluster mass-loss rate. All stars to the right of the vertical dashed line are included in the cumulative mass-loss rate (Fig. 3.11).

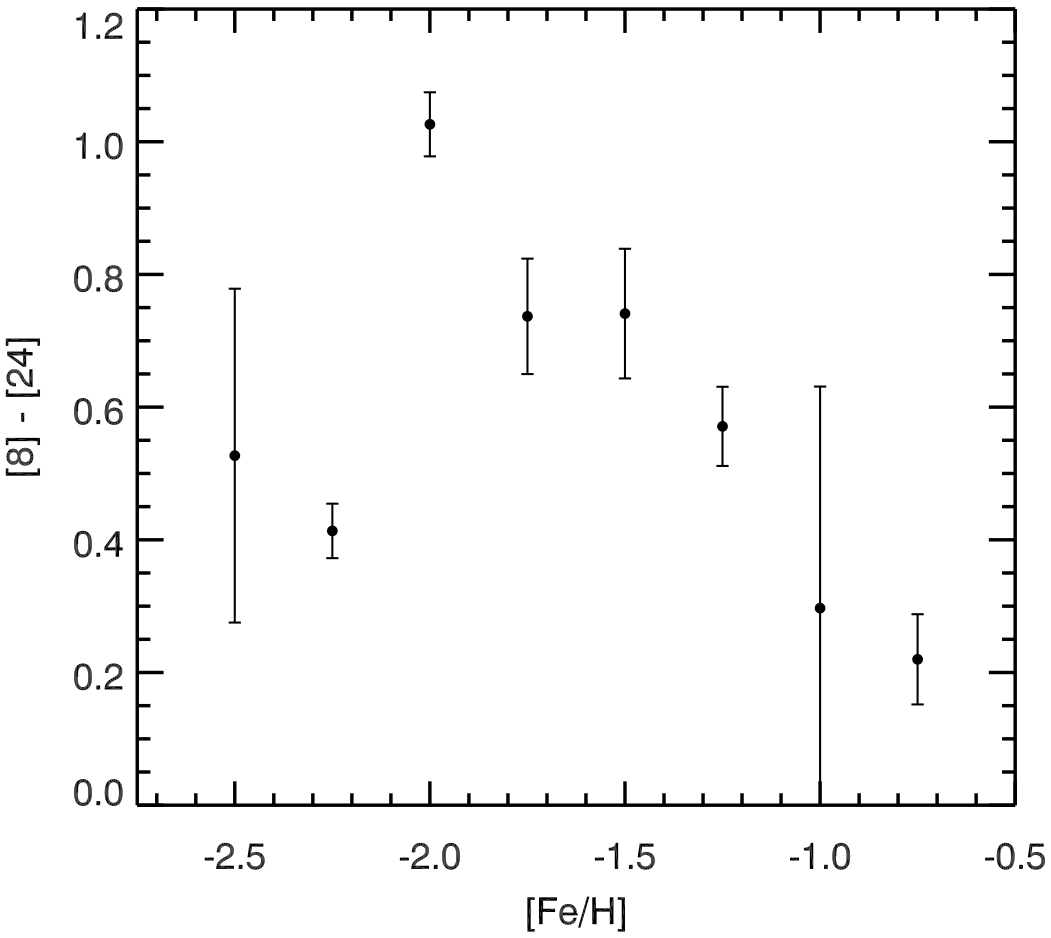

Figure 3.10: Metallicity versus average [8] – [24] color. The color is a weighted average of all stars with a particular metallicity. Metallicities are determined by optical spectroscopy (van Loon et al. 2007). Dust production does not appear to be inhibited at low metallicity.

3.4.3 Mass-Loss Rates

Since mass-loss rates ($\dot{M}$) scale directly with dust optical depth (τ), all dusty stars have the potential to drive a wind (Ivezić & Elitzur 1995). However, the value for $\dot{M}$ derived from the optical depth also scales with the square root of the luminosity, so the brightest stars contribute a larger fraction of the cluster's cumulative mass-loss rate than the fainter stars. Of the ≈140 red cluster members that remain after eliminating blends and non-members such as LEID 34041, which, as a bright M-type star with a period of 509 days, would dominate the cumulative mass-loss rate of the cluster if included. We used the AGB models computed by Groenewegen (2006) to determine the mass-loss rates corresponding to the color of the red member stars with $0.15 \gtrsim$ [8] – [24] $\gtrsim 3.1$. Luminosities were determined by scaling to the Groenewegen (2006) mass-loss tracks for AGB stars with temperatures of 3297 and 3850 K and with silicate and AlO_x dust compositions, however differing bolometric corrections for stars with different temperatures and metallicities are not taken into account. For reference, the colors corresponding to two sample optical depths are marked on the CMD in Figure 3.9 and listed in Table 3.5. The final mass-loss rates ($\dot{M}_{\rm Final}$) were scaled according to the following relationship:

$$\left(\frac{\dot{M}_{\rm Final}}{\dot{M}_{\rm G}}\right) = \left(\frac{v}{10\ {\rm km\ s^{-1}}}\right)\left(\frac{0.005}{\psi}\right)\left(\frac{L}{3000\ L_{\odot}}\right)^{\frac{1}{2}}, \tag{3.1}$$

where $\dot{M}_{\rm G}$ is the unscaled mass-loss rate from Groenewegen (2006), v is the wind velocity, ψ is the dust-to-gas mass ratio ($\psi \approx 0.005$ at solar metallicity), and L is the luminosity. Following van Loon (2000) and Marshall et al. (2004), the velocity scales approximately as:

$$\left(\frac{v}{10\ {\rm km\ s^{-1}}}\right) = \left(\frac{\psi}{0.005}\right)^{\frac{1}{2}}\left(\frac{L}{10,000\ L_{\odot}}\right)^{\frac{1}{4}}. \tag{3.2}$$

From equation (3.2), the wind velocities of even the strongest mass-losing stars in ω Cen

are slow ($v < 2$ km s^{-1}). Winds this slow may have difficulty driving a massive wind; it is possible that the wind is driven by some other mechanism and that the dust is a by-product. McDonald & van Loon (2007) suggest wind velocities of 5 – 10 km s^{-1} for AGB stars in GCs; if wind velocities are 5× higher, the mass-loss rates would increase by the same factor.

The Groenewegen (2006) models were calculated assuming spherical circumstellar dust shells, a constant mass-loss rate, and photospheres with solar metallicity. The last of these assumptions affects the stellar colors, which we used to determine the mass-loss rates. While we do take metallicity into account in the dust-to-gas ratio, increasing the mass-loss rates by a factor of seven, the metallicity dependence is not yet well established. The mass-loss rates computed using the Groenewegen (2006) models should therefore be considered a rough estimate. Bolometric luminosities of the ω Cen sources can be estimated through fitting the SED or spectrum of each star, facilitating a better estimate of the real mass-loss rates (McDonald et al. 2008).

Assuming that all stars have the metallicity that comprises the majority of the population and that ψ scales with metallicity (van Loon 2000, 2006, [Fe/H] = –1.7, $\psi \sim 10^{-4}$), we find that the three brightest M-type stars (Fig. 3.9) contribute a total of $\dot{M}$ (gas + dust) = 1.8 – 2.8 × 10^{-7} $M_{\odot}$ yr^{-1}, depending on the temperature and dust composition. The combined mass-loss rate of these three stars is an order of magnitude less than the mass-loss rate measured for V1 in 47 Tuc with IR spectroscopy (van Loon et al. 2006a), suggesting either that we have underestimated the mass-loss rates or that the variance of $\dot{M}$ with metallicity is not a linear relation. Figure 3.11 and Table 3.6 shows that the cumulative mass-loss rate ($\Sigma\,\dot{M}$) of the ≈140 dusty stars together is less than twice the combined mass-loss rate of the three brightest M-type stars (LEID 33062, 44262, 35250). However, the fainter stars may be contributing more to the total mass-loss rate of the cluster if their dust-to-gas ratios are smaller.

Table 3.5. Sample Optical Depths Corresponding to [8] – [24] = 0.25 and 1.7

		Silicate Dust		AlO_x Dust	
Optical Depth	[8] – [24]	$T = 3297$ K	$T = 3850$ K	$T = 3297$ K	$T = 3850$ K
τ_1	0.25	0.013	0.001	0.030	0.021
τ_2	1.70	0.120	0.056	0.220	0.090

Note. — τ_1 and τ_2 are examples of optical depth from Groenewegen (2006) that correspond to [8] – [24] colors of 0.25 and 1.7. These colors are marked in Figure 3.9.

Table 3.6. Mass-Loss Rates of the Three Brightest M-type Stars

		$\dot{M}$ ($M_\odot$ yr^{-1})			
		Silicate Dust		AlO_x Dust	
LEID	Source ID[a]	$T = 3297$ K	$T = 3850$ K	$T = 3297$ K	$T = 3850$ K
33062	J132630.19−472427.89	1.7×10^{-7}	1.3×10^{-7}	2.1×10^{-7}	1.5×10^{-7}
44262	J132646.37−472930.35	3.4×10^{-8}	2.8×10^{-8}	4.4×10^{-8}	3.5×10^{-8}
35250	J132737.72−472517.37	2.3×10^{-8}	1.8×10^{-8}	2.8×10^{-8}	2.2×10^{-8}
Total $\dot{M}$ for all dusty members		3.4×10^{-7}	2.9×10^{-7}	4.2×10^{-7}	3.4×10^{-7}

[a]To save space, source IDs are listed here without the SSTOCEN preffix.

To compare $\Sigma \dot{M}$ to the number of dusty stars present at each magnitude, we also plot the percentage of stars that are dusty (f_D) in Figure 3.11, binned by half magnitudes. f_D remains roughly constant at 10% – 20% for [24] > 9.5, causing the cumulative mass-loss rate to slowly increase at [24] > 8. The increase in $\Sigma \dot{M}$ at [24] $\approx$ 11 is due to the very red sources ([8] – [24] > 1.0) at these magnitudes. It is possible that many of the faint stars with red excess are not truly dusty (see §3.4.2). Since the cumulative mass-loss rate does not increase much over more than 2 magnitudes on the upper-RGB, it is unlikely that even fainter stars, which are generally warmer and do not pulsate strongly, contribute significantly to the dust-traced mass loss.

In a *Spitzer* study of 47 Tuc, Origlia et al. (2007) find that red stars occupy the CMD from the TRGB down to the HB and conclude that mass-loss is occurring at a significant rate along the entire RGB. However, at least 25% of the red sources in ω Cen have proven to have red colors because of blending effects at 24 μm (see § 3.3.2). Figure 3.11 shows that these blended sources can increase the cumulative mass-loss rate by up to 17%. In more crowded clusters like 47 Tuc, blending will affect an even larger percentage of red stars. Indeed, it is evident in Figure 2 of Origlia et al. (2007) that the CMD covering the central region of the cluster is affected by blending, since the many red sources claimed to exist between $-2 < M_{\rm bolometric} < 0$ have no equivalent in the CMD for the outer regions of the cluster. By eliminating these blends, we find that significant dusty mass loss occurs only at or near the TRGB.

Two previous mid-IR studies of GCs detected several very red, faint sources (Boyer et al. 2006; Ita et al. 2007). Both studies offer the possibility that these sources are dusty, mass-losing stars. While the nature of the sources has yet to be established, we find that, after weeding out pesky field stars and background galaxies via proper motion information, very few of the confirmed ω Cen cluster members reside in this region of the CMD (Fig. 3.9), and significant dusty mass loss occurs only near the very tip of the RGB or AGB. In the case of NGC 362 (Ita et al. 2007), these faint, red sources may

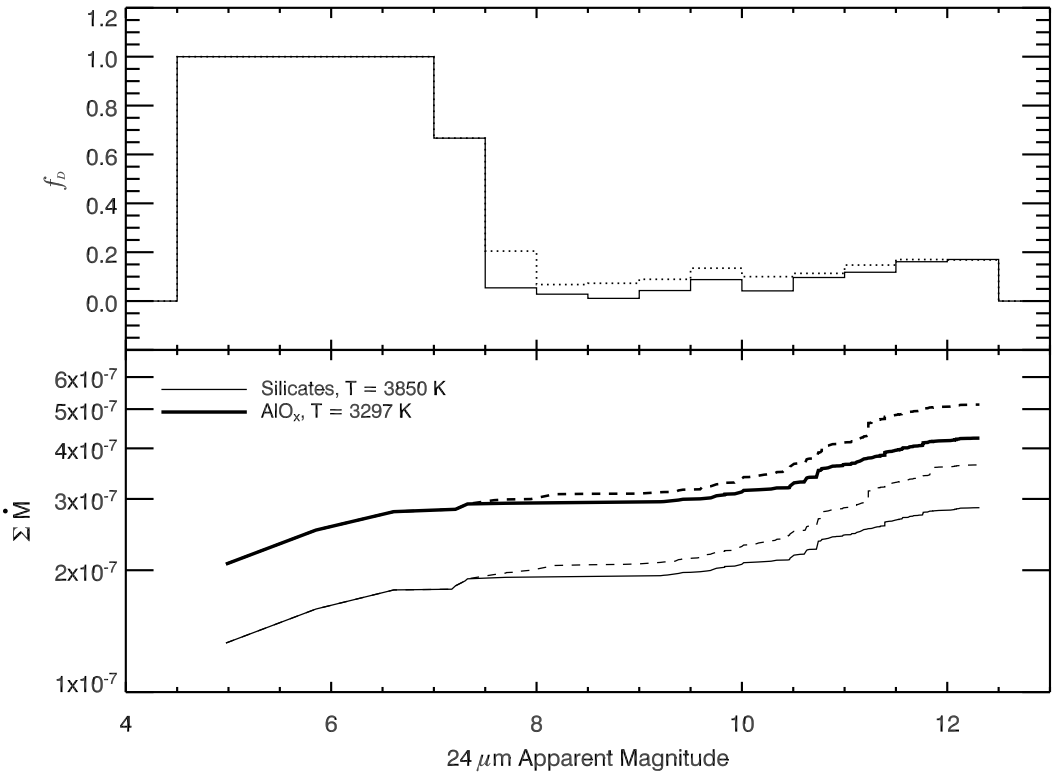

Figure 3.11: Cumulative mass-loss rate ($\Sigma\ \dot{M}$) for ω Cen. The upper panel shows the ratio of dusty to non-dusty stars (f_D). The dotted line includes all observed members, while the solid line excludes potential source blends. The bin size is 0.5 magnitudes, but the large bin between $4.5 < [24] < 7$ includes only the 3 brightest M-type stars, all of which are dusty. In the lower panel, individual mass-loss rates are derived from Groenewegen (2006) models scaled to reflect the luminosity and metallicity dependence of the dust-to-gas ratio, and consequently, the wind speed. Sources to the right of the vertical dashed line in Figure 3.9 are included in the summation and plotted with a solid line. The mass-loss rates are computed for four dust composition/temperature combinations, the most extreme of which are plotted; colder silicate and warmer AlO_x grains fall intermediate to the plotted lines. The dashed line shows the cumulative mass-loss rate obtained if potential blends are included, which can increase the total mass-loss rate by 12% – 17% even in the relatively sparse environment of ω Cen compared to other GCs. The sharp increases in $\Sigma\ \dot{M}$ beyond $[24] \approx 10.5$ are due to a few extremely red sources ($[8] - [24] > 2$). The total mass-loss rate for the cluster is $2.9 - 4.2 \times 10^{-7}$ $M_\odot$ yr^{-1}, 63% – 66% of which comes solely from the three brightest M-type stars, depending on the dust temperature and composition.

be background AGB stars belonging to the Small Magellanic Cloud, however in other GCs, these sources are more likely to be background galaxies.

If the current population in ω Cen is representative of the cluster's population at all times, then the cluster has lost at least 1 – 2 $M_{\odot}$ of material (1 – 2 $\times$ 10^{-4} $M_{\odot}$ of dust) through stellar mass loss since its last Galactic plane crossing, which occurred more than 3.4 $\times$ 10^{6} years ago (Tayler & Wood 1975). van Loon et al. (2007) find a few post-AGB stars in ω Cen. Assuming a post-AGB lifetime of several 10^{4} yr and 0.1 $M_{\odot}$ of mass shed on the AGB, this could have produced up to 100 $M_{\odot}$ of lost mass. This comparison suggests that either these AGB stars lose on average less than 0.1 $M_{\odot}$ on the AGB, or that our mass-loss rate estimates are too low (for instance because the wind velocity is actually higher and/or the dust-to-gas ratio is lower than assumed here).

3.4.4 Background Galaxies

Background galaxies (green points in Fig. 3.5) dominate the faint, red plume in the [3.6] – [8] CMD due to strong PAH emission at 8 μm (Blum et al. 2006; Bolatto et al. 2007). The coverage overlap between the 3.6 μm and 8 μm mosaics is $\approx$0.3 deg^2, yielding a density of 2823 galaxies/deg^2. This number increases to 3174 galaxies/deg^2 if we consider undetected galaxies behind the cluster center (an area of $\approx$11 arcmin^2, see Fig. 3.7). The red and faint region of the [3.6] – [24] CMD is also heavily populated with sources. If these 24 μm sources are all background galaxies, the galaxy density derived from this CMD is 2681 galaxies/deg^2. This density increases to 3015 galaxies/deg^2 when considering sources located behind the cluster core. When including all sources with very red colors and faint magnitudes at all wavelengths, we find a total background galaxy density of $\approx$1 $\times$ 10^{4} galaxies/deg^2 (Fig. 3.7).

To determine the expected background galaxy density, we queried the SWIRE extragalactic database (Lonsdale et al. 2004) for sources located in the same region of

the CMD as our galaxy candidates. In the six SWIRE fields, there are ≈900 – 2200 sources/deg^2 in the [3.6] – [8] CMD and 900 – 1900 sources/deg^2 in the [3.6] – [24] CMD. Our images are slightly more sensitive than the SWIRE data, but when comparing identical regions of the CMD, the galaxy densities in our CMDs fall within the range of the SWIRE galaxy densities, strengthening the argument that the sources we have identified as galaxy candidates are indeed background galaxies. It is also possible that the faintest sources in the red [3.6] – [8] and [3.6] – [24] plumes are either stellar blends or regular RGB stars whose fluxes are poorly determined due to their proximity to the completion limit, causing them to have a non-zero color.

3.4.5 70 μm Sources

Nine point-sources appear in the 70 μm mosaic, although none are the red, possibly dusty cluster members discussed in § 3.4.2 and § 3.4.3. One of these sources is resolved at the shorter wavelengths and appears to be a background spiral galaxy (2MASX J13272621–4746042; Fig. 3.12). This galaxy shows a ring of PAH emission at 8 μm that is reminiscent of the famous star-forming "Ring of Fire", seen in M31 (Barmby et al. 2006; Gordon et al. 2006). Two of 70 μm sources are near confirmed cluster members (van Leeuwen et al. 2000; van Loon et al. 2007); source 1 is 3.7″ from LEID 27094, a distance that is within the half-width, half-maximum of the 70 μm PSF, and source 4 is 1.0″ from LEID 46055. Optical spectra for both LEID stars are reported by van Loon et al. (2007) and reveal that both stars have [Fe/H] $\simeq$ –1.25 and $T_{\rm eff} \simeq$ 5000 K. LEID 27094 is CH strong and appears to be a normal RGB star, while LEID 46055 is CH and CN strong, and is Ba-rich, suggesting that it may be enriched in carbon from third dredge-up. Despite the proximity in position between these two LEID sources and sources 1 and 4, the LEID sources may be associated with warmer stars that appear in the IRAC mosaics as secondary stars blended with sources 1 and 4, and not with the corresponding 70 μm source. The remaining six 70 μm sources are not near any known

cluster members.

We measured 70 μm fluxes for the eight point-sources with the aperture feature of *Imexamine* in version 2.12.2 of IRAF[3]. Aperture radii were initially set to 3× the FWHM of each source and three iterations were performed to find the optimal radius. The median of the background was subtracted from the flux and the appropriate MIPS aperture correction was applied. Fluxes are listed in Table 3.7 and the 3.6 to 70 μm SEDs are shown in Figure 3.13. Aside from sources 1 and 4, all of the sources appear to be unaffected by blends at all IRAC wavelengths.

For each 70 μm source, we performed a reduced-χ^2 fit of a two-component blackbody curve that include 2MASS JHK fluxes to better define the warmer blackbody. Source 8 falls off of our IRAC images, so its IRAC fluxes were determined by using an earlier epoch of data from the Gehrz Guaranteed Time Observing Program (GGTOP) with *Spitzer* (PID 132) with data reduction identical to that described in § 3.2. The fits take the photometric errors into account. Sources 3, 5, 7, and 8 are underconstrained for this fitting technique when we exclude the anomalously bright 5.8 and 8 μm points from the fit; for these sources, we decreased the number of fitting parameters by fixing the temperatures to 1000 to 14,000 K and 40 to 90 K for the blue and red blackbodies, respectively, and choosing the temperatures that gave the best reduced-χ^2. The IRAC and MIPS color corrections were applied by iterating the fit until the corrections remained constant within 1%. While a dual-blackbody fits well with most of the 70 μm sources, we point out that the dust around these sources may be emitting over a range of temperatures.

Better fits were obtained by excluding the 8 μm point, which is above the blue blackbody for all eight sources. To a lesser degree, the 5.8 μm point is also systematically brighter than the blue blackbody component, suggesting that there is a range of dust

[3]IRAF is distributed by the National Optical Astronomy Observatories, which are operated by the Association of Universities for Research in Astronomy, Inc., under cooperative agreement with the National Science Foundation.

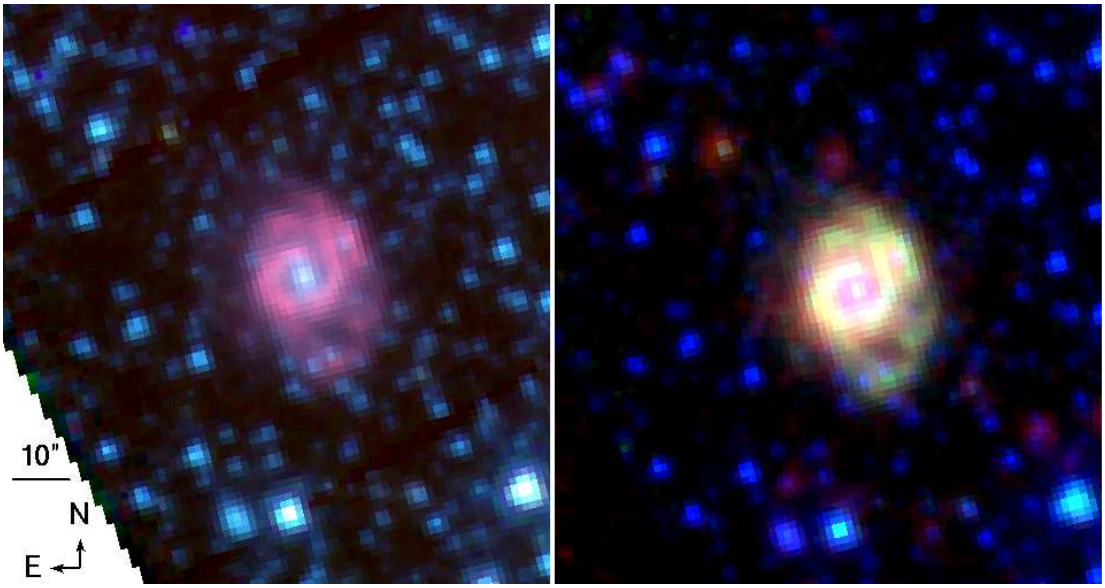

Figure 3.12: Three-color images of a resolved spiral galaxy (2MASX J13272621–4746042). *Left:* Blue is 3.6 μm, green is 4.5 μm, and red is 8 μm. *Right:* Blue is 3.6 μm, green is 8 μm, and red is 24 μm. 8 μm PAH emission appears red in the left panel and green in the right panel. Dust appears red in the right panel. The SED of this galaxy (Fig. 3.14) resembles the SEDs of the other 70 μm sources (Fig. 3.13).

temperatures causing warm dust to radiate above the blackbody at 5.8 μm and perhaps also at 8 μm. However, the 5.8 μm points are still included in the fit for source 3 in order to keep the fit properly constrained. The resulting blackbodies are overplotted in Figure 3.13 and fitting results are shown in Table 3.8.

The emission features at 5.8 and 8 μm, where PAH emission dominates, and the relatively flat SEDs of the non-blended sources suggests that all or most of these sources are background galaxies (for examples of *Spitzer* galaxy SEDs, see Dale et al. 2005). For comparison, an SED of the resolved spiral galaxy is shown in Figure 3.14. We determined the flux by placing square apertures of roughly $45'' \times 50''$ on the galaxy and subtracting the median background. As with source 8, the galaxy falls off of our IRAC coverage, so data from PID 132 is used to determine its IRAC fluxes. This SED is similar to the other eight, except that it lacks the slight excess emission at 5.8 μm that many of the other sources exhibit.

The cold dust component of the blackbody fits for the eight unidentified sources ranges in temperature from $\approx$50 K to 68 K – a temperature commensurate with these objects being post-thermal pulse stars, stars suffering from episodic mass loss on the RGB, or post-AGB stars. However, the temperatures of all eight sources are also consistent with dust in star forming regions that dominate the galactic far-IR emission. At a temperature of 48.8 ± 0.8 K, the cold blackbody component of the resolved galaxy is colder than the other eight 70 μm sources, which may suggest that the warmer sources are of a different nature. However, with so few constraints in the blackbody fits, one might argue that the temperatures of all nine sources are consistent with each other.

Table 3.7: Fluxes of 70 μm Sources

Source #	Source ID	Flux (mJy) 3.6 μm	4.5 μm	5.8 μm	8 μm	24 μm	70 μm
1	SSTOCEN J132723.86−472130.00	15.94(0.32)	10.23(0.20)	6.66(0.13)	5.59(0.11)	2.42(0.05)	75.79(17.31)
2	SSTOCEN J132521.01−472623.43	1.96(0.04)	1.49(0.03)	1.96(0.04)	12.33(0.25)	14.33(0.29)	226.70(8.18)
3	SSTOCEN J132523.57−472813.61	···	0.17(0.00)	0.16(0.00)	0.79(0.02)	2.82(0.06)	246.73(18.94)
4	SSTOCEN J132615.23−473024.56	46.46(0.93)	30.02(0.60)	19.52(0.39)	11.56(0.23)	10.74(0.47)	158.02(7.96)
5	SSTOCEN J132426.26−473905.88	···	···	···	···	0.74(0.05)	82.01(9.44)
6	SSTOCEN J132714.06−474112.83	0.93(0.02)	0.63(0.01)	0.60(0.01)	2.60(0.05)	3.54(0.07)	53.04(11.19)
7	SSTOCEN J132655.87−474445.02	0.12(0.01)	0.11(0.01)	0.12(0.01)	0.69(0.01)	3.81(0.08)	131.46(23.81)
8	SSTOCEN J132712.89−474739.59	0.07(0.01)	0.05(0.01)	0.05(0.01)	0.06(0.01)	0.75(0.02)	107.50(23.54)
9[a]	2MASX J13272621−4746042	2.92(0.07)	3.38(0.09)	3.06(0.08)	9.27(0.21)	5.20(0.21)	617.08(73.84)

NOTE.—Fluxes for 3.6 – 24 μm were determined by PRF fitting with DAOphot and 70 μm fluxes were determined by aperture photometry with IRAF. Flux uncertainties are quoted in parentheses. For example, a flux of 15.94 ± 0.32 mJy is listed as 15.94(0.32).

[a] Source 9 is a resolved spiral galaxy (see Fig. 3.12), while sources 1 through 8 are point sources.

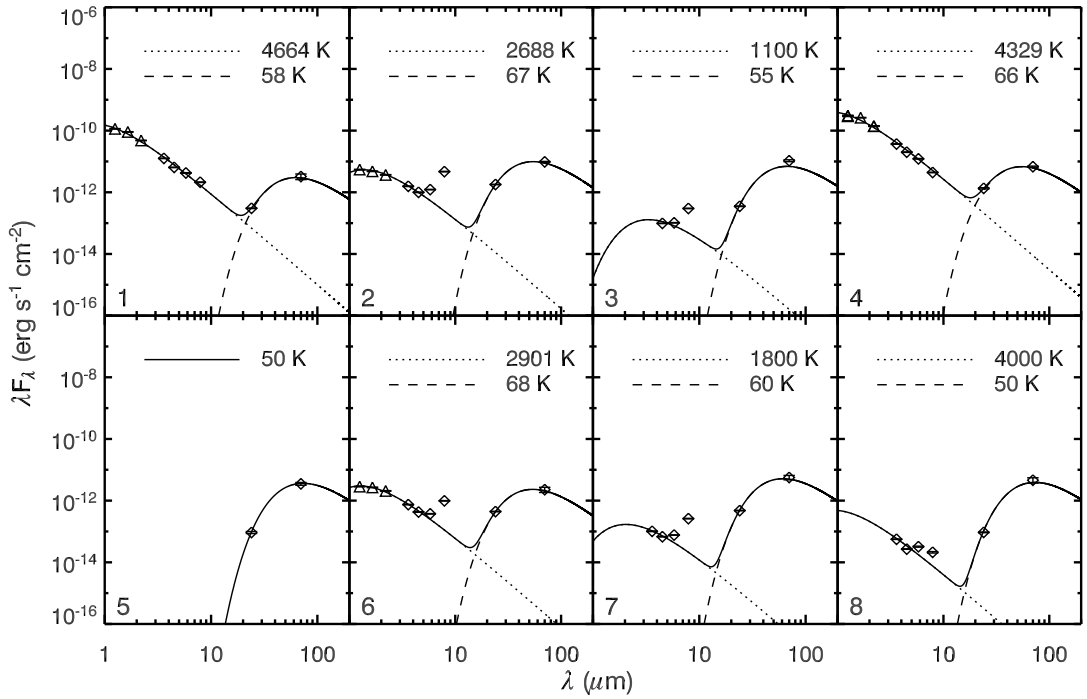

Figure 3.13: SEDs of 70 μm sources. Fluxes are corrected for reddening ($E(B-V) = 0.11$; Lub 2002). Sources 1 and 4 are spatially coincident with known cluster members and are potentially affected by blending between the known source and a fainter source that is the real counterpart of the 70 μm emission. The 5.8 and/or 8 μm emission in sources 2, 3, 6, 7, and 8 lies significantly above the blackbody and is excluded from the fit. Fitting results are summarized in Table 3.8. While the cold blackbody temperatures are consistent with a detached dust envelope such as those seen around post-AGB stars, they are also typical of the dust in star forming regions that dominate the galactic far-IR emission. The strong excess at 8 μm and the slight excess at 5.8 μm could be due to either silicate emission or PAH emission.

Table 3.8. Fitting Results for 70 μm Sources

Source #	Source ID	χ^2/dof	T_1 (K)	T_2 (K)
1	SSTOCEN J132723.86−472130.00	35.8	4664 ± 19	58.5 ± 1.7
2	SSTOCEN J132521.01−472623.43	3.3	2688 ± 25	67.5 ± 0.5
3	SSTOCEN J132523.57−472813.61	199.7	1100 ± 200[a]	55.0 ± 10[a]
4	SSTOCEN J132615.23−473024.56	40.1	4329 ± 16	66.5 ± 0.8
5	SSTOCEN J132426.26−473905.88	75.0	···	50.0 ± 10[a]
6	SSTOCEN J132714.06−474112.83	15.4	2901 ± 28	68.0 ± 2.0
7	SSTOCEN J132655.87−474445.02	52.2	1800 ± 200[a]	60.0 ± 10[a]
8	SSTOCEN J132712.89−474739.59	15.7	4000 ± 200[a]	50.0 ± 10[a]
9[b]	2MASX J13272621−4746042	2.5	1084 ± 29	48.8 ± 0.8

[a] The marked uncertainties represent twice the temperature increment in the range of fixed temperatures used for the underconstrained fits.

[b] Source 9 is a resolved spiral galaxy (see Fig. 3.12), while sources 1 through 8 are point sources.

If the 70 μm sources are dusty AGB stars, the flux at 8 μm may be included in the wing of a broad emission feature centered at 9.5 μm due to amorphous silicate grains that overlaps with the IRAC 8 μm bandpass. The 9.5 μm feature is also detected in the 8 – 13 μm spectrum of a particularly red, large-amplitude variable star in 47 Tuc (van Loon et al. 2006a; Lebzelter et al. 2006). The positions of the 70 μm sources on the [8] – [24] CMD are marked in Figure 3.8b. All sources lie redward of the RGB and near the brighter end of the CMD. However, the 3.6 and 4.5 μm magnitudes of sources 2, 3, 6, 7, and 8 (triangles) are fainter than 12.5 magnitudes, suggesting that these sources are indeed galaxies. Sources 1 and 4 lie on the brighter end of the RGB, but they are blended with the aforementioned LEID sources at the shorter wavelengths, which will cause an artificial increase in brightness. While near-IR redshift measurements or radial velocity measurements would conclusively determine the nature of these sources, analysis of the *Spitzer* data strongly suggests that they are all background galaxies.

3.4.6 The Intracluster Medium

Despite ongoing stellar mass loss in ω Cen, there are no known detections of any phase of ICM material in the cluster. The wind velocities discussed in § 3.4.3 are $\ll$ 10 km s^{-1} for metal-poor, dust-driven winds from low-mass AGB stars. Such velocities are much less than the escape velocity of ω Cen at 1 r_{hm} (v_{esc} = 44 km s^{-1}; Gnedin et al. 2002), but if the dust and gas are not well coupled, then the dust velocity may be higher. RGB and AGB wind velocities measured from Hα emission wings can be as high as the cluster escape velocity, however it is likely that Hα wings are due to pulsation and/or chromospheric activity instead of the circumstellar shells of stars. Core velocities originate in the chromospheres and are typically lower ($<$ 15 km s^{-1}), but there have been at least two observations of high velocities from the IR He I line (Dupree et al. 1992; Smith et al. 2004).

If the winds are indeed slow and the total mass-loss rate discussed in § 3.4.3 has

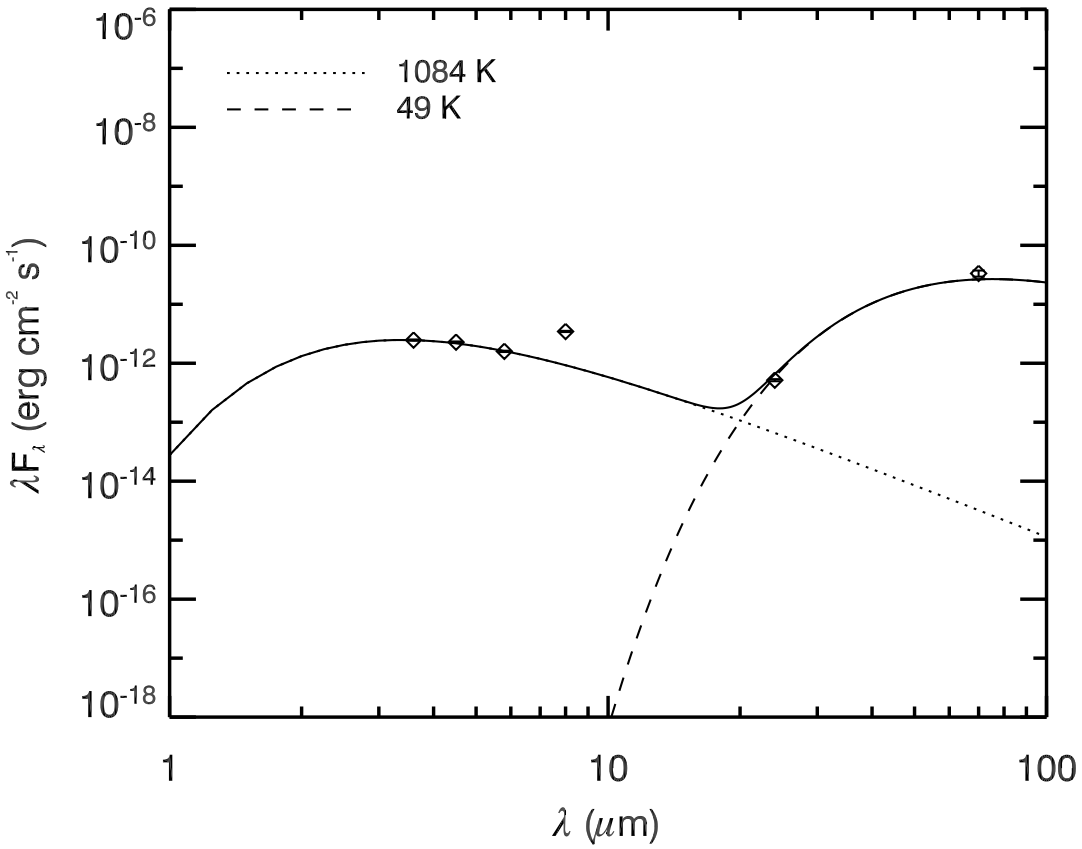

Figure 3.14: SED of galaxy 2MASX J13272621–4746042. The 8 μm excess is suggestive of PAH emission. Blackbody fitting results are summarized in Table 3.8. This SED resembles the SEDs of the other eight 70 μm sources, suggesting that they are also galaxies.

been constant since the last Galactic plane crossing, then, barring any ICM removal mechanisms and assuming that all stars belong to the population with the lowest metallicity, 1 – 2 $M_{\odot}$ of material should have accumulated in the cluster. This mass estimate includes only dusty mass loss on the RGB and AGB; mass loss from non-dusty stars on the RGB and from stars that lose significant mass in such a brief period of time that it may easily have been missed (e.g., associated with the formation of a planetary nebula) may cause this estimate to increase by a factor of two or three. Based on the total amount of AGB mass loss, which is the only source of dust, we expect a dust mass of $M_{\rm d} = \psi\, M_{\rm gas} \sim 1 - 2 \times 10^{-4}\ M_{\odot}$ of dust. Since the estimate of the time since the last Galactic plane crossing is a lower limit ($> 3.4 \times 10^{6}$ yr; Tayler & Wood 1975), the predicted ICM dust mass may be higher.

The average 1 σ sensitivity of our 24 μm mosaic is $\approx$2.5 $\times$ 10^{-2} MJy/str. Following Evans et al. (2003), the relationship between the dust mass and the expected IR flux density is:

$$\frac{M_d}{M_{\odot}} = 4.79 \times 10^{-17}\ f_{\nu}(\mathrm{mJy})\ \frac{D^2_{\rm kpc}}{\kappa_{\nu} B(\nu, T_d)}, \tag{3.3}$$

where $D_{\rm kpc}$ is the distance to ω Cen, κ_{ν} is the dust absorption coefficient (cm^2 g^{-1}), T_d is the dust temperature (K), and $B(\nu, T_d)$ is the Planck function in cgs units. Assuming a standard Mathis-Rumpl-Nordsieck dust distribution (Mathis et al. 1977) and an ISM-type dust composition of graphite and silicate grains, κ_{ν} is taken to be 56 $\pm$ 11 cm^2 g^{-1} (Ossenkopf & Henning 1994), although this value could be up to a decade larger. A cloud with 1 – 2 $\times$ 10^{-4} $M_{\odot}$ of dust and an equilibrium temperature of 70 K would yield a 24 μm flux density of 23 – 45 mJy. With our sensitivity, we are capable of detecting 23 mJy to the 3 σ level in our 24 μm mosaic if all of the dust is uniformly distributed within an area of 2$'$ $\times$ 2$'$, or a radius of $\approx$ 1/4 $r_{\rm hm}$. A small, centrally located cloud at the 3 σ level would be detectable over the background stellar emission in the 24 and 70 μm mosaics, but, unlike in M15 (Boyer et al. 2006), our MIPS images

do not show a large dust cloud located at the center of ω Cen.

While there is no central ICM dust cloud in ω Cen, there is faint, diffuse emission covering nearly the entire 24 μm image to the south of the cluster center, including several small regions of concentrated extended emission on the outskirts of the cluster that appear near the 3 σ limit (Figs. 3.15 and 3.16). Feature A (Fig. 3.17) appears at 8, 24, and 70 μm, features B and C appear at 8 and 24 μm, and feature D appears only at 24 μm, as the coverage is not identical across all bands. The probability that these features are artifacts is quite low as they each appear in more than 95% of the BCD images at various array positions.

It is uncertain whether features A – D are associated with the cluster or are part of the foreground. The morphology of feature A provides the strongest evidence for cluster association, as the warmer 8 μm emission lies closer to the cluster center than the cooler 24 and 70 μm emission (Figs. 3.16 and 3.17). Moreover, the warmer portion is approximately perpendicular to the direction towards the cluster center. This configuration suggests the possibilities that either a warm wind is pushing the ICM out of the cluster or that the 8 μm arc is optically thick and is being irradiated by the cluster's stellar radiation field with cold dust in its shadow. A determination of the dust temperature would aid in ascertaining the origin of feature A. Unfortunately, only very small portions of feature A are present in the *Spitzer* mosaics at all wavebands (Fig. 3.17), and the limited coverage makes it impossible to reliably determine the temperature of the dust from an SED.

The case for an ICM origin for features A – D is strengthened by our discovery of an unreported H I cloud near the velocity of ω Cen (Fig. 3.18) in public data from the H I Parkes All-Sky Survey (HIPASS; Barnes et al. 2001), which may have also been detected by Smith et al. (1990) in earlier observations. The center of this H I feature is not spatially coincident with any of the dust features, but rather lies $\approx 15'$ to the southeast of the cluster center, just on the edge of the coverage of our MIPS mosaic

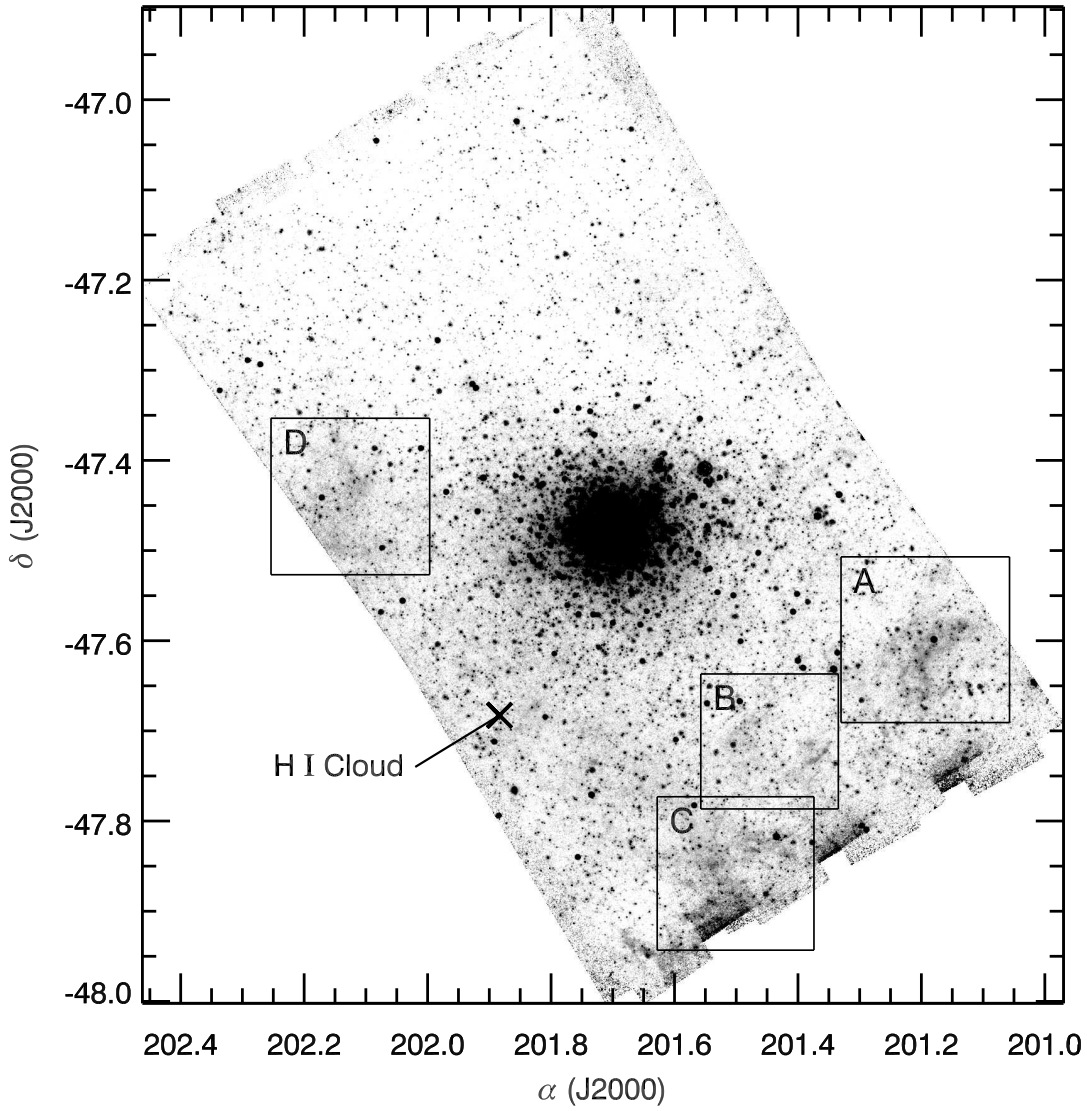

Figure 3.15: 24 μm image showing the locations of four regions of extended emission. The boxed regions are shown in Figure 3.16 overlaid with contours. Region A is shown in more detail in Figure 3.17. An H I feature is marked with an "X" (Fig. 3.18). Low-level diffuse emission is also visible covering most of the image south of the cluster center. All dust clouds are outside of the cluster half-mass radius, suggesting that if they are part of the ICM, they may be in the process of leaving the cluster.

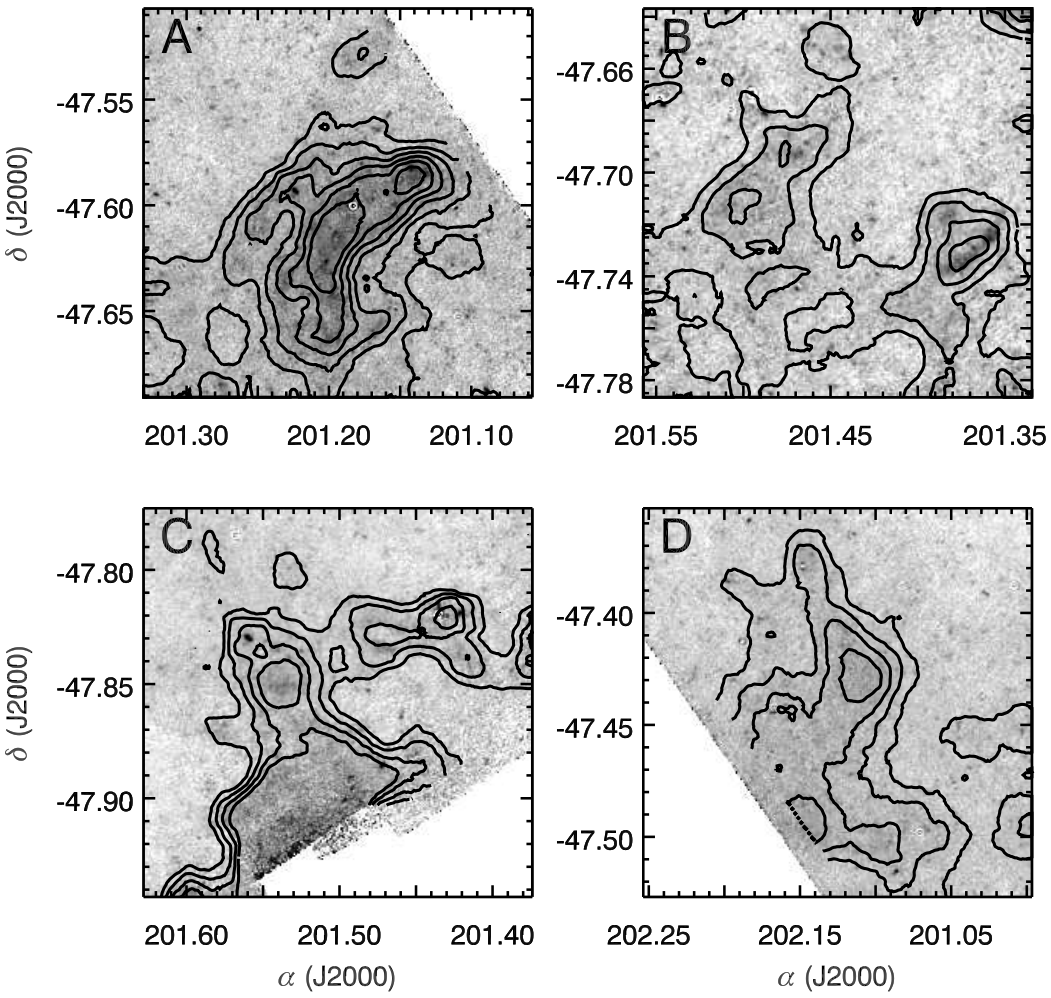

Figure 3.16: Residual 24 μm image showing several regions of extended emission. Contours smoothed with a 25 pixel ($\approx 60''$) window are overlaid to show the morphology of each region. The bright region on the edge of the frame in panel C is a data artifact.

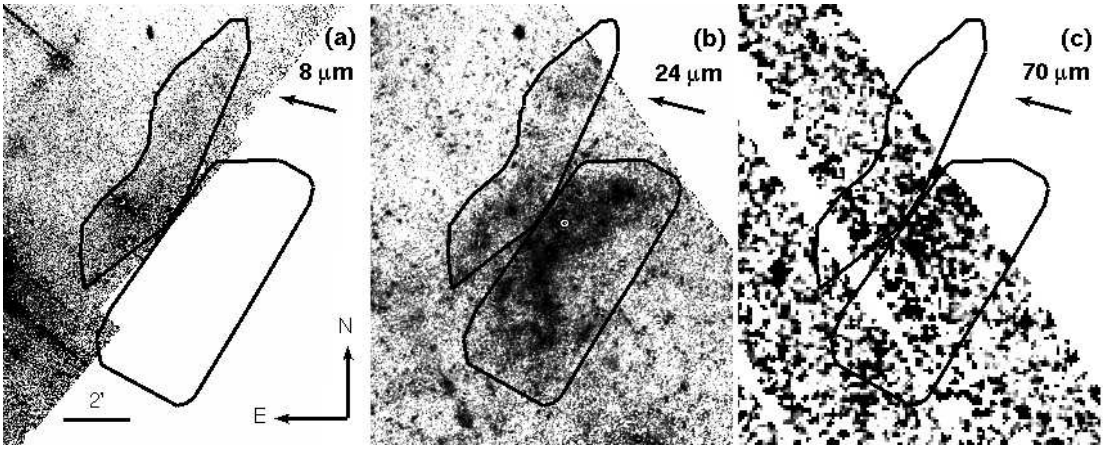

Figure 3.17: (a) Residual 8 μm mosaic. (b) Residual 24 μm mosaic. (c) 70 μm mosaic. Each panel shows a close-up of possible ICM feature A located $\approx 20'$ from the cluster center. The arrows point towards the center of the cluster. The warm 8 μm feature lies closer to the cluster center than the cooler feature at 70 μm. Both features appear at 24 μm. This morphology suggests a possible association with the cluster. Note that the region of bright emission to the lower left of feature A at 8 μm is strongly affected by residual emission from an extremely bright source, and is not likely a real extended feature.

(Fig. 3.15). The velocity of the H I feature ($v_{\rm LSR} \sim 190$ km s^{-1}) suggests a connection to ω Cen ($v_{\rm LSR} \simeq 230$ km s^{-1}). Smith et al. (1990) argue instead that, because the feature is detected on only one side of the cluster, it is more likely to be a small high-velocity cloud that is part of the Magellanic Stream (Bajaja et al. 1985, $v_{\rm LSR} = 200$ km s^{-1}). While an association between the H I feature and the Magellanic Stream is a possibility, similar offset H I clouds have been discovered in larger dSph galaxies (Bouchard et al. 2003, 2006; Young et al. 2007), so finding a cloud that is associated with ω Cen may not come as a surprise. In M15, dust and H I trace each other in the ICM (van Loon et al. 2006b). Therefore, if the H I feature is indeed associated with ω Cen, it is reasonable to assume that dust is also present. Since both the dust and the H I feature are located well outside 1 $r_{\rm hm}$, it is possible that we are seeing the ICM in the process of escaping the cluster.

3.5 Conclusions

Our *Spitzer* multi-wavelength and dual-epoch study of the most massive Galactic globular cluster, ω Cen, and the resulting point-source catalog provide the most complete mid- to far-IR atlas of any GC to date. Despite ω Cen's rather unusual stellar population, the *Spitzer* CMDs show little structure beyond the division between the RGB stars belonging to the cluster and background galaxies. The HB stars and RGB-a stars are not separated from the RGB, except for a slightly blue [3.6] – [4.5] color for the RGB-a.

Nine sources are detected at 70 μm, one of which is a resolved spiral galaxy, and two of which are spatially coincident with optical sources that are known cluster members. If emission at 5.8 and 8 μm in the SEDs of the eight point sources is PAH emission, then these sources are background galaxies.

By cross-referencing with a catalog of optical spectra (van Loon et al. 2007), we

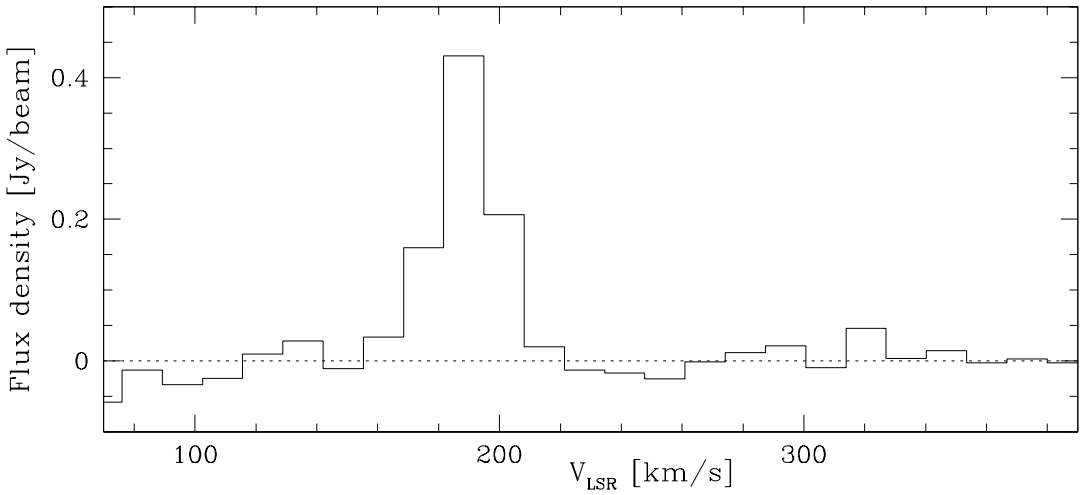

Figure 3.18: H I detection near the velocity of ω Cen ($v_{\rm LSR} \sim 230$ km s^{-1}) in the HIPASS survey. This feature is located $\approx 15'$ southeast of the cluster center (see Fig. 3.15). The presence of H I suggests that dust might also be present in the ICM of the cluster.

confirm that super-Ba-rich stars delineate the tip of the AGB, likely due to a third dredge-up, and find that three M-type stars not only have strong red excess, but are brighter than the 24 μm TRGB. Attributing the excess IR luminosity to dust suggests that the three bright M-type stars dominate the cluster's cumulative mass-loss rate (gas + dust) of 2.9 – 4.2 $\times$ 10^{-7} $M_{\odot}$ yr^{-1}. If the cluster mass-loss rate has remained constant since the last Galactic plane crossing, then the cluster has lost at least 1 – 2 $M_{\odot}$ of dust-traced material over the last 3.4 $\times$ 10^{6} years.

The dusty stars in our sample range over $\approx$1.5 dex in metallicity, suggesting that dust production is not inhibited even in stars with very low metal contents. In addition, our results show that, in ω Cen, significant dusty mass loss occurs near the very tip of the RGB or AGB, concentrated in only a few individual stars, with little evidence for such mass loss lower on the RGB.

While our images are sensitive enough to detect the amount of dust expected in ω Cen based on the current mass-loss rate, no obvious ICM dust clouds are apparent in the cluster center at 24 or 70 μm. We do find several regions of faint extended 24 μm emission on the outskirts of the cluster, but it is unclear whether these clouds are associated with the ICM or are in the foreground. If the dust features are associated with the cluster, they are well outside the cluster half-mass radius, and could therefore be ICM material that is in the process of escaping the cluster.

Chapter 4

A *Spitzer* Study of Asymptotic Giant Branch Stars. III. Dust Production and Gas Return in Local Group Dwarf Irregular Galaxies

A slightly modified version of this chapter has been submitted for publication to the Astrophysical Journal, with the following bibliographic reference: Boyer, M. L., Skillman, E. D., van Loon, J. Th., Gehrz, R. D. & Woodward, C. E. 2008, ApJ, Submitted. Reproduced with the permission of the American Astronomical Society.

Abstract

We present the third and final part of a census of Asymptotic Giant Branch (AGB) stars in Local Group dwarf irregular galaxies. Papers I and II presented the results for

WLM and IC 1613. Included here are Phoenix, LGS 3, DDO 210, Leo A, Pegasus dIrr, and Sextans A. *Spitzer* photometry at 3.6, 4.5, 5.8, and 8 μm are presented, along with a more thorough treatment of background galaxy contamination than was presented in papers I and II. We find that at least a small population of completely optically obscured AGB stars exists in each galaxy, regardless of the galaxy's metallicity, but that higher-metallicity galaxies tend to harbor more stars with slight IR excesses. Overall, there is an underrepresentation of 30% – 40% in the optical AGB within the $1\,\sigma$ errors for all of the galaxies in our sample. This undetected population is large enough to affect star formation histories derived from optical color-magnitude diagrams. As measured from the $[3.6]-[4.5]$ color excesses, we find average stellar mass-loss rates ranging from 3.1×10^{-7} – 6.6×10^{-6} $M_{\odot}$ yr^{-1}, and integrated galaxy mass-loss rates ranging from 4.4×10^{-5} – 1.4×10^{-3} $M_{\odot}$ yr^{-1}. The integrated mass-loss rate is sufficient to sustain the current star formation rate in only LGS 3 and DDO 210, requiring either significant non-dusty mass loss or gas accretion in Phoenix, Leo A, Pegasus dIrr, Sextans A, WLM, and IC 1613 if they are to maintain their status as gas-rich galaxies.

4.1 Introduction

After a star with mass $0.8\ M_{\odot} < M < 8\ M_{\odot}$ has exhausted the helium in its core, it will experience a short stay (≈1 – 13 Myr; Vassiliadis & Wood 1993) on the Asymptotic Giant Branch (AGB), where it will burn hydrogen and helium in concentric shells around a degenerate C/O core. During the final 0.2 – 2 Myr of its life, an AGB star will undergo radial pulses, which may allow dust condensation in the circumstellar envelope. Radiation pressure on the dust grains and momentum coupling between the grains and the gas results in the formation of an additional slow, dense wind (Gehrz & Woolf 1971). This wind causes the star to lose 20 – 60% of its mass, truncating its subsequent evolution.

AGB stars are uniquely important to many aspects of galactic and stellar astronomy.

Mass-losing AGB stars are the main source of long-term gas return to the interstellar medium (ISM), prolonging the star-formation life of gas-rich dwarf galaxies. AGB winds are heavily enriched in Li, C, N, F, and s-process elements, and are the largest source of dust input into the ISM (Gehrz 1989), making AGB stars an important driver of chemical evolution in galaxies. The intermediate masses of AGB stars make them ideal candidates for probing the star formation histories (SFHs) across much of a galaxy's lifetime. Also, because they are widely distributed and easily detected, AGB stars are excellent tracers of galactic structure. While unobscured AGB stars are among the brightest stars in optical band-passes, they are best studied in the infrared (IR), where emission from warm circumstellar dust peaks and circumstellar extinction is minimal. However, until the launch of the *Spitzer Space Telescope*, a lack of sufficient sensitivity and resolution has prevented comprehensive IR studies of extragalactic AGB stars in systems other than the Magellanic Clouds (e.g., Loup et al. 1997; Trams et al. 1999; Cioni et al. 2003; Whitelock et al. 2003).

Dwarf irregular (dIrr) galaxies in the Local Group provide us with ideal laboratories to study AGB stars. Most of these galaxies are undergoing recent or on-going star formation, resulting in a population of AGB stars representative of the entire mass range rather than a snapshot of a single AGB mass. The nearby dwarf irregular galaxies are populous enough to capture a substantial number of AGB stars in the short-lived mass-loss phase, near enough to resolve the stellar population, and distant enough to encompass the entire galaxy with a small field of view. *Spitzer's* ability to detect the entire AGB population in a given galaxy also provides us with the means to study the mass and dust injection rate into the Interstellar Medium (ISM), the fate of the ISM, and the effect on continued star formation and chemical evolution of the galaxy.

This paper is the third and final part of our *Spitzer* mid-IR IRAC survey of Local Group dIrr galaxies, designed to obtain a complete census of AGB stars. Jackson et al. (2007a) (hereafter paper I), and Jackson et al. (2007b) (hereafter paper II) presented a

complete AGB census in WLM and IC 1613, respectively. Here, we present the results for six more Local Group dIrr galaxies and provide a comprehensive summary of the results for all eight galaxies. Our total sample of eight galaxies spans 1 dex in metallicity, allowing us to study AGB dust production and mass loss in metal-poor environments as a function of metallicity. This metallicity range also enables us to investigate the degree to which optical studies of these targets are biased by the inability to detect the entire AGB population due to dust obscuration.

In § 4.2, we describe the observations, data reduction, and ancillary data. We present and describe the IR color-magnitude diagrams (CMDs) in § 4.3 and also discuss the stellar spatial distributions, detection statistics, stellar luminosity, and stellar mass. § 4.4 details a complete census of the AGB stars in all eight galaxies and estimates of AGB mass-loss rates (MLRs) and ISM gas return. We summarize our results in § 4.5.

4.2 Observations and Data Reduction

4.2.1 Sample Selection

Papers I and II discuss the AGB populations in the Local Group dIrr galaxies WLM and IC 1613. IC 1613 and WLM are very similar in luminosity, gas content, and metallicity. In order to broaden the environments for which we have complete AGB censuses, we have chosen six more Local Group dIrr galaxies for this study: Phoenix dwarf, LGS 3 (Pisces dIrr), DDO 210 (Aquarius dIrr), Leo A (DDO 69), Pegasus dIrr (DDO 216), and Sextans A (DDO 75). Including these six galaxies with WLM and IC 1613 increases the luminosity range to 4.6 mag, the range in H I mass by a factor of 800, and the range in $12 + \log(\mathrm{O/H})$ to 0.92. See Tables 4.1 and 4.2 for a list of basic galaxy properties.

Table 4.1. Basic Galaxy Properties. Part I.

Quantity	Phoenix	LGS 3	DDO 210	Leo A
Right Ascension, α(J2000)	$01^h51^m06^s$	$01^h03^m57^s$	$20^h46^m52^s$	$09^h59^m27^s$
Declination, δ(J2000)	$-44°26'.7$	$+21°53'.7$	$-12°50'.9$	$+30°44'.8$
$(m-M)_0$ (mag)[a]	23.24 ± 0.12	24.54 ± 0.15	25.15 ± 0.08 [3]	24.51 ± 0.12 [1]
Morphological Type	dIrr/dSph	dIrr/dSph	dIrr/dSph	dIrr
M_V (mag)	-10.1	-10.35 [4]	-10.6 [5]	-11.4
12 + log (O/H)[b]	7.26 ± 0.26	7.01 ± 0.24	7.32 ± 0.26	7.30 ± 0.05
Holmberg semiaxes, a_H, b_H	···	···	$0.9'$, $1.6'$	$2.3'$, $3.5'$
$\log(M_{HI})$ ($M_\odot$)	6.5 [7]	5.0 [6]	5.3 [6]	7.0 [7]
$\log(M_{Dynamical})$ ($M_\odot$)	7.5	7.1	6.7	7.0
$\log(M_*)$ ($M_\odot$)[c]	5.40	4.56	5.60	5.89
$TRGB_{3.6\ \mu m}$ (mag)[d]	-6.38 ± 0.25	-5.88 ± 0.25	-6.13 ± 0.25	-6.88 ± 0.25

Note. — All values in this table are from Mateo (1998), unless marked otherwise in brackets.

References. — [1] Dolphin et al. (2002); [2] Mateo (1998); [3] McConnachie et al. (2006); [4] Lee (1995); [5] Lee et al. (1999a); [6] Lo et al. (1993); [7] Volders & Högbom (1961).

[a] Distance modulus.

[b] Values of 12 + log(O/H) for galaxies containing H II regions (Leo A) are taken from van Zee et al. (2006). For galaxies without H II regions (Phoenix, LGS 3, and DDO 210), the *L-Z* relationship determined by Lee et al. (2006) was used to determine 12 + log(O/H). To compute mass-loss rates, Z was determined using $Z_\odot = 0.0122$ and $12 + \log(O/H)_\odot = 8.66$ (Asplund et al. 2004).

[c] Stellar masses for Leo A is taken directly from Lee et al. (2006). For Phoenix, LGS 3, and DDO 210, we used the mass-metallicity relation derived by Lee et al. (2006) with 4.5 μm fluxes from Jackson et al. (2006).

[d] The 3.6 μm TRGBs as determined from this work (see § 4.3.2).

Table 4.2. Basic Galaxy Properties. Part II.

Quantity	Pegasus dIrr	Sextans A	WLM	IC 1613
Right Ascension, α(J2000)	$23^{\rm h}28^{\rm m}36^{\rm s}$	$10^{\rm h}11^{\rm m}01^{\rm s}$	$00^{\rm h}01^{\rm m}58^{\rm s}$	$01^{\rm h}0^{\rm m}454^{\rm s}$
Declination, δ(J2000)	$+14°44'.6$	$-04°41'.5$	$-15°27'.8$	$+02°08'.0$
$(m-M)_0$ (mag)[a]	24.9 ± 0.1	25.61 ± 0.07 [3]	24.81 ± 08 [7]	24.32 ± 0.06 [2]
Morphological Type	dIrr/dSph	dIrr	IrrIV-V	IrrV
M_V (mag)	-12.9	-14.6	-14.5	-14.7
12 + log (O/H)[b]	7.93 ± 0.14	7.54 ± 0.10	7.83 ± 0.06	7.62 ± 0.05
Holmberg semiaxes, $a_{\rm H}, b_{\rm H}$	$2.3'$, $3.9'$	$3.2'$, $4.0'$	$2.2'$, $5.5'$	...
$\log(M_{\rm H\,I})$ $(M_\odot)$	6.5 [4]	7.9 [1]	7.7 [5]	7.8 [8]
$\log(M_{\rm Dynamical})$ $(M_\odot)$	7.8	8.6	8.2	8.9
$\log(M_*)$ $(M_\odot)$[c]	6.98	6.24	6.88	6.82
$\rm TRGB_{3.6\ \mu m}$ (mag)[d]	-6.38 ± 0.25	-6.13 ± 0.25[e]	-6.6 ± 0.25	-6.2 ± 0.20

Note. — All values in this table are from Mateo (1998), unless marked otherwise in brackets.

References. — [1] Barnes & de Blok (2004); [2] Dolphin et al. (2001); [3] Dolphin et al. (2003a); [4] Hoffman et al. (1996); [5] Huchtmeier et al. (1981); [6] Mateo (1998); [7] Lee et al. (2006); [8] Volders & Högbom (1961).

[a] Distance modulus.

[b] Values of 12 + log(O/H) for galaxies containing H II regions (Pegasus dIrr, Sextans A, WLM, and IC 1613) are taken from van Zee et al. (2006). To compute mass-loss rates, Z was determined using $Z_\odot = 0.0122$ and $12 + \log({\rm O/H})_\odot = 8.66$ (Asplund et al. 2004).

[c] Stellar masses for Pegasus dIrr and Sextans A are taken from Lee et al. (2006).

[d] The 3.6 μm TRGBs as determined from this work (see § 4.3.2), except for WLM (Paper I) and IC 1613 (Paper II).

[e] The Sextans A 3.6 μm TRGB is not measured from the IRAC data directly, but by plotting the 3.6 μm luminosity function of optical sub-TRGB stars (see § 4.3.2).

The angular sizes of the galaxies presented here are small enough to obtain complete coverage, and the galaxies are near enough to resolve stars down to or below the tip of the Red Giant Branch (TRGB), above which mass-losing AGB stars reside. The span in metallicity ($Z \approx 2\%$ – 19% $Z_{\odot}$; Lee et al. 2006; van Zee et al. 2006), provides us with the opportunity to examine how metal content affects dust production, mass return, and optical completeness (§ 4.4).

Each galaxy shows some evidence for recent star formation (age < 3 Gyr; Dolphin et al. 2005), providing a large sample of intermediate-aged stars, and consequently, a large sample of AGB stars. LGS 3 has the lowest rate of recent star formation in our sample, followed closely by Phoenix. Sextans A, WLM, and IC 1613 are forming stars at a rate two orders of magnitude higher than LGS 3. A brief summary of the star formation histories from Dolphin et al. (2005) is given in § 4.3.

4.2.2 Infrared Data and Photometry

New observations were obtained with the Infrared Array Camera (IRAC; Fazio et al. 2004) onboard the *Spitzer Space Telescope* (Werner et al. 2004; Gehrz et al. 2007). The observing program (PID 40524) was designed to image Phoenix, LGS 3, DDO 210, Leo A, and Pegasus dIrr at 3.6 and 5.8 μm. The same five galaxies were also observed earlier at 4.5 and 8 μm as part of a larger guaranteed time observing (GTO) program (PID 128; PI: R. D. Gehrz). Sextans A was observed as part of the GTO program at all four IRAC wavelengths. See Table 4.3 for a summary of the observations. GTO 4.5 and 8 μm data were observed with a 5-point Gaussian dither pattern (*Spitzer* Science Center 2006a) and an exposure time of 193.6 s, yielding a total depth of 968 s. To build a better redundancy against outliers and artifacts while maintaining a similar exposure depth, images obtained as part of PID 40524 were observed with a 36-point reuleaux dither pattern (*Spitzer* Science Center 2006a) and exposure time of 26.8 s, for a total depth of 965 s. Sextans A was observed at 3.6 and 5.8 μm as part of PID 128 with a

16-point reuleaux dither pattern and exposure time of 26.8 s, for a total depth of 858 s. For all observatiosn, we used small-scale dither patterns to allow for sub-pixel sampling. These observations yielded $5\,\sigma$ point-source sensitivities of 1.3, 2.3, 15.0, and 17.5 μJy at 3.6, 4.5, 5.8, and 8 μm respectively. Sextans A $5\,\sigma$ sensitivities are 1.4 μJy at 3.6 μm and 15.9 μJy at 5.8 μm. The coverage area for all six galaxies is approximately $5.8'$ $\times$ $5.8'$, centered at the coordinates listed in Table 4.3. Figure 4.1 displays the field of view overlaid on the Digitized Sky Survey images of the six selected galaxies.

GTO and PID 40524 IRAC data were processed with pipelines S14.0.0 and S16.1.0, repectively, with the exception of the PID 40524 data for Leo A, which was processed with pipeline S17.0.4. The Basic Calibrated Data (BCD) were reduced and mosaicked with the MOPEX[1] reduction package (Makovoz & Marleau 2005) after applying an array distortion correction. We implemented the MOPEX overlap routine to match backgrounds between overlapping areas of the images and the MOPEX mosaicker for outlier elimination, image interpolation, and co-addition. The final mosaics have pixel sizes of $0.86''$ pix^{-1} and are presented in Jackson et al. (2006). The 8 μm mosaics are affected by persistent images resulting from observations of very bright objects immediately preceding our program. These artifacts were removed by subtracting a median-combined image from each individual frame before proceeding with MOPEX.

[1]MOPEX is available from the *Spitzer* Science Center at http://ssc.spitzer.caltech.edu/postbcd

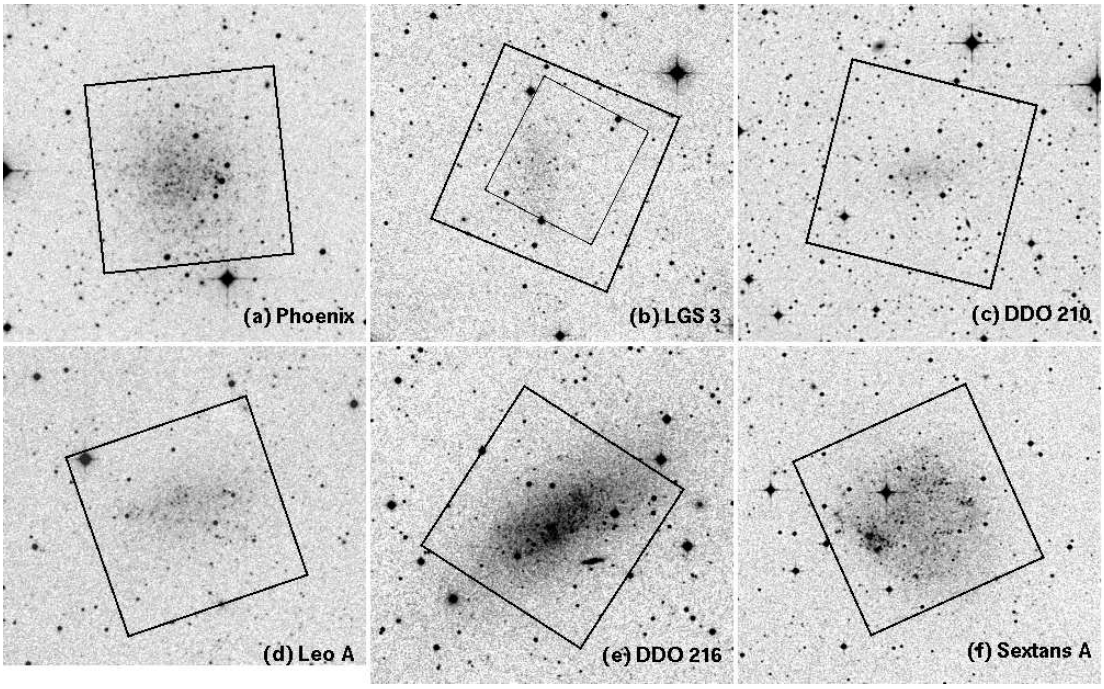

Figure 4.1: Digitized Sky Survey (DSS) images of (a) Phoenix, (b) LGS 3, (c) DDO 210, (d) Leo A, (e) Pegasus dIrr, and (f) Sextans A. The field shown in each panel is $9.7' \times 9.5'$. The IRAC field of view is overplotted with a thick line. The optical coverage for each galaxy, with the exception of LGS 3, is larger than the DSS image shown. (b) shows the HST ACS field of view for LGS 3 plotted as a thin black line. In all six galaxies, the IRAC coverage contains the vast majority of the stellar population.

Table 4.3: Observation Details

Galaxy Name	AOR key	α (J2000)	δ (J2000)	PID	Date (UT)	λ (μm)	Depth (s)
LGS 3	5051393	01:03:52.65	+21:53:00.2	128	2005 Jul 23	4.5, 8.0	968
	23043072	01:03:58.86	+21:49:57.1	40524	2007 Aug 12	3.6, 5.8	965
Phoenix	5052160	01:51:05.65	−44:26:42.0	128	2003 Dec 06	4.5, 8.0	968
	23043328	01:51:04.84	−44:30:02.9	40524	2007 Sep 07	3.6, 5.8	965
Leo A	5052416	09:59:26.23	+30:44:47.8	128	2003 Dec 06	4.5, 8.0	968
	23042816	09:59:26.63	+30:44:47.5	40524	2007 Dec 28	3.6, 5.8	965
Sextans A	5053696	10:11:06.45	−04:38:27.9	128	2003 Dec 06	4.5, 8.0	968
	15892224	10:10:55.20	−04:44:38.6	128	2005 Dec 24	3.6, 5.8	858
DDO 210	5054976	20:46:51.70	−12:50:47.0	128	2004 Oct 09	4.5, 8.0	968
	23043328	20:46:52.01	−12:50:51.2	40524	2007 Nov 13	3.6, 5.8	965
Pegasus dIrr	5055744	23:28:36.16	+14:44:35.1	128	2004 Jul 26	4.5, 8.0	968
	23043840	23:28:44.24	+14:41:49.6	40524	2007 Aug 16	3.6, 5.8	965

Point-source extraction was performed with the DAOphot II package (Stetson 1987). PSFs were created from a minimum of 10 isolated stars in each mosaic, and sources $4\,\sigma$ above the background were chosen for extraction. Extended galaxies and outliers that are broader or narrower than the PSF were rejected based on sharpness and roundness cut-offs. The final fluxes are color-corrected (*Spitzer* Science Center 2006a) using a 5000 K blackbody, which is an appropriate temperature for a typical Red Giant star. The color correction listed for a 2000 K star in *Spitzer* Science Center (2006a) differs by less than 1%. A pixel-phase-dependent correction (Reach et al. 2005) has been applied to the 3.6 μm photometry. Photometric errors include standard DAOphot errors and the IRAC absolute calibration errors (Reach et al. 2005). Magnitudes relative to α Lyr (Vega) are derived using the zero magnitudes quoted in the *Spitzer* IRAC data handbook (*Spitzer* Science Center 2006a).

4.2.3 Optical Photometry

We used optical data for each galaxy to aid in source classification, which is challenging with IRAC data alone (see § 4.3). Broadband V and I images of Sextans A, Pegasus dIrr, and Phoenix were obtained from the Local Group Galaxies Survey[2] (LGGS; Massey et al. 2006). The LGGS survey nicely complements IRAC data because the coverage includes the entire IRAC field of view, and the angular resolution is similar to the IRAC resolution (median seeing $\approx 1''$). The published LGGS photometry only includes sources $10\,\sigma$ above the background, rendering an incomplete CMD. In order to reliably identify different regions of the CMD, it was necessary to recover sources down to $4\,\sigma$ above the background. We performed PSF photometry on the LGGS images ourselves with DAOphot II. Precise absolute photometry was not required since the V and I data were used only to identify sources in optical CMDs. We therefore

[2]LGGS data are publicly available at http://www.lowell.edu/ massey/lgsurvey/.

used "stacked" images with relative photometric errors of ≈10% instead of photometric images since image processing, including co-addition and astrometric calibration, had already been performed on the former. To calibrate the LGGS magnitude offsets between instrumental and true magnitudes, we compared our photometry to the published LGGS calibrated $10\,\sigma$ photometry lists. The magnitude offsets and color terms were computed using least-squares fitting.

V and I photometry of DDO 210 and Leo A was obtained with the SUBARU telescope by McConnachie et al. (2006) and Vansevičius et al. (2004). As with the LGGS, the SUBARU coverage includes the entire IRAC field of view and the angular resolution is similar to the IRAC resolution ($0.8''$ seeing for both DDO 210 and Leo A). The calibrated photometry lists compiled by McConnachie et al. (2006) for DDO 210 and Vansevičius et al. (2004) for Leo A are sufficiently complete and have relative photometry errors $\lesssim 10\%$.

Optical photometry of LGS 3 was obtained with permission from the Local Cosmology from Isolated Dwarfs Survey (LCID; Gallart 2008), which imaged several Local Group Dwarfs with the ACS camera onboard the *Hubble Space Telescope* (HST) with the F475W and F814W filters. The total optical coverage for ACS is $\approx 3.3' \times 3.3'$ (Fig. 4.1). The resolution and PSF of the ACS camera is vastly superior to those of IRAC, making cross-correlation between the IR and optical data difficult for LGS 3. To facilitate comparisons between optical and IR photometry of AGB candidates in LGS 3, we inspected the IRAC and ACS images by eye to be sure we found the correct IR counterparts of the optical point sources above the I-band TRGB. All optical sub-TRGB sources in LGS 3 remain unmatched to *Spitzer* sources.

4.2.4 Source Contamination

The main contributors of contamination to the *Spitzer* and optical photometry lists are unresolved background galaxies and foreground stars. We used the Milky Way

stellar population synthesis model of Robin et al. (2003) to estimate the degree of contamination in each IRAC field from the latter. Foreground stellar counts for 1 deg^2 fields centered on the Galactic coordinates of each galaxy were generated to reduce statistical error. The Robin et al. (2003) model provides Johnson-Cousins L band magnitudes, which is similar to the IRAC 3.6 μm band. In the IRAC coverage area, we expect to find 6 foreground stars in the Phoenix and Leo A mosaics, 10 foreground stars in the Pegasus dIrr, Sextans A, and LGS 3 mosaics, and 32 foreground stars in the DDO 210 mosaic. These stars are expected to have [3.6] – [4.5] colors near zero and $-6 \lesssim M_L \lesssim -20$. The contamination from foreground stars is therefore only 0.5% – 3.5% of the total number of point sources detected at 3.6 μm. This contamination is reflected in error bars and uncertainties throughout this paper. Background galaxies are a more insidious contamination, accounting for anywhere from 20% – 70% of the sources brighter than the 3.6 μm TRGB and residing in an IRAC color-magnitude locus similar to that of obscured AGB stars. The effect of background contamination on the analyses presented in this paper is discussed in detail in § 4.3.4.

4.3 Comparison of Optical and IR Photometry

4.3.1 Optical Color-Magnitude Diagrams

IRAC data sample the Rayleigh-Jeans tail of the Planck function, providing very little information about stellar effective temperatures and making it necessary to identify source types in the optical. Optical CMDs are shown as Hess diagrams in Figure 4.2. Lines divide the regions where (*a*) blue objects, (*b*) AGB stars, (*c*) red supergiants (RSGs), and (*d*) red giants (RGs) below the TRGB reside. Sources located in (*d*) will hereafter be referred to as sub-TRGB stars. The gap widths between the regions reflect the 1 σ photometric errors and reduce misidentification solely due to photometric uncertainty. Circumstellar and interstellar reddening can also cause source misidentification

that is not corrected for in Figure 4.2.

The optical CMDs show features that indicate a wide variety of star formation histories (SFHs) among these six galaxies. Sextans A shows the strongest evidence for recent and intermediate age star formation with prominent plumes of blue helium burning stars, RSGs, and AGB stars that are consistent with an increase in star formation rate (SFR) by a factor of three 1 Gyr ago and a factor of five 100 Myr ago (Dolphin et al. 2005, 2003b). Leo A also shows a prominent branch of blue helium burning stars, reflecting a twofold increase in the recent SFR over the lifetime average ≈1 Gyr ago (Dolphin et al. 2005).

Pegasus dIrr has been forming stars at a moderately high rate over its lifetime, but the SFR has steadily decreased during the last 1 Gyr. Blue stars in DDO 210 suggest some star formation 3 – 6 Gyr ago (McConnachie et al. 2006), and the SFR has remained steady throughout the lifetime of the galaxy (Dolphin et al. 2005). The SFH of Phoenix (Holtzman et al. 2000; Dolphin et al. 2005; Young et al. 2007) reveals that star formation ceased ∼100 Myr ago. LGS 3 is similar to Phoenix because it has been forming stars at a low, but constant level since its initial star formation event (Miller et al. 2001; Dolphin et al. 2005), but a lack of blue stars in LGS 3 suggests very little recent star formation.

4.3.2 IRAC Color-Magnitude Diagrams

The $M_{3.6}$ versus [3.6] − [4.5] CMDs are shown in Figure 4.3. These CMDs show all sources detected at 3.6 and 4.5 μm along with the photometric errors, averaged over one-magnitude bins. The 50% completeness limits, averaged over the entire fields of view, are also shown as a solid black line. Unlike WLM, none of the galaxies in this sample are particularly crowded in the infrared, so the photometric completeness does not decline significantly towards the centers of the galaxies. Sources that fall along [3.6] − [4.5] = 0 sample the Rayleigh-Jeans tail of the Planck function at both 3.6

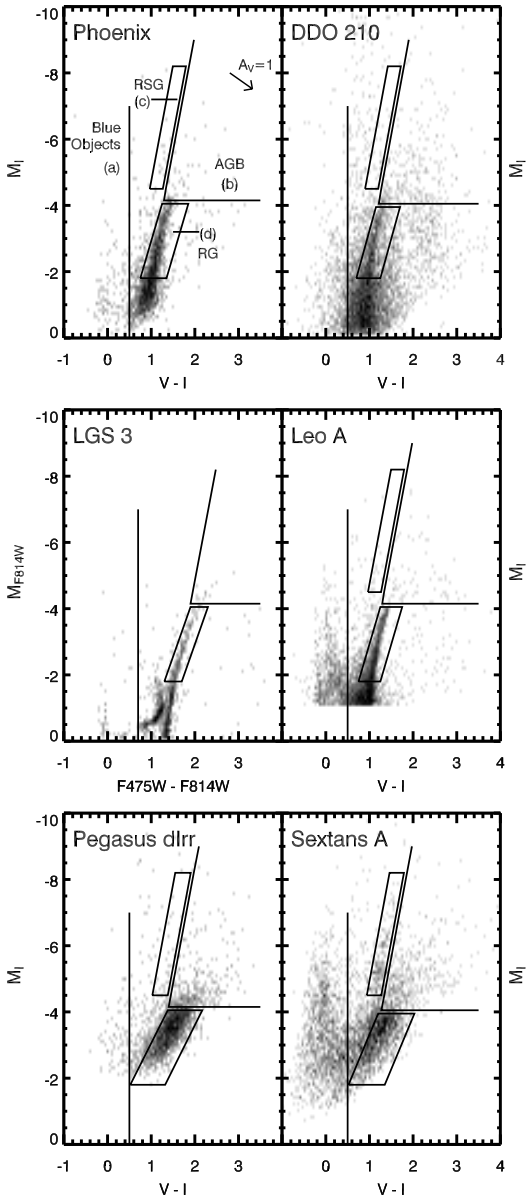

Figure 4.2: Optical color-magnitude diagrams. See § 4.2.3 for a description of optical photometry. The color magnitude diagrams are represented by Hess diagrams with color bins and magnitude bins of 0.5 mag. Regions are labeled containing (a) blue objects, (b) AGB stars, (c) RSGs, and (d) red giant stars. These optical identifications are used to aid in the identification of different source types in the infrared color-magnitude diagrams. The *I*-band TRGB is approximately $M_{\rm I} = -4.0$ mag for each galaxy. The space between the gaps represent the approximate $1\,\sigma$ photometric uncertainties. A vector in the first panel shows 1 magnitude of extinction and the associated reddening.

and 4.5 μm. Other sources are reddened by circumstellar dust emission. The region redward of $[3.6] - [4.5] = 0$ is also populated by background galaxies, although these should mostly fall below the dashed line (see § 4.3.4).

The $M_{3.6}$ versus $[3.6]-[4.5]$ CMDs of all eight galaxies (including WLM and IC 1613 from papers I and II) are very similar and differ significantly only in the depth of the photometry. Phoenix has the fewest bright, red sources ($M_{3.6} < -8, [3.6]-[4.5] > 0.5$), while WLM, IC 1613, and Sextans A contain the largest number of sources in this region. These magnitudes and colors are consistent with obscured, mass-losing AGB stars (see § 4.4).

Isochrones from Marigo et al. (2008), computed for single-aged populations of $\log(t)$ = 8.25 (black), 8.75 (magenta), and 9.25 (blue) at the metallicity of each galaxy (Tables 4.1 and 4.2), are overlaid on the $M_{3.6}$ versus $[3.6] - [4.5]$ CMDs in Figure 4.4. The thick lines show the isochrones that do not include dust, and the thin lines show isochrones computed with 60% Silicate + 40% AlO_x for O-stars, and 85% AMC + 15% SiC for C-stars. It is clear from these isochrones that dusty, mass-losing AGB stars are not only red in color, but are also some of the brightest stars on the CMD. These isochrones are not a good match to faint, red stars ($M_{3.6} \gtrsim -7$ mag, $[3.6]-[4.5] \gtrsim 0.5$). This discrepancy may be due to a combination of photometric uncertainty in this region of the CMD and contamination from other source types, particularly background galaxies.

Figure 4.5 shows point-sources residing in regions (*a*), (*b*), (*c*), or (*d*) of the optical CMDs (Fig. 4.2) of Phoenix, DDO 210, Leo A, Pegasus dIrr, and Sextans A; red squares are red giants, green triangles are optical AGB stars, black stars are RSGs, and blue circles are blue objects. LGS 3 is excluded from Figure 4.2 due to difficulty in matching the *Spitzer* sources to the ACS sources. A vector in the first panel shows the displacement corresponding to 10 magnitudes of visual extinction and the associated reddening (Rieke & Lebofsky 1985; Indebetouw et al. 2005), although this vector does not take

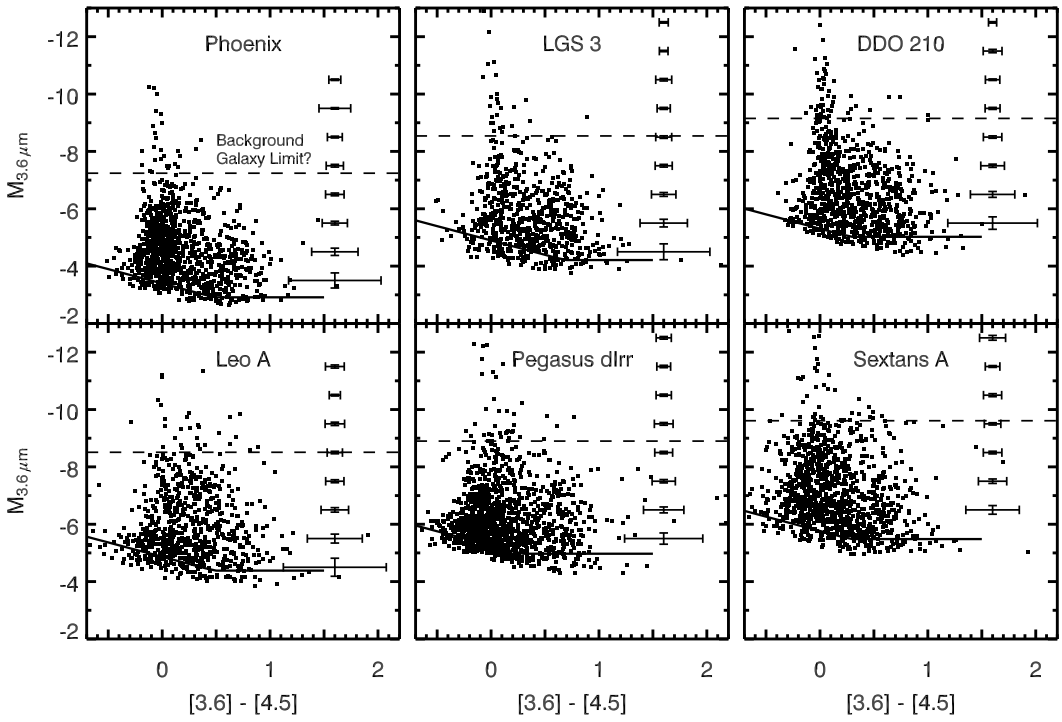

Figure 4.3: [3.6] vs. [3.6]−[4.5] color-magnitude diagrams. All point sources detected at 3.6 and 4.5 μm are included. 1 σ photometric errors averaged over 1 mag bins are shown on the right of each panel. The solid lines represent the 50% completeness limits. The dashed line shows the position of $m_{3.6} = 16$ mag, which is the approximate maximum apparent magnitude of point-source background galaxies. Red sources above this line are very likely obscured AGB stars, since background galaxies brighter than this limit are likely extended and subsequently rejected during PSF fitting.

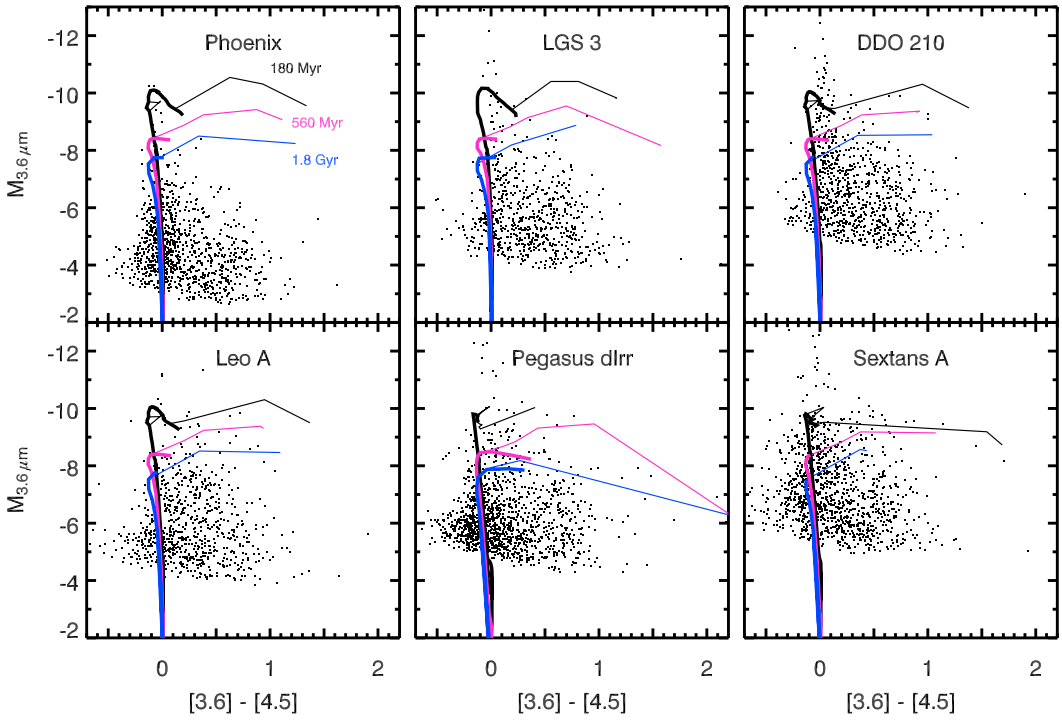

Figure 4.4: Color-magnitude diagrams, as in Figure 4.3, with overlaid isochrones from Marigo et al. (2008). Isochrones were computed at the metallicity of each galaxy for three separate single-age populations: $\log(t) = 8.25$ (black), 8.75 (magenta), and 9.25 (blue). The thick lines represent isochrones for stars with no circumstellar dust, and the thin lines are isochrones for stars with dust. Dust compositions are assumed to be 60% silicates plus 40% aluminum oxides for O-rich stars and 85% amorphous carbon plus 15% SiC for C-rich stars. Mass-losing AGB stars are expected to be among the brightest and reddest stars in the CMDs.

into account the effect of dust emission, which can be considerable in the infrared. The AGB limit was determined by scaling AGB stars with $T_{\rm eff} = 2650$ and 3600 K and negligible mass loss (Groenewegen 2006) to bolometric magnitudes of $M_{\rm bol} = -7.1$ mag. The lines shown in Figure 4.5 connect the limits of these two hypothetical stars. AGB stars that are undergoing heavy mass loss can attain 3.6 μm fluxes brighter than this limit due to thermal emission from the expelled material. Such stars would also have red $[3.6] - [4.5]$ colors, as is the case for one star in Leo A (Fig. 4.3). All other stars above the AGB limit in our galaxy sample are likely RSGs. Note that few of the stars following the isochrones in Figure 4.4 are detected in the optical, especially in Leo A. Moreover, of those stars that are detected in V and I, many are not optically identified as AGB stars.

The Tip of the Red Giant Branch:

Figure 4.5 also shows the locations of the 3.6 μm TRGB. The TRGB was identified by plotting the luminosity functions of stars detected at both 3.6 and 4.5 μm (Fig. 4.6) and determining the magnitude where the source count decreases significantly. We adopt TRGB values of $M_{3.6} = -6.38 \pm 0.25$, $M_{3.6} = -5.88 \pm 0.25$, $M_{3.6} = -6.13 \pm 0.25$, $M_{3.6} = -5.88 \pm 0.25$, and $M_{3.6} = -6.38 \pm 0.25$ mag for Phoenix, LGS 3, DDO 210, Leo A, and Pegasus dIrr, respectively. The dotted lines in Figure 4.6 represent the IR luminosity function of sub-TRGB stars identified in the optical. In each case, the number counts of the sub-TRGB stars support what we have determined is the location of the TRGB. Sub-TRGB stars that are brighter than the 3.6 μm TRGB have very red colors that are consistent with heavily obscured, mass-losing AGB stars and might be reddened enough in the optical to be misidentified as sub-TRGB.

The IRAC photometry of Sextans A is not deep enough to reliably determine the 3.6 μm TRGB, but the luminosity function of the sub-TRGB stars seems to suggest a TRGB of approximately $M_{3.6} = -6.13$ mag. In papers I and II, we found 3.6 μm TRGBs

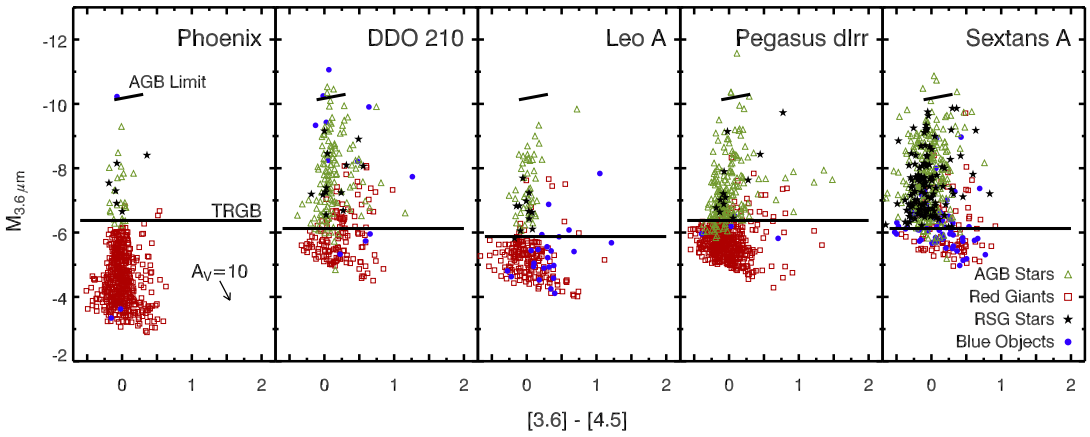

Figure 4.5: Optically identified sources in the [3.6] vs. [3.6] − [4.5] color-magnitude diagrams. Red squares are red giants, black stars are RSGs, blue circles are blue objects, and green triangles are optical AGB stars, as identified in Figure 4.2. The first panel displays a vector showing 10 visual magnitudes of extinction and the associated reddening. Each panel shows the AGB limit and the location of the TRGB. Note that red stars above the TRGB, evident if Figures 4.3 and 4.4, are largely undetected in the optical.

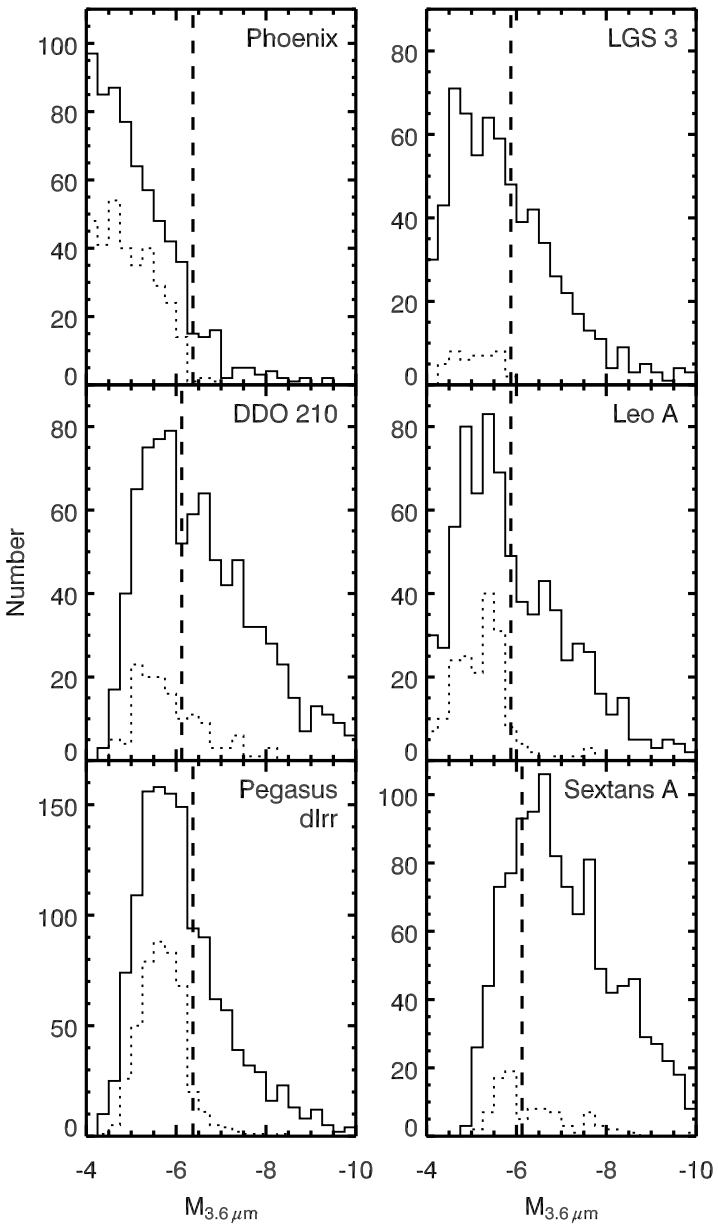

Figure 4.6: 3.6 μm luminosity functions. The solid line represents all sources detected at 3.6 *and* 4.5 μm. The dotted line shows optically classified sub-TRGB stars. The adopted TRGB values are marked with a dashed line. In the case of Sextans A, where the IRAC luminosity function drops off at a magnitude brighter than the TRGB, the optical sub-TRGB luminosity function provides a first-order estimate of the 3.6 μm TRGB.

of $M_{3.6} = -6.6 \pm 0.2$ mag for WLM and $M_{3.6} = -6.2 \pm 0.2$ mag for IC 1613. Most of our values are a few tenths of a magnitude fainter than the TRGB found in the Large Magellanic Cloud (LMC; $M_{3.6} = -6.65$ mag; Blum et al. 2006), but this discrepancy is not necessarily unexpected since different SFHs will yield different TRGBs due to varying ages and metallicities of RGB stars. The 3.6 μm TRGBs in old star clusters in the Magellanic Clouds is $M_{L'} \approx -6$ mag (van Loon et al. 2005), which is more consistent with the TRGB values measured here.

8 μm Color-Magnitude Diagrams:

The $M_{8.0}$ versus $[4.5] - [8.0]$ CMD is presented in Figure 4.7. In these CMDs, sources below the 3.6 μm TRGB are plotted as open circles. As with Figure 4.3, this CMD is similar for all eight galaxies. The main features are a narrow plume centered at $[4.5] - [8.0] = 0$ and a bright, red plume with $M_{8.0} > -8.0$ mag and $[4.5] - [8.0] > 1.0$. The red plume is strongly populated in all eight galaxies, with the exception of Phoenix, which has fewer than 10 stars in this region that are brighter than the TRGB. Based on the colors of background galaxies in ω Cen (Boyer et al. 2008a), the reddest regions of the CMDs in Figure 4.7 are contaminated by background galaxies ($[4.5] - [8.0] > 2$), although the most heavily obscured AGB stars can also reach colors as red as $[4.5] - [8.0] \approx 5$.

Isochrones for two different ages are overlaid in Figure 4.7 ($\approx$0.5 and 2 Gyr; Marigo et al. 2008) and demonstrate that obscured AGB stars are bright at 8 μm. Because the isochrones appear to be systematically bluer than the data, we do not attempt a fit, but it is clear that the locus of the bright, red plume of sources in each galaxy is consistent with obscured AGB stars, while fainter red sources may be other source-types such as background galaxies or young stellar objects.

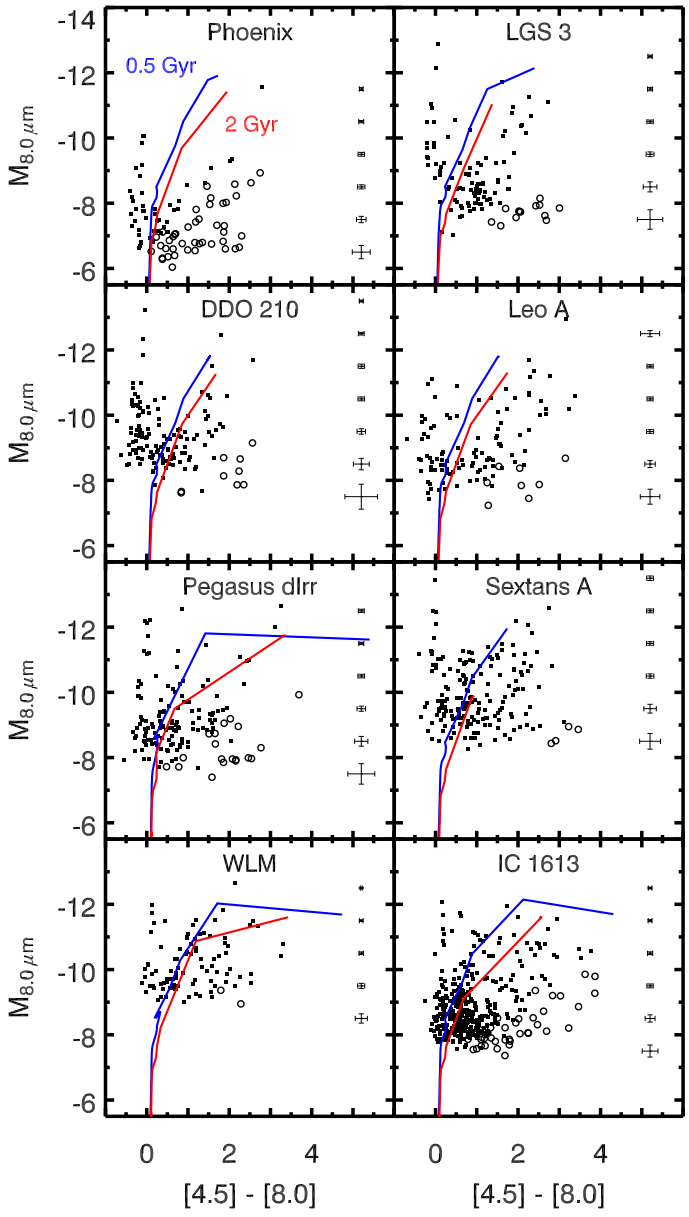

Figure 4.7: [8.0] vs. [4.5] − [8.0] color-magnitude diagrams. Photometric $1\,\sigma$ errors, averaged over 1 magnitude bins, are shown on the right side of each panel. Open circles mark sources that are below the 3.6 μm TRGB. In each galaxy, a plume of bright, red stars generally falls just redward of the isochrones for mass-losing AGB stars (Marigo et al. 2008). The isochrones were computed using the metallicities listed in Tables 4.1 and 4.2, and a single-age population of 2 Gyr (red line) and 0.5 Gyr (blue line). Assumed dust compositions are identical to those in Figure 4.4.

4.3.3 Detection Statistics

The detection statistics for the regions shared by optical and IRAC photometry are presented in Table 4.4 (note that the LGS 3 optical coverage is smaller than the IR coverage due to the small field of view of the ACS camera). We consider a source to be detected in V and I only if it is brighter than $M_{\rm I} = -2.5$ mag, which is the approximate limiting magnitude of the shallowest optical data. Sextans A has the largest 8 μm population, followed by Pegasus dIrr. The number of detections in the IRAC data of IC 1613 and WLM presented in papers I and II are much higher than all six of the galaxies presented here, but that is due to an increased areal coverage (more IRAC fields) rather than to an intrinsic property of the galaxies themselves.

In each galaxy, we find between 27 – 67 sources that are detected in all four IRAC bands, but not in V and I. The majority of these sources lie between the TRGB and the AGB limit and may be either optically obscured AGB stars or background galaxies. We are unable to determine the corresponding numbers for LGS 3 due to the difficulty of matching IRAC data to ACS data. However, we have inspected the bright optical sources by eye and note that there are a mere 12 stars brighter than the I-band TRGB in LGS 3 that are also detected in IRAC. For comparison, in the IRAC images, there are 102 sources located between the 3.6 μm TRGB and the AGB limit in LGS 3 in the area covered by the ACS data.

A small number of the IRAC detections with no optical counterparts are above the AGB limit and have colors near zero. These bright sources are probably foreground stars or RSG stars, as any AGB star above the AGB limit would have a very red color.

Table 4.4: Detection Statistics

Filter	Phoenix	LGS 3	DDO 210	Leo A	Pegasus dIrr	Sextans A	WLM	IC 1613
Total Point-Source 4 σ Detections in All Wavebands								
					(Number)			
Both V and I	2026	369	1532	2525	2251	2968	4896	7574
3.6 μm	1087	283	907	778	1422	1162	2855	5556
4.5 μm	1061	285	893	784	1369	1204	2019	3362
5.8 μm	462	49	326	261	451	360	300	998
8.0 μm	107	50	184	148	204	283	122	696
4 σ Detections in All Four IRAC Bands, But Not V and I								
Object Type					(Number)			
Total	40	···	27	63	67	66	46	190
Above AGB limit	1	···	3	3	5	11	3	4
Above TRGB, below AGB limit	14	···	22	60	58	55	42	183
Below TRGB	25	···	2	0	4	0	1	6
3.6 μm Point-Source Flux								
Total Flux (mJy)	19.6	13.0	22.9	19.6	23.9	26.9	40.1	74.0
Average 3.6 μm flux (mJy arcmin^{-2})	0.6	0.4	0.7	0.6	0.7	0.8	1.2	2.2
Flux 1 mag Above/Below TRGB[a]	0.60	1.59	1.78	1.36	1.11	3.30	1.41	1.13
$f_{1\ \mathrm{Gyr}}$ (Orban et al. 2008)[b]	0.027	0.015	0.037	0.13	0.057	0.15	0.14	0.059

NOTE.—Numbers in this table are computed only for areas where the IRAC and optical coverage overlaps. Some entries for LGS 3 are left blank due to the difficulty of matching IRAC data with the high-resolution HST data. Stars brighter than the I-band TRGB in LGS 3 were matched to their IR counterparts by eye. See Papers I and II for similar tables for WLM and IC 1613.

[a] The ratio of the cumulative flux one magnitude brighter than (above) to one magnitude fainter than (below) the 3.6 μm. The uncertainty of this quantity ranges from 5% to 18%.

[b] The fraction of the total stellar mass that has been formed within the last 1 Gyr (Orban et al. 2008).

There is strong evidence for confusion by background galaxies in our sample (see § 4.3.4), especially below the 3.6 μm TRGB. Phoenix, the nearest of the eight galaxies in our sample, hosts the largest number of sources that are below the 3.6 μm TRGB and not detected in the optical (25 sources total; Table 4.4). The region occupied by background galaxies in Figure 4.3 is at the faintest absolute magnitude for Phoenix, pushing many of the background galaxies below the 3.6 μm TRGB. As a result, Phoenix has the smallest number of background galaxies *above* the TRGB at 3.6 μm.

4.3.4 Background Galaxy Contamination

Unresolved background galaxies tend to have very similar [3.6] – [4.5] colors as optically obscured AGB stars. Based on inspection of IRAC CMDs alone, background galaxies are easily identified in observations of nearby stellar populations such as the Magellanic Clouds (Blum et al. 2006; Bolatto et al. 2007) and ω Centauri (Boyer et al. 2008a) because the AGB stars in these nearby systems have far brighter apparent magnitudes than the background objects. Unfortunately, the distances to our target dIrr galaxies are just large enough so that dusty AGB stars and unresolved background galaxies occupy the same color-magnitude space and are impossible to disentangle, potentially causing an overestimate of the dust production and integrated mass-loss rate in each galaxy. Because WLM and IC 1613 have the highest stellar surface densities in the sample, the effects of unresolved background galaxies were more subtle and not dealt with in papers I and II. The lower stellar surface densities of the galaxies in the new sample makes the effects of unresolved background galaxies more obvious, and thus we can address these effects in this study.

In the *Spitzer* observations of ω Centauri (Boyer et al. 2008a), the unresolved background galaxies remained confined to 3.6 μm apparent magnitudes fainter than $\approx$16 mag and colors $-0.3 \gtrsim [3.6]-[4.5] \lesssim 1.0$. This limit suggests that we may be confident that any red point-sources brighter than $m_{3.6} = 16$ mag are mass-losing AGB stars.

Below this limit, we cannot distinguish between mass-losing AGB stars, background galaxies, and other red IR sources (e.g., young stellar objects) with IRAC data alone. It is clear in Figure 4.3 that the pack of red sources fainter than $m_{3.6} = 16$ mag has a similar shape in each galaxy and slides up and down with respect to the rest of the IR population, depending on the distance to the galaxy. Phoenix, which is the nearest galaxy in our sample, is the least affected by contamination since the background galaxy limit is only one magnitude brighter than the TRGB. In Sextans A, on the other hand, the region occupied by galaxies reaches up to 3.5 mag brighter than the TRGB.

In fact, if we assume that the background galaxy populations in the images of Phoenix, LGS 3, DDO 210, Leo A, Pegasus dIrr, and Sextans A are the same (the IRAC images for these six galaxies have the same areal coverage), we should find approximately the same number of sources fainter than $m_{3.6} = 16$ mag and redder than $[3.6] - [4.5] \approx 0$. We created Hess diagrams with 0.1 mag color bins and 0.5 mag magnitude bins for Figure 4.3 and subtracted the Phoenix Hess diagram from the others, since the Phoenix background population is the least mixed with real AGB stars. We find that, in the region of contamination, the subtraction leaves only ± 10 sources in each bin, suggesting that the majority of sources in this region of the CMD are in fact background galaxies.

In order to obtain a first-order estimate of the degree of contamination above the TRGB in each of our targets, we inspected the IRAC CMDs produced with photometry from the *Spitzer*-Cosmic Evolution (S-COSMOS) database (Sanders et al. 2007), which is a *Spitzer* Legacy survey covering a 2 deg^2 dark portion of the sky. S-COSMOS is complete to more than one magnitude below the 3.6 μm TRGB of our most distant galaxy, allowing a direct comparison of the background galaxies in S-COSMOS to the number of and distribution of sources above the TRGB in each galaxy in our sample. We applied the distance modulus of each galaxy to the S-COSMOS CMD and counted sources with magnitudes brighter than the TRGB and $[3.6] - [4.5]$ colors redder than

0.2. After correcting for the field size, we find that background galaxies may account for anywhere from 21% to 50% of the sources brighter than the 3.6 μm TRGB (Table 4.4).

For targets that lie in the direction towards a large galaxy cluster, the galaxy counts can be significantly larger. LGS 3 and IC 1613 are each located within $30'$ from the center of one galaxy cluster and Leo A and WLM are each located within $30'$ from the centers of two such clusters (see Table 4.5 for a list of galaxy clusters within 1 degree of our targets; Abell 1995; Fernandez et al. 1996). None of these clusters are particularly large or heavily populated, but their presence could potentially double the number of background galaxies above the average population. Moreover, LGS 3 is projected onto the fringes of the Pisces-Pegasus Supercluster of galaxies, which may cause an even larger increase in the background galaxy counts in the LGS 3 images.

In order to measure the background galaxy contamination directly from the data, a large field of view is necessary. A search of the *Spitzer* archive revealed IRAC off-fields for Phoenix, DDO 210, Leo A, and Pegasus dIrr as part of the Large Volume Legacy Survey (Kennicutt et al. 2007), but the depth of these observations is less than 20% the depth of our observations, preventing reliable photometry of sources down to the TRGB.

Figures 4.8 and 4.9 display the spatial distributions of IR sources with (*right*) and without (*left*) optical counterparts. While not completely avoiding the central parts of each galaxy, IR sources without optical counterparts are more numerous on the outskirts, where unresolved background galaxies are expected to begin to dominate the source counts. Despite the small fields of view of the galaxies in our sample, it is clear from Figures 4.8 and 4.9 that background galaxies do, sometimes significantly, contaminate the IR source count. We attempt to measure the contribution from background galaxies in each of our targets using the radial density profiles, a task that would be more robust given a larger field of view but that nonetheless provides interesting results with the available data.

Table 4.5. Nearby background Galaxy Clusters

dIrr Galaxy	Cluster Name	Angular Distance[a]	Angular Cluster Radius	Cluster Population (No. Galaxies)
LGS 3	Zwicky 317	20′	16.2′	64
	Zwicky 337	43′	9′	66
Leo A	Zwicky 2776	15′	7′	90
	Zwicky 2778	22′	13′	107
	Zwicky 2827	40′	16′	123
	Zwicky 2813	50′	7′	76
	Zwicky 2866	58′	6′	77
Pegasus dIrr	Zwicky 8949	60′	8′	57
	Zwicky 8933	60′	58′	352
WLM	CEDAG 12	26′	···	50 – 80
	CEDAG 10405	26′	···	80 – 130
IC 1613	Zwicky 336	25′	13′	114
	CEDAG 461	55′	···	30 – 40

Note. — Galaxy clusters within one degree of our targets are listed here (Abell 1995; Fernandez et al. 1996).

[a] Projected angular distance of the dIrr galaxy from the center of the background galaxy cluster.

Radial density profiles of sources with and without optical counterparts and brighter than the TRGB are shown in Figure 4.10, with the latter population normalized to the former. The profiles were determined by placing ellipsoidal annuli on each galaxy at semi-major axis intervals of $0.5'$. We have assumed that the radial profiles should have similar shapes, and that any deviation is due to a flat contribution from background galaxies. Leo A shows the largest difference between the profiles, as might be expected considering the number of background galaxy clusters in that direction (Table 4.5). DDO 210 shows the flattest overall distribution, which suggests that, for this galaxy, there may be significant contamination in the optical as well as the infrared.

Using a least squares fitting routine, we have fit a combination of a declining profile (the profile for AGB candidates with optical counterparts) plus a flat distribution (background galaxies) to the profile of AGB candidates without optical counterparts. The resulting fits agree with the predictions from S-COSMOS to within 25% for four galaxies (Phoenix, Leo A, Pegasus dIrr, and WLM), 40% for three (LGS 3, DDO 210, and Sextans A), and 78% for IC 1613. The resulting total background contamination for the galaxies in our sample ranges from 25% to 67% of the sources above the TRGB (compared to 21% – 50% from S-COSMOS). For DDO 210, the fit has increased the number of galaxies predicted by S-COSMOS by 37%, resulting in a larger number of background galaxies than there are optical AGB stars. This suggests that either there are no obscured AGB stars in DDO 210, or that DDO 210 is significantly contaminated in the optical, as well as in the infrared.

4.3.5 Stellar Spatial Distributions

The spatial distributions of different stellar types are displayed in Figures 4.11 and 4.12. From left to right, the panels show the optically-identified red giant stars, AGB stars, and blue objects, followed by the IR-identified AGB star candidates, which we define as any object between the TRGB and the AGB limit that is not identified as an RSG or a

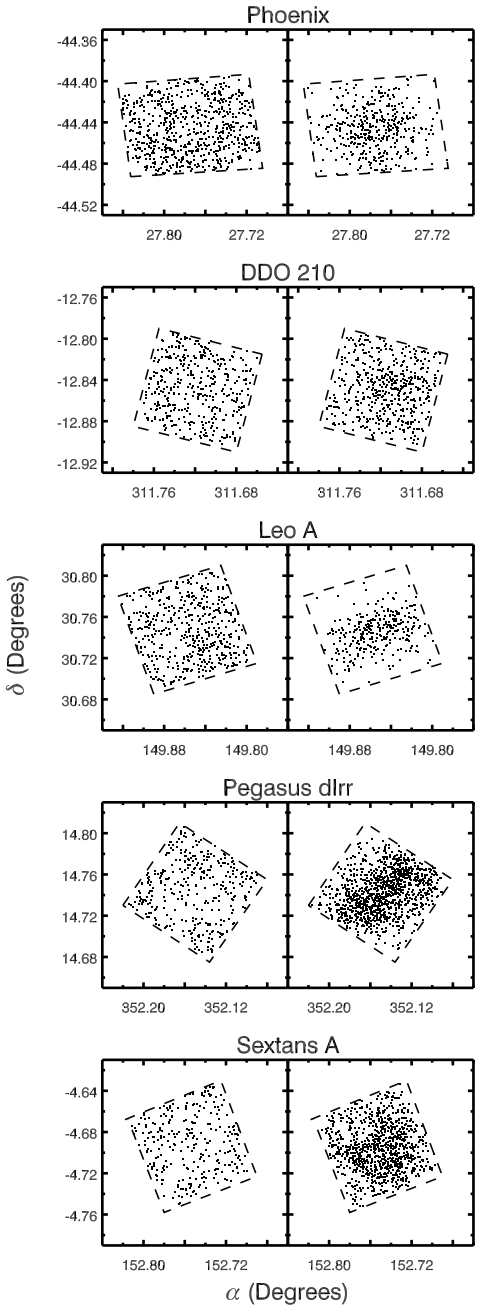

Figure 4.8: Spatial distributions of *all* IR sources without (*left*) and with (*right*) optical counterparts, where a source is considered undetected in the optical if $M_{\rm I} > -2.5$ mag. Sources without optical counterparts are likely either dust-enshrouded AGB stars or background galaxies (and possibly young stellar objects). The sources in the left panels do not cluster towards the centers of the galaxies, suggesting at least some of them are not truely AGB stars.

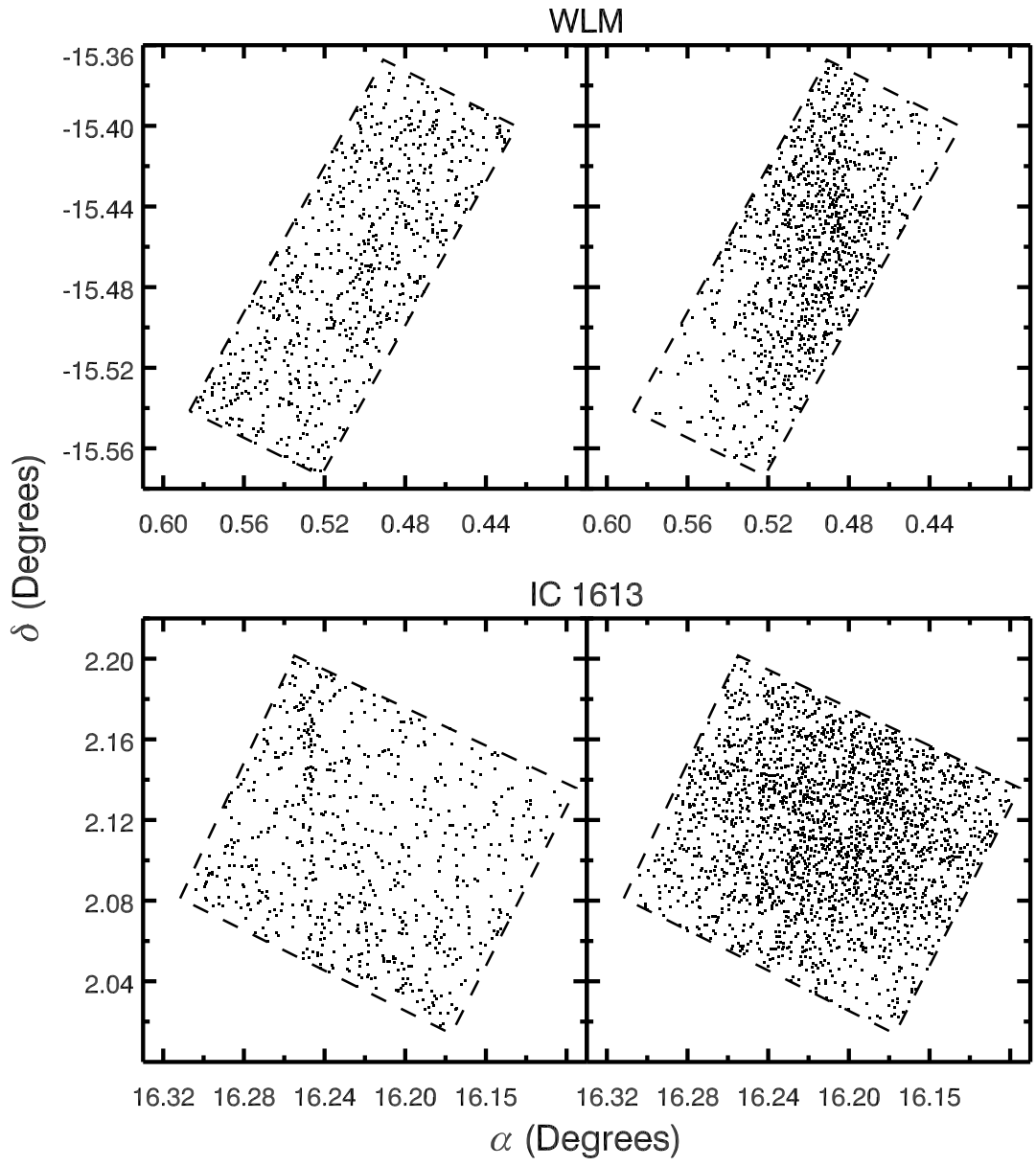

Figure 4.9: Same as Figure 4.8 for WLM and IC 1613.

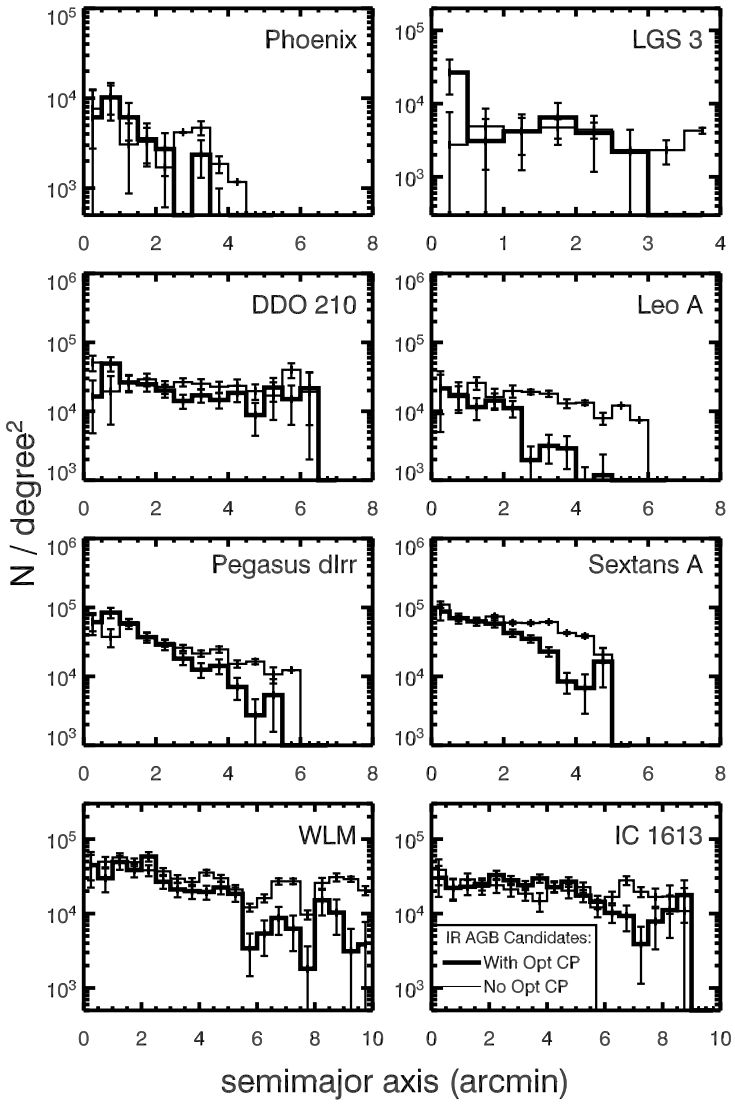

Figure 4.10: Radial density profiles for IR AGB candidates with optical counterparts ("Opt CPs") brighter than (thick line) and fainter than (thin line) the *I*-band TRGB, with the latter normalized to the former. Profiles were determined using ellipsoidal annuli with semi-major axis bins of $0.5'$ centered on each galaxy. If these two populations are obscured and non-obscured AGB stars, the two profiles should be identical. However, it is clear that a flat distribution of background galaxies is contaminating most of our targets. We have fit the declining profile plus a flat distribution to each profile for sources without optical counterparts to measure the background contamination, but the uncertainties in the fits are large and would be much improved by observing larger fields of view.

blue object in the optical (§ 4.4). The analogous figure in paper I for WLM shows the effects of crowding, illustrated by a deficit of fainter red giants in the regions densely populated with blue stars (i.e., the regions containing the youngest stellar populations). Similar crowding is not seen in IC 1613 (Paper II) nor in any of the six other galaxies presented here due to a combination of a lower density of stars and smaller inclination angle (each galaxy, aside from WLM, has $i < 55°$; Mateo 1998, and references therein). It is clear from Figures 4.11 and 4.12 that the IRAC data do not cover the entire areal spans of all six galaxies since the stellar densities are still decreasing at the edges of the coverage.

The few IR AGB candidates detected in Phoenix span a similar area to their optically-identified counterparts. Red giants and blue objects in Pegasus dIrr and DDO 210 trace a line from east to west across the fields of view, but the IR AGB candidates are more smoothly distributed. The brightest IR AGB candidates (red circles) in both galaxies tend to cluster more towards the center. Sextans A shows a mildly clumpy structure with the IR AGB candidates loosely tracing the young blue objects and RGB stars.

For LGS 3, it is difficult to draw connections between the distributions of the different stellar types due to the small optical coverage. However, in LGS 3, the distribution of IR AGB candidates is generally smooth across the entire IRAC field of view, with no increase in the number of sources in the regions of highest stellar density. This distribution supports the claim made in § 4.3.4 that LGS 3 is strongly contaminated by background galaxies. However, even the brightest IR AGB candidates ($m_{3.6} < 16$ mag), marked with red circles in Figure 4.11, span the entire LGS 3 coverage, suggesting that AGB stars have a broader distribution than the Red Giant Branch (RGB) stars. Leo A, which is also potentially strongly contaminated by background galaxy clusters, has a slightly higher density of IR AGB candidates on the west edge of the field, which is offset from the centers of the blue object and optical red giant distributions. None of

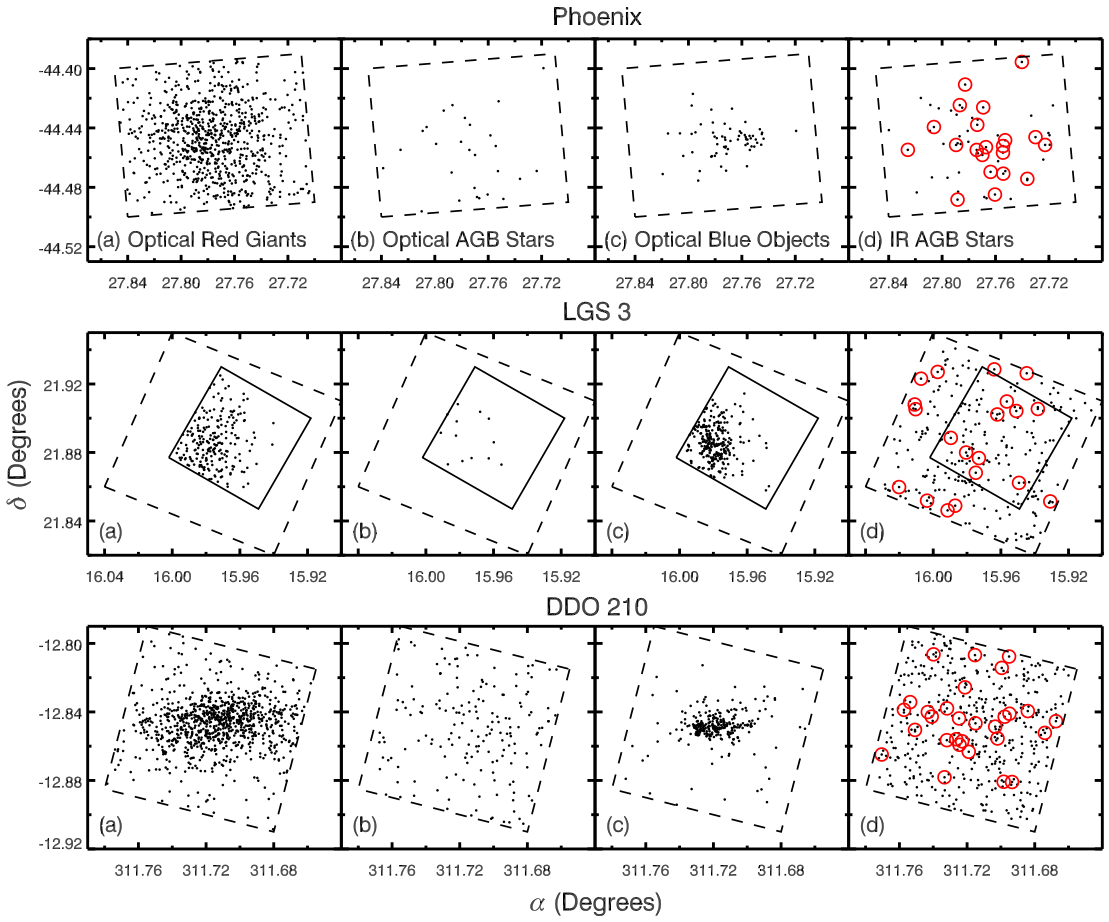

Figure 4.11: Stellar spatial distributions of (a) optical red giants, (b) optical AGB stars, (c) optical blue objects, and (d) IR-identified AGB candidates in Phoenix, LGS 3, and DDO 210. The dashed lines outline the *Spitzer* coverage. The solid box in each LGS 3 panel shows the area covered by optical data. In each panel (d), AGB candidates brighter than $m_{3.6} = 16$ mag are plotted with open red circles in order to show the distribution of AGB stars with little to no contamination from background galaxies.

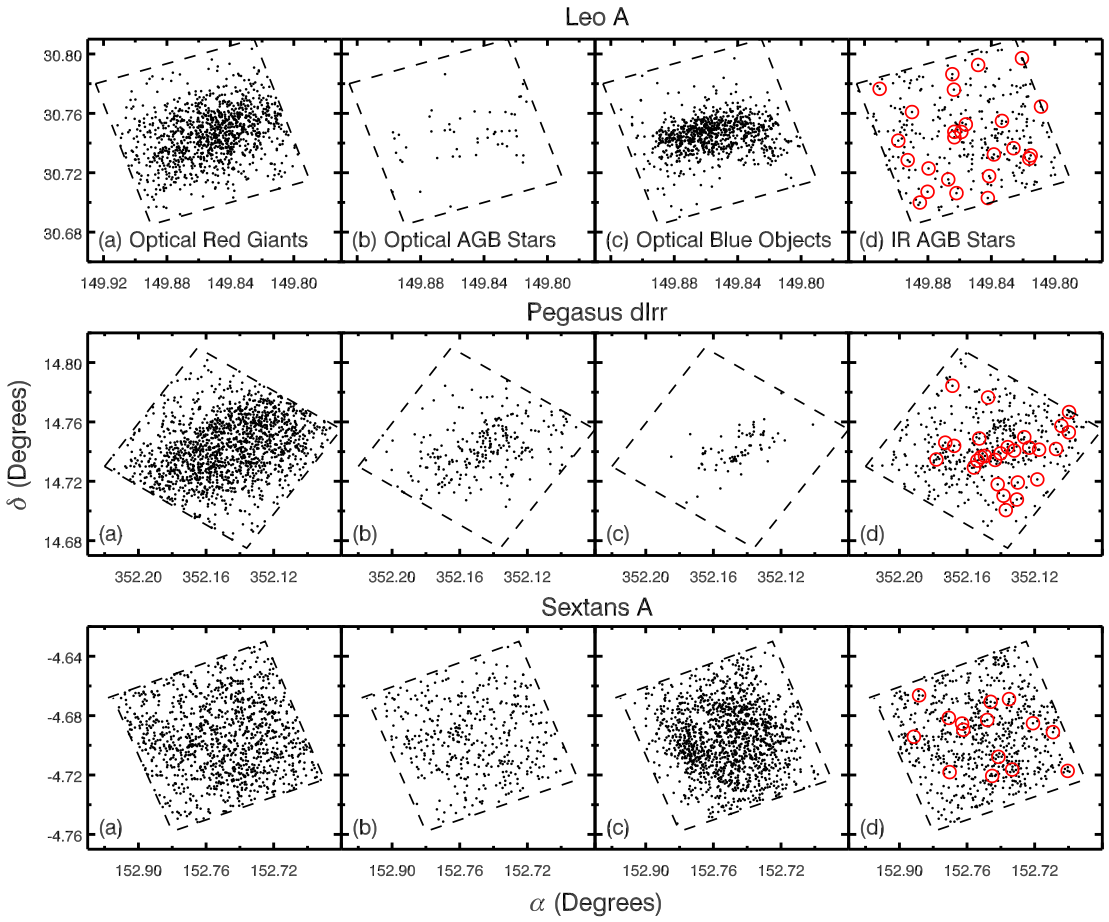

Figure 4.12: Stellar spatial distributions for Leo A, Pegasus dIrr, and Sextans A. The panels are the same as in Figure 4.11.

the known background galaxy clusters (Table 4.5) are located near this overdensity. The brightest AGB candidates in Leo A are more broadly distributed (red circles). In both Leo A and LGS 3, the broad distributions of AGB stars are not likely to be a reflection of the true distributions, but rather the result of low number statistics in these lightly populated galaxies. However, we note a recent study of variable stars in the Fornax dwarf galaxy (Whitelock et al. 2008) that suggests that AGB stars in that galaxy are more broadly distributed than the bulk population.

4.3.6 Luminosity Contribution from Super-TRGB Stars

The total fluxes measured from all point sources detected at both 3.6 and 4.5 μm are listed in Table 4.4. To avoid including bright foreground stars, sources brighter than an apparent magnitudes of $m_{3.6} = 14$ mag are excluded from the total flux unless they are optically identified as an AGB or RSG star or have colors $[3.6] - [4.5] > 0.3$. The 3.6 μm flux values quoted here tend to be higher than the integrated 4.5 μm fluxes presented in Lee et al. (2006) and Jackson et al. (2006), which include only the optical and near-IR extent of each galaxy instead of the entire 3.6 and 4.5 μm IRAC coverage. The flux estimates presented here are, of course, overestimates, as they do not exclude the contribution from background galaxies.

In Table 4.4, we also compare the summed flux of sources one magnitude above the TRGB to that of one magnitude below the TRGB. Choosing to compare the relative fluxes within narrow magnitude intervals directly above and below the TRGB makes this approach less susceptible to the effects of magnitude-dependent completeness and contamination (from galaxies). We find that, in general, this ratio is higher for galaxies with more recent star formation. This correlation confirms that older stellar populations have fewer high-luminosity stars. DDO 210 and Sextans A do not follow the trend, but this is due to incompleteness within one magnitude below the TRGB, since these galaxies are the most distant. LGS 3 is the only other galaxy that does not follow

the trend; this may be due to a combination of photometric incompleteness and low number counting statistics.

4.3.7 Derived Stellar Mass

As discussed in the previous section, the number of super-TRGB stars decreases as a galaxy ages, so that the older the stellar population, the higher the underlying stellar mass represented by each super-TRGB star. Following this premise, the van Loon et al. (2005) prescription for determining the total stellar mass of a galaxy based on the number of stars brighter than the TRGB in the L'-band (3.76 μm) yields stellar masses ranging from $5.5 \times 10^5 - 1.2 \times 10^7 M_\odot$ (Tables 4.6 and 4.7), assuming an age of 2 Gyr for the current super-TRGB population and excluding estimates of the numbers of background galaxies from S-COSMOS and foreground stars from Robin et al. (2003). These masses are uncertain because they are determined using a single age population and because of incomplete sky coverage in some galaxies. If we adjust the age to coincide with past star formation events (see § 4.3), we find a wider range of stellar masses (Tables 4.6 and 4.7). Because of the assumption of a single-aged stellar population, our mass estimates, with the exception of the estimates for Pegasus dIrr and WLM, are somewhat larger than, but are still within reasonable agreement to, those found by Lee et al. (2006) from the mass-to-metallicity relation.

Table 4.6. Detection Statistics of IR-Identified AGB Candidates. Part I.

	Phoenix	LGS 3	DDO 210	Leo A
No. IR AGB candidates[a]	57	102	447	302
No. foreground stars[b]	6	10	32	6
No. background galaxies[c]	20	68	287	180
No. known carbon stars[d]	3	0	7	0
IR AGB Candidates Detected With:				
$M_{\rm I} < -2.5$ mag	68%	···	64%	28%
$M_{\rm I} < I$-band TRGB	44%	12%	40%	21%
Corrected[e]	84%	50%	140%	54%
Stellar Mass Derived from IR AGB Candidates:				
$\log(M^*_{2Gyr})$ $(M_\odot)$[f]	5.74	6.20	6.51	6.36
$\log(M^*_{SFH})$ $(M_\odot)$[g]	5.20 – 5.74	5.75 – 6.20	5.92 – 6.81	5.77 – 5.91
$\log(M_*)$ $(M_\odot)$[h]	5.40	4.56	5.60	5.89

Note. — Numbers in this table are computed only for areas where the IRAC and optical coverage overlaps. Some entries for LGS 3 are left blank due to the difficulty of matching IRAC data with the high-resolution HST data. Stars brighter than the I-band TRGB in LGS 3 were matched to their IR counterparts by eye.

[a] IR-identified AGB candidates are those between the 3.6 μm TRGB and the AGB limit that are not identified as either a blue object or an RSG in the optical (§ 4.4). This quantity includes contamination from background galaxies and foreground stars, also listed in this Table.

[b] Estimated number of foreground stars from Robin et al. (2003).

[c] Estimated number of unresolved background galaxies above the 3.6 μm TRGB found through fitting the radial profiles of AGB candidates (see § 4.3.4). These estimates are within 25% of the estimates measured from S-COSMOS data for Phoenix and Leo A, and 40% for LGS 3 and DDO 210.

[d] Carbon stars listed are those detected in IRAC. The carbon star searches were carried out by: Battinelli & Demers (2000) for DDO 210, and Da Costa (1994) and Menzies et al. (2008) for Phoenix.

[e] IR AGB candidates detected with $M_{\rm I} < I$-band TRGB, with subtraction of foreground stars and unresolved background galaxies from radial profile fitting (see § 4.3.4).

[f] Total stellar mass (M^*_{2Gyr}) was determined following van Loon et al. (2005), assuming an age of 2 Gyr, and using the number of 3.6 μm stars above the TRGB, excluding estimates of the numbers of background galaxies from S-COSMOS and foreground stars from Robin et al. (2003).

[g] Total stellar mass (M^*_{SFH}) was determined following van Loon et al. (2005), assuming a single age range based on past star formation events (Dolphin et al. 2005), and using the number of 3.6 μm stars above the TRGB, excluding estimates of the numbers of background galaxies from S-COSMOS and foreground stars from Robin et al. (2003).

[h] Total stellar mass from Tables 4.1 and 4.2.

Table 4.7. Detection Statistics of IR-Identified AGB Candidates. Part II.

	Pegasus dIrr	Sextans A	WLM[a]	IC 1613[a]
No. IR AGB candidates[b]	422	673	612	956
No. foreground stars[c]	10	10	9	15
No. background galaxies[d]	105	195	161	362
No. known carbon stars[e]	32	0	100	70
IR AGB Candidates Detected With:				
$M_{\rm I} < -2.5$ mag	56%	55%	58%	54%
$M_{\rm I} < I$-band TRGB	52%	54%	46%	49%
Corrected[f]	72%	78%	64%	81%
Stellar Mass Derived from IR AGB Candidates:				
$\log(M^*_{2Gyr})$ $(M_\odot)$[g]	6.64	6.77	6.85	7.07
$\log(M^*_{SFH})$ $(M_\odot)$[h]	6.19 – 6.94	6.17 – 6.20	6.40 – 6.85	6.62 –7.374
$\log(M_*)$ $(M_\odot)$[i]	6.98	6.24	6.88	6.82

Note. — Numbers in this table are computed only for areas where the IRAC and optical coverage overlaps.

[a] Similar quantities are presented for WLM in Paper I and for IC 1613 in Paper II. We present updated values here for these two galaxies using the same analysis procedure used for the six new galaxies in the sample.

[b] IR-identified AGB candidates are those between the 3.6 μm TRGB and the AGB limit that are not identified as either a blue object or an RSG in the optical (§ 4.4). This quantity includes contamination from background galaxies and foreground stars, also listed in this Table.

[c] Estimated number of foreground stars from Robin et al. (2003).

[d] Estimated number of unresolved background galaxies above the 3.6 μm TRGB found through fitting the radial profiles of AGB candidates (see § 4.3.4). These estimates are within 25% of the estimates measured from S-COSMOS data for Pegasus dIrr and WLM, 40% for Sextans A, and 78% for IC 1613.

[e] Carbon stars listed are those detected in IRAC. The carbon star searches were carried out by: Battinelli & Demers (2000) for Pegasus dIrr, Battinelli & Demers (2004) for WLM, and Albert et al. (2000) for IC 1613.

[f] IR AGB candidates detected with $M_{\rm I} < I$-band TRGB, with subtraction of foreground stars and unresolved background galaxies from radial profile fitting (see § 4.3.4).

[g] Total stellar mass (M^*_{2Gyr}) was determined following van Loon et al. (2005), assuming an age of 2 Gyr, and using the number of 3.6 μm stars above the TRGB, excluding estimates of the numbers of background galaxies from S-COSMOS and foreground stars from Robin et al. (2003).

[h] Total stellar mass (M^*_{SFH}) was determined following van Loon et al. (2005), assuming a single age range based on past star formation events (Dolphin et al. 2005), and using the number of 3.6 μm stars above the TRGB, excluding estimates of the numbers of background galaxies from S-COSMOS and foreground stars from Robin et al. (2003).

[i] Total stellar mass from Tables 4.1 and 4.2.

4.4 The AGB Stars

It is important to determine if photometric incompleteness affects our AGB statistics. Photometry in Phoenix, LGS 3, DDO 210, Leo A, and Pegasus dIrr is 50% complete to more than one magnitude fainter than the TRGB for the reddest sources. The location of the Sextans A TRGB is unknown, but assuming it is near $M_{3.6} = -6.1$ mag (dotted line in Fig. 4.6), the Sextans A 50% completeness limit is ≈0.4 mag fainter than the TRGB for the reddest sources. The bluest sources are 50% complete down to $\gtrsim 0.3$ mag less than the TRGB in Phoenix, LGS 3, DDO 210, Leo A, and Pegasus dIrr. Photometry of the bluest sources in Sextans A is not complete down to $M_{3.6} = -6.1$ mag. Therefore, without considering the very small number of objects not detected due to crowding, our data represent a complete census of super-TRGB stars in the central $5.8' \times 5.8'$ regions of the sampled galaxies, with the exception of the bluest super-TRGB stars in Sextans A. Note that because the least massive AGBs are also the least luminous, barely reaching luminosities exceeding the TRGB (McDonald et al. 2008), we have underrepresented AGB stars from the first epoch of star formation.

4.4.1 Optical Completeness

After subtracting background galaxies (from S-COSMOS), we detect 37 – 478 IR AGB candidates in the six galaxies discussed in this paper (Tables 4.6 and 4.7). Using the same criteria for defining an AGB candidate, which are slightly different from the criteria used in papers I and II, IC 1613 and WLM contain 594 and 451 AGB candidates, respectively. Of these candidates, 35% – 100% are detected in the optical, *above the I-band TRGB*. While larger percentages are detected in the optical below the *I*-band TRGB, these sources would have been misidentified in the optical and excluded from AGB star studies, thus we define the optical completeness fraction as the fraction of AGB candidates in the IR that are correctly identified in the optical (Tables 4.6 and 4.7). The equivalent percentages in IC 1613 and WLM are not presented in papers I and II,

but are computed here to be 79% and 63%, respectively.

Figure 4.13 shows the metallicity versus optical completeness fractions after correcting for background contamination, as determined from fitting the IR radial profiles (§ 4.3.4). The error bars reflect the fitting uncertainties, which are largely due to the small fields of view. We have adopted $12 + \log(\mathrm{O/H})$ values from van Zee et al. (2006), and used the luminosity-metallicity (L-Z) relationship from Lee et al. (2006) to estimate $12 + \log(\mathrm{O/H})$ for Phoenix, DDO 210, and LGS 3, all of which have no H II regions. No trend with metallicity is apparent in Figure 4.13, and it is clear that an optical completeness fraction of roughly 60% –70% is consistent within the errors in all eight galaxies. The AGB in optical surveys is therefore underrepresented by ≈35%, which may have important consequences for SFHs derived from isochrone fitting to optical CMDs.

In Figure 4.14, we show the fraction of optical completeness (as defined in this paper) as a function of $[3.6]-[4.5]$ color. The optical extinction (A_V) is shown in the lower right panel. The optical completeness declines as a function of color, approaching 0% for the reddest sources, as expected if the incompleteness is due to circumstellar extinction. For DDO 210, Pegasus dIrr, Sextans A, WLM, and IC 1613, the completeness fraction approaches zero roughly between $0.5 < [3.6] - [4.5] < 1.0$. In Phoenix, LGS 3, and Leo A, the completeness approaches 0% at bluer colors ($[3.6] - [4.5] \approx 0.25$), which is due to the small populations of very dusty AGB stars and to strong background galaxy contamination in these galaxies. Background galaxies are particularly red objects and thus drop out of the optical at fairly blue colors compared to dusty AGB stars.

As discussed in § 4.3.4, the IR AGB candidate populations are heavily contaminated by background galaxies, and the same trend of decreasing optical completeness with IR color is also consistent with this contamination. Based on fits to the stellar radial profiles, Pegasus dIrr, Sextans A, and WLM have the smallest percentage background galaxy contamination in the IR AGB candidate population. It is interesting to note that

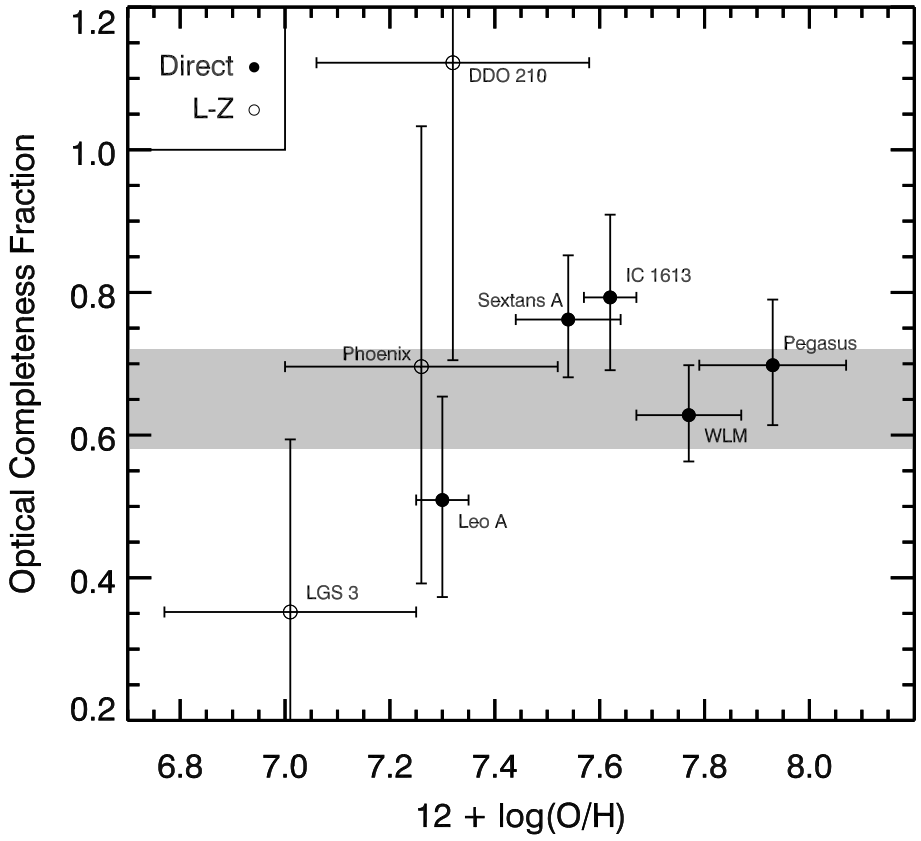

Figure 4.13: Optical completeness fraction vs. metallicity. Closed circles are galaxies with metallicities from van Zee et al. (2006), and open circles show galaxies whose metallicities were determined using the *L-Z* relationship from Lee et al. (2006). The optical completeness fraction is computed by first estimating the true background galaxy contamination by fitting a flat contribution to the radial density profile of IR AGB candidates (Fig. 4.10). The errors include the $1\,\sigma$ uncertainties in the fit, Poisson statistics, and foreground star contamination. We find no convincing correlation between optical completeness and metallicity, indicating that dust production is not inhibited at low metallicity. An optical completeness fraction of approximately 60% to 70% is consistent with all eight galaxies (shaded region).

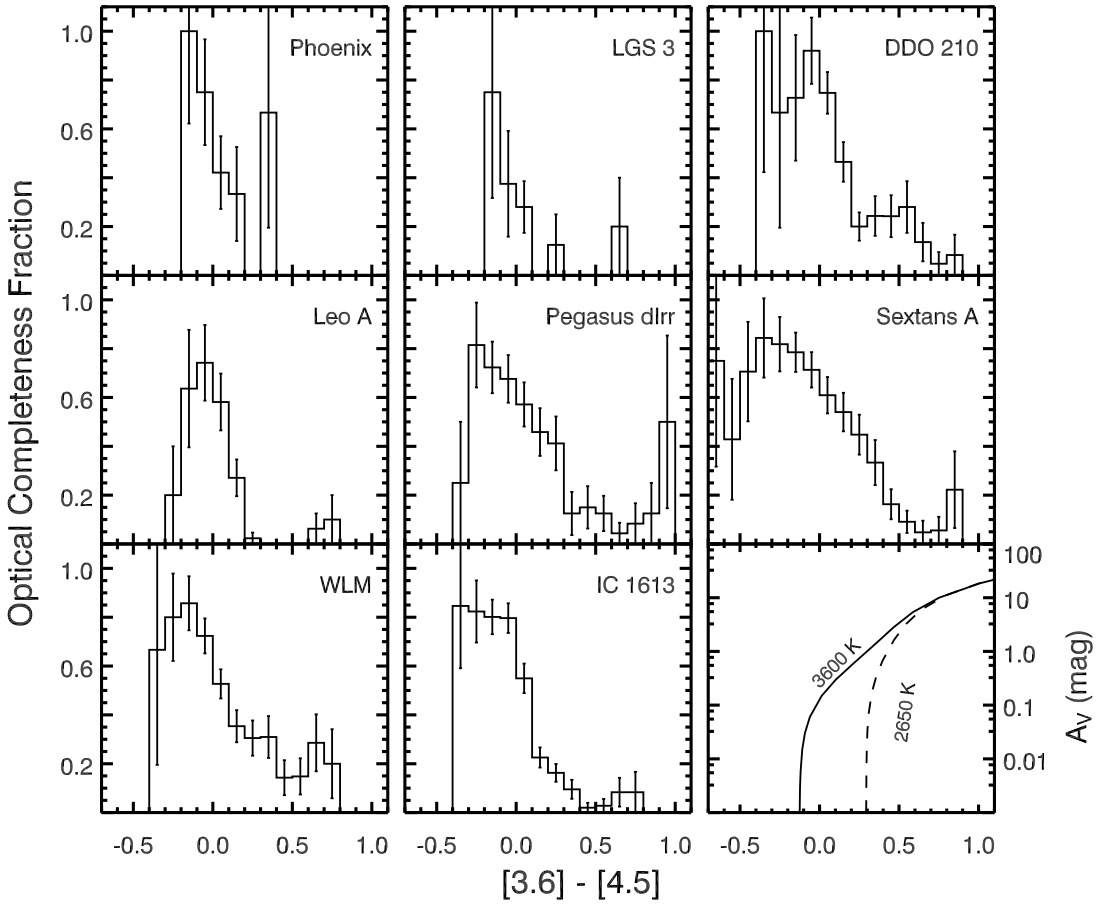

Figure 4.14: Fraction of stars detected in the optical as a function of $[3.6]-[4.5]$. The optical completeness fraction includes only stars detected above the 3.6 μm TRGB *and* the *I*-band TRGB. The errors bars were determined by taking the square root of the number of optically detected AGB stars and dividing by the total number of IR-identified AGB candidates and therefore only represent the degree to which small-number statistics might affect the trend. The lower right panel shows the visual extinction as a function of $[3.6]-[4.5]$ for a dust composition of 85% AMC and 15% SiC and effective temperatures of 3600 K (solid line) and 2650 K (dashed line). In all eight galaxies, the optical completeness decreases as a function of optical depth, as expected, reaching zero near $[3.6]-[4.5] \approx 0.5$ in most cases. In all galaxies but Sextans A and WLM, there is a secondary dip in completeness near a color of 0.2, which may be due to the presense of background galaxies and indicates that, in these galaxies, there are very few AGB stars redward of this drop-off.

two of these three low-contamination galaxies are the only two galaxies in our sample that do not show a sudden drop in completeness near $0.1 < [3.6]-[4.5] < 0.2$, and in the case of Pegasus dIrr, the drop occurs at an intermediate color ($[3.6]-[4.5] \approx 0.3$). This may suggest that at the $[3.6]-[4.5] = 0.1-0.2$ color transition, background galaxies become the dominate source type. In galaxies that show a drop in completeness beyond this color transition, there may be few, if any, *very red* AGB stars.

Figure 4.15 shows the fraction of IR AGB candidates *with* optical counterparts (i.e., *not* background galaxies) that have $[3.6]-[4.5] > 0.2$. The trend in Figure 4.15 suggests a scarcity of very red AGB stars in some galaxies in our sample. With the exception of DDO 210, there is a clear correlation between metallicity and the fraction of red stars, as expected if dust is produced more efficiently in environments that are rich in metals.

An alternate interpretation of Figure 4.15 is that stellar populations older than $\approx$ 3.0 Gyr are unable to produce many stars with $[3.6]-[4.5] > 0.2$, regardless of metallicity (Marigo et al. 2008). The galaxies with the smallest fraction of their current stellar population formed within the last 3 Gyr (Orban et al. 2008) are indeed the galaxies with the fewest very red stars, with the exception of DDO 210.

It is generally assumed that lower metallicity systems will be less dusty than their higher-metallicity counterparts, resulting in a smaller population of dust-enshrouded AGB stars. This is indeed what we see in Figure 4.15. This should lead to a trend of decreasing optical completeness with increasing metallicity. Nevertheless, we see no convincing correlation between optical completeness and metallicity in Figure 4.13, suggesting that even environments with very low metallicity ($Z < 2\%\ Z_{\odot}$, assuming $Z_{\odot} = 0.0122$; Asplund et al. 2004) are capable of forming at least a few heavily enshrouded stars. This is the case even if the majority of the stars in these galaxies harbor little to no dust at all, either due to low metallicity or to an older stellar population.

This result supports an increasing number of observations suggesting that dust formation is not prohibited at low metallicity (Cannon et al. 2002; Boyer et al. 2006;

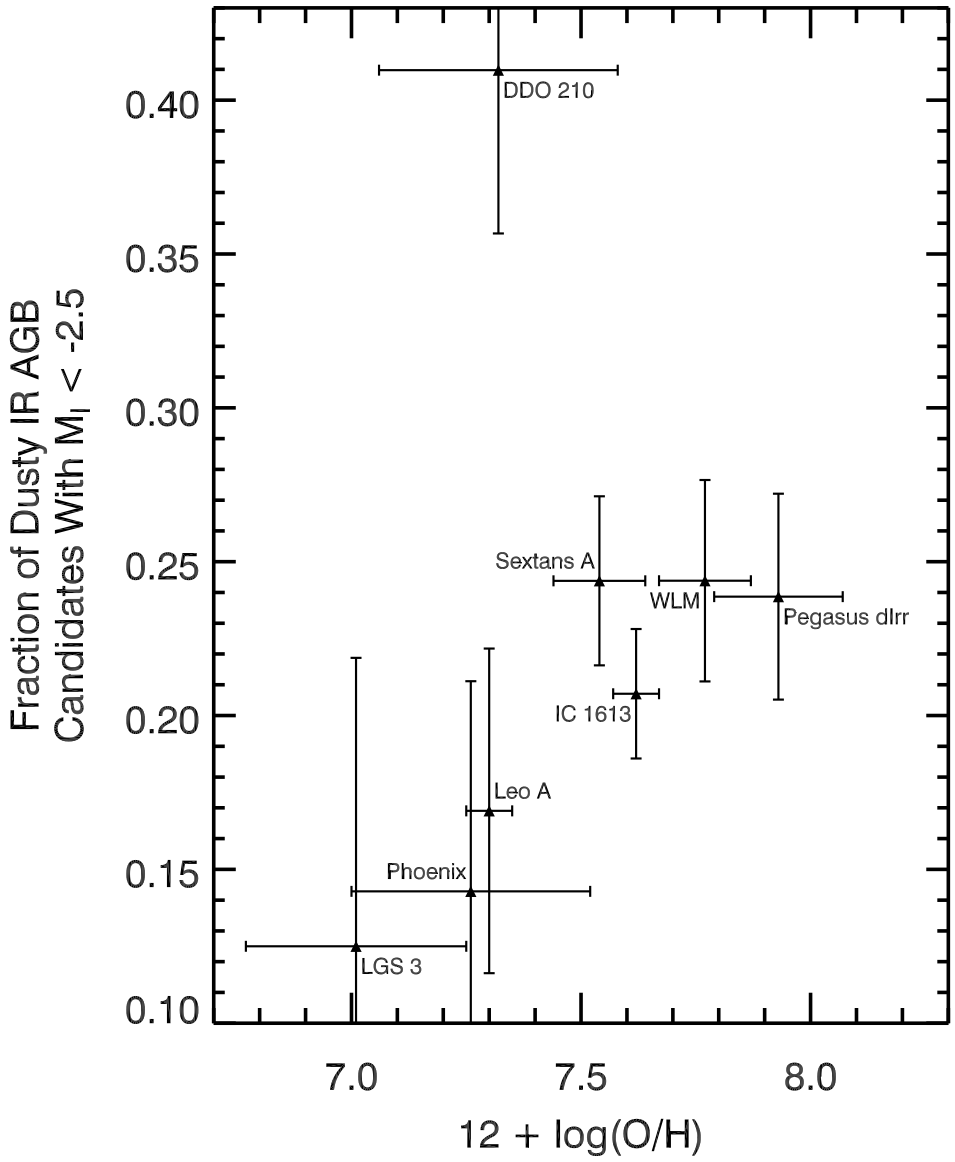

Figure 4.15: Fraction of red stars in each galaxy. The fraction includes only IR AGB candidates that are detected in the optical with $M_{\rm I} < -2.5$ mag, and therefore does not include the most extreme dusty stars. A source is considered "red" if $[3.6]-[4.5] > 0.2$. With the exception of DDO 210, we see a clear trend for higher metallicity galaxies to have a higher fraction of moderately red stars. This trend may be due to metallicity, but may also be due to the age of the populations.

Gruendl et al. 2008; Sloan et al. 2008; Lagadec & Zijlstra 2008), although it is forming in smaller quantities (Boyer et al. 2006; McDonald & van Loon 2007; van Loon et al. 2008). It may be that the ability to form dust has little or no dependence on the initial metal-content, rather, nucleosynthesis in the stars themselves and dredge-up in radial-pulsing AGB stars is the dominant source of dust-forming metals in the circumstellar envelope. However, we must emphasize that we do not have metallicity measurements for any individual stars in our sample, and it is therefore possible that the reddest (i.e., dustiest) stars have higher metallicities than the bulk population.

4.4.2 The Carbon Stars

In addition to the carbon stars in WLM and IC 1613 (Papers I and II), populations of carbon stars are known in three of the galaxies studied here: DDO 210, Phoenix, and Pegasus dIrr. The remaining three galaxies may also contain carbon stars, but to our knowledge no searches have yet been carried out. Given the rough estimates of the C/M ratios below, we might expect at least a handful of carbon stars in LGS 3, Leo A, and Sextans A. Although, since carbon stars require a mass larger than 1 $M_{\odot}$ to form, we might expect few, if any, carbon stars in metal-poor, low star forming galaxies like LGS 3.

Phoenix:

Phoenix appears to have a very small population of three carbon stars (Da Costa 1994; Menzies et al. 2008). These three stars were identified through spectroscopic measurements. The brightest carbon star (Fig. 4.16) is a Mira variable with a period of 425 days (Menzies et al. 2008). All three carbon stars in Phoenix have relatively blue $[3.6] - [4.5]$ colors, which may be due to the low metallicity of the galaxy causing a low optical depth in the circumstellar envelope. If all three stars belong to Phoenix, and the remaining 28 IR-identified AGB candidates identified in this work are M-stars,

then the C/M ratio for Phoenix is a mere 0.11.

DDO 210:

Using the CN/TiO technique with narrowband optical photometry, Battinelli & Demers (2000) found 3 carbon stars in DDO 210, two of which are located within the *Spitzer* coverage and are detected in IRAC. With broadband near-IR photometry, Gullieuszik et al. (2007) found an additional 6 carbon stars, 4 of which are located within our *Spitzer* coverage and are detected in IRAC. The two Gullieuszik et al. (2007) stars with the reddest $[3.6]-[4.5]$ colors in Figure 4.16 appear to be Long Period Variables, typical of mass-losing carbon stars. One other carbon star is quite red, while the remaining three have relatively blue colors, similar to the carbon stars in Phoenix.

Battinelli & Demers (2000) also find 158 M-stars in an $8.2' \times 8.2'$ field. By measuring the density of M-stars on the outskirts of their CCD image, Battinelli & Demers (2000) claim that all 158 M-stars are in the foreground, however a later estimate of the C/M ratio in Battinelli & Demers (2005) using modified a distance and reddening computes a C/M ratio of 0.09 ± 0.08. Assuming an even distribution of all 158 M-stars, we expect 79 of these stars to fall within our IRAC coverage. In § 4.2.4, we found that only 32 foreground stars are expected in the area covered by our IRAC images. If Battinelli & Demers (2000) overestimated the number of foreground M-stars, we are left with 47 M-stars and 6 carbon stars covered in our IRAC images, yielding a C/M ratio of 0.13. If all of the IR-identified AGB candidates (minus background and foreground contamination) reported here (Table 4.4) are truly AGB stars belonging to DDO 210, then only 26% of the total IR AGB star population is used to compute this ratio, and it should not be over-interpreted.

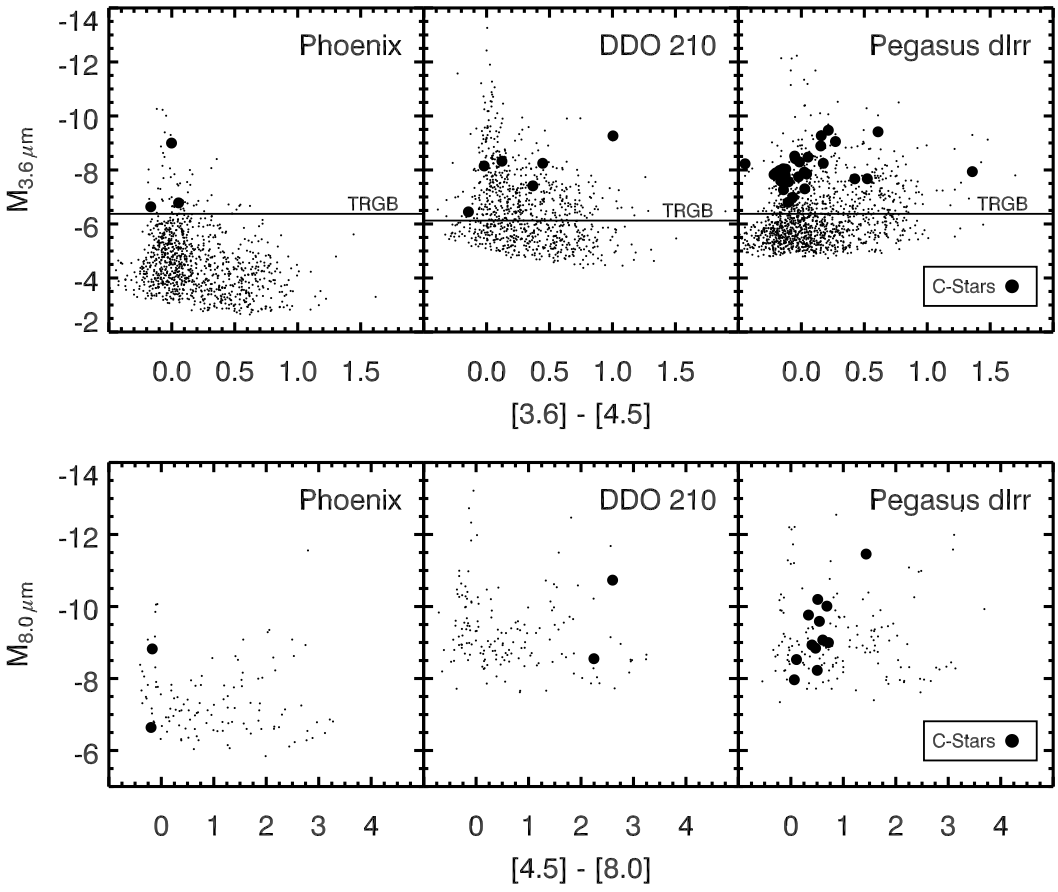

Figure 4.16: Carbon stars on the [3.6] vs. [3.6] − [4.5] and [8.0] vs. [4.5] − [8.0] color magnitude diagrams. The small black dots mark all of the IRAC detections, and the large black circles mark carbon stars identified in Phoenix (Da Costa 1994; Menzies et al. 2008), DDO 210 (Battinelli & Demers 2000), and Pegasus dIrr (Battinelli & Demers 2000). The carbon stars with [3.6] − [4.5] > 0.2 are likely losing significant mass.

Pegasus dIrr:

The population of carbon stars in Pegasus dIrr is comparable to the populations found in IC 1613 and WLM. With optical narrowband observations, Battinelli & Demers (2000) find 40 carbon stars in Pegasus dIrr, 35 of which fall inside our IRAC coverage, and 32 of which are detected here (three are undetected due to crowding). The bulk of the carbon stars have relatively blue $[3.6]-[4.5]$ colors (Fig. 4.16); four are very red, and five are very bright at 3.6 μm. Pegasus dIrr has the highest metallicity of the galaxies in our sample ($12+\log(\mathrm{O/H}) = 7.93$), so it seems less likely that the colors are blue entirely because of a low optical depth, as may be the case for Phoenix and DDO 210. Comparison to Figure 4.4 shows that the brightest carbon stars in Pegasus dIrr match the 560 Myr population better than the older and younger isochrones, which agrees with the burst of star formation that occured just short of 1 Gyr ago (Dolphin et al. 2005).

Assuming a color excess of E(B–V) = 0.03, the C/M ratio quoted by Battinelli & Demers (2000) is 0.73, using a total of 175 AGB stars in an area roughly twice the size of our IRAC coverage. However, based on the numbers of C-stars and M-stars quoted in Table 6 of Battinelli & Demers (2000), we cannot reproduce the C/M ratio and suspect a typographical error; with their numbers, we recalculate C/M = 0.50.[3] A later modification of the distance and reddening towards Pegasus dIrr adjusts the C/M ratio to 0.62 ± 0.22 (Battinelli & Demers 2005). According to the population synthesis models of Robin et al. (2003) (see § 4.2.4), Battinelli & Demers (2000) overestimated the contamination of M-stars in the foreground by a factor of ≈2.8. Therefore, assuming the population synthesis model is correct and that the distribution of M-stars is flat, yielding 58 M-stars in the IRAC coverage, we recompute the C/M ratio to be 0.60, well within agreement to the most recent C/M ratio calculated by Battinelli & Demers

[3]Private communication with S. Demers has confirmed this recalculation.

(2005). This ratio is computed with a total of 93 AGB stars, which is only 34% of the IR AGB candidates reported here.

4.4.3 Mass-Loss Rates

As in papers I and II, we have estimated the MLRs of the AGB candidates in each galaxy by comparing the IR fluxes to the radiative transfer models of Groenewegen (2006). We linearly interpolated the $[3.6]-[4.5]$ colors onto the Groenewegen (2006) models to estimate the optical depth (τ), which corresponds to a particular IR color given assumptions about the wind composition and stellar effective temperature ($T_{\rm eff}$). The resulting MLRs were then scaled according to van Loon (2006), where $\dot{M} \propto \tau\psi^{-(1/2)}L^{(3/4)}$, ψ is the dust-to-gas ratio, and L is the stellar luminosity. The dust-to-gas ratio scales as $\psi = \psi_{\odot}10^{[Fe/H]}$ and $\psi_{\odot} = 0.005$ (van Loon et al. 2005). See Table 4.8 for the average stellar MLRs and Tables 4.9 and 4.10 for integrated galaxy MLRs.

The integrated and average MLRs computed using the entire population of IR AGB candidates are most certainly overestimates, as 21% – 67% of these populations are background galaxies. For this reason, we have also computed the integrated and average MLRs for only sources that have optical counterparts with $M_{\rm I} < -2.5$ mag. This approach excludes any AGB stars that are obscured in the optical, and thus excludes the stars with the most dust and highest MLRs. To regain some of these interesting sources, we have also computed the integrated MLRs for all sources that either have optical counterparts *or* are brighter than $m_{3.6} = 16$ mag, the approximate cut-off between unresolved background galaxies and AGB stars. These totals are listed in Tables 4.9 and 4.10. We have also computed the integrated MLR by subtracting the contribution from the number of galaxies predicted in the S-COSMOS data, assuming each source has the average MLR. This approach inserts more uncertainty into the resulting integrated MLR since background galaxies can artificially inflate or deflate the average, depending on their (incorrectly-assigned) absolute magnitudes.

Table 4.8. Average Stellar Mass-Loss Rates

All IR Sources With $M_{3.6} <$ TRGB (10^{-6} $M_{\odot}$ yr^{-1})					
Galaxy	C-rich 1[a]	C-rich 2[b]	O-rich 1[c]	O-rich 2[d]	O-rich 3[e]
Phoenix	0.53	0.31	1.4	1.2	1.1
LGS 3	2.21	1.4	5.4	4.6	4.6
DDO 210	2.7	1.4	5.8	4.9	4.6
Leo A	1.6	1.2	4.0	3.4	3.7
Pegasus dIrr	2.1	0.88	4.4	3.9	2.6
Sextans A	2.4	1.2	5.4	4.5	3.6
WLM	3.5	1.1	6.6	5.7	3.5
IC 1613	1.1	0.47	2.1	1.8	1.5

Note. — The mass-loss rates quoted here include only sources located between the 3.6 μm TRGB and the AGB limit that are not optically identified as a blue object or RSG. Due to color limits in the Groenewegen (2006) models, C-rich 2 and O-rich 1 include the most sources, while C-rich 1 includes the fewest.

[a] C-rich AGB star, $T_{\rm eff} = 2650$ K, dust composition is 85% amorphous carbon, 15% SiC.

[b] C-rich AGB star, $T_{\rm eff} = 3600$ K, dust composition is 85% amorphous carbon, 15% SiC.

[c] O-rich AGB star, $T_{\rm eff} = 2500$ K, dust composition is 60% silicates, 40% aluminum oxides.

[d] O-rich AGB star, $T_{\rm eff} = 2500$ K, dust composition is 100% silicates.

[e] O-rich AGB star, $T_{\rm eff} = 3300$ K, dust composition is 60% silicates, 40% aluminum oxides.

Table 4.9. Integrated Galaxy Mass-Loss Rates. Part I.

All AGB Candidates ($M_{3.6}$ < TRGB; 10^{-4} $M_\odot$ yr^{-1})					
Galaxy	C-rich 1[a]	C-rich 2[a]	O-rich 1[a]	O-rich 2[a]	O-rich 3[a]
Phoenix	0.05	0.18	0.29	0.25	0.65
LGS 3	2.4	3.7	9.5	7.9	12
DDO 210	39	39	75	94	76
Leo A	2.0	3.3	8.6	7.3	11
Pegasus dIrr	4.1	4.7	12	12	13
Sextans A	5.0	6.9	19	16	23
WLM	7.8	9.2	25	23	28
IC 1613	2.4	4.2	10	8.8	14
All AGB Candidates With $M_{\rm I} < -2.5$ (10^{-4} $M_\odot$ yr^{-1})					
Phoenix	0.03	0.11	0.15	0.13	0.20
LGS 3	...	...	...	...	...
DDO 210	1.1	2.3	5.0	4.3	8.0
Leo A	0.57	0.82	2.0	1.6	2.6
Pegasus dIrr	3.3	3.7	9.3	9.2	10
Sextans A	1.6	2.8	6.9	5.7	9.5
WLM	2.2	2.8	8.0	6.9	9.5
IC 1613	0.67	1.6	3.4	2.9	5.7

Note. — The mass-loss rates quoted here include only stars located between the 3.6 μm TRGB and the AGB limit that are not optically identified as a blue object or RSG.Due to color limits in the Groenewegen (2006) models, C-rich 2 and O-rich 1 include the most sources, while C-rich 1 includes the fewest.

[a] See Table 4.8 for descriptions of these labels.

Table 4.10. Integrated Galaxy Mass-Loss Rates. Part II.

Galaxy	C-rich 1[a]	C-rich 2[a]	O-rich 1[a]	O-rich 2[a]	O-rich 3[a]
All AGB Candidates With $M_{\rm I} < -2.5$ Or With $m_{3.6} < 16$ (10^{-4} $M_\odot$ yr^{-1})					
Phoenix	0.03	0.12	0.15	0.13	0.44
LGS 3	...	...	...	...	...
DDO 210	1.5	2.7	6.1	5.2	9.2
Leo A	0.94	1.5	3.7	3.1	4.8
Pegasus dIrr	3.3	3.8	9.4	9.4	10
Sextans A	1.6	2.8	7.1	5.9	9.8
WLM	3.4	4.2	12	10	14
IC 1613	1.2	2.3	5.3	4.5	8.0
All AGB Candidates Minus the No. Galaxies Times the Average Stellar MLR (10^{-4} $M_\odot$ yr^{-1})[b]					
Phoenix	0.0	0.11	0.04	0.03	0.42
LGS 3	0.11	1.4	0.84	0.71	4.7
DDO 210	0.25	3.2	4.0	3.4	11
Leo A	0.38	1.5	2.5	2.1	5.1
Pegasus dIrr	0.38	1.8	2.1	1.8	5.9
Sextans A	0.0	2.5	0.13	0.11	9.2
WLM	1.2	4.3	6.6	5.7	15
IC 1613	0.64	2.8	4.8	4.0	9.6

Note. — The mass-loss rates quoted here include only stars located between the 3.6 μm TRGB and the AGB limit that are not optically identified as a blue object or RSG.Due to color limits in the Groenewegen (2006) models, C-rich 2 and O-rich 1 include the most sources, while C-rich 1 includes the fewest.

[a] See Table 4.8 for descriptions of these labels.

[b] The number of galaxies here were estimated from S-COSMOS data.

The stellar MLR versus bolometric magnitude for each galaxy is shown in Figure 4.17, assuming a dust composition of 85% AMC + 15% SiC and $T_{\rm eff} = 3600$ K. We have included in this figure only sources that fall between the 3.6 μm TRGB and the AGB limit and are not identified in the optical as an RSG or a blue object. Sources below the background galaxy cut-off at $m_{3.6} = 16$ mag that do not have optical counterparts are plotted in small yellow points (except for LGS 3, which is not matched to the optical data); these points represent the population that is likely dominated by background galaxies. Carbon stars are plotted in filled blue circles. We find that the most heavily mass-losing stars are among the most luminous AGB candidates. The maximum MLRs in all eight galaxies are in good agreement with that found in the LMC (van Loon et al. 1999), which is somewhat higher than the classical single-scattering MLR limit predicted by Jura (1984), above which a dusty circumstellar envelope results in multiple scattering of photons (Gail & Sedlmayr 1986). The sources that lie above the single-scattering limit are indeed those with the largest optical depths, as determined from their $[3.6] - [4.5]$ colors.

While the vast majority of the AGB candidates have moderate MLRs ($< 10^{-6} M_{\odot}$ yr^{-1}), there are a handful of sources in each galaxy, with the exception of Phoenix, that are near or above the classical single-scattering limit (short-dashed line in Figure 4.17; Jura 1984). The brightest of these have the strongest MLRs and dominate each galaxy's integrated MLR. A few of these heavily mass-losing sources are also undetected in the optical (yellow points) and may prove to be background galaxies. However, in Leo A, Sextans A, WLM, and IC 1613, many of these optically obscured, heavily mass-losing sources (1, 2, 4, and 5 sources, respectively) are brighter than the background galaxy cut-off ($m_{3.6} < 16$ mag), and are likely true obscured AGB stars.

The majority of the AGB candidates are in the superwind phase (van Loon et al. 2005; Girardi & Marigo 2007), i.e., the MLRs exceed the nuclear-burning mass consumption rate ($\dot{M}_{\rm nuc}$; long-dashed line in Fig. 4.17). Mass loss is the dominant evolutionary

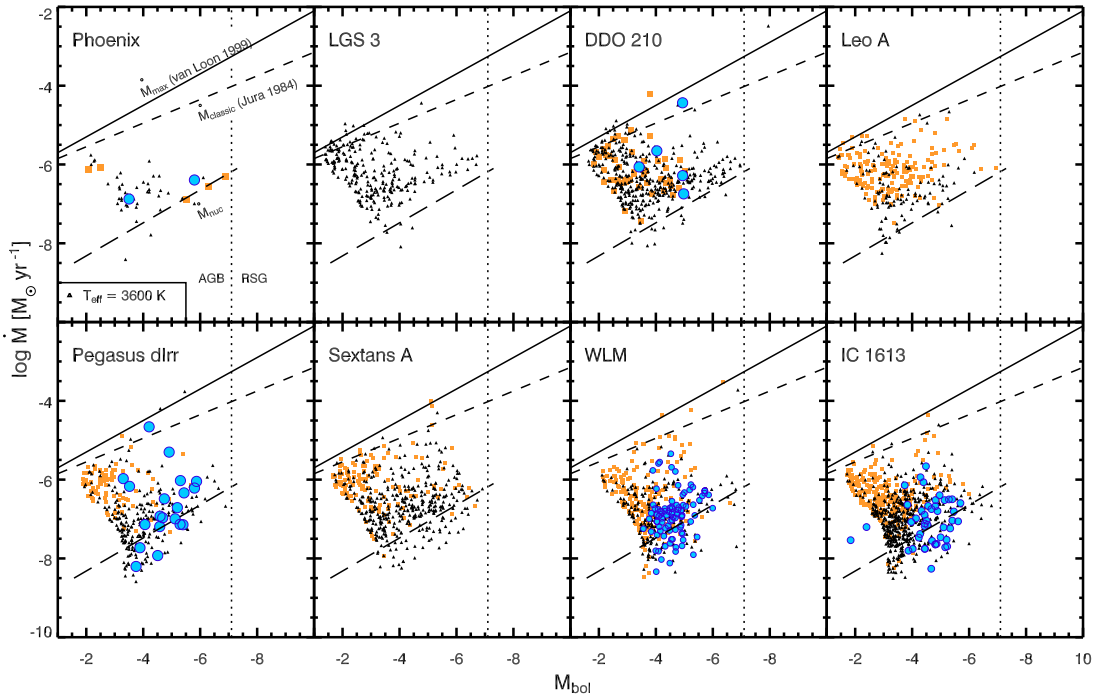

Figure 4.17: Mass-loss rates vs. bolometric magnitudes for all objects brighter than the 3.6 μm TRGB, fainter than the AGB limit, and *not* optically identified as an RSG or a blue object. Yellow squares are sources with $M_{\rm I} > -2.5$ mag and $m_{3.6} > 16$ mag and are heavily contaminated with background galaxies. Large blue circles are carbon stars. There are no yellow squares in LGS 3 due to the difficulty in matching IRAC sources to ACS sources. Mass-loss rates were derived using the Groenewegen (2006) models (§ 4.4.3), assuming a wind composition of 85% AMC and 15% SiC and an effective temperature of $T_{\rm eff} = 3600$ K. The short-dashed line marks the classical single-scattering limit from Jura (1984) ($\dot{M}_{\rm classic}$) and the solid line marks the maximum mass-loss rates ($\dot{M}_{\rm max}$) observed in the Large Magellanic Cloud (van Loon et al. 1999). The lower, long-dashed line marks the nuclear-burning mass cunsumption rate ($\dot{M}_{\rm nuc}$) and the vertical, dotted line marks the AGB limit at $M_{\rm bol} = -7.1$ mag. Several stars in each galaxy, save Phoenix, are above the single-scattering limit and have large optical depths.

driver for these stars since they will expel their outer layers before exhausting their nuclear fuel.

The timescale of the AGB superwind phase is short ($\sim 10^6$ yr; van Loon et al. 2005; Girardi & Marigo 2007). If we assume that each galaxy hosts a broad range of AGB star masses, then we may also assume that each AGB star loses an average total of 1.5 $M_{\odot}$. Using the mean individual MLRs listed in Table 4.8 (averaged over all five combinations of dust composition and effective temperature), the superwind timescale we derive ranges from $4 \times 10^5 - 2 \times 10^6$ yr, which agrees well with previous estimates. A consequence of this short timescale is that the integrated MLR of low-mass galaxies may be highly time-variable, as is the case for star clusters (van Loon et al. 2008; McDonald et al. 2008), and must not be over-interpreted. Within a few million years, a mere handful of new, strongly mass-losing AGB stars may appear in some galaxies, but not in others, causing a strong increase in the integrated MLR of the former. Therefore, we do not claim that the integrated MLRs quoted here are representative of any particular galaxy trait.

Uncertainties in the Mass-Loss Rates:

As emphasized in papers I & II, there are major uncertainties in deriving MLRs for AGB stars using only 3.6 and 4.5 μm photometry. The first is a degeneracy between τ and $T_{\rm eff}$: cool stars with small MLRs can have the same $[3.6]-[4.5]$ color as warmer stars with strong MLRs. This uncertainty most strongly affects the bluest AGB candidates($[3.6]-[4.5] < 0.5$), but is of little consequence for the redder AGB candidates, where the MLR is much less sensitive to $T_{\rm eff}$. This uncertainty may also be exacerbated by atmospheric molecular absorption, which can affect IRAC colors, although these effects have not yet been quantified (Marengo et al. 2007). Since the reddest AGB stars also have the strongest MLRs, the integrated MLR for each galaxy and the individual MLRs for the red stars is robust.

The second major uncertainty lies with the choice of the chemical composition of the AGB winds. With no information about the wind compositions, we must make the unlikely assumption of a single composition for the entire AGB population. The integrated MLRs computed for different wind compositions vary by up to a factor of eight.

While these uncertainties affect the MLRs of individual sources, the integrated MLR is heavily affected by the unfortunate placement of background galaxies in the same region of the CMD as the mass-losing AGB stars, as discussed above. While we have attempted to remove this contamination, we must still emphasize that the integrated MLRs reported here are meant as first-order estimates only.

ISM Gas Return:

While massive stars occasionally provide bursts of feedback to the ISM when they explode as supernovae, it is the more numerous, mass-losing stars that dominate long-term gas return. Gas return from massive stars occurs only during and shortly after a burst of star formation, whereas AGB gas return is continuous over time and allows galaxies to gradually rebuild an ISM while remaining in quiescensce with regard to star formation. A comparison between the the returned mass and the mass used to form stars ($f_{\rm return} = \dot{M}_{\rm dusty}/{\rm SFR}_{(1\,{\rm Gyr})}$), computed using current integrated MLRs (bottom panel of Tables 4.9 and 4.10) and the average SFRs over the last 1 Gyr (Orban et al. 2008), shows that each galaxy in our sample has been undergoing a SFR that is unsustainable, with the exception of LGS 3 and DDO 210. Without another source of gas to the ISM or a change in star formation rate, these galaxies will exhaust their supply of interstellar gas (see Table 4.11). We note that the SFRs and MLRs used here are are estimates, however, we assume that they are accurate to within an order of magnitude.

Table 4.11: ISM Gas Return

Galaxy	$\dot{M}_{\rm dusty}$[a] ($M_\odot$ yr^{-1})	SFR$_{(1\,\rm Gyr)}$[b] ($M_\odot$ yr^{-1})	SFR$_{(5\,\rm Gyr)}$[b] ($M_\odot$ yr^{-1})	$f_{\rm return}$[c]	$\tau_{\rm R}$[d] (Gyr)	$\tau_{\rm R,corrected}$[e] (Gyr)	$\tau_{\rm lifetime}$[f] (Gyr)	$\tau_{\rm age}$[b] (Gyr)
Phoenix	1.2×10^{-5}	5.4×10^{-5}	9.2×10^{-5}	0.22	59	76	43	10.3
LGS 3	1.6×10^{-4}	3.0×10^{-5}	6.4×10^{-5}	5.30	3.3	···	···	9.8
DDO 210	4.4×10^{-4}	1.9×10^{-4}	1.2×10^{-4}	2.32	1.1	···	···	12.0
Leo A	2.3×10^{-4}	8.2×10^{-4}	8.2×10^{-4}	0.24	12	17	18	6.2
Pegasus dIrr	2.4×10^{-4}	8.0×10^{-4}	1.3×10^{-3}	0.30	3.5	4.8	12	7.4
Sextans A	2.4×10^{-4}	1.2×10^{-2}	6.0×10^{-3}	0.02	6.6	6.8	14	9.3
WLM	6.6×10^{-4}	2.2×10^{-2}	1.7×10^{-2}	0.03	2.4	2.5	3.7	6.7
IC 1613	4.4×10^{-4}	1.2×10^{-2}	1.7×10^{-2}	0.04	5.5	5.7	4.3	7.7

NOTE.—An empty entry indicates an indefinite timescale.

[a] $\dot{M}_{\rm dusty}$ is the MLR from the bottom panel of Table 4.10, averaged over all compositions.

[b] Average SFRs and the mean mass-weighted stellar age ($\tau_{\rm age}$) are from Orban et al. (2008).

[c] $f_{\rm return} = \dot{M}_{\rm dusty}$ / SFR$_{(1\,\rm Gyr)}$.

[d] $\tau_{\rm R}$ is the Roberts Time: $\tau_{\rm R} = M_{\rm gas}$ / SFR$_{(1\,\rm Gyr)}$. The correction factor (recycling factor) for $\tau_{\rm R}$ is $(1 - \dot{M}_{\rm dusty}$ / SFR$_{(1\,\rm Gyr)})^{-1}$.

[e] $\tau_{\rm lifetime}$ is the expected total gas-rich lifetime of a galaxy assuming a total initial mass that includes the stellar and H I mass, that the current dusty MLR has remained constant, and that the 5 Gyr average SFR represents the lifetime average SFR: $\tau_{\rm lifetime} = M_{\rm Total}$ / (SFR$_{(5\,\rm Gyr)} - \dot{M}_{\rm dusty}$).

It is unlikely that these galaxies can accrete significant amounts of gas from their surrounding environments, as they are all isolated from other systems. If these galaxies are to maintain their current SFRs, there must be some non-dusty mass loss in addition to the dust-traced mass loss measured here. If the ISM is replenished solely by stellar mass loss (dusty plus non-dusty), then $f_{\rm return}$ (Table 4.11) reflects what fraction of the total stellar mass loss is traced by dust. We find that in Sextans A, WLM, and IC 1613, dusty mass loss accounts for only 2% – 4% of the total mass loss required to replenish the ISM at a rate equal to the current SFR, while in Phoenix, Leo A, and Pegasus dIrr, this fraction rises to 22% – 30%. Previous work by McDonald & van Loon (2007) and McDonald et al. (2008) found that roughly 50% of the mass loss is traced by dust in globular clusters. The very large amount of non-dusty mass loss required to balance the SFRs in Sextans A, WLM, and IC 1613 suggests that the current SFRs in these galaxies are indeed unsustainable.

The AGB stars in LGS 3 and DDO 210 are losing mass at a rate faster than new stars are currently being formed. Therefore, barring any outside influences, the mass loss traced by dust in these galaxies is sufficient to replenish the ISM at a rate that can sustain the ISM recycling rate indefinitely, eliminating the need for other gas return mechanisms such as non-dusty mass loss and gas accretion.

By comparing the H I mass in each galaxy with the current SFR and dusty MLR, we can compute the life expectancy of each galaxy, or the timescale before the galaxy runs out of H I gas. This timescale is known as the "Roberts time" (Sandage 1986), corrected so that it now includes gas return:

$$\tau_{\rm R,corrected} = \left(1 - \frac{\dot{M}_{\rm dusty}}{\rm SFR}\right)^{-1} \frac{M_{\rm gas}}{\rm SFR}. \tag{4.1}$$

The correction factor is referred to as the recycling factor. We find that Leo A and Phoenix can survive as gas-rich dwarf galaxies for 17 Gyr and 76 Gyr, respectively, but that Pegasus dIrr, Sextans A, WLM, and IC 1613 can continue star formation activity

at the current rate for only 2.5 Gyr – 6.8 Gyr, with WLM being the first galaxy to become inactive (Table 4.11). For Leo A, Phoenix, and Pegasus dIrr, dusty mass loss is responsible for an increase of 29% – 40% over the uncorrected $\tau_{\rm R}$, while in the remaining three galaxies, dusty mass loss is responsible for a mere 2% – 4% increase. For disk galaxies, Kennicutt et al. (1994) finds that this increase can be significantly larger, although we note that those estimates include mass lost during all stages of stellar evolution.

Assuming a closed-box model, and that the average SFR over the last 5 Gyr represents the average rate over each galaxies' lifetime, then when including gas return from dusty stellar mass loss, we find that the predicted gas-rich lifetimes of WLM and IC 1613 ($\tau_{\rm lifetime}$ = 3.7 and 4.3 Gyr, respectively, see Table 4.11) are shorter than the current estimate of the mean mass-weighted stellar ages for each galaxy ($\tau_{\rm age}$ = 6.7 and 7.7 Gyr, respectively; Orban et al. 2008). Even if we assume that dusty mass loss accounts for only 10% of the total mass loss, we still find lifetimes that are too short to allow for any current star formation in WLM and IC 1613 ($\tau_{\rm lifetime}$ =5.8 and 5.7 Gyr, respectively). This indicates that either these galaxies have been accreting gas from the outside or that they have been very inefficient at using up their initial gas to form stars, although it is unclear what might cause the latter (Orban et al. 2008).

4.5 Summary of Results and Conclusions

We present part III of a *Spitzer* IRAC census of AGB stars in eight Local Group dwarf irregular galaxies: Phoenix, LGS 3, DDO 210, Leo A, Pegasus dIrr, Sextans A, WLM, and IC 1613. Stars brighter than the 3.6 μm TRGB are identified as AGB candidates, and we find that 50% – 100% of these sources are detected and identified as AGB stars in broadband optical photometry. An optical completeness fraction of 70% agrees within the errors of all eight galaxies in our sample, suggesting that optical surveys of dwarf galaxies are underrepresenting the AGB by 30% – 40%, due to extinction from

circumstellar dust.

We find no trend of decreasing optical completeness with increasing metallicity, as would be expected assuming that dust is more efficiently produced at high metallicities. This suggests that dust production is not suppressed at low metallicity, although it may form in smaller quantities. We do however see that the fraction of moderately red (dusty) stars that are not obscured in the optical increases in galaxies with higher metallicity.

Known carbon stars were identified in our IRAC data, and we find that previous studies have used only a small fraction (26% – 34%) of the population of M and C stars to compute C/M ratios.

Using the $[3.6] - [4.5]$ color excess, we compute average individual stellar mass-loss rates ranging from $3.1 \times 10^{-7} - 6.6 \times 10^{-6}$ $M_{\odot}$ yr^{-1}, agreeing well with estimates of AGB MLRs in other studies. Mass loss traced by dust does not appear to be inhibited at low metallicity.

The integrated MLRs for each galaxy range from $4.4 \times 10^{-5} - 1.4 \times 10^{-3}$ $M_{\odot}$ yr^{-1}. Normalized to the total stellar mass, we find a range of $\dot{M}_{\rm Tot}/M_{*} = 2 \times 10^{-8}$ for LGS 3, to $\dot{M}_{\rm Tot}/M_{*} = 6 \times 10^{-10}$ for Leo A. These rates do not include mass loss that is unaccompanied by dust.

A comparison of the recent (within 1 Gyr) SFR and the current MLRs reveals that all but two of our galaxies (LGS 3 and DDO 210) cannot sustain their current SFR solely through ISM gas return from the stellar mass-loss rates measured here. Phoenix, Leo A, Pegasus dIrr, Sextans A, WLM, and IC 1613 will all eventually extinguish their gas supply unless there is an additional supply of gas. In these galaxies, mass loss traced by dust can account for only 2% – 30% of the material required to maintain the current SFR.

Chapter 5

Summary of Conclusions and Related Work

Abstract

This chapter summarizes chapters 2 through 4 and includes a discussion of the broader implications. I have also collaborated on three projects, related to the work in this dissertation, that have recently been completed. The studies include a search for ICM dust in eight Galactic GCs, a detailed follow-up study on dust production in ω Cen, based on data presented in chapter 3, and an investigation of mass loss in a super-solar-metallicity open cluster. The results of these works are summarized and discussed here.

5.1 Dust in M15

5.1.1 Primary Results

In chapter 2 we discussed the first secure, high signal-to-noise detection of intracluster (ICM) dust in a globular cluster (GC) along with a population of dusty asymptotic

giant branch (AGB) star and post-AGB star candidates (Boyer et al. 2006). The mass of the ICM dust is 2 – 4 times less than the mass predicted based on the number of Horizontal Branch stars and is consistent with mass lost by 100 or so stars, a number that can easily pass through the superwind phase of mass loss within 10^6 years. Since this timescale is nearly two orders of magnitude smaller than the time between Galactic plane crossings, when ICM material is stripped from a GC, it appears as though ICM dust is short-lived, and may be present only at the discretion of episodic mass loss and/or stochastic ICM removal processes.

5.1.2 Discussion

The amount of dust discovered in M15 is an incredible surprise. How could a cluster with such a low metallicity (less than 0.5% solar) produce so many dust-enshrouded stars? It's possible that dust is actually formed *more* easily at low metallicity (e.g., see Fig. 3.10), since carbon stars are able to form due to the low oxygen abundance (less oxygen results in less carbon being tied up in CO molecules; Daulton et al. 2002; Amari et al. 2001). However, low-metallicity stars are lacking the seeds necessary for dust formation, making it difficult to efficiently form dust even with abundant carbon. It is possible that dust-forming seeds are created in the stars themselves and dredged-up to the circumstellar envelope. However the dust may form, it is clear that dust formation was not prohibited in the early Universe, where metallicities were comparable to that in M15. Dust observed at high redshift is usually believed to originate in supernovae explosions, but it may actually be the result of dust formation in primordial AGB atmospheres.

The presence of ICM dust in M15 is also a surprise not only because of M15's low metallicity, but also because no other GC shows evidence of a significant ICM (Hopwood et al. 1999; Matsunaga et al. 2008; Barmby et al. 2008). Is there something as yet undiscovered about M15 that makes it uniquely able do retain its ICM? It seems

more likely that we have simply caught M15 at the right moment in time. All GCs may, in fact, retain ICM gas and dust for a short time before they are stripped away into the Galactic halo. There is also evidence that mass loss is an episodic process itself (Origlia et al. 2002; Meszaros et al. 2008; McDonald et al. 2008); it is possible that a large number of stars in M15 just happened to lose mass at the same time and that whatever ICM removal process is at work in the cluster has not yet been able to catch up. Whether M15 is unique or has simply been serendipitously observed during a short evolutionary phase, it appears to represent an extremely rare phase of GC evolution.

5.2 AGB Mass Loss and Dust in ω Centauri

5.2.1 Primary Results

In chapter 3, we present a complete mid-IR catalog of point sources in the most massive GC, ω Cen. A small population of dust-enshrouded mass-losing stars are found near the tip of the RGB, and the cluster mass-loss rate is dominated by the three most extreme of these stars. We see no tendency for the higher metallicity stars in the cluster to have redder colors, i.e., dustier atmospheres, and dusty mass-loss is not found further down the RGB, as was suggested by work in 47 Tucanae (Origlia et al. 2007). Stars that are super-Ba-enriched collect near the upper part of the RGB, suggesting that the extra Barium may be due to third dredge-up and that these stars delineate the thermal-pulsating AGB. Several 70 μm sources are detected in our MIPS images, but these all appear to be background galaxies rather than obscured AGB stars.

There is no prominent ICM dust feature in ω Cen despite the fact that the current cluster mass-loss rate suggests a total of 1 – 2 $M_{\odot}$ of material (or $1 - 2 \times 10^{-4} M_{\odot}$ of dust) has been lost by the stellar population since the last Galactic plane crossing. The few faint, extended dust features detected well outside the cluster half-mass radius may be either foreground dust emission or ICM material in the process of being removed.

5.2.2 Discussion

The motivation for observing ω Cen with *Spitzer* was the opportunity to study AGB populations that are similar in most respects yet have three different metallicities. We find no correlation between metallicity and dust content in AGB circumstellar envelopes, suggesting that, as in M15, dust production is not prohibited at low metallicity. However, despite the modest amount of dust in stellar atmospheres, ω Cen has not been unable to retain dust in its ICM. If the extended dust features that appear on the outskirts of the *Spitzer* images are indeed associated with the cluster, the dust appears to be escaping. Therefore, either dust escapes the cluster on relatively short timescales, or dust does not settle towards the cluster center, remaining too diffuse to detect with *Spitzer*.

Even though several sources in ω Cen do appear to be dusty, no stars appear to be so heavily enshrouded as to obscure them at shorter wavelengths. The few sources we do detect at 70 μm are very likely dominated by background galaxies. Therefore, while dust formation is not *prohibited* at low metallicity (as discussed above), it is indeed forming in smaller quantities, allowing only a population of *moderately* dusty stars.

5.3 AGB Star Census in Local Group Dwarf Irregular Galaxies

5.3.1 Primary Results

Chapter 4 presents an AGB census in eight Local Group dwarf irregular galaxies that cover an order of magnitude range in metallicity. We find that a sizable portion of AGB stars have produced enough dust to be totally obscured in the optical in all eight of the galaxies, with no correlation with metallicity. We do, however, find a tendency for higher metallicity galaxies to harbor a higher fraction of moderately dusty, partially

obscured stars ($A_{\rm v} \gtrsim 1$) than low metallicity galaxies, although the age of the galaxy may be the determining characteristic rather than metal content.

Mass loss rates of the AGB candidates were determined and compared to the star formation rates and interstellar medium (ISM) H I contents. We find that only two of the galaxies (LGS 3 and DDO 210) are capable of sustaining their current star forming rates without a secondary source of gas return in addition to mass loss traced by dust.

5.3.2 Discussion

On average, it appears that roughly 30% to 40% of AGB stars are so heavily enshrouded in dust that they are undetected or misidentified in the optical. Until recently, most AGB studies have been conducted at optical or near-IR wavelengths, and their inability to detect all AGB stars biases these studies away from the most extreme mass-losing stars. In order to properly characterize and model AGB mass loss, further AGB studies must be carried out in the mid-IR in a wider variety of stellar systems. The underrepresentation of the AGB population in the optical may also affect star formation histories determined from isochrone fitting to optical color-magnitude diagrams. This is especially true of star formation histories of intermediate-mass stars, which are determined from matching isochrones to the AGB.

As in M15 and ω Cen, we find that low metallicity environments are capable of producing dust, although perhaps not in quantities comparable to those seen in high-metallicity environments. Galaxies at all metallicities produce evolved stars that are entirely obscured by dust, but higher metallicity galaxies produce more *partially* obscured stars. Dusty stars may therefore not have been ubiquitous in the early Universe, but it appears that they should have been forming at least in small quantities among the first generations of stars. We must, however, note that the metallicities of individual stars have not been measured, and it is possible that the dustiest stars are part of small populations with metallicities higher than the bulk populations.

Only two of the galaxies in our sample are able to sustain their current star formation rates indefinitely, with recycled mass from AGB stars continually replenishing the ISM at a high rate. Three of the remaining galaxies can continue forming stars, at most, for another few billion years. If these galaxies are truly isolated, i.e., they are not accreting outside material, then they would require an increase of a factor of 25 – 50 in the mass-loss rate to sustain their current star formation rates. The remaining three galaxies require a factor of 3 – 5 increase in the total mass-loss to maintain their status as gas-rich galaxies. This extra mass loss may be driven by non-dusty processes, such as acoustic waves in heated chromospheres.

5.4 A Search for Intracluster dust in Globular Clusters

This section summarizes work presented in a manuscript accepted for publication in the Astronomical Journal in October 2008 entitled "A Spitzer Search for Cold Dust within Globular Clusters" by Pauline Barmby, Martha L. Boyer, Charles E. Woodward, Robert D. Gehrz, Jacco Th. van Loon, Giovanni G. Fazio, Massimo Marengo, and Elisha Polomski.

5.4.1 Primary Results

We have observed eight Galactic GCs with *Spitzer* in search of the elusive ICM (Barmby et al. 2008). The project was motivated by the successful detection of ICM dust in M15, and by the fact that *Spitzer's* unprecedented sensitivity allows for the detection of small amounts of dust in GCs. We chose GCs that we deemed have the strongest possibility of retaining an ICM: they are nearby, far outside of the Galactic plane (to reduce confusion with fore- and backgrounds), and have large escape velocities.

No significant extended emission is detected in the images of any of the GCs in our sample. However, very diffuse, small amounts of dust may be hidden beneath the

foreground Galactic cirrus. All dust mass upper limits are $< 4 \times 10^{-4} M_{\odot}$, much less than the predicted dust masses of $10^{-0.8} - 10^{-3.6} M_{\odot}$, based on the number of Horizontal Branch stars present in each GC. The strongest evidence for ICM dust is in NGC 6341, but 90 μm images from the AKARI telescope (Matsunaga et al. 2008) do not confirm its presence. Moreover, the dust masses (secure detections and upper limits) show no trend with various cluster characteristics such as the time since the last Galactic plane crossing, the escape velocity, the metallicity, or the bolometric luminosity (see Figure 5.1).

5.4.2 Discussion

The apparent lack of ICM dust and ICM gas (e.g., van Loon et al. 2006b) in GCs suggests that either: (1) evolved GCs produce less dust than predicted, or (2) the ICM escapes from GCs on very short timescales. The first possibility seems unlikely, given the mounting evidence pointing to significant, although less efficient, dust formation at low metallicity both in this dissertation and other works. The ICM appears to be removed from GCs at an extremely efficient rate, a scenario that has very nontrivial consequences. Significant mass loss over the course of a cluster's life can significantly alter its dynamical evolution and possibly threaten its survival as a bound system (van Loon & McDonald 2008).

The paucity of ICM material requires a removal mechanism in addition to Galactic-plane crossings. Hopwood et al. (1999) found the sputtering of dust grains by halo gas to be insufficient for several GCs, as it removes $\leq 1\%$ of the ICM dust during each orbit around the Milky Way. Freire et al. (2001) argue that the stellar radiation field in a GC is sufficient to ionize all hydrogen, but the amounts of ionized hydrogen detected in M15 and 47 Tuc are insufficient to account for all missing ICM. The photodestruction of dust grains is another possibility; however, this would leave gaseous components behind. Ram pressure stripping from ambient halo gas is another possibility(Hopwood

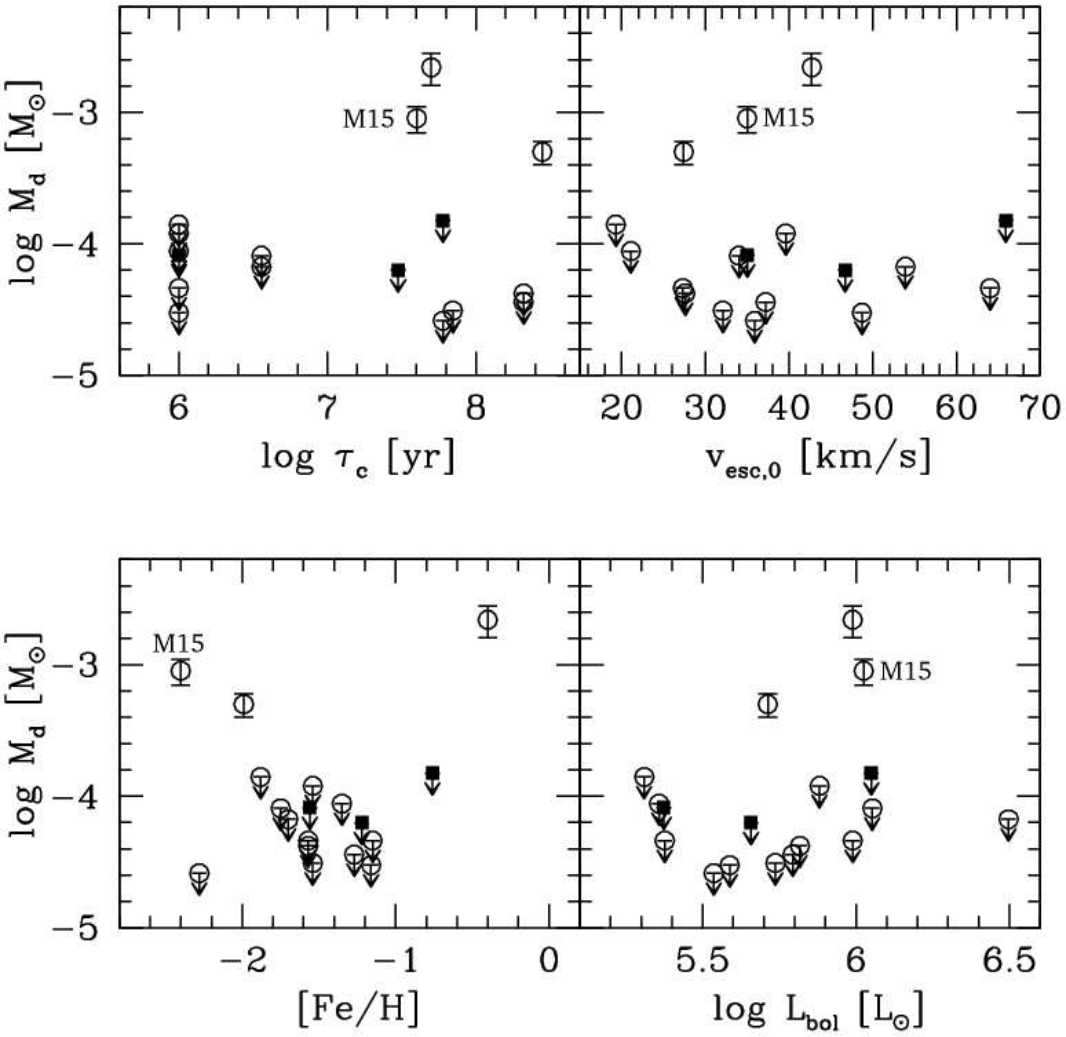

Figure 5.1: Derived cluster dust masses and upper limits versus the time since the last Galactic plane crossing ($\tau_{\rm c}$), the central escape velocity ($v_{\rm esc}$), the metallicity ([Fe/H]), and the bolometric luminosity ($L_{\rm bol}$). Filled symbols: results from Barmby et al. (2008) (total masses). Open symbols: previously published work. An uncertainty of 20% has been assigned to $M_{\rm d}$ for NGC 5024 as no value was given in the original work (Matsunaga et al. 2008). ICM dust mass does not appear to correlate with any of the cluster characteristics shown here.

et al. 2000), perhaps akin to the mechanism producing the HI gas in/near dwarf galaxies. Stellar collisions may also provide enough energy to eject ICM material (Umbreit et al. 2008). Giant stars with winds larger than the escape velocity of the cluster have been observed and may play a role in clearing material (Smith et al. 2004; Dupree et al. 1992). In fact, metal-rich AGB stars do tend to have stronger winds, which might explain why M15, the most metal-poor cluster, has been able to retain its ICM. Clearly, different environments may favor one removal mechanism over others. The best constraints on these theories will come from sensitive measurements (or meaningful upper limits) of ICM masses in as many GCs as possible. With current observations, it is impossible to distinguish between possible removal mechanisms, as illustrated in Figure 5.2 which shows no obvious trends pointing towards ram pressure stripping in the halo or to stellar collisions within the clusters.

5.5 Dust Production in ω Centauri

This section summarizes work presented in a manuscript accepted for publication in the Monthly Notices of the Royal Astronomical Society in November 2008 entitled "Dust Production in the Globular Cluster ω Centauri" by Iain McDonald, Jacco Th. van Loon, Leen Decin, Martha L. Boyer, Charles E. Woodward, Robert D. Gehrz, Aneurin Evans, and Andrea K. Dupree.

5.5.1 Primary Results

Based on the *Spitzer* photometry published in Boyer et al. (2008a) and discussed in chapter 3, we have performed spectral energy distribution modeling of 6875 stars in ω Centauri, obtaining stellar luminosities, temperatures, and mass-loss rates, down to $\approx 7 \times 10^{-8}\ M_{\odot}\ \mathrm{yr}^{-1}$. Figure 5.3 shows the resulting physical Hertzprung-Russell diagram. We find a total cluster mass-loss rate of $1.2 \pm^{0.8}_{0.5} \times 10^{-6}\ M_{\odot}\ \mathrm{yr}^{-1}$, with a total

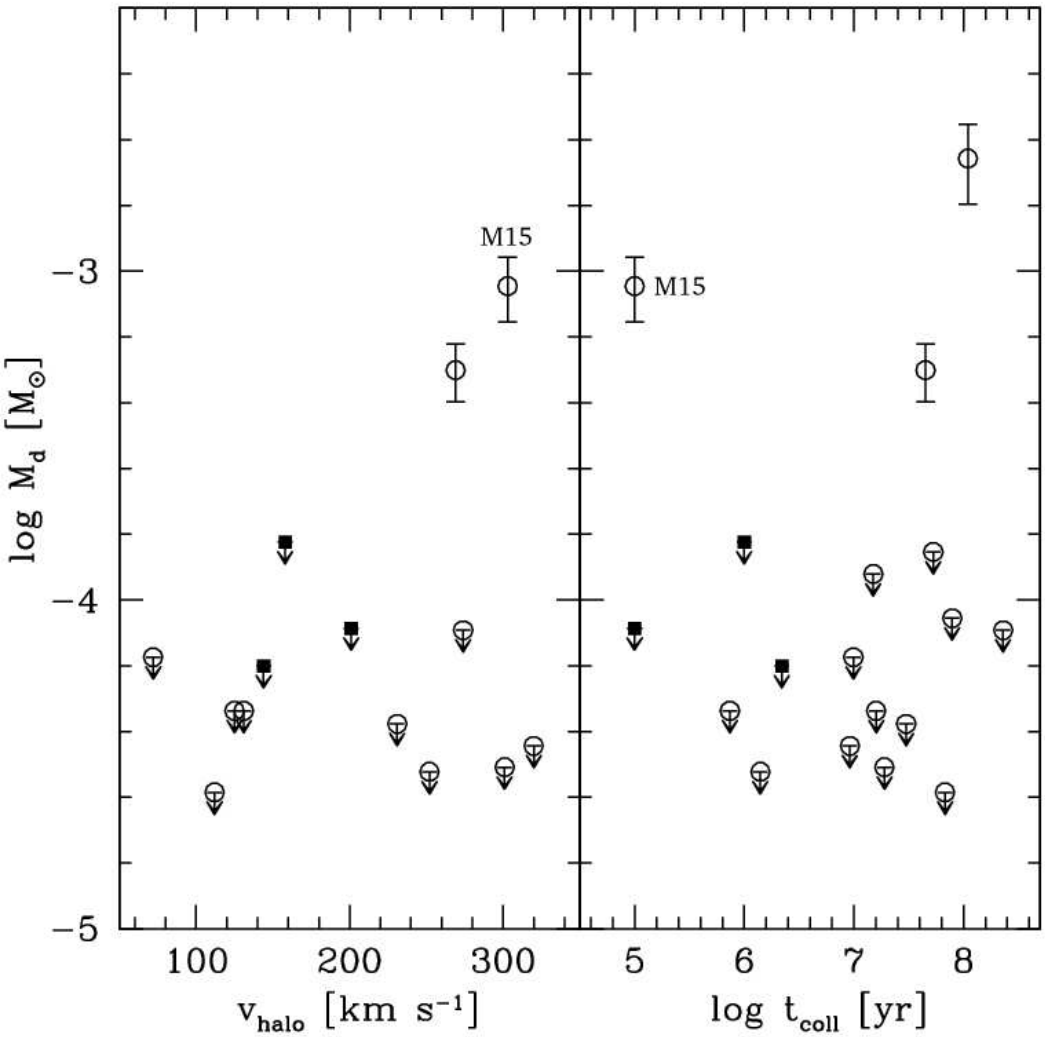

Figure 5.2: Derived cluster masses and upper limits versus velocity relative to the halo (left) and estimated time between stellar collisions in the core (right). Symbols as in Figure 5.1. In the left panel, clusters NGC 1261, 5646, 6356, and 6402 are not shown, as orbital parameters were not available. In the right panel, both NGC 6752 and M15 are plotted at $t_{\rm coll}/N = 10^5$yr; these clusters are core-collapsed and should have short collision times.

dust mass-loss rate three orders of magnitude smaller. The two most extreme stars, V6 and V42, are responsible for 50% of the total dust mass loss and 30% of the total gas mass loss. Based on Gemini-S/T-ReCS mid-infrared spectroscopy (see Figure 5.4), V42 appears to have carbon-rich dust despite its oxygen-rich nature. We also identify several post-EAGB candidates.

Figure 5.5 shows that mass loss in the cluster does not appear to correlate with metallicity but does correlate with Ba enhancement, which tends to occur mostly on the higher-metallicity anomalous RGB (RGB-a). The Ba-enhancement may thus *not* be due to third dredge-up, as suggested in chapter 3, since stars on the RGB have not yet experienced one. We also find that significant dusty mass loss appears to occur on the upper RGB, with a $\sim$25% loss of the initial stellar mass.

The apparent variable mid-IR spectra of V42 suggest that Mid-IR excess, attributed to dust, may be highly variable in pulsating stars on short timescales ($<$ 1 month). Therefore, the mass-loss rates are also variable, and should not be considered accurate unless measured throughout a pulsation cycle.

5.5.2 Discussion

The star V42 is an interesting case. Its high mass loss rate in combination with its relatively small luminosity point towards the possibility that V42 has recently undergone a thermal pulse and is currently in an associated luminosity minimum. The presence of carbon dust in the T-ReCS spectrum differs from the oxygen-rich dust inferred from literature photometry. This may be explained if the dust formation criteria are met only during part of a pulsation cycle, resulting in the formation of carbon-rich dust at some times (possibly during dredge-up) and oxygen-rich dust at other times.

At the current cluster mass-loss rate, the cluster will lose about 0.5% of its mass each year. This percentage was certainly larger in the past (even a mere 3 Gyr ago), when more massive stars were losing mass at a higher rate. This suggests that the

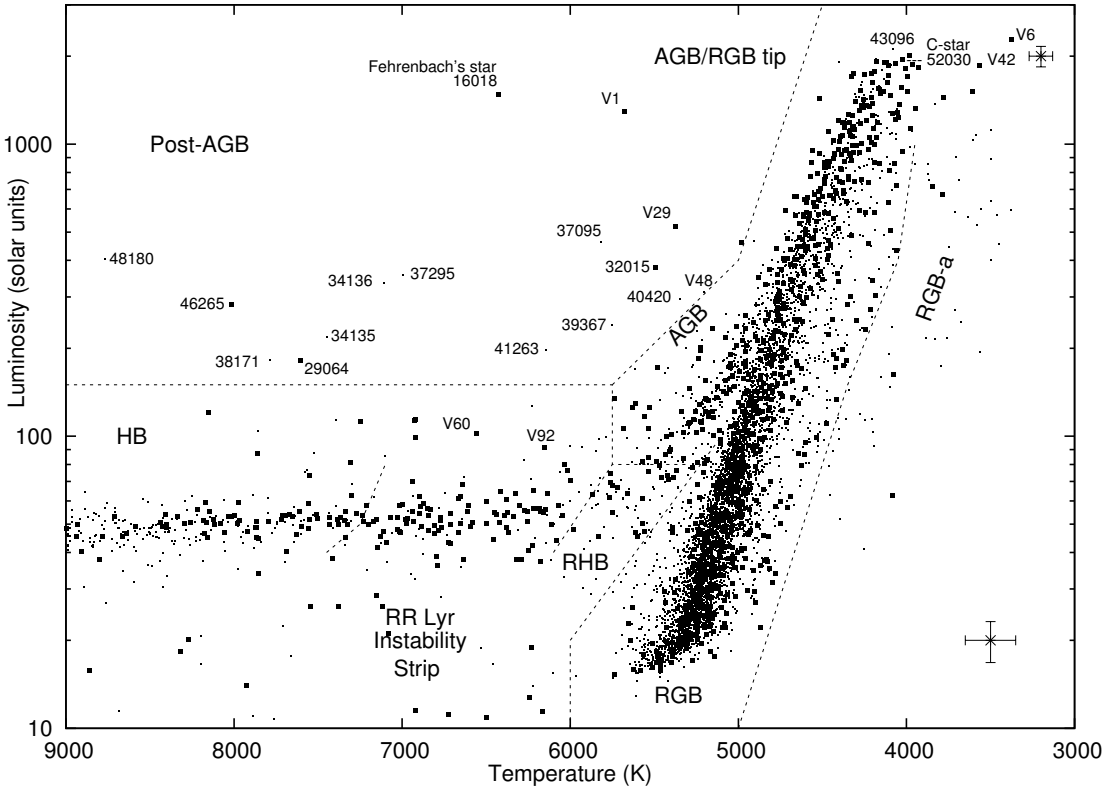

Figure 5.3: A physical Hertzprung-Russell diagram for the giant branch of ω Cen. Small squares show proper motion cluster members ($> 50\%$ probability); large dots show objects that are (also) confirmed radial velocity members ($v_{\rm LSR} > 100$ km s^{-1}). Representative statistical errors for individual objects are shown in the lower- and upper-right corners. The limits to the RR Lyrae instability strip are taken from Bono et al. (1995).

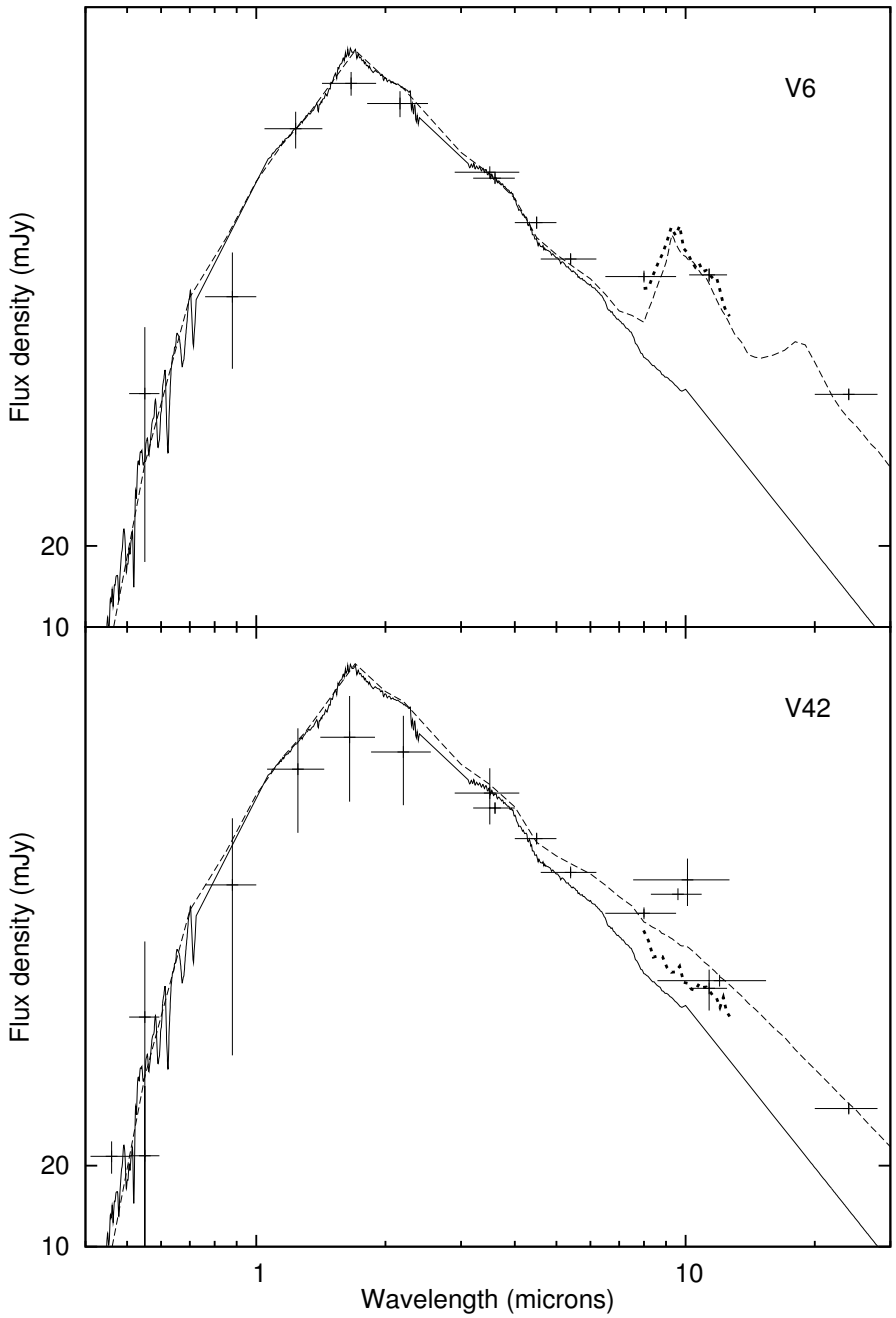

Figure 5.4: Spectral Energy Distribution models of V6 (top) and V42 (bottom), showing MARCS models smoothed to R = 200 (solid lines), smoothed Gemini-S/T-ReCS spectra (dotted lines), and literature photometry (crosses with error bars). The error bars in the latter reflect either the photometric variability or the measured error (for details, see McDonald et al. 2008). The dashed curve shows the corresponding DUSTY model, fit to the Gemini spectrum and 24 μm *Spitzer* datum in the case of V6 and the literature photometry, including *Spitzer* data, in the case of V42.

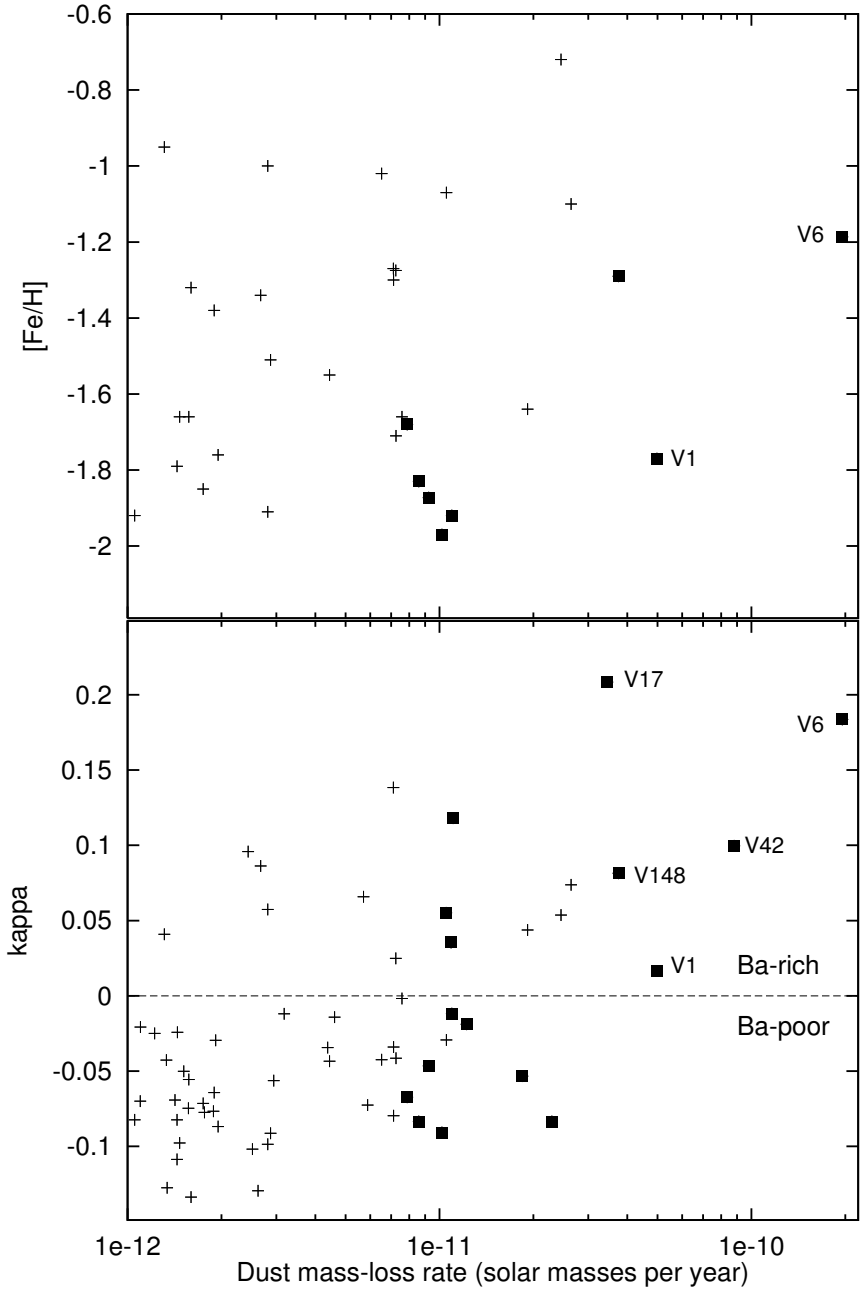

Figure 5.5: Dust mass-loss rates for stars with $L > 500\ L_{\odot}$ and their dependence on [Fe/H] (top panel), and the barium (lower panel) richness indicator κ (see McDonald et al. 2008). There is no correlation between metallicity and mass-loss rates, but there is a correlation between mass-loss rates and Ba-richness.

cluster has lost more than 10% of its mass over its lifetime from AGB and RGB stellar winds, altering its dynamical evolution even after massive stars had already exploded within the first few million years of the cluster's lifetime.

Based on the current cluster mass-loss rate measured in this work, it would appear that neutral ICM gas is removed from the cluster on timescales less than 3×10^5 years and dust is removed within 1×10^5 years. If ICM were being removed by a 10 km s^{-1} wind, it would take 8×10^6 years to escape, and if the material was being stripped by ram pressure by the Galactic halo, it would take 1.2×10^6 years to escape, both more than an order of magnitude longer than the inferred escape timescale. It appears that while these two processes are certainly taking place, an additional mechanism is required for removing mass lost from AGB and RGB stars.

Our modeling shows that many stars in ω Cen appear to be leaving the AGB early, never reaching the AGB tip. This leaves a depleted number of stars that will develop high mass-loss rates. Currently, the cluster's total mass loss is dominated by only a handful of stars; along with the variable nature of mass loss in individual stars, this suggests that GC mass loss is episodic. It may therefore not be a surprise that material may clear out of the ICM before it has time to collect in large quantities.

5.6 No Super Mass Loss at Super-Solar Metallicity: The Case of NGC 6791

This section summarizes work published in the Astrophysical Journal Letters entitled "Spitzer Space Telescope Evidence in NGC 6791: No Super-Solar-Mass-Loss at Super-Solar Metallicity to Explain Helium White Dwarfs?". The bibliographic reference is: van Loon, J. Th., Boyer, M. L., & McDonald, I. 2008, ApJL, 680, L49

5.6.1 Primary Results

We used archival *Spitzer* IRAC data to produce IR photometry for the super-solar metallicity, massive open cluster NGC 6791. The purpose was to investigate the idea recently postulated by Hansen (2005) and Kalirai et al. (2007) that invoked super-mass-loss in RGB stars to explain the presence in undermassive helium white dwarfs in the cluster. Those studies estimate that super-mass-loss is occurring in at least 40% of the RGB stars, truncating the evolution of these stars and resulting in an early departure from the RGB before the helium flash. We investigate this claim in two ways: (1) by looking for circumstellar dust expected to form in the winds of cool, metal-rich RGB stars, and (2) by comparing the IR and optical luminosity functions with state-of-the-art model predictions. We find a lack of evidence for a premature truncation of RGB evolution.

5.6.2 Discussion

Despite the super-solar-metallicity in NGC 6791, the stars do not appear to harbor much dust based on their [3.6] - [8] colors. In fact, we find only 14 out of 72 stars (19 $\pm$ 5%) have red colors, and that these colors are only marginally red (see Figure 5.6). The mass-loss rates determined for these stars following Groenewegen (2006) are $\dot{M} \lesssim 10^{-8}$ $M_{\odot}$ yr^{-1}. This mass-loss rate is only sufficient for an RGB star to lose 0.2 $M_{\odot}$,

which is insufficient to avoid the helium flash. Given an initial mass of $M_{\rm initial} = 1.1\ M_{\odot}$, the stars in this cluster would have to shed at least $\Delta M_{\rm implied} = 0.7\ M_{\odot}$ to produce white dwarfs with the masses measured by Kalirai et al. (2007). Based on the estimates of the mass-loss rates ($\dot{M}$), the fraction of dusty stars ($f_{\rm dusty}$), and the RGB lifetime ($t_{\rm RGB}$), we find that $\dot{M} t_{\rm RGB}/\Delta M_{\rm implied} \times f_{\rm dusty}$, or $\lesssim$20%, of the stars in this cluster could potentially lose enough mass to skip the helium flash, half as many as predicted by Hansen (2005) and Kalirai et al. (2007).

Figure 5.7 presents a comparison of the IR and optical luminosity functions to the model luminosity functions (Marigo et al. 2008). This figure shows that the data is in good agreement with the models, allowing for small stocastic effects, especially in scarcely populated regions of the luminosity function. Red clump stars are post-helium flash stars, and the population in the cluster matches the population predicted by the models, suggesting that the majority of the stars in the cluster are not losing enough mass to skip the helium flash. There is therefore no evidence that these super-metallicity stars are undergoing unusually strong mass loss.

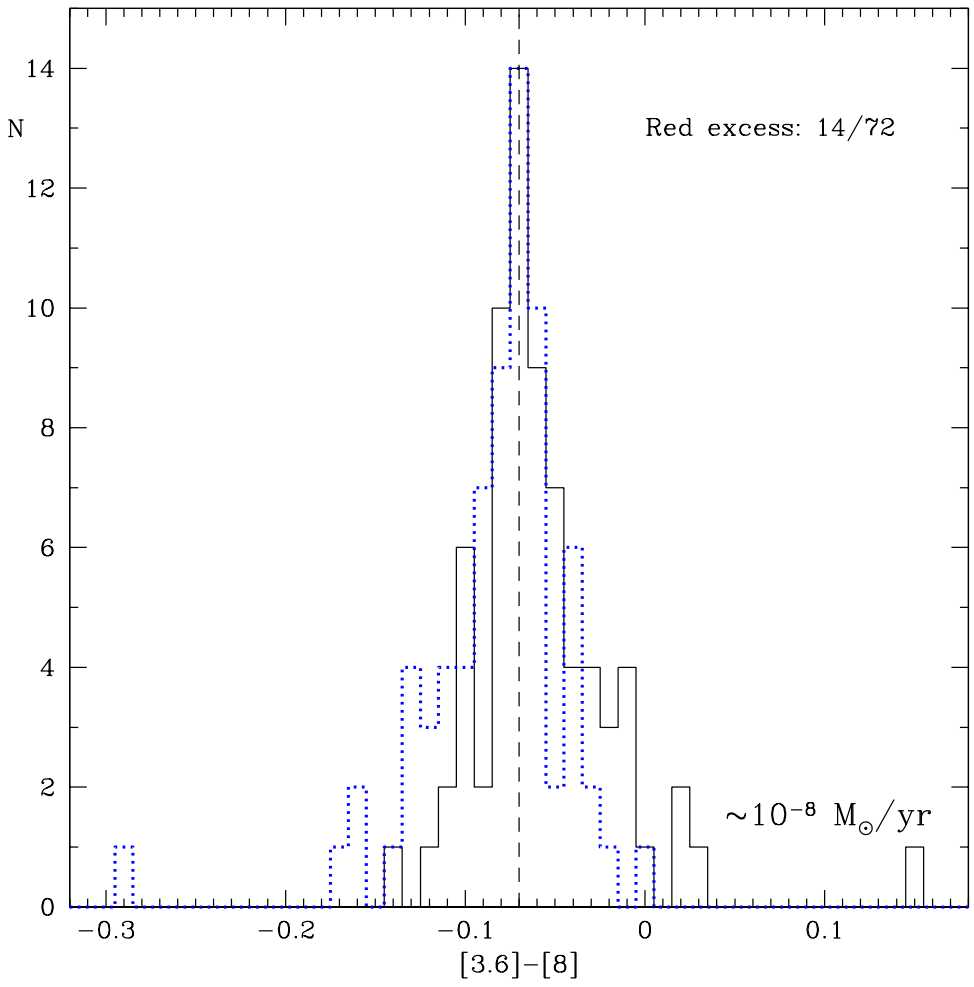

Figure 5.6: *Spitzer* IRAC color distribution along the RGB in NGC 6791. Overplotted (dotted) is the same histogram, but mirrored with respect to its peak. This clearly shows which stars are redder than the bulk of the RGB stars. Even these stars are only marginally red, with colors corresponding to mass-loss rates of order 10^{-8} $M_{\odot}$ yr^{-1}.

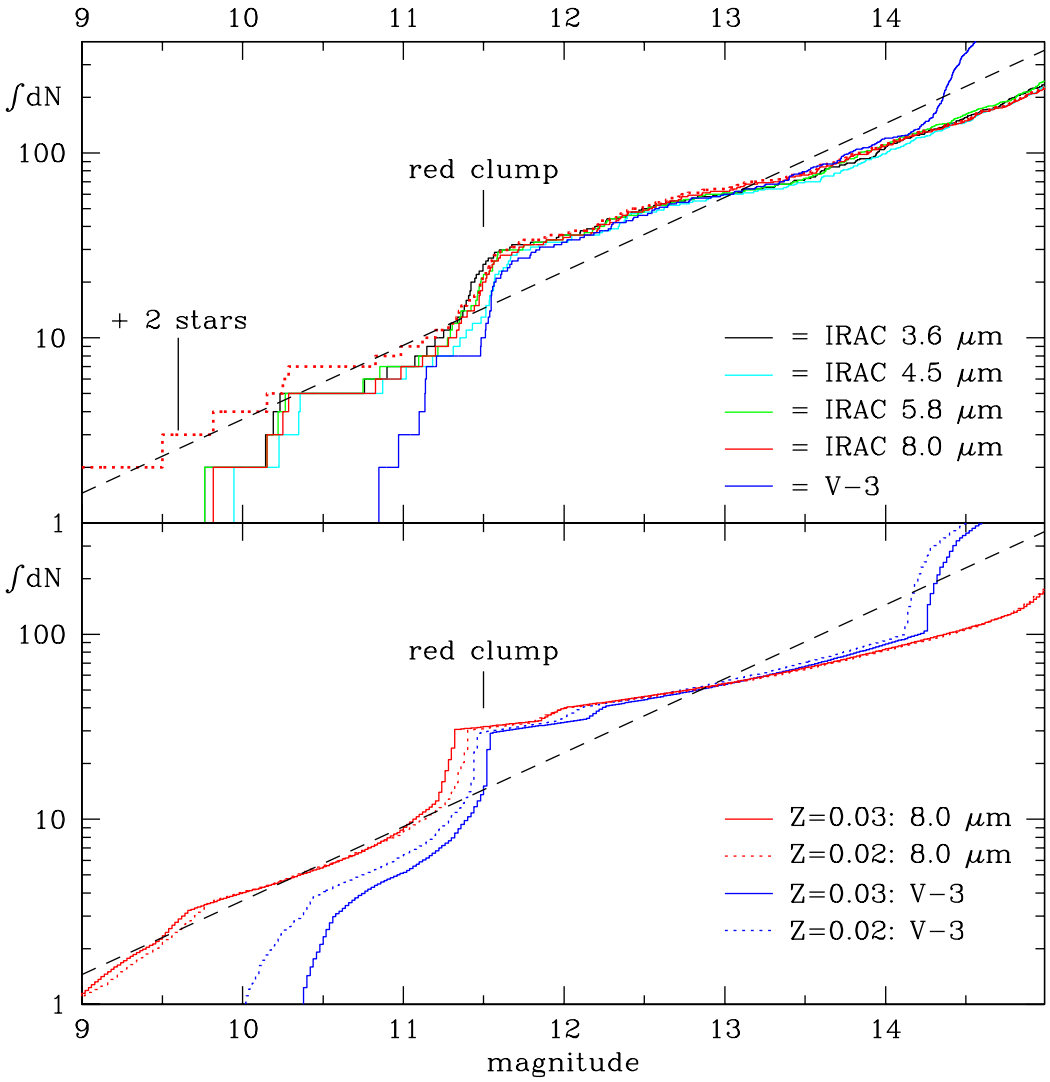

Figure 5.7: *Spitzer* IRAC and optical *V*-band (Stetson et al. 2003) luminosity functions in NGC 6791. The 8 μm luminosity function is also plotted after adding just two more stars near the expected tip of the RGB. A comparison with 8 Gyr models (Marigo et al. 2008) shows good agreement, especially considering that NGC 6791 is more metal-rich than the most metal-rich models. Stochastics introduced by sampling the small number of stars on the upper RGB can fully explain the discrepancy between IRAC data and models, e.g., a mere two stars added to the tip of the RGB brings the observed luminosity function in excellent agreement with theoretical prediction.

Chapter 6

Future Work

Abstract

The work presented in this dissertation represents some of the first results of an ongoing effort to better understand AGB star mass loss and dust production at low metallicity. This work launches naturally into several follow-up studies of AGB stars and GC ICM dust, each designed to add to what we have already learned. This chapter describes a few of these studies, some of which are already underway, and others that will be implemented in the very near future.

6.1 Ongoing Work On AGB Star Mass Loss

6.1.1 Local Group Dwarf Galaxies: Broadening the Sample Size

In chapter 4, we have presented an AGB star census in eight Local Group dwarf irregular galaxies. These eight galaxies were chosen not only because they span a broad metallicity range, but also because they are relatively nearby, with the most distant galaxy, Sextans A, being ≈1.3 Mpc away. For AGB studies, it is important that target galaxies are nearby enough for photometry to be complete down to below the TRGB. With Sextans A, we had difficulty determining the location of the TRGB with IR data

alone because of the lack of sub-TRGB sources in the *Spitzer* images. We were, however, able to use optical photometry to estimate where the IR TRGB is located, and we found that photometry is 50% complete down to 0.4 mag fainter than the TRGB. This limit allows for the detection of all super-TRGB stars, especially the reddest of these stars. Therefore, we can reasonably detect all AGB stars in other dwarf irregular galaxies with distance moduli $\sim$0.2 mag fainter than Sextans A (or distance $\lesssim$ 1.5 Myr). With *Spitzer*, it is not possible to obtain a *complete* census of AGB stars in galaxies more distant than this limit, but at the very least, we detect the most extreme mass-losing AGB stars since these are the brightest sources in any given galaxy.

In addition to the eight galaxies presented in chapter 4, we have observed eight more galaxies with distances ranging from 1.1 – 1.6 Mpc at 4.5 and 8 μm with *Spitzer* (see Figure 6.1). Assuming TRGBs of $M_{3.6} = -6.0$ mag and similar completeness limits as in the nearer eight galaxies, we can expect that the photometry for these galaxies is 50% complete down to the TRGB but that almost no sub-TRGB stars are detected. Therefore, while we may have some difficulty obtaining a complete census in the most distant of these remaining galaxies, we can use the data we have to identify the brighter AGB stars.

With only 4.5 μm and 8 μm data at our disposal, we will be unable to carry out similar analyses discussed in chapter 4. If preliminary analyses reveal substantial populations of interesting AGB stars in these galaxies, we will propose to observe them at 3.6 μm as part of *Spitzer's* warm mission. The extra wavelength coverage will allow us to carry out a complete IR analysis on the AGB population as a whole and will assist in any future SED modeling of individual AGB stars.

6.1.2 Local Group Dwarf Galaxies: Measuring Contamination

All of the dwarf irregular galaxies that we have observed with *Spitzer* are just distant enough so that unresolved background galaxies occupy the same region of the IR

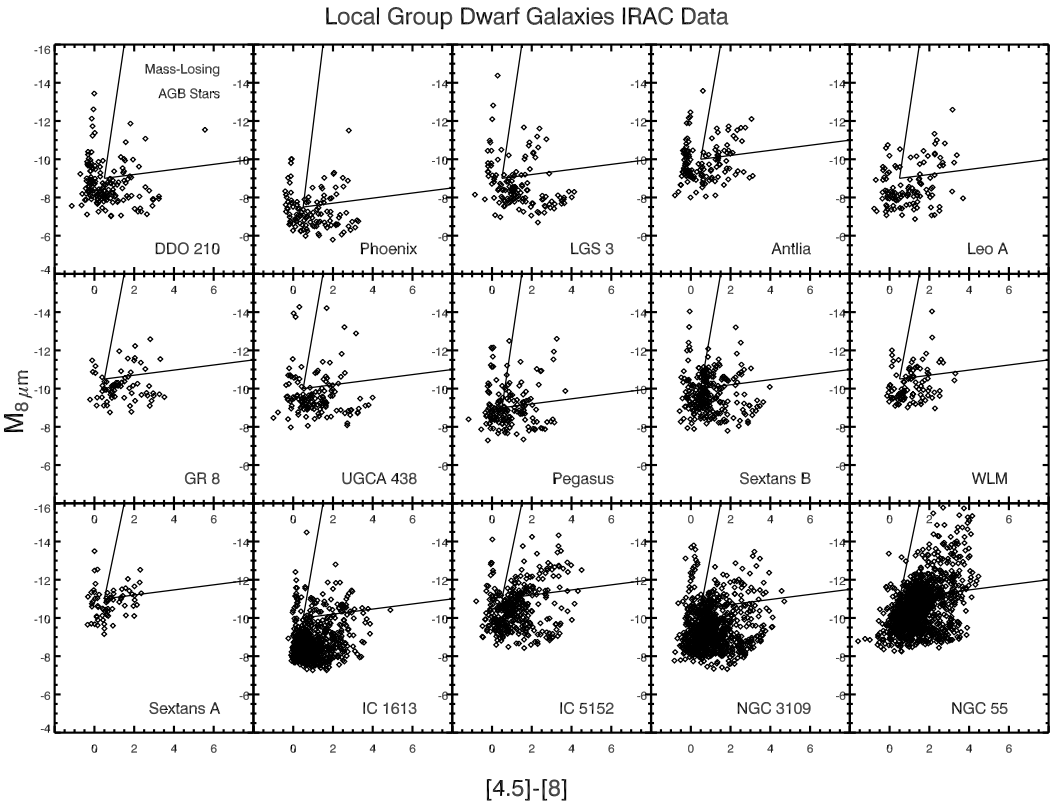

Figure 6.1: 4.5 μm vs. 8 μm CMDs of Local Group dwarf irregular galaxies that we have observed with *Spitzer*. Sources located within the approximate enclosed area on the top, right side of each panel are likely mass-losing AGB stars. We discussed the analysis of eight of these galaxies in chapter 4, and we plan to follow up with the remaining seven, plus the galaxy SagDIG, which is not shown here.

color-magnitude diagram that is occupied by obscured, mass-losing AGB stars. This unfortunate placement makes it impossible to disentangle background sources from AGB stars with current data alone. We have attempted to measure the background source contamination in section 4.3.4, but this measurement is highly uncertain because it inaccurately assumes that large portions of the images obtain only background sources and no sources belonging to the dwarf galaxies. In order to properly measure the contamination from a flat distribution of background sources, we require an image covering a large field of view for each galaxy with large portions of off-galaxy imaging.

We plan to propose wide-field imaging at 3.6 μm of the eight dwarf galaxies discussed in chapter 4 as part of *Spitzer's* warm mission. The large spatial coverage will allow not only the robust subtraction of the background sources, but also the recovery of any AGB stars located on the outskirts of the galaxies. Because these data will be observed at a new epoch, we may also discover AGB stars that are potentially variable, which would indicate strong mass loss. If any significant stellar variability is detected, we will proposed to obtain more epochs of data, allowing robust measurements of periods and amplitudes.

6.1.3 SED modeling of AGB stars

In this dissertation, we presented IR photometry of AGB stars in many different stellar systems. With the exception of the follow-up ω Cen study briefly described in chapter 5, only the IR photometric colors are used to determine mass-loss rates and dust characteristics. When using only colors, the IR is the best region of the electromagnetic spectrum to carry out these types of analyses; IR colors such as *Spitzer's* [3.6] − [8] are highly sensitive to the presence of circumstellar dust, as dust shows up as excess emission at 8 μm, whilst leaving the 3.6 μm photometry unaffected. However, the information gathered from colors alone can be considered only a first-order estimate because there are many degeneracies in dust and stellar characteristics.

In order to obtain more accurate estimates of dust compositions and mass-loss rates, we need to construct more complete SEDs of AGB stars and fit these SEDs to models (e.g., DUSTY or MARCS models, Nenkova et al. 1999; Gustafsson et al. 2008). This type of analysis has proven successful in ω Cen, and we plan to extend it to other stellar systems. Ground- and space-based optical observations have been carried out for most of the Local Group dwarf galaxies and Galactic GCs that we have discussed in this thesis. For GCs, we can collect all of the *Spitzer* data (3.6, 4.5, 5.8, 8, 24, and 70 μm) and public near-IR 2MASS data (J-, H-, and K-bands) in addition to the optical data to populate the SED sufficiently for accurate fitting. AKARI data, which has a similar sensitivity to *Spitzer* data, ranging from 2.4 – 90 μm, can also be included once these data are made public.

Ancillary observations for the dwarf galaxies have not yet been completed. We have proposed and have been approved to obtain near-IR observations of the dwarf galaxies using the soon-to-be-installed WFPC3 camera on the *Hubble Space Telescope*. WFPC3 should be conducting science observations by late-2009. We have also been awarded time on *Spitzer* to use the IRS peak-up array to observe the dwarf galaxies at 16 μm, although it is uncertain whether these observations will be completed before the cryogens onboard *Spitzer* are depleted. As with GCs, AKARI data can be used to populate the IR portion of the SED once it is made available.

With SEDs populated from the optical through the mid-IR, we will be able to fit MARCS and/or DUSTY models to individual super-TRGB sources, yielding estimates not only of dust mass-loss rates, but also of dust compositions. Silicate dust tends to emit a strong, very broad feature around 9 μm, which is covered by *Spitzer* and AKARI filters. Amorphous carbon dust has no strong emission features, rather it smoothly increases the flux over the blackbody flux at wavelengths redward of $\approx$5 μm. Figure 6.2 shows how SED fitting over the mid-IR wavelength range will allow us to distinguish between these two compositions.

With a large enough sample of AGB stars in a wide variety of stellar systems, we can estimate how metallicity affects mass-loss rates and dust production and composition. SED fitting may also prove useful for distinguishing between AGB stars and background galaxies in the Local Group dwarf irregular galaxies.

6.2 Possible Future Observations of AGB Stars

Before the launch of *Spitzer*, IR observatories were not sensitive enough to detect and resolve extragalactic AGB stars. As a result, *Spitzer* has been responsible for a great leap forward in our understanding of AGB star mass loss and dust production. *Spitzer* has provided us with the first IR measurements of many distant extragalactic systems, including the observations of Local Group dwarf galaxies and globular clusters. On the other hand, the observations in this dissertation pushed *Spitzer* to its limits, and while photometry was attainable, IR spectroscopy of individual stars has remained out-of-reach for faint sources in these distant systems. Fortunately, there are many IR and sub-mm observatories that will be operating within the next few years, meaning that our understanding of AGB stars will continue to grow.

Possibly the most exciting of these new observatories is the *James Webb Space Telescope* (JWST). JWST is a 6.5 m IR telescope expected to launch in 2013. Imagers and spectrometers onboard JWST will cover 0.6 – 26 μm with sensitivity three orders of magnitude better than *Spitzer*. Analysis of *Spitzer* low-resolution spectra of AGB stars in the Magellanic Clouds (MCs) have provided us with an incredible amount of information about mass-losing stars. For example, Sloan et al. (2008) discovered a tentative correlation between the dust-production rate and the metallicity for oxygen-rich stars, but not for carbon-rich stars. However, the metallicities considered in this study were only those of the MCs, ranging from $-0.8 < [\mathrm{Fe/H}] < -0.4$, which is much more metal-rich than the dwarf galaxies and GCs studied in this dissertation. JWST will be sensitive enough to obtain spectra of stars in more distant stellar systems than

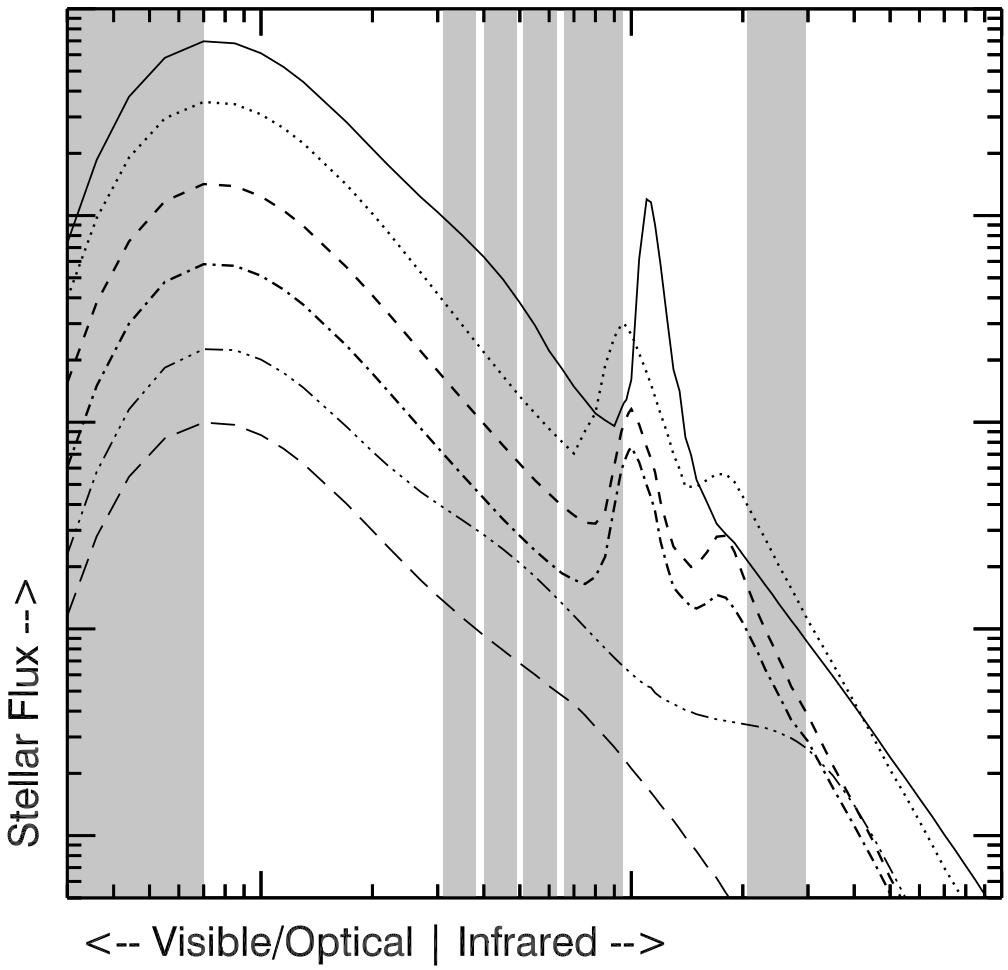

Figure 6.2: Sample DUSTY model spectra of AGB stars. Each spectrum shows a different dust composition (each line is shifted up or down to prevent confusion from crowding). The shaded areas show the wavelength regions covered by *Spitzer* data and ancillary optical data. The addition of AKARI and WFP3 data will fill in some of the missing regions, making the SED fitting more robust.

the MCs, and with high-resolution spectroscopy of individual stars in these distant systems, we will significantly broaden our stellar age and metallicity baselines for studies of this type.

6.3 Future Work on The Intracluster Medium in GCs

As discussed in chapter 2, *Spitzer's* unprecedented sensitivity allowed us to securely detect and image intracluster dust in a GC for the first time. Observations of at least 14 other GCs with *Spitzer* and AKARI (chapters 5 and 3, Boyer et al. 2008a; Barmby et al. 2008; Matsunaga et al. 2008) reveal no large intracluster dust clouds, providing dust mass upper limits $< 4 \times 10^{-4}$ $M_{\odot}$. The question, however, remains: are all GCs devoid of dust, or is the dust simply too diffuse or too cold to be measured with *Spitzer* and AKARI? It appears that some mechanism appears to be removing dust on short timescales from GCs, but current data prevents us from determining what this mechanism might be. The only way to answer any of these questions is to conduct a survey of all, or most, Galactic GCs with a mid-IR to sub-mm observatory, eliminating any selection biases introduced in the small sample sizes of past studies. The cold era for *Spitzer* will be ending soon, so we are setting our sights on the next generation of observatories such as the Stratospheric Observatory for Infrared Astronomy (SOFIA), and especially the Herschel Space Observatory.

Herschel is a far-IR, sub-mm observatory to be launched in 2009. Simultaneous imaging at 110, 160, 250, 350, and 500 μm, with sensitivity better than *Spitzer*, will detect any cold dust present in GCs. In addition, [C II] high-resolution spectroscopy will detect cooling from warm, neutral/ionized gas, making it possible to associate any emission with the cluster. Once Herschel is launched and scientific verification has been completed, we will propose to observe any GCs near enough to be detectable by Herschel's instruments. Such a program will allow us to (1) detect or place stringent limits on the ICM dust mass, and (2) investigate various ICM removal mechanisms (see

chapter 5).

SOFIA is another option for ICM observations. SOFIA is about one order of magnitude less sensitive than Herschel around 100 μm, similar to that of the Infrared Space Observatory, which was used to detect the ICM in M15 at the $3\,\sigma$ level (Evans et al. 2003). Since the ICM in M15 is by far the most massive (and therefore brightest) dusty ICM detected in any GC to date, SOFIA will likely not be useful for ICM photometry in large numbers of other GCs. However, SOFIA will be useful for follow-up spectroscopy and photometry of any bright ICMs discovered with Herschel, allowing us to populate the SED and potentially ascertain the ICM chemistry.

References

Abell, G. O. 1995, VizieR Online Data Catalog, 7004, 0

Adams, S., Seaton, M. J., Howarth, I. D., Auriére, M., & Walsh, J. R. 1984, MNRAS, 207, 471

Albert, L., Demers, S., & Kunkel, W. E. 2000, AJ, 119, 2780

Alves, D. R., Bond, H. E., & Livio, M. 2000, AJ, 120, 2044

Amari, S., et al. 2001, ApJ, 546, 248

Asplund, M., Grevesse, N., Sauval, A. J., Allende Prieto, C., & Kiselman, D. 2004, A&A, 417, 751

Auriére, M., Le Févre, O., & Terzan, A. 1984, A&A, 138, 415

Bajaja, E., Cappa de Nicolau, C. E., Cersosimo, J. C., Martin, M. C., Loiseau, N., Morras, R., Olano, C. A., & Poeppel, W. G. L. 1985, ApJS, 58, 143

Barker, T. 1983, ApJ, 270, 641

Barmby, P., Boyer, M. L., Woodward, C. E., Gehrz, R. D., van Loon, J. T., Fazio, G. G., Marengo, M., & Polomski, E. 2008, arXiv:0810.1902

Barmby, P., et al. 2006, ApJL, 650, L45

Barnes, D. G., & de Blok, W. J. G. 2004, MNRAS, 351, 333

Barnes, D. G., et al. 2001, MNRAS, 322, 486

Battinelli, P., & Demers, S. 2000, AJ, 120, 1801

Battinelli, P., & Demers, S. 2004, A&A, 416, 111

Battinelli, P., & Demers, S. 2005, A&A, 434, 657

Becker, S. A. 2000, in Allen's Astrophysical Quantitites, ed. A. N. Cox (4^{th} ed.; New York: AIP), 515

Bellazzini, M., Ferraro, F. R., Sollima, A., Pancino, E., & Origlia, L. 2004, A&A, 424, 199

Bianchi, L., et al. 2001, AJ, 122, 1538

Birkinshaw, M., Ho, P. T. P., & Baud, B. 1983, A&A, 125, 271

Blum, R. D., et al. 2006, AJ, 132, 2034

Bolatto, A. D., et al. 2007, ApJ, 655, 212

Bono, G., Caputo, F., & Marconi, M. 1995, AJ, 110, 2365

Bouchard, A., Carignan, C., & Mashchenko, S. 2003, AJ, 126, 1295

Bouchard, A., Carignan, C., & Staveley-Smith, L. 2006, AJ, 131, 2913

Boyer, M. L., McDonald, I., van Loon, J. Th., Woodward, C. E., Gehrz, R. D., Evans, A., Dupree, A. K. 2008a, AJ, 135,1395

Boyer, M. L., Skillman, E. D., van Loon, J. Th., Gehrz, R. D., & Woodward, C. E. 2008b, ApJ, Submitted.

Boyer, M. L., Woodward, C. E., van Loon, J. Th., Gordon, K. D., Evans, A., Gehrz, R. D., Helton, L. A., & Polomski, E. F. 2006, AJ, 132, 1415

Cacciari, C. et al. 2004, A&A, 413, 343

Cannon, J. M., Skillman, E. D., Garnett, D. R., & Dufour, R. J. 2002, ApJ, 565, 931

Charles, P. A., Jones, D. C., & Naylor, T. 1986, Nature, 323, 417

Chiosi, C., & Maeder, A. 1986, ARA&A, 24, 329

Cioni, M.-R. L., et al. 2003, A&A, 406, 51

Cohen, J. G., Briley, M. M., & Stetson, P. B. 2005, AJ, 130, 1177

Cole, A. A., et al. 2007, ApJL, 659, L17

Condon, J. J., Cotton, W. D., Greisen, E. W., Yin, Q. F., Perley, R. A., Taylor, G. B., & Broderick, J. J. 1998, AJ, 115, 1693

Da Costa, G. S. 1994, Dwarf Galaxies, 221

Dale, D. A., et al. 2005, ApJ, 633, 857

Daulton, T. L., et al. 2002, Science, 296, 1852

Del Principe, M., et al. 2006, ApJ, 652, 362

Dinerstein, H. L., Richter, M. J., Lacy, J. H., & Sellgren, K. 2003, AJ, 125, 265

Diolaiti, E., Bendinelli, O., Bonaccini, D., Close, L., Currie, D., & Parmeggiani, G. 2000, A&AS, 147, 335

Dolphin, A. E., et al. 2001, ApJ, 550, 554

Dolphin, A. E., et al. 2002, AJ, 123, 3154

Dolphin, A. E., et al. 2003a, AJ, 125, 1261

Dolphin, A. E., et al. 2003b, AJ, 126, 187

Dolphin, A. E., Weisz, D. R., Skillman, E. D., & Holtzman, J. A. 2005, ArXiv Astrophysics e-prints, arXiv:astro-ph/0506430

Dupree, A. K., Hartmann, L., & Avrett, E.H. 1984, ApJ, 281, L37

Dupree, A. K., Sasselov, D. D., & Lester, J. B. 1992, ApJL, 387, L85

Engelbracht, C. W., et al. 2007, PASP, 119, 994

Evans, A., Stickel, M., van Loon, J. Th., Eyres, S. P. S., Hopwood, M. E. L., & Penny, A. J. 2003, A&A, 408, L9

Faulkner, D. J., Scott, T. R., Wood, P. R., & Wright, A. E. 1991, ApJL, 374, L45

Fazio, G. G., et al. 2004, ApJS, 154, 10

Fehrenbach, C. H. & Duflot, M. 1962, ESO Comm., No. 2

Fernandez, A., Mathez, G., & Nottale, L. 1996, VizieR Online Data Catalog, 7088, 0

Forte, J. C., Bassino, L. P., Vega, E. I., Pellizza González, L. J., Cellone, S. A., & Méndez, M. R. 2002, AJ, 123, 3263

Freeman, K. C. 1993, The Globular Cluster-Galaxy Connection, 48, 608

Freire, P. C., Kramer, M., Lyne, A. G., Camilo, F., Manchester, R. N., & D'Amico, N. 2001, ApJL, 557, L105

Gail, H.-P., & Sedlmayr, E. 1986, A&A, 161, 201

Gail, H.-P., & Sedlmayr, E. 1987, A&A, 177, 186

Gallagher, J. S., Tolstoy, E., Dohm-Palmer, R. .C., Skillman, E. D., Cole, A. A., Hoessel, J. G., Saha, A., & Mateo, M. 1998, AJ, 115, 1869

Gallart, C. 2008, Pathways Through an Eclectic Universe, 390, 278

Garnett, D. R., & Lacy, J. R. 1993, ApJ, 419, L93

Gauger, A., Sedlmayr, E., & Gail, H.-P. 1990, A&A, 235, 345

Gehrz, R. 1989, Interstellar Dust, 135, 445

Gehrz, R. D., et al. 2007, Review of Scientific Instruments, 78, 011302

Gehrz, R. D., & Woolf, N. J. 1971, ApJ, 165, 285

Gehrz, R. D., Woodward, C. E., Temim, T., Lyke, J. E., & Mason, C. 2005, AJ, 623, 1105

Gehrz, R. D., & Woolf, N. J. 1971, ApJ, 165, 285

Giovanelli, R., & Haynes, M. P. 1993, AJ, 105, 1271

Girardi, L., & Marigo, P. 2007, A&A, 462, 237

Gnedin, O. Y., Zhao, H., Pringle, J. E., Fall, S. M., Livio, M., & Meylan, G. 2002, ApJ, 568, L23

Gordon, K. D., et al. 2005, PASP, 117, 503

Gordon, K. D., et al. 2006, ApJL, 638, L87

Gordon, K. D., et al. 2007, PASP, 119, 1019

Gould, R. J., & Salpeter, E. E. 1963, ApJ, 138, 393

Gratton, R., Sneden, C., & Carretta, E. 2004, ARA&A, 42, 385

Groenewegen, M. A. T. 2006, A&A, 448, 181

Gruendl, R. A., Chu, Y. -., Seale, J. P., Matsuura, M., Speck, A. K., Sloan, G. C., & Looney, L. W. 2008, arXiv:0809.5107

Gullieuszik, M., Rejkuba, M., Cioni, M. R., Habing, H. J., & Held, E. V. 2007, A&A, 475, 467

Gustafsson, B., Edvardsson, B., Eriksson, K., Jørgensen, U. G., Nordlund, Å., & Plez, B. 2008, A&A, 486, 951

Habing, H. J., & Olofsson, H. 2003, Asymptotic giant branch stars, (New York: Springer)

Hansen, B. M. S. 2005, ApJ, 635, 522

Harris, W. E. 1996, AJ, 112, 1487

Hoffman, G. L., Salpeter, E. E., Farhat, B., Roos, T., Williams, H., & Helou, G. 1996, ApJS, 105, 269

Höfner, S., & Dorfi, E. A. 1997, A&A, 319, 648

Holtzman, J. A., Afonso, C., & Dolphin, A. 2006, ApJS, 166, 534

Holtzman, J. A., Smith, G. H., & Grillmair, C. 2000, AJ, 120, 3060

Hopwood, M. E. L., Eyres, S. P. S., Evans, A., Penny, A., & Odenkirchen, M. 1999, A&A, 350, 49

Hopwood, M. E. L., et al. 2000, MNRAS, 316, L5

Houck, J., et al. 2004, ApJS, 154, 10

Howard, J. W., Henry, R. B. C., & McCartney, S. 1997, MNRAS, 284, 465

Huchtmeier, W. K., Seiradakis, J. H., & Materne, J. 1981, A&A, 102, 134

Hummer, D. G., Berrington, K. A., Eissner, W., Pradhan, Anil K., Saraph, H. E., & Tully, J. A. 1993, A&A, 279, 298

Hummer, D. G., & Storey, P. J. 1987, MNRAS, 224, 801

Iben, I. Jr., & Renzini, A. 1983, ARA&A, 21, 271

Indebetouw, R., et al. 2005, ApJ, 619, 931

Ita, Y., et al. 2007, PASJ, 59, 437

Ivezić, Ž., & Elitzur, M. 1995, ApJ, 445, 415

Jackson, D. C., Cannon, J. M., Skillman, E. D., Lee, H., Gehrz, R. D., Woodward, C. E., Polomski, E. 2006, ApJ, 646, 192

Jackson, D. C., Skillman, E. D., Gehrz, R. D., Polomski, E., Woodward, C. E. 2007a, ApJ, 656, 818

Jackson, D. C., Skillman, E. D., Gehrz, R. D., Polomski, E., Woodward, C. E. 2007b, ApJ, 667, 891

Jacoby, G. H., Morse, J. A., Fullton, L. K., Kwitter, K. B., & Henry, R. B. C. 1997, AJ, 114, 2611

Jeong, K. S., Winters, J. M., & Sedlmayr, E. 1999, IAU Symp. 191: Asymptotic Giant Branch Stars, 191, 233

Jura, M. 1984, ApJ, 282, 200

Jura, M., & Morris, M. 1985, ApJ, 292, 487

Kalirai, J. S., Bergeron, P., Hansen, B. M. S., Kelson, D. D., Reitzel, D. B., Rich, R. M., & Richer, H. B. 2007, ApJ, 671, 748

Kennicutt, R., et al. 2007, Bulletin of the American Astronomical Society, 38, 894

Kennicutt, R. C., Jr., Tamblyn, P., & Congdon, C. E. 1994, ApJ, 435, 22

Krist, J. 2002, Tiny Tim/*SIRTF* User's Guide (Pasadena: *Spitzer* Sci. Center)

Kulkarni, S. R., & Anderson, S. B. 1996, IAU Symp. 174, Dynamical Evolution of Star Clusters: Confrontation of Theory and Observations, ed. P. Hut, & J. Makino (Dordrecht: Kluwer), 181

Lagadec, E., & Zijlstra, A. A. 2008, MNRAS, 390, L59

Lattanzio, J. C. 2002, New Astronomy Review, 46, 469

Lebzelter, Th., Posch, Th., Hinkle, K., Wood, P. R., & Bouwman, J. 2006, ApJ, 653, L145

Lee, H., Skillman, E. D., Cannon, J. M., Jackson, D. C., Gehrz, R. D., Polomski, E. F., & Woodward, C. E. 2006, ApJ, 647, 970

Lee, M. G. 1995, AJ, 110, 1129

Lee, M. G., Aparicio, A., Tikonov, N., Byun, Y.-I., & Kim, E. 1999a, AJ, 118, 853

Lee, Y.-W., Joo, J.-M., Sohn, Y.-J., Rey, S.-C., Lee, H.-C., & Walker, A. R. 1999b, Nature, 402, 55

Leinert, C., Ábrahám, P., Acosta-Pulido, J., Lemke, D., & Siebenmorgen, R. 2002, A&A, 393, 1073

Lo, K. Y., Sargent, W. L. W., & Young, K. 1993, AJ, 106, 507

Lonsdale, C., et al. 2004, ApJS, 154, 54

Loup, C., Zijlstra, A. A., Waters, L. B. F. M., & Groenewegen, M. A. T. 1997, A&AS, 125, 419

Lub, J. 2002, Omega Centauri, A Unique Window into Astrophysics, 265, 95

Makovoz, D., & Marleau, F. R. 2005, PASP, 117, 1113

Marengo, M., Hora, J. L., Barmby, P., Willner, S. P., Allen, L. E., Schuster, M. T., & Fazio, G. G. 2007, Why Galaxies Care About AGB Stars: Their Importance as Actors and Probes, 378, 80

Marigo, P., Girardi, L., Bressan, A., Groenewegen, M. A. T., Silva, L., & Granato, G. L. 2008, A&A, 482, 883

Marshall, J. R., van Loon, J. Th., Matsuura, M., Wood, P. R., Zijlstra, A. A. & Whitelock, P. A. 2004, MNRAS, 355, 1348

Massey, P., Olsen, K. A. G., Hodge, P. W., Strong, S. B., Jacoby, G. H., Schlingman, W., & Smith, R. C. 2006, AJ, 131, 2478

Mateo, M. L. 1998, ARA&A, 36, 435

Mathis, J. S., Rumpl, W., & Nordsieck, K. H. 1977, ApJ, 217, 425

Matsunaga, N., et al. 2008, arXiv:0809.2853

McConnachie, A. W., Arimoto, N., Irwin, M., & Tolstoy, E. 2006, MNRAS, 373, 715

McDonald, I., & van Loon, J. T. 2007, A&A, 476, 1261

McDonald, I., van Loon, J. Th., Decin, L., Boyer, M .L., Woodward, C. E., Gehrz, R. D., Evans, A., & Dupree, A. K. 2008, MNRAS, In press.

McNamara, B. J., Harrison, T. E., & Baumgardt, H. 2004, ApJ, 602, 264

Menzies, J., Feast, M., Whitelock, P., Olivier, E., Matsunaga, N., & Da Costa, G. 2008, MNRAS, 385, 1045

Meszaros, S., Dupree, A. K., & Szentgyorgyi, A. 2008, AJ, 135, 1117

Miller, B. W., Dolphin, A. E., Lee, M. G., Kim, S. C., & Hodge, P. 2001, ApJ, 562, 713

Moore, B. D., Hester, J. J., & Dufour, R. J. 2004, AJ, 127, 3484

Nenkova, M., Ivezic, Z., & Elitzur, M. 1999, LPI Contributions, 969, 20

Norris, J. E. 1996, ApJ, 462, 241

Norris, J. E. 2004, ApJ, 612, L25

Odenkirchen, M., Brosche, P., Geffert, M., & Tucholke, H.-J. 1997, NewA, 2, 477

Orban, C., Gnedin, O. Y., Weisz, D. R., Skillman, E. D., Dolphin, A. E., & Holtzman, J. A. 2008, arXiv:0805.1058

Origlia, L., Ferraro, F. R., Bellazzini, M., & Pancino, E. 2003, ApJ, 591, 9160

Origlia, L., Ferraro, F. R., Fusi Pecci, F., & Rood, R. T. 2002, ApJ, 571, 458

Origlia, L., Rood, R. T., Fabbri, S., Ferraro, F. R., Fusi Pecci, F., & Rich, R. M. 2007, ApJL, 667, L85

Ossenkopf, V., & Henning, Th. 1994, A&A, 291, 943

Osterbrock, D. E. 1999, Astrophysics of Gaseous Nebulae and Active Galactic Nuclei (Mill Valley: University Science)

Pancino, E., Ferraro, F. R., Bellazzini, M., Piotto, G., & Zoccali, M. 2000, ApJ, 534, L83

Pancino, E., Pasquini, L., Hill, V., Ferraro, F. R., & Bellazzini, M. 2002, ApJ, 568, L101

Pease, F. G. 1928, PASP, 40, 342

Peña, M., Torres-Peimbert, S., Peimbert, M., & Dufour, R. J. 1993, Rev. Mex. AA, 27, 175

Phinney, F. S. 1996, in ASP Conf. Ser. 90, The Origins, Evolution, and Destinies of Binary Stars in Clusters, ed. E. F. Milone, J.-C. Mermilliod (San Francisco: ASP), 163

Pilachowski, C. A., Sneden, C., Kraft, R. P., Harmer, D., & Willmarth, D. 2000, AJ, 119, 2895

Ramdani A., & Jorissen, A. 2001, A&A, 372, 85

Rank, D. M., Dinerstein, H. L., Lester, D. F., Bregman, J. D., Aitken, D. K., & Jones, B. 1978, MNRAS, 185, 179

Reach, W. T., et al. 2005, PASP, 117, 978

Rieke, G. H., & Lebofsky, M. J. 1985, ApJ, 288, 618

Rieke, G. H., et al. 2004, ApJS, 154, 25

Robin, A. C., Reylé, C., Derrière, S., & Picaud, S. 2003, A&A, 409, 523

Rood, R. T. 1973, ApJ, 184, 815

Salpeter, E. E. 1974, ApJ, 193, 579

Sandage, A. 1986, A&A, 161, 89

Sanders, D. B., et al. 2007, ApJS, 172, 86

Saraph, H. E., & Tully, J. A. 1994, A&AS, 107, 29

Schlegel, D. J., Finkbeiner, D. P., & Davis, M. 1998, ApJ, 500, 525

Schröder, K.-P., & Cuntz, M. 2005, ApJL, 630, L73

Seaton, M. J. 1979, MNRAS, 187, 73P

Shaw, R. A., & Dufour, R. J. 1995, PASP, 107, 896

Skrutskie, M. F., et al. 2006, AJ, 131, 1163

Sloan, G. C., Kraemer, K. E., Matsuura, M., Wood, P. R., Price, S. D., & Egan, M. P. 2006, ApJ, 645, 1118

Sloan, G. C., Kraemer, K. E., Wood, P. R., Zijlstra, A. A., Bernard-Salas, J., Devost, D., & Houck, J. R. 2008, ApJ, 686, 1056

Smith, G. H., Dupree, A. K., & Strader, J. 2004, PASP, 116, 819

Smith, G. H., Wood, P. R., Faulkner, D. J., & Wright, A. E. 1990, ApJ, 353, 168

Smith, V. V., Suntzeff, N. B., Cunha, K., Gallino, R., Busso, M., Lambert, D. L., & Straniero, O. 2000, AJ, 119, 1239

Sneden, C., Kraft, R. P., Shetrone, M. D., Smith, G. H., Langer, G. E., & Prosser, C. F. 1997, AJ, 114, 1964

Sollima, A., Ferraro, F. R., Origlia, L., Pancino, E., & Bellazzini, M. 2004, A&A, 420, 173

Sollima, A., Ferraro, F. R., Origlia, L., Pancino, E., & Bellazzini, M. 2004, VizieR Online Data Catalog, 342, 173

Sollima, A., Pancino, E., Ferraro, F. R., Bellazzini, M., Straniero, O., & Pasquini, L. 2005, ApJ, 634, 332

Spergel, D. N. 1991, Nature, 352, 221

Spitzer, L. 1987, Dynamical Evolution of Globular Clusters (Princeton: Princeton Univ. Press)

Spitzer Science Center. 2006a, Infrared Array Camera Data Handbook (Pasadena: SSC), http://ssc.spitzer.caltech.edu/irac/dh/

Spitzer Science Center. 2006b, Multiband Imaging Photometer for *Spitzer* (MIPS) Data Handbook (Pasadena: SSC), http://ssc.spitzer.caltech.edu/mips/dh/

Stanford, L. M., Da Costa, G. S., Norris, J. E., & Cannon, R. D. 2006, ApJ, 647, 1075

Stetson, P. B. 1987, PASP, 99, 191

Stetson, P. B., Bruntt, H., & Grundahl, F. 2003, PASP, 115, 413

Sun, X.-H., Han, J.-L., & Qiao, G.-J. 2002, Chinese J. Astron. Astrophys., 2, 133

Tayler, R. J., & Wood, P. R. 1975, MNRAS, 171, 467

Taylor, J. H., Manchester, R. N., & Lyne, A. G. 1993, ApJS, 88, 529

Trams, N. R., et al. 1999, A&A, 346, 843

Umbreit, S., Chatterjee, S., & Rasio, F. A. 2008, ApJL, 680, L113

Valenti, E., Ferraro, F. R., & Origlia, L. 2007, AJ, 133, 1287

VandenBergh, D. A. & Faulkner, D. J. 1977, ApJ, 218, 415

van de Ven, G., van den Bosch, R. C. E., Verolme, E. K., & de Zeeuw, P. T. 2006, A&A, 445, 513

van Leeuwen, F., Le Poole, R. S., Reijns, R. A., Freeman, K. C., & de Zeeuw, P. T. 2000, A&A, 360, 472

van Loon, J. Th. 2000, A&A, 354, 125

van Loon, J. Th. 2006, Stellar Evolution at Low Metallicity: Mass Loss, Explosions, Cosmology, 353, 211

van Loon, J. Th., Cohen, M., Oliveira, J. M., Matsuura, M., McDonald, I., Sloan, G. C., Wood, P. R., & Zijlstra, A. A. 2008, A&A, 487, 1055

van Loon, J. Th., Groenewegen, M. A. T., de Koter, A., Trams, N. R., Waters, L. B. F. M., Zijlstra, A. A., Whitelock, P. A., & Loup, C. 1999, A&A, 351, 559

van Loon, J. Th., Marshall, J. R., & Zijlstra, A. A. 2005, A&A, 442, 597

van Loon, J. T., & McDonald, I. 2008, Mass Loss from Stars and the Evolution of Stellar Clusters, 388, 407

van Loon, J. Th., McDonald, I., Oliveira, J. M., Evans, A., Boyer, M. L., Gehrz, R. D., Polomski, E., & Woodward, C. E. 2006a, A&A, 450, 339

van Loon, J. Th., Stanimirović, S., Evans, A., & Muller, E. 2006b, MNRAS, 365, 1277

van Loon, J. Th., van Leeuwen, F., Smalley, B., Smith, A. W., Lyons, N. A., McDonald, I., & Boyer, M. L. 2007, MNRAS, 382, 1353

van Loon, J. Th., Zijlstra, A. A., Whitelock, P. A., Waters, L. B. F. M., Loup, C., & Trams, N. R. 1997, A&A, 325, 585

van Loon, J. Th., et al. 2003, MNRAS, 338, 857

Vansevičius, V., et al. 2004, ApJL, 611, L93

van Zee, L., Skillman, E. D., Haynes, M. P. 2006, ApJ, 637, 269

Vassiliadis, E., & Wood, P. R. 1993, ApJ, 413, 641

Villanova, S., et al. 2007, ApJ, 663, 296

Volders, L. M. J. S., & Högbom, J. A. 1961, BAN, 15, 307

Webbink, R. F. 1985, in IAU Symp. 113, Dynamics of Star Clusters, ed. J. Goodman & P. Hut (Dordrecht: Reidel), 541

Werner, M. W., et al. 2004, ApJS, 154, 1

Whitelock, P. A., Feast, M. W., van Loon, J. T., & Zijlstra, A. A. 2003, MNRAS, 342, 86

Whitelock, P.A., Menzies, J., Feast, M., Matsunaga, N., Tanabé, T., Ita, Y. 2008, MNRAS, Submitted

Young, L. M., & Lo, K. Y. 1996, ApJ, 462, 203

Young, L. M., Skillman, E. D., Weisz, D. R., & Dolphin, A. E. 2007, ApJ, 659, 331

Zijlstra, A. A., Loup, C., Waters, L. B. F. M., Whitelock, P. A., van Loon, J. Th., & Guglielmo, F. 1996, MNRAS, 279, 32

Zinnecker, H., Keable, C. J., Dunlop, J. S., Cannon, R. D., & Griffiths, W. K. 1988, The Harlow-Shapley Symposium on Globular Cluster Systems in Galaxies, 126, 603